



Universidad
Carlos III de Madrid

PhD Thesis

Physical simulation of investment casting of Mar-M247 Ni-based superalloy

Author:

Mehdi Rahimian

Supervisors:

Dr. Ilchat Sabirov

Dr. Srdjan Milenkovic

A Dissertation submitted for the degree of Doctor of Philosophy at the
Department of Materials Science and Engineering
and Chemical Engineering

Carlos III University of Madrid

Leganés, July 2015

TESIS DOCTORAL

Physical simulation of investment casting of Mar- M247 Ni-based superalloy

Autor: Mehdi Rahimian

Directores: Dr. Ilchat Sabirov

Dr. Srdjan Milenkovic

Firma del Tribunal Calificador:

Firma

Presidente: Dr. José Manuel Torralba Castelló

Vocal: Dr. Koldo Mirena Ostolaza Zamora

Secretario: Dr. María Teresa Pérez Prado

Calificación:

Leganés 13 de Julio de 2015

“Science is based on experiment; on a willingness to challenge old dogma; on an openness to see the universe as it really is. Accordingly, science sometimes requires courage - at the very least the courage to question the conventional wisdom”

Carl Sagan

Abstract

Mar-M247 is a Ni-based superalloy developed for high temperatures applications, such as advanced jet engines, where high strength and excellent creep resistance are required. Investment casting process has been widely used for fabrication of complex shape parts and is only commercially technique for fabrication of nozzle guide vanes (NGVs) known as a one of the most important structural parts of engines and gas turbines. Nevertheless, the development of NGVs is hindered by the complexity of investment casting process of complex shape parts. In other words, existing methods for development of investment casting routes, like *trial and error* approach combined with modeling, are suffering from the operation expenses and accurate prediction of microstructural features, respectively. Therefore, there is high demand to find and apply a method to overcome those drawbacks. Physical simulation of investment can be a method to tackle these shortcomings.

Physical simulation of investment casting was developed to mimic solidification of alloy during investment casting of new generation NGVs from Mar-M247 by high capability physical simulator machines. This tool, consisting of thermal model and melting/solidification experiments, is the exact reproduction of the thermal and mechanical history of full scale investment casting process in the laboratory scale. Initially, the Pro-Cast based thermal model was developed, validated and applied to predict local cooling rates at defined points of NGVs. Then, the outcomes of the modeling were used as input parameters for the melting/solidification experiments in the thermo-mechanical simulator Gleeble 3800. Finally, the validation of physical simulation was carried out by comparison of microstructural and hardness properties of Gleeble specimens and as-cast NGV. In addition, in order to get a deeper insight into the correlation between Mar-M247 characteristics with casting/solidification conditions, the effect of solidification variables and double heat treatment process on the microstructural features and hardness were investigated.

It was demonstrated that physical simulation tool predicts well all microstructural aspects including skin features, local secondary dendrite arm spacing (SDAS), grain structure, phase composition, morphology of carbide particles, as well as microhardness. It was observed that increasing cooling rate resulted in microstructural refinement along with an increase of

hardness. Apart from few microstructural variations during double heat treatment, it eliminated or decreased unstable phases. Complementary study on SDAS showed that temperature gradient should be taken into account as an effective factor influencing the SDAS. Furthermore, the skin formation and its grain texture were studied by utilizing the combination of electron back scatter diffraction (EBSD) and nanoindentation method.

Resumen

La aleación Mar-M247 es una superaleación base níquel desarrollada para aplicaciones de alta temperatura, como por ejemplo en motores a reacción avanzados, donde alta resistencia y resistencia a fluencia son necesarias. La fundición de precisión a la cera perdida ha sido utilizada ampliamente para la fabricación de los álabes guía de turbina (NGV, por sus siglas en inglés), una de las partes estructurales más importantes en motores y turbinas. No obstante, el desarrollo de dichos álabes está obstaculizado por la complejidad del proceso de moldeo por colada para formas complejas. En otras palabras, los métodos existentes para el desarrollo de rutas de fundición como *prueba y error*, combinado con la modelización, se ven afectados por los costes de operación en el primer caso y en la precisión de la predicción de las particularidades microestructurales en el segundo. Por ello, existe una alta demanda para encontrar y aplicar un método que salve estas desventajas. La simulación física del proceso de colada puede ser ese método buscado.

La simulación física del proceso de colada fue desarrollada para imitar la solidificación de la aleación Mar-M247 durante la fundición de precisión de la nueva generación de NGVs por máquinas de simulación física de altas capacidades. Esta herramienta, consiste en un modelo térmico sumado a ensayos de fusión/solidificación, y es la reproducción exacta, a nivel de laboratorio, de la historia térmica y mecánica a gran escala del proceso de fundición. Inicialmente fue desarrollado, validado y aplicado el modelo térmico basado en Pro-Cast para predecir las velocidades de enfriamiento locales en puntos definidos de los NGVs. A continuación los resultados de la modelización se usaron como parámetros iniciales para los experimentos de fusión/solidificación en el simulador termo-mecánico Gleeble 3800. Por último la simulación física fue validada por comparación de las propiedades microestructurales y la dureza entre las muestras procesadas en Gleeble y los propios NGVs. Además, con el objetivo de obtener una visión más profunda de la correlación entre las características de la aleación Mar-M247 y las condiciones de fundición/solidificación, se investigaron los efectos de las variables del proceso de solidificación y doble tratamiento térmico en la microestructura y la dureza.

Queda demostrado que la simulación física reproduce y predice correctamente todos los aspectos microestructurales, tales como rasgos de la zona más superficial, espaciamiento local de las dendritas secundarias (SDAS, por sus siglas en inglés), estructura granular, composición de fases, morfología de los carburos formados, así como la microdureza. Se observó que un incremento en la velocidad de deformación resultaba en un refinamiento de la microestructura así como de la dureza. A parte de pequeñas variaciones microestructurales durante el doble tratamiento térmico, se eliminaban o disminuía la cantidad de fases inestables. Un estudio complementario del SDAS mostró que el gradiente de temperatura debe tomarse en cuenta como un factor importante que influencia el SDAS. Además, la formación de la parte más superficial y su textura granular fue estudiada utilizando una combinación de difracción de electrones retrodispersados (EBSD, por sus siglas en inglés) y nanoindentación.

Preface

This dissertation is submitted for the degree of Doctor of Philosophy in the Carlos III University of Madrid. The research described in this thesis was carried out at IMDEA Materials Institute (Madrid, Spain) during the period September 2011 to June 2015 under the supervision of Dr. Ilchat Sabirov, senior researcher at IMDEA Materials Institute and Dr. Srdjan Milenkovic, researcher at IMDEA Materials Institute and Adjunct professor at the Carlos III University of Madrid.

The results obtained during the course of this thesis have been published in peer-reviewed international journals in Materials Science, including Metallurgical and Materials Transactions A, Philosophical Magazine Letters, Metallurgical and Materials Transactions B, Journal of Alloys and Compounds and two papers in Integrating Materials and Manufacturing Innovation and it also is submitted to the Journal of Materials Processing Technology. Moreover, this work has been well received at international conferences and workshops on superalloys as well as solidification and casting.

To the best of my knowledge, the work described in this dissertation is original, except where due reference has been made to the work of others, and nothing is included which is the outcome of work done in collaboration, unless otherwise stated. No part of this dissertation, or any similar to it, has been, or is currently being, submitted for any degree or other qualification at any other university.

Mehdi Rahimian

Madrid

July 2015

Acknowledgements

I gratefully acknowledge the provision of financial support for the work described in this dissertation by IMDEA Materials Institute. This investigation was supported by *EU, ERA-Matera+, 7th Framework Programme* through the project VANCAST “Next generation nozzle guide vanes”.

I would also like to thank a number of people for their help and support during this PhD. Firstly, I wish to thank my supervisors, Dr Ilchat Sabirov and Dr. Srdjan Milenkovic, for their expert guidance, patience, and assistance in all aspects of this research. Their enthusiasm for doing and communicating research of quality has been inspirational. Their scientific guidance and consideration were not limited to my PhD work but also touched other aspects of my life. I sincerely thank all VANCAST project partners, Laura Maestro and Aitor Eguidazu Ruiz de Azua (Precicast Bilbao), Irene Jimeno Ruiz (ITP), Ole Koeser and Loic Calba (Calcom-ESI), Agustin Jose Torroba Dominguez and Efrain Carreño-Morelli (University of Applied Sciences of Switzerland) for fruitful collaboration during this research and sharing the wealth of their expertise with me, which greatly helped to accomplish this thesis. I would also extend grateful thanks to Prof. Javier LLorca, director of IMDEA Materials Institute for coordination of research activities in the VANCAST project.

I acknowledge Mr. Fernando Naya for tutoring my learning of finite element modeling and for his attempt for modeling of physical simulation of skin formation.

I would like to thank all the members (past and present) of IMDEA Materials Institute for creating a very pleasant working environment. The friendly supportive atmosphere inherent to the whole institute contributed to the final outcome of my studies, not only during the working hours at the institute but also during the free time. To all of them, I am truly grateful. I sincerely thank all my friends those who have helped me throughout my PhD study, and throughout my life.

My deep and humble appreciation goes to my family, in particular my parents, Zahra and Nematollah, my brother Hamid and specially my sister, Maryam for their unconditional love, encouragement and companionship.

Table of content

Abstract.....	i
Resumen.....	iii
Preface.....	v
Acknowledgements	vii
1 Introduction	5
1.1 Background	5
1.2 Motivation for physical simulation of investment casting	6
1.3 The objectives and summary of the work	7
1.4 Outline of the thesis.....	8
2 State of the art.....	10
2.1 Ni-based superalloys-materials for high temperature application.....	10
2.1.1 Mar-M247 Ni-based superalloy	12
2.2 Physical metallurgy of Ni-based superalloys	15
2.2.1 The influence of thermal variation on grain structure	16
2.2.2 The influence of thermal variation on dendritic structure	22
2.2.3 The γ , γ' and secondary γ' phases	25
2.2.4 The influence of thermal variation on carbide morphology	29
2.2.5 The influence of thermal variation on γ/γ' eutectic.....	33
2.2.6 Heat treatment of Ni-based superalloys.....	34
2.2.6.1 The effect of heat treatment on grain characteristic	36
2.2.6.2 The effect of heat treatment on phase composition.....	38
2.2.6.3 The effect of heat treatment on carbide characteristic.....	41
3 Material and experimental techniques	43
3.1 Material	43

3.2	Prediction of local cooling rates during investment casting of NGVs from Mar-M247 Ni-based superalloy using thermal model	44
3.2.1	Development of the thermal model.....	44
3.2.2	Experimental validation of the thermal model.....	53
3.2.3	Explanation of discrepancy	54
3.3	Melting/solidification experiments in Gleeble 3800 thermo-mechanical simulator	56
3.3.1	Preparation of samples for melting/solidification experiments	57
3.3.2	Melting/solidification experiments in a Gleeble 3800 system.....	61
3.4	Microstructural characterization	62
3.4.1	Optical Microscopy (OM).....	63
3.4.2	Scanning Electron Microscopy (SEM)	63
3.4.3	Electron Backscatter Diffraction (EBSD).....	65
3.4.4	Energy Dispersive X-ray (EDX) Spectroscopy	68
3.5	Microhardness and Nanohardness testing	69
3.5.1	Microindentation tests.....	69
3.5.2	Nanomechanical testing: Basic principles of instrumented nanoindentation	70
3.5.2.1	Hardness determination	73
3.5.2.2	Elastic modulus determination	74
3.6	Experimental validation of developed physical simulation tools.....	75
4	Effect of thermal variables and post-cast heat treatment on microstructure and hardness of Mar-M247 Ni-based superalloy	80
4.1.1	Grain structure	82
4.1.2	Dendritic structure	85
4.1.3	Phase composition	86
4.1.4	Hardness.....	90
4.1.5	Conclusions.....	94
4.2	Effect of temperature gradient on secondary dendrite arm spacing of Mar-M247 Ni-based superalloy.....	95

5	Physical simulation of investment casting of NGVs from Mar-M247	104
5.1	Secondary dendrite arm spacing	108
5.2	Grain structure.....	109
5.3	Phase composition.....	110
5.3.1	Carbide particles	110
5.3.2	The γ/γ' eutectic	113
5.4	Microhardness	115
5.5	Advantages of application of physical simulation in development of new investment casting process	116
5.6	Conclusions	117
6	Physical simulation of skin formation during investment casting of NGVs from Mar-M247.....	118
6.1	Development of the tool for physical simulation of skin formation	120
6.1.1	Effect of thermal variable on skin formation.....	123
6.1.1.1	Effect of contact time (ceramic tube temperature) on the skin formation	123
6.1.1.2	Effect of cooling rate on the skin formation.....	127
6.1.2	Validation of physical simulation of skin formation (microstructural and nanohardness study)	128
6.1.2.1	OM and SEM investigation of skin	128
6.1.2.2	EBSD investigation of skin	136
6.1.2.3	Nanohardness study of skin.....	142
6.1.3	Conclusions:.....	147
7	References.....	149
8	Publications	164

1 Introduction

1.1 Background

Ni-based superalloys are known as materials with excellent mechanical strength, creep, corrosion and oxidation resistance at elevated temperatures which can increase up to the 0.6 of their melting points. Superalloys based on their main alloying elements are divided into three groups including Ni, Co and Ni-Fe based superalloys among which Ni-based superalloys represent higher strength and creep resistance at high fraction of their melting points. Whereas Ti-based superalloys are used at lower pressure and temperature, Ni-based superalloys are served at harsher operating condition in an aircraft engine [1–6]. Mar-M247 is a Ni-based superalloy developed by Danesi, Lund and others at Martin Metals Corporation in the 1970s [7]. This alloy has been employed in the aerospace industry for advanced jet engines, turbine rotors, stators, etc. during the past two decades [2–10]. Investment casting process has been widely used for fabrication of various parts of aero engines and gas turbines from Mar-M247 Ni-based superalloy [11]. Investment casting process, known as a lost wax casting or precision casting, is a well established process for production of near net-shape components. Having an excellent surface finish and dimensional accuracy, this process is especially useful for casting of complex shape with thin elements [12,13]. Recently, the search for reduced weight and increased efficiency of aero engines and gas turbines is driving

changes in design of parts to more complex shapes and thinner geometries. However, these innovations are often hindered by the complexity of investment casting of parts with thin elements.

1.2 Motivation for physical simulation of investment casting

Despite the outstanding mechanical properties of Mar-M247 Ni-based superalloy in comparison to other Ni-based superalloys, limited studies have been done to find the correlation between thermal history of melting/solidification process and microstructure and mechanical properties of Mar-M247.

On the other hand, published studies in this field are mostly focused on the directional solidification method, so there is a lack of research on investment casting of this material [9,14–16]. In fact, the aero engine parts made from Mar-M247 are often produced by investment casting and then subjected to additional heat treatments.

Development of investment casting routes for the complex shape parts is usually carried out via a *trial and error* approach or, in other words, via experimental casting trials. The casting parameters are varied until good quality castings are produced. However, this strategy is very expensive and time consuming [17]. Modeling of investment casting is another approach to determine the optimum casting parameters [18]. Simulation of casting is reliable when the accurate data of materials are known at processing conditions, and boundary conditions are defined precisely. However, precise prediction of local phase composition, second phase precipitates, segregations, etc. is out of capabilities of the current casting simulation tools, whereas these microstructural features significantly affect the local mechanical and functional properties in the castings from Ni-based superalloys. In spite of this shortcoming, a comprehensive way has not been found and examined to tackle this problem. Therefore, it is highly demanded to seek and employ a reliable tool to overcome this shortage. Consequently, a tool has to be developed to mimic solidification of investment casting of Mar-M247 Ni-based superalloy.

Recent progress in science and technology creates a new opportunity for researchers to mimic the large scale industrial processes in laboratory by high capability physical simulator machines. Physical simulation of metallurgical processes is often employed for development of novel manufacturing routes. Physical simulation involves the exact reproduction of the

thermal and mechanical processes in the laboratory that the material has to undergo in the full scale fabrication process. There is a body of research where physical simulation of continuous casting was successfully performed [19–21]. However, very little is known about the physical simulation of investment casting process on account of the complexity of this process. The investment casting process is characterized by complex three-dimensional heat flow determined by numerous casting parameters including melt temperature, temperature of ceramic mould, casting shape, thermo-physical properties of ceramic mould and metal, etc. Thus, significant variations of local cooling rate during solidification of complex shape part can be expected in its different sections. As is well known, the thermal profile during solidification and cooling process can significantly affect the local dendritic structure, grain structure, phase composition, thus, resulting in varying local properties over as-solidified parts. Combination of thermal model predicting local cooling rate at each point of the casting and melting/solidification experiments in thermo-mechanical simulator under controlled cooling rate, obtained *a priori* by thermal model, should generate a reliable databank for prediction of local microstructure and mechanical properties in the as-cast parts. Moreover, the physical simulation of investment casting was also applied for reproduction of skin microstructure formed during investment casting of Ni-based superalloy on account of freezing effect. The prediction of skin characterization help us to avoid casting defects like misrun which can be occurred because of skin formation in investment casting of thin and complex shape parts such as NGVs.

1.3 The objectives and summary of the work

The first objective has been to establish processing-microstructure relationship to know the materials characteristics in different production conditions. For this purpose the effect of thermal variables and heat treatment on microstructural evolution and microhardness were investigated. The samples were melted and solidified under controlled cooling rates and then subjected to double heat treatments process. Also for further investigation of SDAS, special experimental setup was used to study the variation of SDAS at different temperature gradient. The main objective of this work has been to develop a novel tool for physical simulation of investment casting. It was applied to the investment casting process of NGV from Mar-M247 Ni-based superalloy. The Pro-Cast based thermal model was developed and applied to predict

local cooling rates at defined points of NGV. The validated outcomes of modeling served as input parameters for the melting/solidification experiments in the thermo-mechanical simulator Gleeble 3800. Microstructural and mechanical characterizations of specimens after melting/solidification experiments (Gleeble specimens) were performed to predict the effect of local cooling rate on the local microstructure and hardness of the material in the as-cast NGV parts. Finally, the experimental casting trials of NGV were carried out to compare their microstructure and hardness with those of Gleeble specimens, for validation of physical simulation of investment casting process. The third objective has been to investigate the mechanism of skin formation. The physical simulation was utilized to imitate the skin microstructure in investment casting of NGVs made of Mar-M247 Ni-based superalloys. The ceramic tube with the same composition of ceramic mould used in investment casting was employed to mimic the real investment casting condition. Other experimental conditions followed the same conditions investment casting process. The validation of physical simulation of skin formation was performed by the comparison between skin properties in physical simulation samples and NGV casting trails at each cooling rate.

1.4 Outline of the thesis

The thesis is divided into six main chapters corresponding to the various dimensions of this study. Chapter 2 contains a literature overview on the effect of thermal variables on the microstructure and mechanical properties of Ni-based superalloys. Chapter 3 is devoted to the experimental procedures. First, the development and validation of thermal model, which was employed for the prediction of local cooling rates during investment casting of NGVs from Mar-M247, is described. Then, the melting/solidification experiments in the Gleeble 3800 thermo-mechanical simulator, is briefly explained, which is accompanied by explanation of applied microstructural and hardness characterization techniques. The last section of this chapter is allocated to the procedure applied for the experimental validation of developed physical simulation tools. Chapter 4 discusses processing-microstructure relationship, including the influence of cooling rate and heat treatment on microstructural features and hardness. In order to have more profound insight into the effect of the varying temperature gradient on microstructure, the variation of SDAS due to the change of temperature gradient was also investigated in this chapter. Chapter 5 is focused on the physical simulation of

investment casting made of Mar-M247 Ni-based superalloy, where the microstructural and hardness evolution under controlled cooling rate was assessed. Afterward, the comparison of microstructure and hardness between Gleeble specimens and as-cast NGV was performed for validation of physical simulation method. Chapter 6 focuses on the physical simulation of skin formation in which the effects of thermal variables on the skin features were evaluated. Furthermore, the accurate prediction of skin characteristics by physical simulation technique was demonstrated. For deeper understanding of skin microstructure, various microstructural characterization techniques were utilized.

2 State of the art

2.1 Ni-based superalloys-materials for high temperature application

Superalloys indicate alloys with excellent mechanical strength, creep and corrosion resistance at elevated temperature, even up to the 0.9 of their melting points [11,22–24]. Considering the base alloying elements, superalloys are divided into three subgroups; Ni, Co and Ni-Fe based superalloys. Demonstrating unique characteristics, superalloys are widely used in variety of industries such as aerospace, gas and marine turbine as well as biomaterials [11,22,23].

Ni-based superalloys were developed as materials for high temperature applications where high strength and excellent creep resistance are required at elevated temperatures [1–5]. The development of Ni-based superalloys took place in the 1960s. They are exceptional due to the high degree of strength retained at high fractions of their melting point, compared to other classes of high temperature resistant materials. The high temperature properties of these alloys are outstanding and cannot be challenged by any other alloy system. This is due to the presence of a large volume fraction of L1₂ ordered precipitates, γ' phase, that geometrically constrains plastic deformation [6]. This is also the main reason why they are used, since the cost is not in their favor, at least not when compared to steel. They encompass complex alloy systems and have been widely used in industrial gas turbine, advanced aircraft engines (Figs.

2-1 and 2-2) and marine turbine industries because of their excellent high-temperature strength and oxidation resistance [3–5,25,26]. To reduce the overall costs of engine operation and to reduce the environmental impact, the service temperature of the engines is constantly increasing. The turbine inlet gas temperature in a modern engine can be as high as 1500 °C, which is accomplished by the use of sophisticated composition of Ni-based superalloys and thermal barrier coatings accompanied by modified engine design [11]. That is why today, Ni-based superalloys constitute over fifty percent of the weight of advanced aircraft engine.

Considering the Fig. 2-1, an aircraft engine consists of various parts which are exposed to wide range of pressure and temperature conditions. As a result, different materials should be chosen to meet required standards for any operating condition.

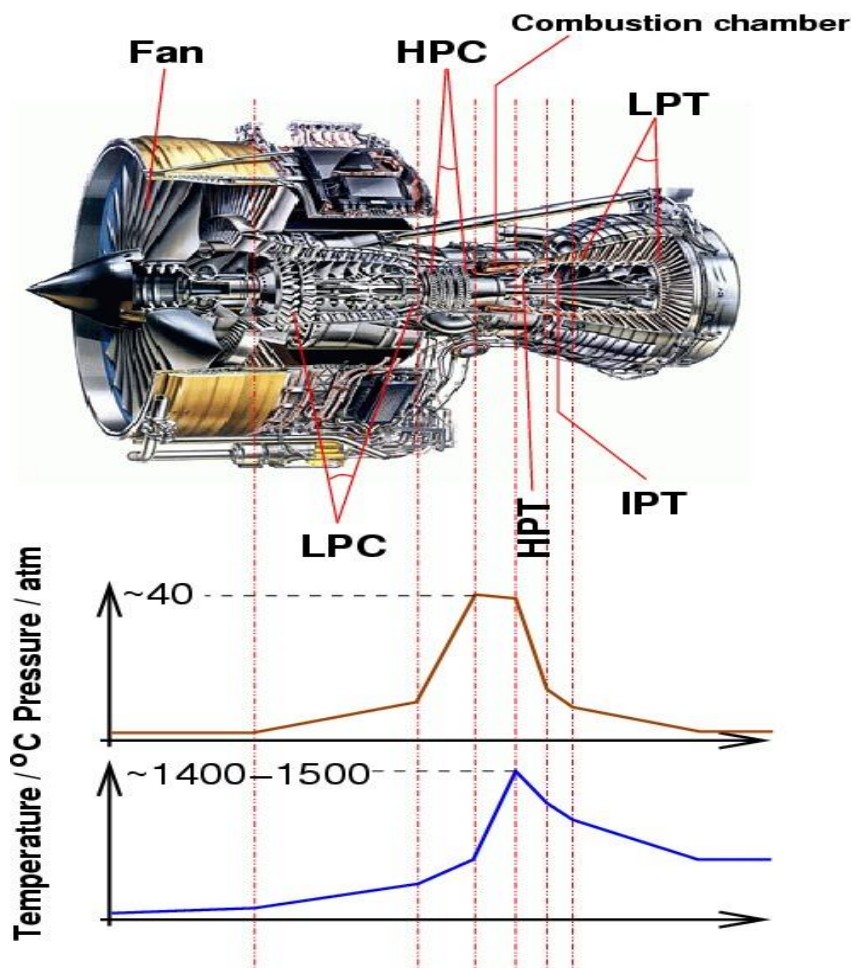


Figure 2-1. Image of the Trent 800 courtesy Rolls-Royce Plc. [27].

Figure 2-2 illustrates the variety and location of materials applied in an aircraft engine. It can be seen that Ti-based superalloys are used at lower pressure and temperature, whereas Ni-

based superalloys are employed at harsh operating condition in an aircraft engine. For instance, compressor's parts, working at low temperature, are produced of titanium alloys, while high temperature and pressure operating parts of engine, containing combustion chamber, NGVs and turbine, are made of Ni-based superalloys.

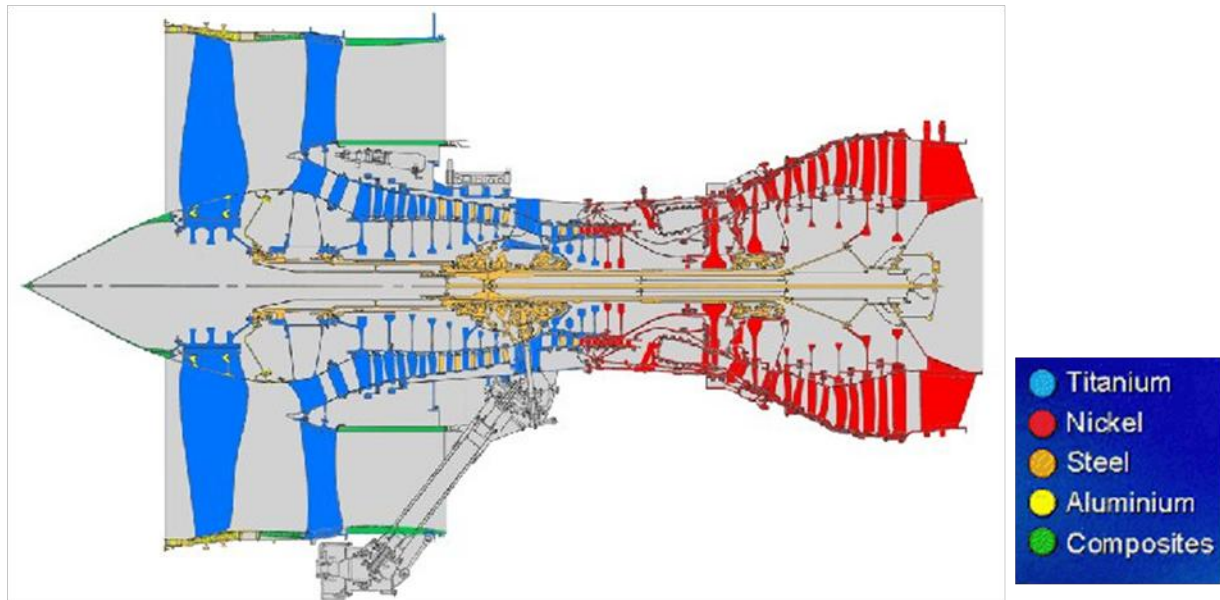


Figure 2-2. The different materials used in a Rolls-Royce jet engine [28].

2.1.1 Mar-M247 Ni-based superalloy

Mar-M247 is a typical polycrystalline Ni-based superalloy applied in investment casting which was developed by Danesi and Lund et al. at the Martin company in the 1970s [7]. Its optimal alloy design and microstructural control make the Mar-M247 Ni-based superalloy highly castable and very strong at high temperatures. Besides, it also exhibits excellent resistance to creep and hot corrosion [7,29,30]. During the past two decades, this alloy has been widely employed in fabricating advanced jet engines (Fig. 2-3 (a)), turbine rotors and NGVs (Fig. 2-3 (b)) in the aerospace industry [7–10,29,31]. The Mar-M247 Ni-based superalloy shows a complex, multiphase microstructure. It is strengthened by solid solution and precipitation strengthening. The most important phase constituent is the γ' -phase, providing strengthening to the γ -matrix at high temperatures, and other microstructural constituents such as γ/γ' eutectic, carbides, etc. can be formed depending on the material chemistry and its thermal profile [22,32–34].

On the other hand, the mechanical properties can be further improved with additions of elements. The high temperature behavior can be improved with the addition of 0.15 wt.% C by forming $M_{23}C_6$ carbides at the grain boundaries (GB). Furthermore, the elongation can be increased by adding about 1.4 wt.% of Hf with the formation of rosette γ/γ' eutectic structure between dendrites and at GBs [22,35,36].

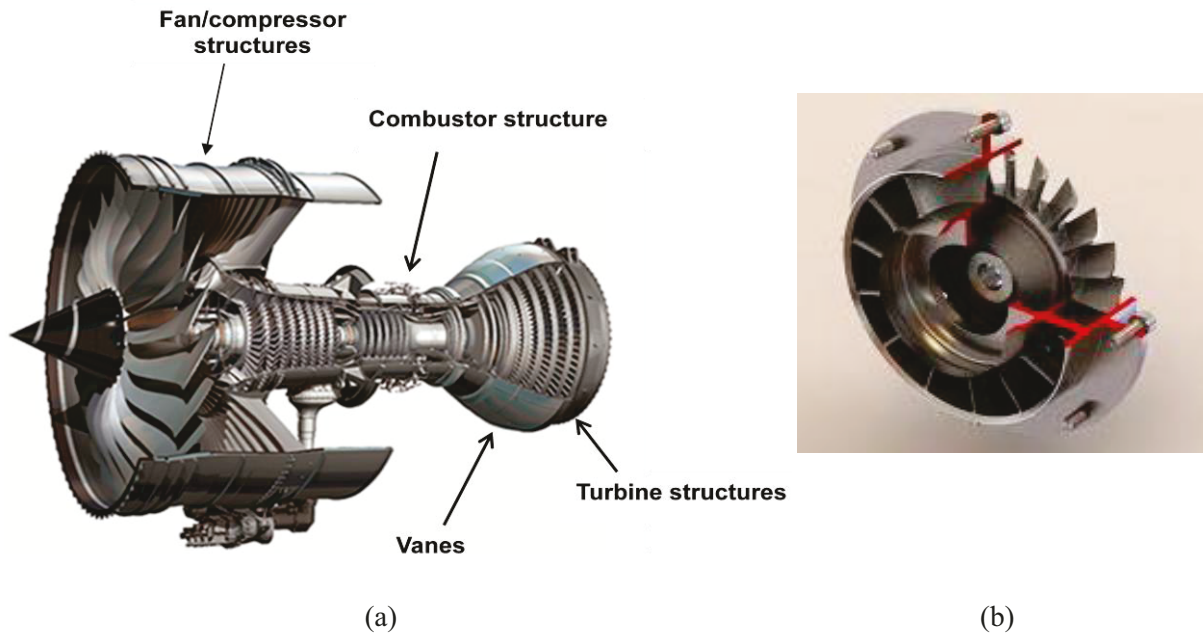


Figure 2-3. (a) The engine of Airbus A350 XWB and (b) nozzle guide vane is used in air craft engine [37].

A question is why Mar-M247 Ni-based superalloy should be chosen among a large number of other Ni-based superalloys. The response can be found at Table 2-1 which depicts the Mar-M247 Ni-based superalloy's yield, ultimate and rupture strength in comparison to other Ni-based superalloys, at various working temperatures. It is seen that the strength of Mar-M247 Ni-based superalloy is one of the highest among other Ni-based superalloys, especially in the case of rupture strength. Table 2-1 shows that the rupture strength of the Mar-M247 Ni-based superalloys, at 980 °C after 1000 hour, is 125 MPa located at the second position after CMSX2 and M22.

Segregation of alloying elements at grain boundaries and interdendritic areas during the solidification is the well known phenomenon for all metallic alloys and especially for Ni-based superalloys with their complex chemistries. For critical applications, like in aircraft engines, the segregation and impurity are reduced and controlled through re-melting, first by

Table 2-1. The comparison of mechanical properties of Mar-M247 with other Ni-based superalloys [23].

Alloy	Ultimate tensile strength at:						0.2% yield strength at:						Rupture strength at:					
	21°C (70°F)		538°C (1000°F)		1093°C (2000°F)		21°C (70°F)		538°C (1000°F)		1093°C (2000°F)		815°C (1500°F)		870°C (1600°F)		980°C (1800°F)	
	Mpa	Ksi	Mpa	Ksi	Mpa	Ksi	Mpa	Ksi	Mpa	Ksi	Mpa	Ksi	Mpa	Ksi	Mpa	Ksi	Mpa	Ksi
MAR-M247	965	140	1035	150	815	118	825	120	585(85)	415 (60)	455 (66)	290 (42)	185 (27)	125 (18)
MAR-M246	965	140	1000	145	345	50	860	125	860	125	525 (76)	435 (62)	440 (63)	290 (42)	195 (28)	125 (18)
M-22	730	106	780	113	685	99	730	106	515 (75)	385 (56)	395 (57)	285 (41)	200 (29)	130 (19)
MAR-M432	1240	180	1105	160	1070	155	910	132	435 (63)	330 (48)	295 (40)	215 (31)	140 (20)	97 (14)
IN-713 C	850	123	860	125	740	107	705	102	370 (54)	305 (44)	305 (44)	215 (31)	130 (19)	70 (10)
IN-713 LC	895	130	895	130	750	109	760	110	425 (62)	325 (47)	295 (43)	240 (35)	140 (20)	105 (15)
B-1900	970	141	1005	146	270	38	825	120	870	126	195	28	510 (74)	380 (55)	385 (56)	250 (36)	180 (26)	110 (26)
IN-162	1005	146	1020	148	815	118	795	115	505 (73)	370 (54)	340 (49)	255 (37)	165 (24)	110 (16)
IN-731	835	121	275	40	725	105	170	25	505 (73)	365 (53)	165 (24)	105 (15)
Nimocast 90	700	102	595	86	520	75	420	61	160 (23)	110 (17)	125 (18)	83 (12)
Nimocast 242	460	67	300	44	110 (16)	83 (12)	90 (13)	59 (8.6)	45 (6.5)	...
Udimet 500	930	135	895	130	815	118	725	105	330 (48)	240 (35)	230 (33)	165 (24)	90 (13)	...
udimet 710	1075	156	240	35	895	130	170	25	420 (61)	325 (47)	305 (44)	215 (31)	150 (22)	76 (11)
CMSX-2	1185	172	1295(b)	188 (b)	1135	165	1245 (b)	181 (b)	345 (50)	...	170 (25)
GMR-235	710	103	640	93	180 (26)	...	75 (11)
IN-939	1050	152	895 (b)	133 (b)	325 (c)	47 (c)	800	116	635 (b)	92 (b)	205 (c)	30 (c)	195 (28)	...	60 (9)
IN-713 Hf	1000	145	1070 (b)	130 (b)	380 (c)	55 (c)	760	110	620 (b)	90 (b)	240 (c)	35 (c)	205 (30)	...	90 (13)
Rene 125 Hf	1070	155	875 (b)	155 (b)	550 (c)	80 (c)	825	120	860 (b)	125 (b)	345 (c)	50 (c)	305 (44)	...	115 (17)
SEL	1020	148	945 (b)	127 (b)	905	131	795 (b)	115 (b)	295 (43)	...	75 (11)
UDM 56	945	137	1090 (b)	137 (b)	850	123	725 (b)	105 (b)	270 (39)	...	125 (18)

(b) at 760°C (1400°F). (c) At 980°C (1800°F).

vacuum induction melting (VIM) which is also followed by vacuum arc re-melting (VAR) [7] or electroslag re-melting (ESR). For the most critical applications a third VAR re-melting is carried out.

The control of the level of segregations at grain boundaries during melting and also the grain size during all subsequent processing steps are crucially important not only for the overall strength of an alloy but also for the fatigue and creep properties at higher temperatures which is critical for materials used in the turbine of aircraft engines [22,23,38]. On the other hand, existence of any inclusion in bulk materials can act as a stress concentration source which facilitates the crack initiation and propagation during working condition, so the casting of the Mar-M247 Ni-based superalloy has to be done carefully to avoid these defects [38]. In order to avoid the formation of inclusion, the Mar-M247 Ni-based superalloy is prepared in a vacuum induction melting (VIM) furnace [7,39].

2.2 Physical metallurgy of Ni-based superalloys

The chemical composition of the Ni-based superalloys is very complex with many elements each of which governs the formation of secondary phases and microconstituents influencing on the characteristics of Ni-based superalloys. The base element of Ni-based superalloys, as it comes from the proper name, is Ni. The main reason for using Ni as the base element is mainly due to the capability of Ni to preserve the high concentrations of alloying elements in solid solution as well as high thermal stability together with an adequate cost. The alloying elements are added to improve properties such as strength, oxidation, corrosion and high temperature resistance. The typical microstructure in a Ni-based superalloy, which consists of γ and γ' phases, is similar to a composite material. Figure 2-4 illustrates the typical microstructure of a Ni-based superalloy in which γ' , observed as the darker areas, acts as a reinforcement in the γ matrix [11]. However, Ni-based superalloys demonstrate higher mechanical properties than either γ or γ' phases [1]. Also, other secondary phases and microconstituents such as MC (metal carbide), MN (metal nitride), $M_{23}C_6$, M_6C , γ'' , δ and Laves phases, can be formed at the γ matrix depending on the alloy composition and solidification condition. Apart from secondary phases, other microstructural aspects like primary dendrites, secondary dendrites and grains can strongly control alloy properties in different operating conditions.

The chemical composition of the Mar-M247, as the member of Ni-based superalloys family, is very complex with many elements containing Ni, C, Cr, Mo, Ti, Co, W, Ta, Al, Hf, Zr, B, Nb. The Mar-M247 Ni-based superalloy consists of approximately 60% semi-coherent γ' phase $\text{Ni}_3(\text{Al,Ti})$, the main strengthening phase, which is in the matrix of γ , as a Ni-rich solid solution strengthened alloy. Mar-M247 Ni-based superalloy contains the refractory elements like Hf, Ta, W, with presence of carbon in alloy, tend to form carbides or the unstable microconstituents like γ/γ' eutectic [33,40–43]. It should be noted that on account of the lack of research studies on the physical metallurgy of Mar-M247 Ni-based superalloy, other Ni-based superalloys are also considered in this chapter.

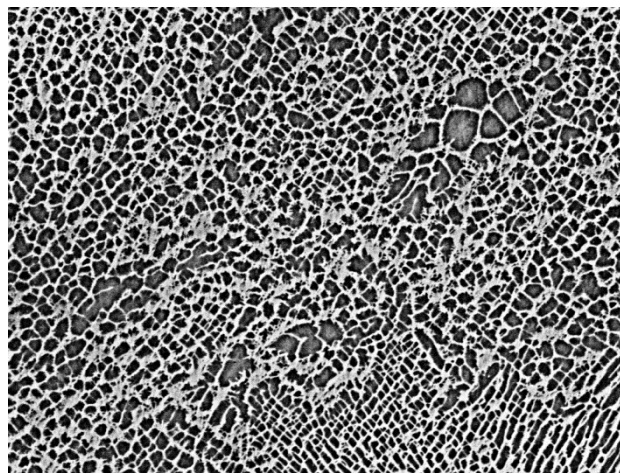


Figure 2-4. γ/γ' (darker area) microstructure in Mar-M247 Ni-based superalloy.

2.2.1 The influence of thermal variation on grain structure

A polycrystalline material is composed of grains. A grain boundary, involving the interface of two adjacent grains, has undeniable role for controlling the mechanical properties of crystalline materials.

Mechanical characteristics such as hardness, yield and ultimate stress can be remarkably improved, due to GB strengthening mechanisms, by grain refinement. There are different viewpoints for interpretation of this mechanism. Hall and Petch demonstrated that finer grains increase dislocation pile up causing higher stress concentration in the grain boundary and activation of dislocation sources at neighboring grains [38,44,45]. According to the Ashby's dislocation interaction model [46], smaller grains decrease the mean free path of dislocation movement resulting in more dislocation interactions and increasing work

hardening. With respect to the Li and Chou idea grain boundaries are considered as a source of dislocation cooperating in work hardening [47].

Despite the positive effect of smaller grain size on the materials strength, it deteriorates the creep resistance. According to literature [48], atomic diffusion at a grain boundary, or grain boundary diffusion, is easier than bulk diffusion because the activation energy of grain boundary diffusion is 40-60 percent that of bulk diffusion. Hence, grain boundaries are considered as areas weakening the high temperature and creep resistance of alloys [48,49]. As a result, controlling grain size is vital to promote the performance of Ni-based superalloys, designed for high temperature applications [50].

Solidification parameters, such as cooling and solidification rate as well as thermal gradient, dictate the microstructural features and mechanical properties of any alloy.

The effect of average cooling rate on grain refinement of Inconel 718 Ni-based superalloy is presented in Fig. 2-5. It is shown that the grain size increases remarkably with the decrease of cooling rate. The relationship can be described as following equation:

$$d = 1.0196e^{0.0656V} \quad (2-1)$$

Where d and V are grain size and solidification rate, respectively. It should be noticed that at the same cooling rate, the composition variations also result in the change of grain size in Inconel 718 Ni-based superalloy. In addition, the value of the constant, in equation (2-1), changes on account of variation of chemical composition [51].

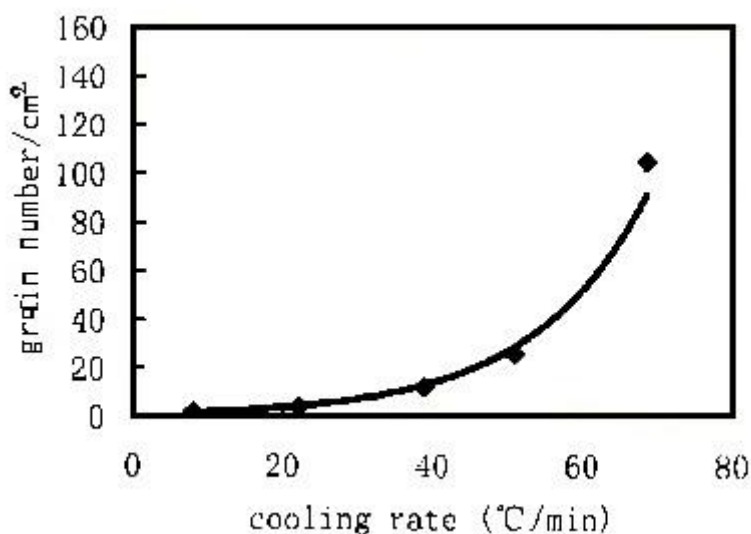


Figure 2-5. The effect of average solidification cooling rate on grain refinement [51].

In addition of controlling grain size, the governing of grain orientation growth helps us to improve casting properties too. Wagner et al. [52] showed that having preferred $\langle 001 \rangle$ solidification direction parallel to the component axis, which coincides with the minimum in Young's modulus, thermal stress and thermal fatigue resistance improved considerably.

The generally accepted model for competitive grain growth considers that a grain, which has the fast growing crystallographic $\langle 001 \rangle$ direction most closely aligned to the temperature gradient, will overgrow all less favourably oriented grains. This is considered to occur by the well-aligned grain emitting a secondary dendrite to block the lagging misaligned grain, which must grow at a higher undercooling.

Considering the Fig. 2-6 which represents the orientation maps of CMSX4 Ni-based superalloy, the arrows indicate the orientations of the primary dendrite trunks in adjoining grains; the temperature gradient direction is indicated as the vertical dash-pointed line. The bold numbers give the deviation of the $\langle 001 \rangle$ crystallographic direction in the growing grains from the temperature gradient direction. The dashed line indicates the macroscopic deviations of the grain boundary planes from the temperature gradient direction and the numbers in italics give the inclination of the grain boundary to the temperature gradient.

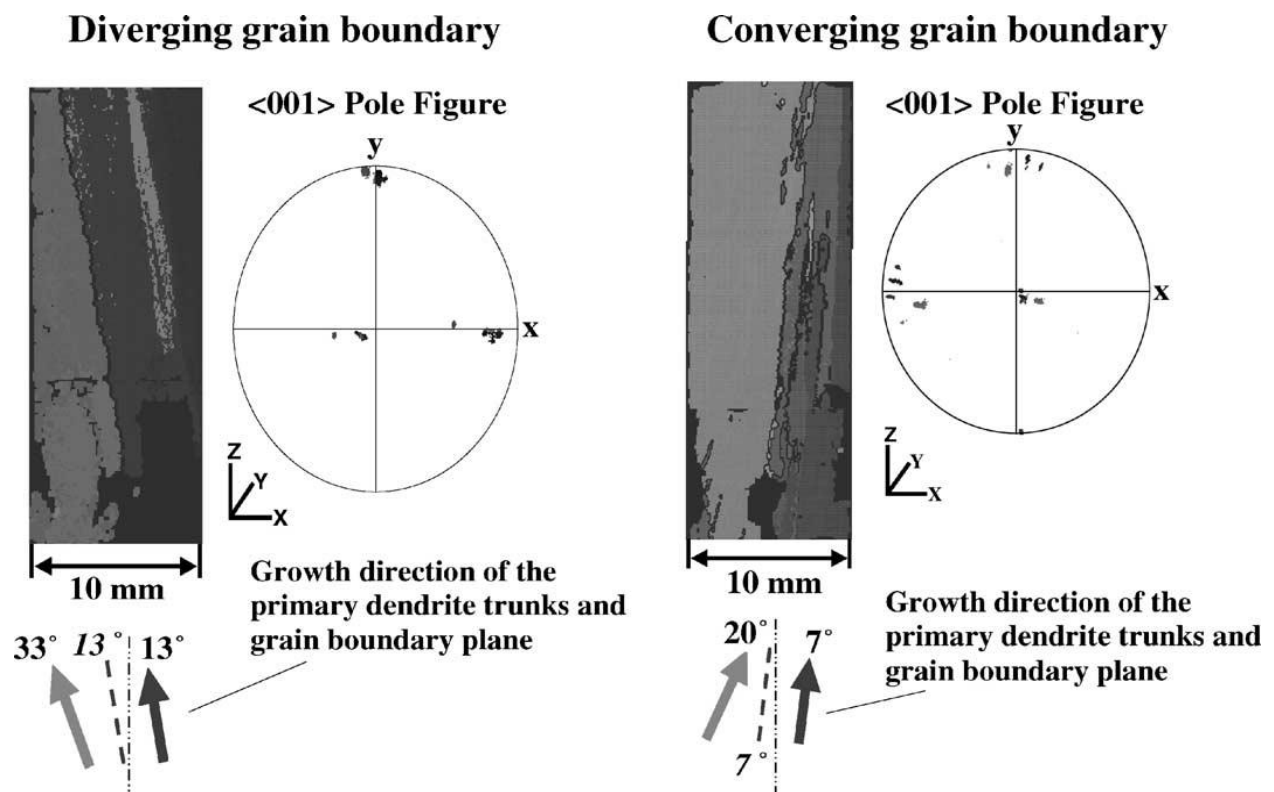


Figure 2-6. Orientation maps and $\langle 001 \rangle$ pole figures for diverging and for converging grains [52].

According to the Fig. 2-6, in the case of the diverging dendrites, the grain boundary is inclined such that the 13° misaligned grain slowly overgrows the 33° misaligned grain [52]. The grain boundary is parallel to the 13° misaligned grain; secondary dendrite arms grow exclusively from the 33° misaligned grain to fill the gap between the diverging grains; as shown in Fig. 2-7 (a) [52,53]. In Fig. 2-7 optical micrographs of the resulting dendrite structure at the grain boundaries are shown for both diverging and converging dendrites produced under similar growth conditions [53]. In the case of the converging $\langle 0\ 0\ 1 \rangle$ directions, shown in Fig. 2-6, the 20° misaligned grain overgrows the more favourably oriented 7° misaligned grain. The resulting grain boundary orientation is parallel to the primary dendrites in the grain with its $\langle 0\ 0\ 1 \rangle$ direction 7° misaligned to the heat flow, indicating that secondary dendrite arm formation is suppressed at the grain boundary under these particular growth conditions, as shown in Fig. 2-7 (b) [52,53].

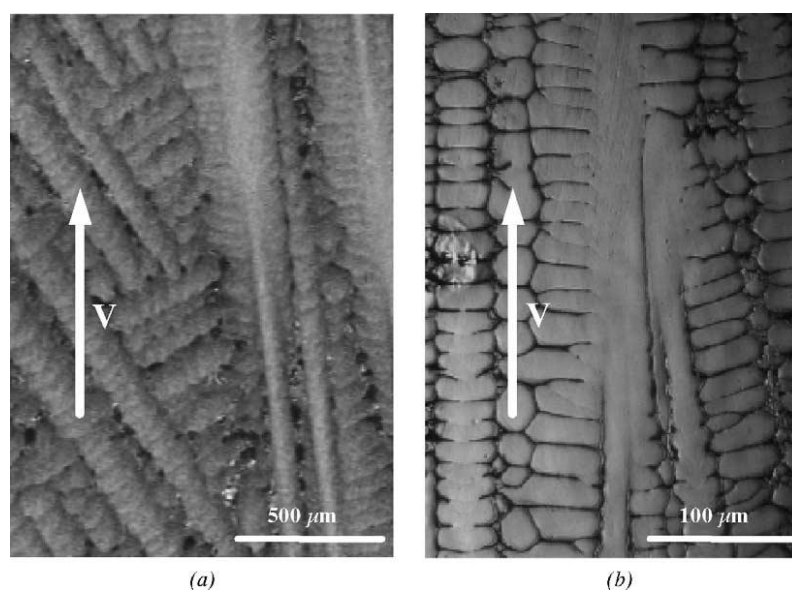


Figure 2-7. Secondary dendrite arm formation in CMSX4: (a) diverging grain boundary, (b) converging grain boundary [53].

The experiment shows that misaligned grains can grow parallel to more favourably oriented grains and can, in certain circumstances, overgrow them. The important point for converging dendrites is that competition for solute between the dendrites in adjacent crystals suppresses the development of secondary dendrites so that the misaligned primary dendrites are terminated when they impact the well-aligned dendrites. Consequently relative grain growth

depends on the inclination of the primary dendrite of the well-aligned crystal to the temperature gradient.

For diverging grains, there is an excess of solute in the liquid between the diverging dendrites. Consequently, dendrites have to be produced to fill the evolving gap between the diverging grains. Secondary dendrite arms develop in the less favourably oriented grain, which can be seen from the dendrite morphology at the grain boundary in Fig. 2-7 (a) [52,53]. This is due to these secondary dendrites being more highly undercooled and being more aligned with the temperature gradient than the secondary dendrites from the well-aligned grains. There is no evidence of significant growth of secondary dendrites to expand the size of the well aligned crystal. The orientation of the grain boundary is, therefore, largely parallel to the more favourably oriented grain. However, there is no evidence of effective texture development by the commonly accepted mechanism of secondary dendrite blocking of primary dendrites of misaligned crystals. Nevertheless, the grain boundaries, for both converging and diverging dendrites, appear to largely parallel the primary dendrites of the crystals having $\langle 0\ 0\ 1 \rangle$ most closely aligned to the temperature gradient. This mechanism does not favour the fastest growing $\langle 0\ 0\ 1 \rangle$ oriented grains and can lead to the development of grains remote from $\langle 0\ 0\ 1 \rangle$ [52].

Basically, the microstructure of materials during solidification or heat treatment process, similar to any system in the nature, tends to minimize its energy by means of various mechanisms an important of which is the reduction of grain boundary energy. The lowest grain boundary energy belongs to the coincidental site lattice (CSL) of type $\Sigma 3$, which is known as a twin boundary. It should be expected that a certain number of the atoms in each lattice have coincidental locations from one grain to the next, which is defined as a coincidental site lattice. The meaning of $\Sigma 3$ is that one out of every three atoms is in coincidence from one grain to the next (Fig. 2-8 (a)). Considering the Fig. 2-8 (b), we see a group of atoms that are in perfect agreement with the supercell background (bottom left). By taking a 60° twist rotation about the (1 1 1) plane (top right), the ordering of the atoms are deviated such that once again the red and silver atoms do not align with the background lattice, thus one out of three atoms are in coincidental lattice locations denoting the $\Sigma 3$ GB (twin) [54]. Figure 2-9 illustrates that the coherent twin grain boundary has the lowest GB energy and mobility, meanwhile GBs with higher energy also have higher mobility [54–56]. Hence, GBs with higher energies have a higher mobility and force to reorient the GB normal into a lower energy configuration [54].

2.2.2 The influence of thermal variation on dendritic structure

Primary dendrite arm spacing (PDAS) λ_1 and secondary dendrite arm spacing (SDAS) λ_2 are key microstructural features of solidified castings since many mechanical properties are influenced by them. It has been reported that both PDAS and SDAS are determined by processing parameters such as thermal gradient (G), solidification rate (V) and cooling rate (R) [57]. Numerous studies have been carried out to investigate the effect of the processing parameters on SDAS [1,57–62].

Secondary dendrites result from capillarity instabilities at the dendrite tip. These perturbations are small at first and then grow at the expense of the smaller arms in a process similar to Ostwald ripening. The driving force for this coarsening is the increase in interfacial energy at the tips of the smaller arms due to the higher curvature there. The coarsening kinetics generally produce the following relationship for secondary dendrite arm spacing [63]:

$$\lambda = Mt_f^3 \quad (2-2)$$

where M is an alloy-dependent constant and t_f is the local solidification time given approximately by $T_0(GV)^{-1}$, where T_0 is the equilibrium freezing range and (GV) which is equal to cooling rate (R) [57,64].

The microstructure of primary dendrite of Mar-M247 Ni-based superalloy samples, grown at a various G and V conditions, are shown in Figs. 2-10 (a-c) [57]. While temperature gradients (G) are 36, 38.3 and 43 °C/cm for pictures 2-10 (a), (b) and (c), respectively, solidification rates (V) are reported 0.01, 0.005 and 0.0005 cm/s for them. As expected, the microstructure of the Mar-M247 Ni-based superalloy exhibits a decreasing PDAS as the thermal gradient decreases or the solidification rate increases. Although the details of the phases and microconstituent formed in interdendritic area such as carbides and laves phases varied from alloy to alloy, depending on the composition and the solidification parameters employed, λ_1 for all alloys represents the similar behavior [57,65–69].

Figures 2-10 (d-f) illustrates typical λ_2 of PWA-1484 Ni-based superalloy displaying some well-aligned primary dendrite trunks with secondary dendrite arms. There is an obvious transition from dendritic (Figs. 2-10 (d, e)), to cellular growth (Figs. 2-10 (f)) at a cooling rate of 0.031 °C/s.

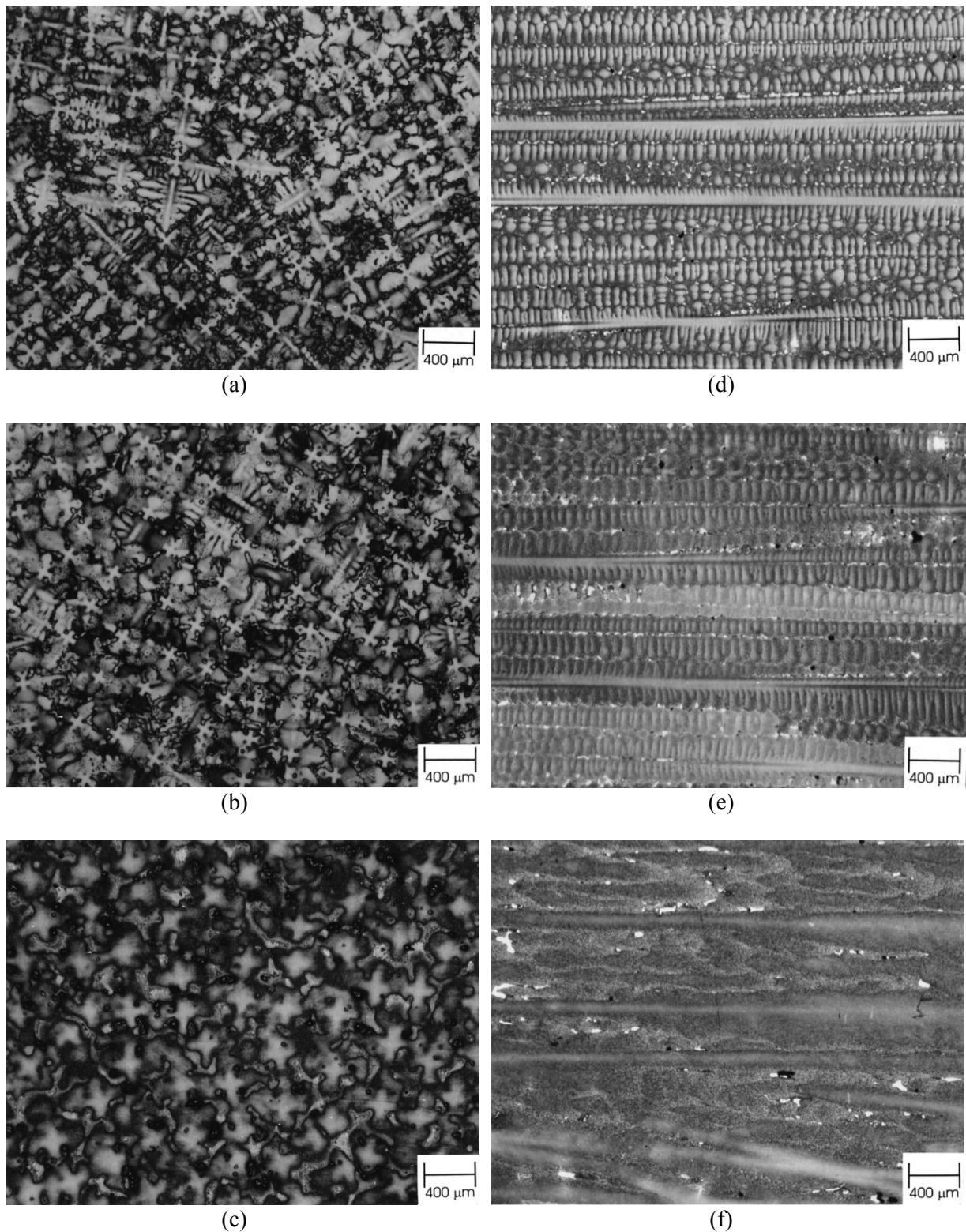


Figure 2-10. The microstructure of primary dendrites of Mar-M247 Ni-based superalloy grown at (a) 0.36, (b) 0.192 and (c) 0.022 °C/s cooling rates. Dendritic microstructure of PWA-1484 Ni-based superalloy grown at (e) 0.204, (d) 0.117 and (f) 0.031 °C/s cooling rates [57].

The dendritic structures in Figs. 2-10 (d, e) are formed at $G = 20.4 \text{ }^\circ\text{C/cm}$, $V = 0.01 \text{ cm/s}$ and $G = 23.4 \text{ }^\circ\text{C/cm}$, $V = 0.005 \text{ cm/s}$, respectively. Decreasing the solidification and cooling rate, the coarser microstructure is formed, as it is seen in Figs. 2-10 (d, e). Finally, with changing the thermal gradient to $31.1 \text{ }^\circ\text{C/cm}$ and the reduction of solidification rate to 0.001 cm/s , dendritic structure is transformed to the cellular microstructure (Fig. 2-10 (e)).

The correlation between cooling rate and SDAS was also studied by Whitesell et al. for several Ni-based superalloys [57]. The variation of λ_2 versus cooling rate is plotted in Fig. 2-11. Considering the outcomes, in general, SDAS decreases with increasing cooling rate for all studied alloys. The result is in good agreement with other literature data [1,14,31,60,61,70–72]. According to the Kurz–Fisher model, which also shows a good accordance with the Feurer/Wunderlin model [71], the relation between the secondary dendrite arm spacing and the cooling rate is expressed by

$$\lambda_2 = AR^{-1/3} \quad (2-3)$$

where λ_2 is the SDAS, R the cooling rate and A a constant [64].

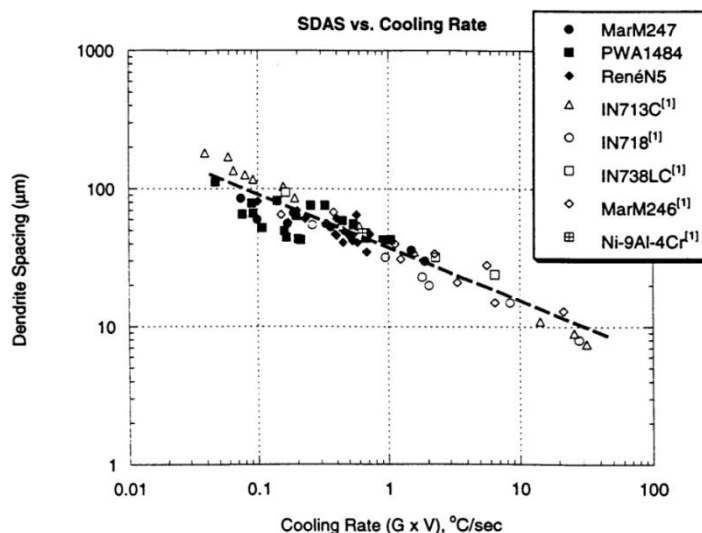


Figure 2-11. SDAS for a wide range of Ni-based superalloys as a function of the cooling rate (R) [57].

Similar behavior is reported for the relation between the SDAS and solidification rate, as SDAS increases with reduction of solidification rate. The same results were also reported in earlier works [1,15,57,59–61,73].

2.2.3 The γ , γ' and secondary γ' phases

The γ phase, known as the matrix in Ni-based superalloys, is a solid solution of Ni with high fraction of Co, Cr, W, Mo and Al in which atoms are placed randomly in a face centered cubic (FCC) structure [72]. The volume fraction of γ phase varies among different Ni-based superalloys [22], which is almost 38 % for Mar-M247 Ni-based superalloy [74].

The γ' phase is an intermetallic compound with ordered FCC structure in which Ni atoms are located at face centers and aluminium and/or titanium atoms at the cube corners (Fig. 2-12).

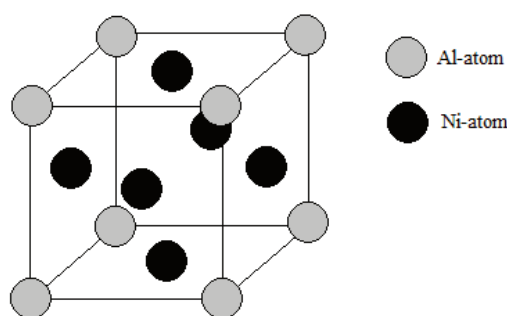


Figure 2-12. The crystal structure of γ' phase.

The addition of Al and Ti elements promotes the formation of γ' phase. While atomic arrangement of γ' phase has the chemical formula Ni_3Al , Ni_3Ti or $\text{Ni}_3(\text{Al,Ti})$, the γ' phase size and shape can be controlled precisely applying heat treatment. The volume fraction of γ' phase is governed by solidification variables like cooling rate, whereas heat treatments have no effect on the volume fraction or composition of γ' precipitation, as demonstrated by Caron and Khan [75]. The mechanical properties of Ni-based superalloys are strongly affected by volume fraction, size, shape of γ' as well as the coherency between γ matrix and γ' precipitation.

Precipitate shapes in Ni-based superalloys vary with alloy composition, partitioning of elements to the disordered gamma matrix and the ordered γ' precipitates as well as the heat treatment process. These shapes vary from spherical to cuboidal to rod-like precipitations. Based on two-dimensional images, precipitates in Ni-base alloys are typically categorized as cuboidal or spherical [6,75–77]. The irregular shape of γ' is referred to those particles which do not have distinct spherical or cuboidal appearance [6,75,78].

Extremely small γ' precipitates always occur as spheres. In fact, for a given volume of precipitate, the area of sphere is 1.24 times less than a cube, so it is the preferred shape to

minimize surface energy. However, in the case of coherent interfaces the interfacial energy can be minimized by forming cube shapes precipitates. The coherency of matrix and precipitation, which is quantified as a lattice misfit (δ), is defined by following equation

$$\delta = 2 \times \frac{a_{\gamma} - a_{\gamma'}}{a_{\gamma} + a_{\gamma'}} \quad (2-4)$$

Where δ is called lattice misfit and a_{γ} and $a_{\gamma'}$ are lattice parameters of γ and γ' , respectively [11].

Small lattice misfit results a cuboidal shape γ' precipitation with sharp corners for which higher thermal stability is reported [79], whereas higher misfit leads to more spherical γ' . The lattice misfit is also dependent on temperature, since γ has the higher thermal expansion compared with γ' and in consequence lattice misfit increases with rising temperature. Hence, due to the elastic stresses, associated with the misfit, precipitates undergo an evolution in shape during elevated temperature exposures [80,81].

Considering the matrix/precipitate lattice mismatch and external stress, the morphology of γ' can change from spheres to cubes or plates during the γ' growth [6,76,81,82]. Having higher values of lattice mismatch, the critical precipitation size, in which sphere shape converts to the cube or plate shape precipitations, declines. The degree of coherency can be decreased by over aging.

The transition of the γ' shape on account of chemical composition in the alloys containing 13Al–2.5Pt–1Re–2Ta–0.1Hf (at.%), with exception of Cr, Ru and W additions, is shown in Fig. 2-13. Increasing the Ru and W content by 1at. %, causes the significant conversion of γ' shape from the cuboidal to spherical shape precipitations (Figs. 2-13 (a,b)). Similar manner is seen with adding of Cr content by 5 at. % (Figs. 2-13 (a,c)). However, rising the Cr, Ru, and W concentrations by 5, 1, and 1at. %, respectively, the γ' shape remains constant (Fig. 2-13 (d)) [6].

The finer γ' has a better contribution to the precipitate strengthening. In addition to this, fine γ' size is also desirable for fatigue-crack propagation resistance, yield strength and creep behavior [83]. Two factors, including the degree of supercooling and supersaturation, determine the precipitating behavior of γ' phase. Higher cooling rate results in increase of supercooling and, in consequence, nucleation promotion of γ' precipitates. Moreover, the increase of the cooling rate reduces the growing time of this phase. As a result, the higher volume fractions of γ' with significant reduction in the size are revealed in the microstructure

[73,83–85]. Figure 2-14 depicts the different sizes of γ' phase arising from the various cooling rates. It is seen that the γ' size reduces with rising cooling rate [84].

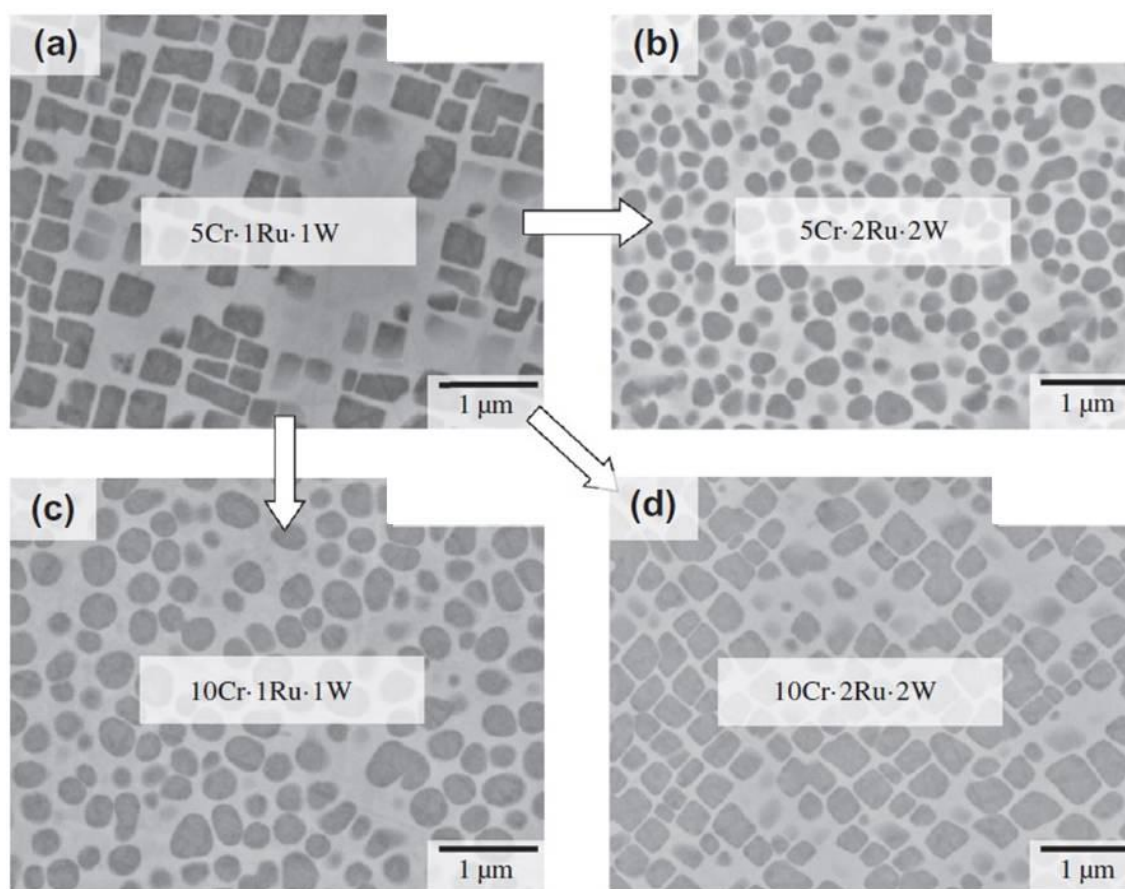


Figure 2-13. Effect of Cr, Ru, and/or W on γ' shape. Alloys (a,b,c and d) contain the following compositions (at.%): 13Al–2.5Pt–1Re–2Ta–0.1Hf. The nominal compositions of Cr, Ru, and W are provided within each image [6].

Also the shape of γ' particles varies at different cooling rates, as with increasing cooling rate the bigger cuboidal γ' particles transform to the smaller spherical particles (Fig. 2-15) [86]. Two types of primary and secondary γ' precipitate in Ni-based superalloys (Fig. 2-16) at high and low temperature, respectively [87]. The secondary γ' crystal structure, known as γ'' phase, is a body centered tetragonal (BCT) Ni_3Nb phase [22,88,89]. In both phases Co, Cr and Fe can substitute for Ni whereas Nb for Al and Ti [22]. In addition, the chemical composition of primary γ' compared with secondary γ' is closer to γ matrix [90]. Although secondary γ' precipitation plays a constructive role for hardening of Ni-based superalloys, it declines the creep resistance and consequently industries try to avoid that with employing heat treatment [91,92].

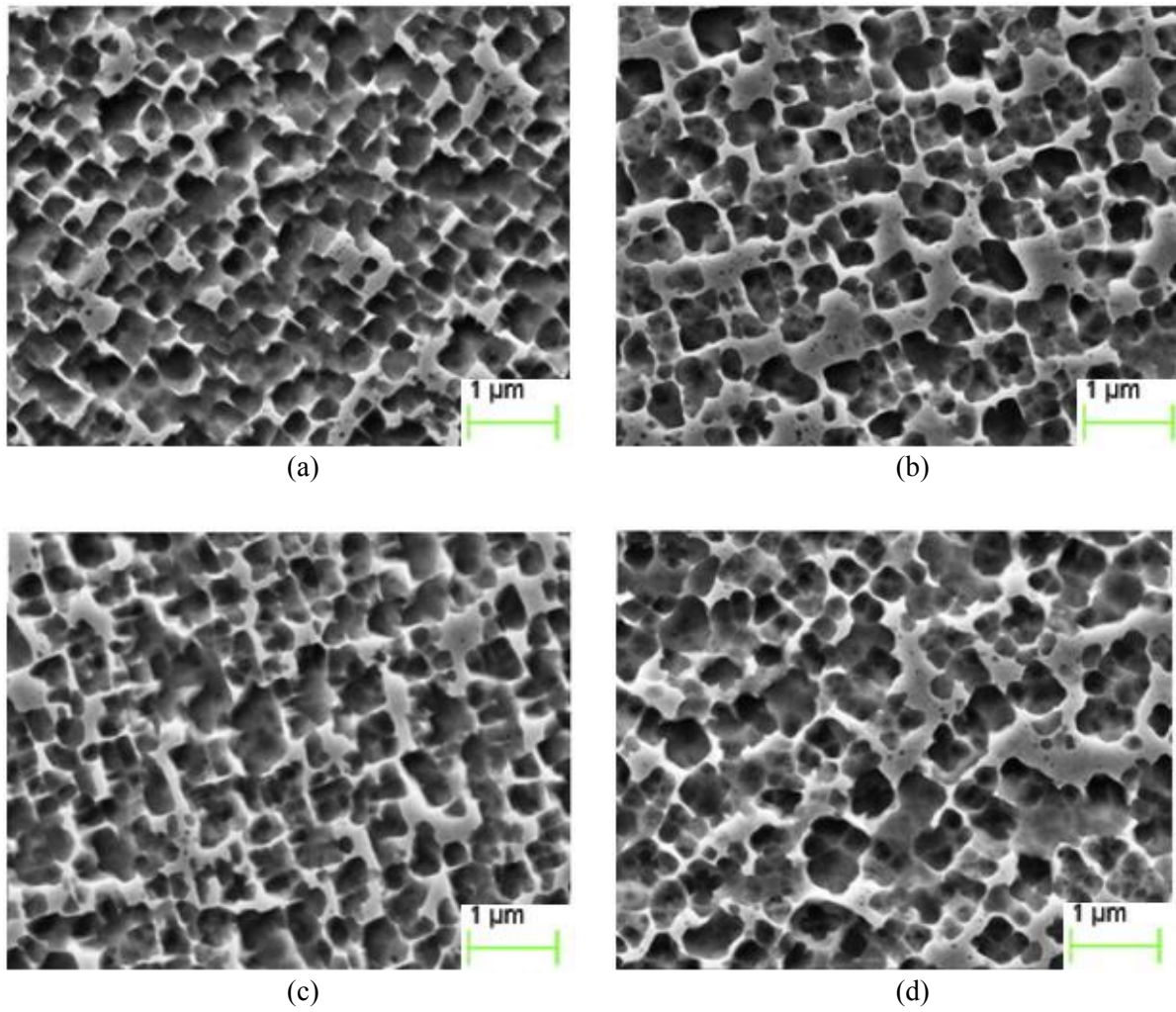


Figure 2-14. Morphologies of γ' in the dendritic cores at (a) 1.2, (b) 0.15, (c) 1.08 and (d) 0.08°C/s cooling rates [84].

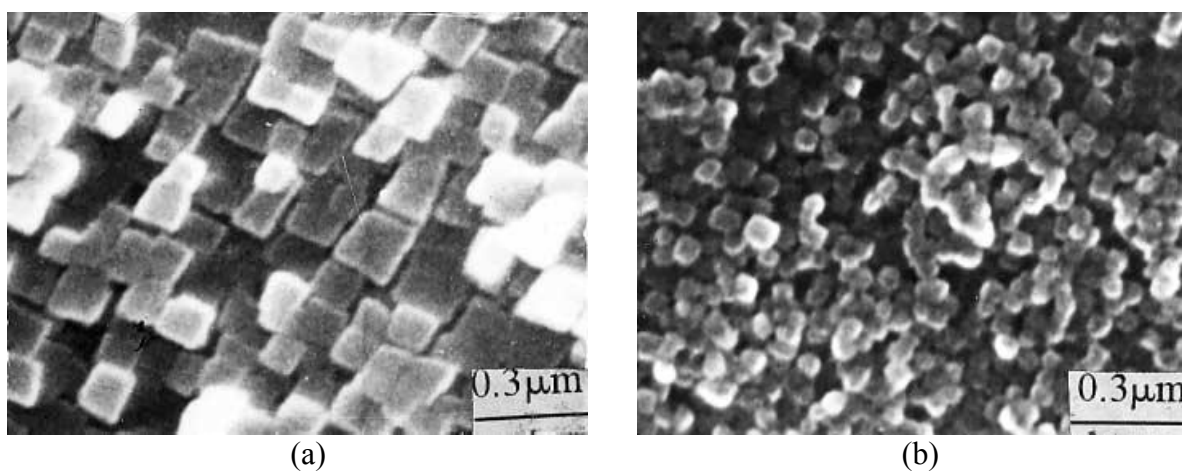


Figure 2-15. Morphology of γ' particles cooled at (a) 12.42 and (b) 50.16 °C/s [86].

The γ' phase has a low mismatch with the matrix due to fast precipitation and low coarsening rate, whereas higher degree of mismatch between γ'' phase and γ matrix lead to increasing the coherency strains in γ matrix. As a result, γ'' induces higher strength to matrix in comparison to the γ' . The secondary γ' phase is relatively stable at high temperature, and disperses uniformly and homogeneously in the matrix [42].

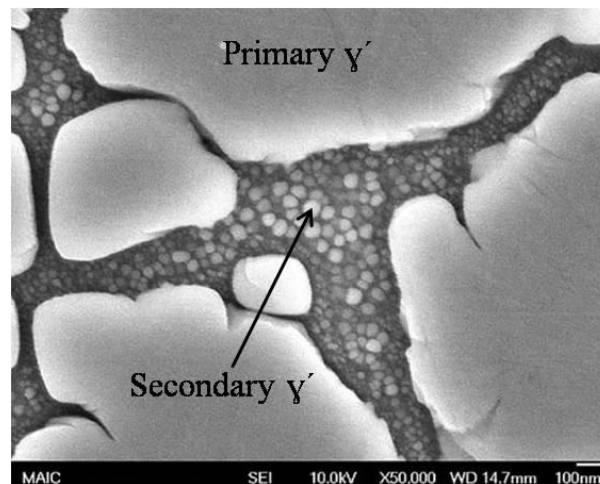


Figure 2-16. The secondary γ' precipitates in PWA-1480 Ni-based superalloy [91].

2.2.4 The influence of thermal variation on carbide morphology

Carbides are another phases that play an important role in hardening of Ni-based superalloys [22,93,94]. Grain boundary carbides prevent or retard grain-boundary sliding and make the grain boundary stronger. Carbides can also tie up certain elements that would otherwise promote phase instability during service [7,34,95,96]. Formation of carbides is initiated already in the liquid by the strong segregation of C and N. These two elements then separately or jointly react with active elements. Addition of carbon in amount from 0.05 to 0.2 % and carbide forming elements, such as Cr, W, Mo, Nb, Ta, Ti, and Hf, enables the precipitation of mainly $M_{23}C_6$, MC and M_6C types carbides in Ni-based superalloys [22,95]. Numerous investigations have characterized the formation sequence, composition and morphological evolution of carbides, for slow to rapid solidification conditions. The results indicate that the processing parameters such as sample growth rate, cooling rate, thermal gradient, solidification interface shape and chemical composition are important factors governing carbides morphology, size, volume fraction, composition as well as growth

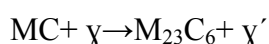
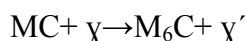
mechanism [14,95,97,98]. The preferred location of the carbide precipitation is interdendritic area [99]. The carbide forming element enrichment and interface energy control carbide nucleation. Heterogeneous carbide nucleation can occur above the alloy liquidus temperature. Carbide forming element enrichment and trapping behavior of the solid-liquid interface control carbide growth, which occurs at inter-secondary γ -dendrite arm positions and the bottom of mushy zone which are rich in carbide forming elements. At low cooling rates, most of these carbides are found to be located at the grain boundary and interdendritic regions, while the coupled growth of some carbides in the center of γ grains occurs at high cooling rate [14]. As it is shown in Fig. 2-17, the carbides are located at the grain boundaries (Fig. 2-17 (b)) and in the interdendritic regions (Figs. 12-7 (a,c,d)). It can be seen that the carbide morphology varies from coarse script-like (Fig. 2-17 (d)), fine script-like (Fig. 2-17 (b)), isolated blocky (Figs. 2-17 (d,c)) and discontinuous or irregular particles (Fig. 2-17 (b)). The blocky MC carbides contained significantly higher Hf content than the needle-shaped carbides [95].

Some kinds of carbide such as HfC, TaC and WC are very stable. Especially, HfC is very stable, therefore, its formation is strongly favored by thermodynamics, especially when the Hf content is more than 1 % [14,22,100]. The carbide formation reaction can be expressed as



This reaction is temperature dependent, whereby the equilibrium moves towards the right side as the temperature decreases. It is also alloy composition dependent and moves towards the right side as the content and the activity coefficient of the carbide forming elements increase [14,101]. The main elements forming MC carbide are Ta, W, and Hf [100].

Under the influence of heat treatment and long thermal exposure they may undergo transformations changing their kind, size and morphology. MC carbide are transformed into M_6C or M_{23}C_6 type carbides [23,92,94–96,102–106], according to following reactions:



These decomposed carbides usually form with discontinuous or granular γ' precipitations at the grain boundaries [22,106–110].

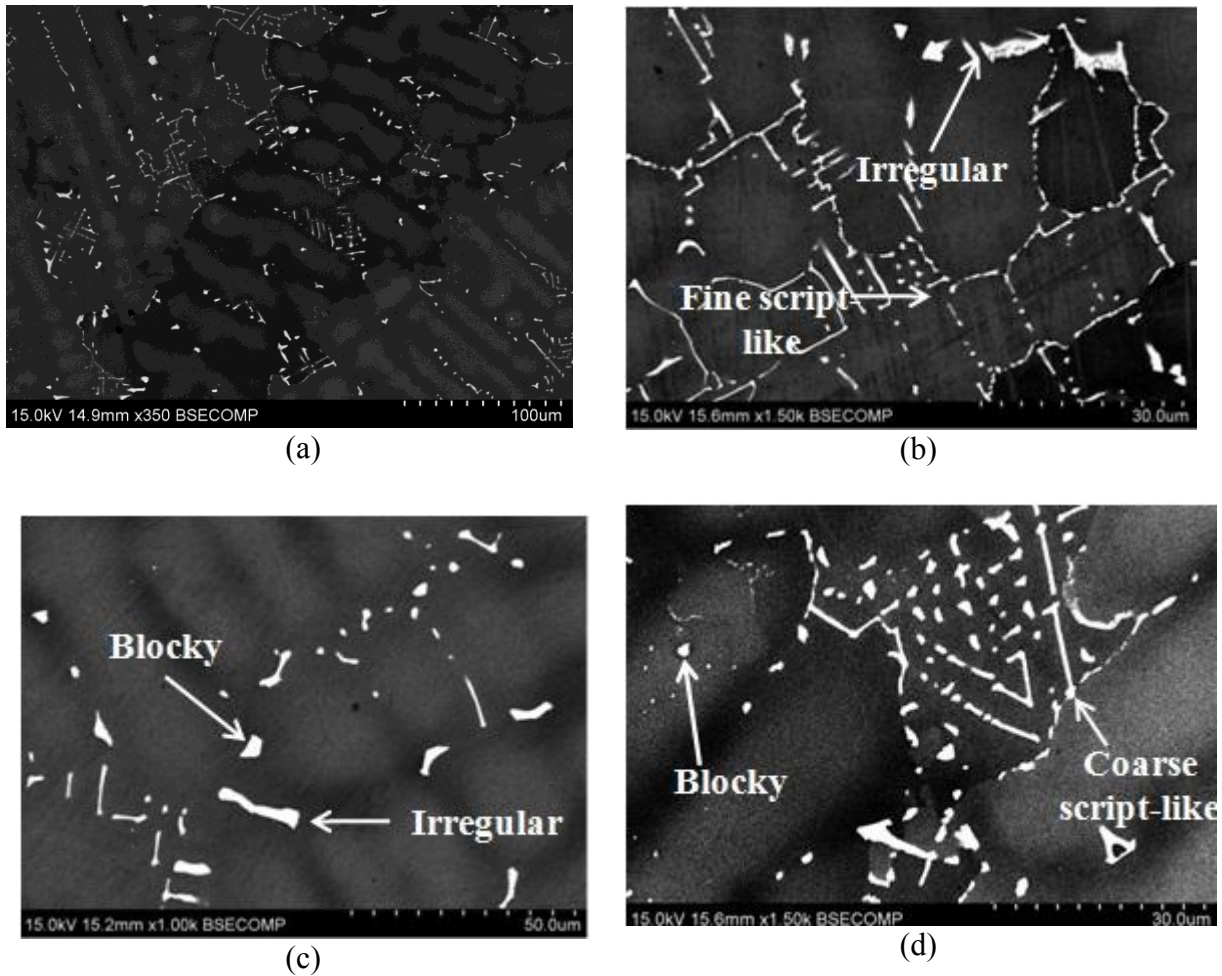


Figure 2-17. Variety of the carbide morphologies and sizes in Mar-M247 Ni-based superalloy microstructure [95].

The carbide morphology changes with carbide growth rate and carbide growth space, which is schematically shown in Fig. 2-18. At very slow carbide growth rates, the carbide grown by layered growth on the faceted surface, tries to maintain the equilibrium octahedron shape (Fig. 2-18 (a)). When the growth rate increases, some carbide hillocks grow on the surface or the edge of the octahedron (Fig. 2-18 (b)). When the growth rate continues increasing, some γ matrixes incorporate into the carbide, and carbide hillocks overlap with the master carbide (Figs. 2-18 (c, d)). When the growth rate increases again, carbide arms start to develop from the octahedron apex (Fig. 2-18 (e)). When the growth rate further increases, carbide arms grow upward and downward to form the hole-containing carbide (Figs. 2-18 (f, g)). When the growth rate continues increasing, thin and long carbide arms extend quickly from the octahedron apex, and the carbide becomes irregularly- or dendrite-shaped (Figs. 2-18 (h, i)).

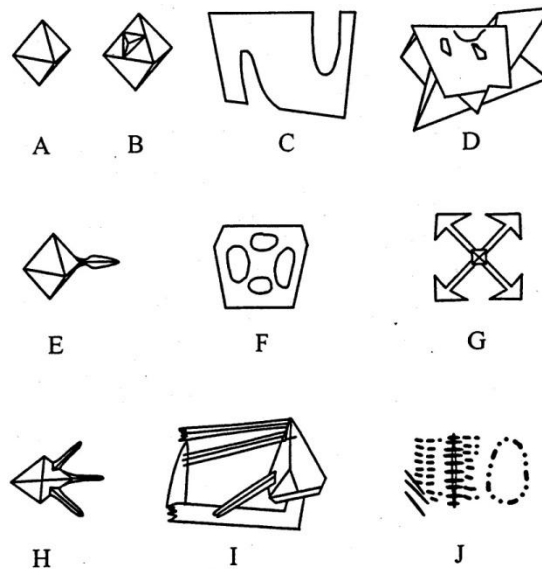


Figure 2-18. Schematic illustration of the carbide morphology at different carbide growth rates. The carbide growth rate increases gradually from A to J [14].

At extremely fast growth rates, like in the quenching process, fine needle, flake or dendrite-shaped script carbides are formed (Fig. 2-18 (j)) [14,100,114,115].

The growth rate also influences the carbide volume fraction and size. According to the Fig. 2-19, carbide volume fraction increases with rising growth rate at slow rates, but it becomes nearly constant at fast rates [14,116–118]. Also the average carbide size decreases quickly with increasing sample growth rate, but this trend declines at higher growth rates [14,100,118].

Other phase can be observed in the microstructure of a Ni-based superalloy is δ Phase with the formulation of Ni_3Nb which has the orthorhombic crystallographic structure. δ phase establishes an incoherent interface with γ matrix and does not confer any strength to alloy, whereas it decreases the ductility of alloy [11,22]. The formation of this phase takes place by solid solution diffusion mechanism and the temperature of formation varies in different alloys [11,22,119]. Applying the solution heat treatment at high temperature treatment, the δ phase and some of carbides are dissolved, but the grain growth occurs simultaneously [23].

Mar-M247 Ni-based superalloy is a Hf-modified Ni-based superalloy. Hf has been known to have a strong effect on carbide morphology in cast alloys, and subsequently on the mechanical properties [95,111]. Two kinds of MC carbides and fine Cr-rich M_{23}C_6 carbides were present in the microstructure of Mar-M247 Ni-based superalloy after heat treatment [95]. Precipitation of carbides at grain boundaries prevents grain boundary sliding at elevated temperatures and hence improves creep and rupture strength [11,112]. In contrast, a

continuous network of script carbides drastically reduces ductility of the alloy by facilitating crack initiation and propagation along the carbides [14,95,111,113]. Therefore, small equiaxed carbides are the preferred morphology in Ni-based superalloys.

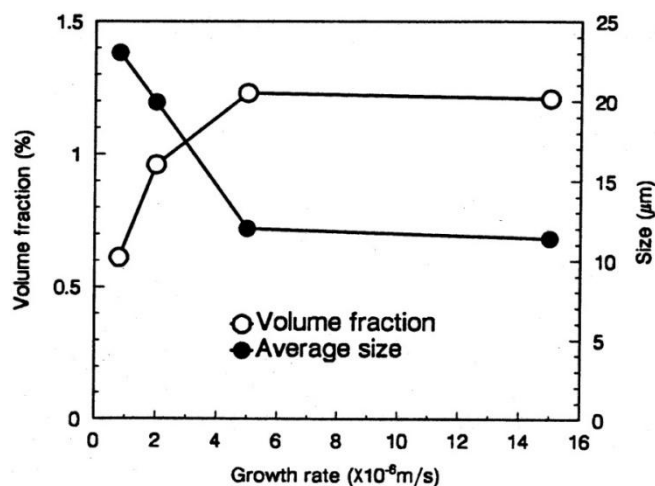


Figure 2-19. Volume fraction and average size of the carbides in the directionally solidified part of Mar-M247 LC Ni-based superalloy grown at different growth rates [14].

2.2.5 The influence of thermal variation on γ/γ' eutectic

In Ni-based superalloys, γ/γ' eutectic is a non-equilibrium solidification microconstituent formed by the segregation of eutectic forming elements such as Ti, Al and Ta in interdendritic areas during solidification process [84,120]. As we know the degree of homogeneity, which is controlled by final microstructure size such as dendrite arm spacing and eutectic phase [1], influences strongly on the phase stability and mechanical properties of Ni-based superalloys [120,121]. It should be noted that the most of the secondary creep cracks, formed at matrix-eutectic interface or within γ/γ' eutectic phase, are relevant to the existence of γ/γ' eutectic phase [61]. Moreover, Gasko et al. demonstrated that having higher volume fraction of γ/γ' eutectic, room temperature yield strength decreases, while elongation-to-failure increases [122].

Formation of γ/γ' eutectic pools, taking place at final stage of solidification [31], is controlled by chemical composition of the alloy and cooling rate during alloy solidification [31,120]. Figure 2-20 shows the effect of cooling rate on the size and volume fraction of γ/γ' eutectic phases for the Ni-based superalloy. Considering the picture, rising cooling rate,

which is obtained by increasing withdrawal rate at constant thermal gradient, eutectic phase size and eutectic volume fraction reduce [61]. Similar trend is reported by Seo et al. [120].

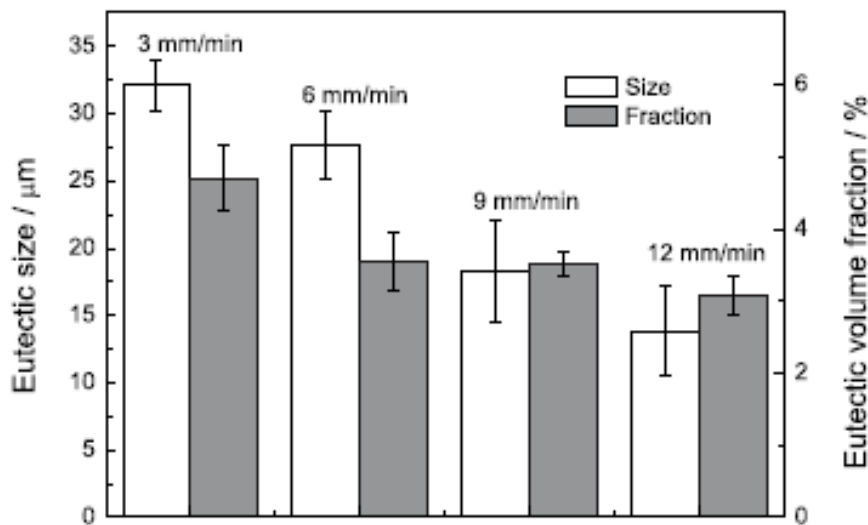


Figure 2-20. Size and volume fraction of the γ/γ' eutectic in the DD10 single crystal Ni-based superalloy cooled at different withdrawal rates [61].

Figure 2-21 presents the distribution of the γ/γ' eutectic at various cooling rates in CMSX-10 and CMSX-4 Ni-based superalloys. The γ/γ' eutectic pools located at the interdendritic region are clearly obvious in the dendritic structure.

Considering the Fig. 2-21, the γ/γ' eutectic pools were observed to be rather isolated and dispersed at relatively low cooling rates, whereas an interconnected morphology was seen as the cooling rate increases. The qualitative examination of the as-cast microstructure indicated that the volume fraction and size of γ/γ' eutectic pools decreases with increasing the cooling rate in both alloys. This might be because increasing the cooling rate causes the decrease in the dendrite arm spacing, and thus the decrease in the liquid pool size between dendrites, where γ/γ' eutectic forms at the last stage of solidification [31,120].

2.2.6 Heat treatment of Ni-based superalloys

It is well-known that the tensile and creep properties of Ni-based superalloys at elevated temperatures vary significantly with heat treatment, even for a constant grain size [123,124]. After the manufacturing processes such as casting and welding, many different kinds of heat treatments are carried out for annealing, homogenization and stress relieving. Heat treatment for precipitation strengthening is usually carried out in two steps; a solution treatment

followed by one or two aging treatments. The promotion in various mechanical properties after heat treatment in Ni-based superalloys is related to the phase transformation and modification of morphology, volume fraction and size of existed phase and microconstituents in as-cast part [124].

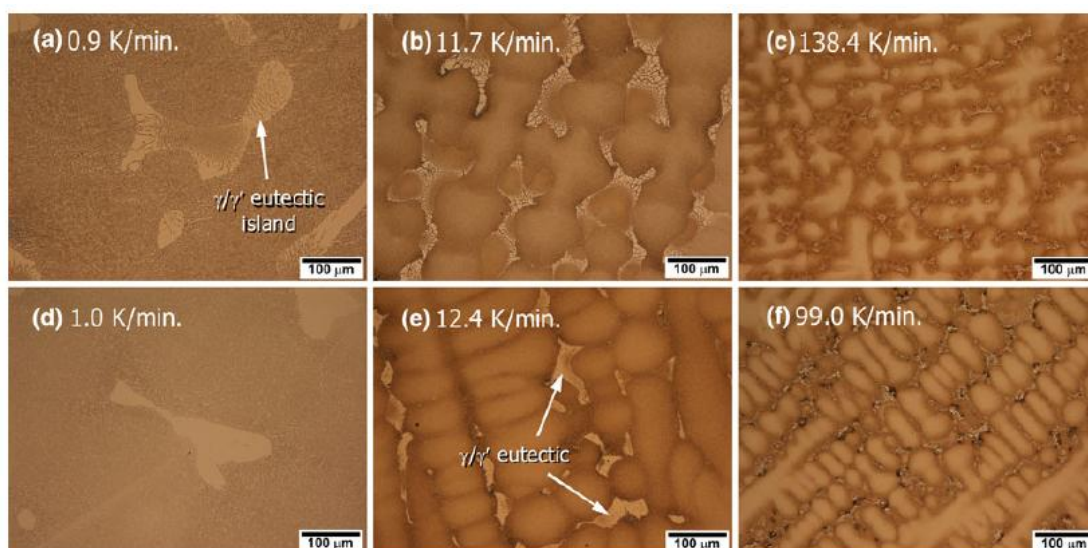


Figure 2-21. influence of cooling rate on the size and morphology distribution of γ/γ' eutectic pools in the alloys (a-c) CMSX-10 and (d-f) CMSX-4 Ni-based superalloys [120].

Solution heat-treatments are common in Ni-based superalloys and play a key role for the application of these materials at high temperatures [39,125]. The objectives of this heat-treatment are the complete dissolution of γ' phase in the γ matrix and minimizing the segregation from non-equilibrium solidification in preparation for the aging heat-treatment [126]. Although the primary γ' precipitates dissolve quickly in the γ matrix, a noticeable time is required for the dissolution of γ/γ' eutectic regions and minimizing the segregation of the materials, because these materials usually have several heavy alloy elements that diffuse slowly in the matrix [39,42]. Theoretically, the solution heat treatment should be carried out between γ' solvus and solidus temperatures in Ni-based superalloys, as described by Semiatin et al.[127]. Then, by aging heat treatments, producing an uniform and coherent material, it is possible to achieve a controlled γ' phase re-precipitation [39,83,103,128].

Although Mar-M247 Ni-based superalloy has interesting properties as an cast alloy, heat treatment via solutioning and aging is usually applied to improve mechanical properties. Generally, the solutioning temperature is above 1090 °C and the temperature below 1090 °C is utilized for aging treatment [7,40,41]. Several heat treatment conditions have been reported

in the literature for Mar-M247 Ni-based superalloy. Baldan et al. carried out the solution heat treatment between 1185 and 1270 °C and after that aged them between 770 and 980 °C [40]. Lee and Lee [42] propose that solution heat treatment at 1240 °C for 2 h causes the overall decomposition of primary γ' into secondary γ' . Wolff [129] performed a solution heat treatment in multiple steps with heating at 1230 °C for 2 h and then at 1260 °C for 2 h followed by air cooling. The purpose of solution treatment in multiple steps is to increase the incipient melting point of the alloy to enable complete dissolution of primary γ' phase through decomposition into secondary γ' and to achieve more than 90 % dissolution of γ/γ' eutectic. One-step aging treatment after solutioning typically consists of heating at 870 °C for 20 h followed by air cooling. Two-step aging treatment, consisting of aging at 980 °C for 5 h and then at 870 °C for 20 h, was performed by Kattus [41]. At the first aging step, coarse γ' precipitates and improves the morphology of carbides and their distribution at grain boundaries, while at the second step, usually at a lower temperature, precipitates finer γ' phase and contributes to the tensile strength as well as rupture life [40].

2.2.6.1 The effect of heat treatment on grain characteristic

Since heat treatment is carried out at high temperature the grain growth mechanism can be activated. However, the grain growth at high temperature is governed by particles such as γ' and carbides, dispersed in alloy, as they can pin the grain boundary sliding at elevated temperature. Nevertheless, grain growth occurs when the pinning force is not enough effective to suppress grain boundary sliding.

Figures 2-22 (a-d) show the microstructural changes after solution treatment of CM-247 LC Ni-based superalloy, which is the modified Ni-based superalloy based on the chemical composition of Mar-M247 Ni-based superalloy at 1221–1254 °C for 2 h. It is seen that the grain size is not influenced by the solution treatment, as grain size is in the range of 60–70 μm . Although, Fig. 2-22 (e) indicates that the grain grew at the temperature of 1260 °C after 2 h [130].

The variation of grain size with heat treatment time at various temperatures is plotted in Fig. 2-23. It is seen that for the samples heat treated at 1110 °C and 1127 °C, grain growth is almost suppressed after 30 minutes, because of particle pinning effect, while stable grain growth is observed after 300 min at 1132, 1177, and 1216 °C temperatures. This is because of pinning force at these higher temperatures will be much smaller due to the lower V_f of the γ'

phase. For a small pinning force, it is more likely that some thermal unpinning occurs [131], and thus it would take a longer time to reach a stable grain size [132].

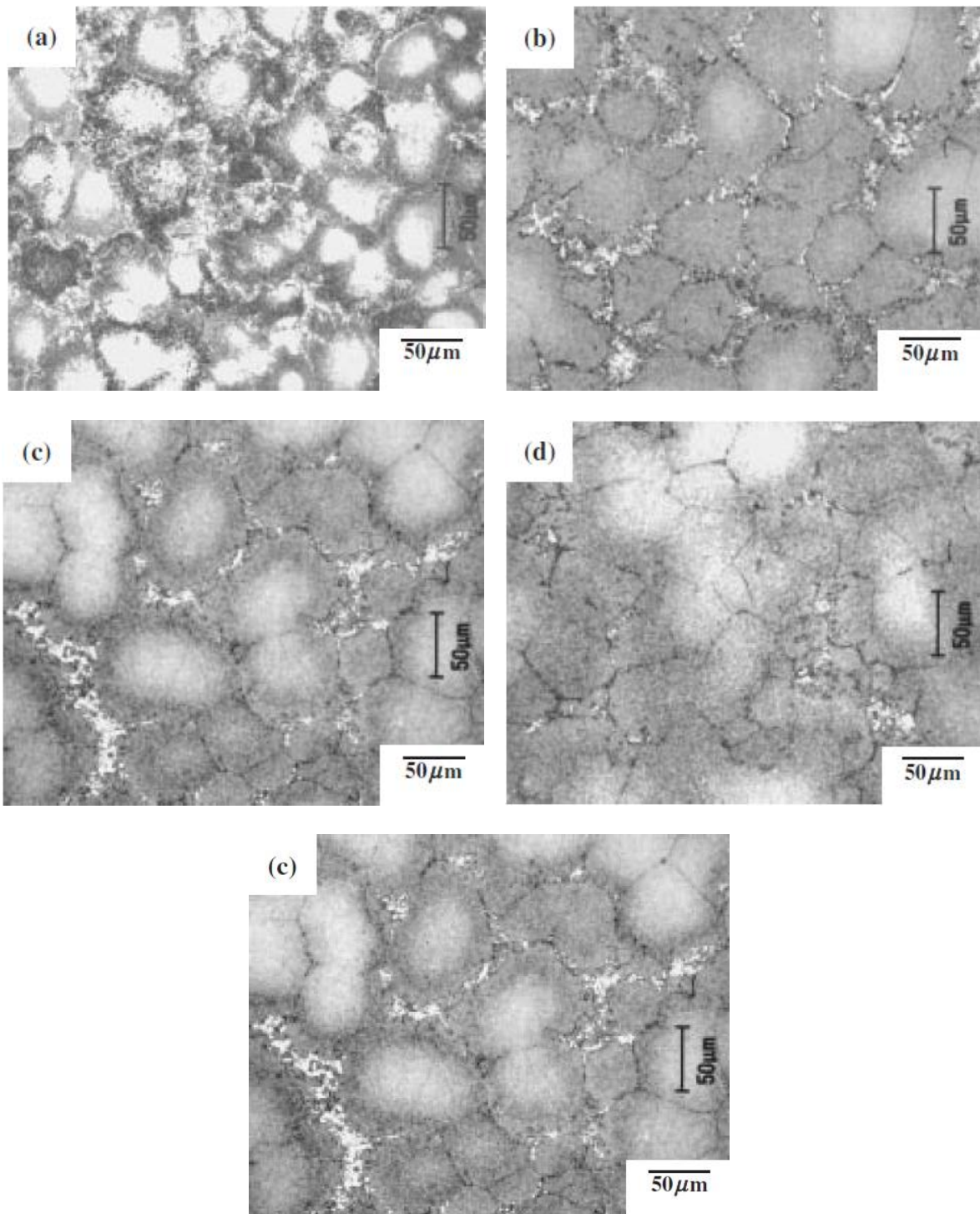


Figure 2-22. Optical micrographs showing the grain size after solution-treatment: (a) 1221 °C/2h, (b) 1240 °C/2h, (c) 1249 °C/2h, (d) 1254 °C/2h and (e) 1260 °C/2h [130].

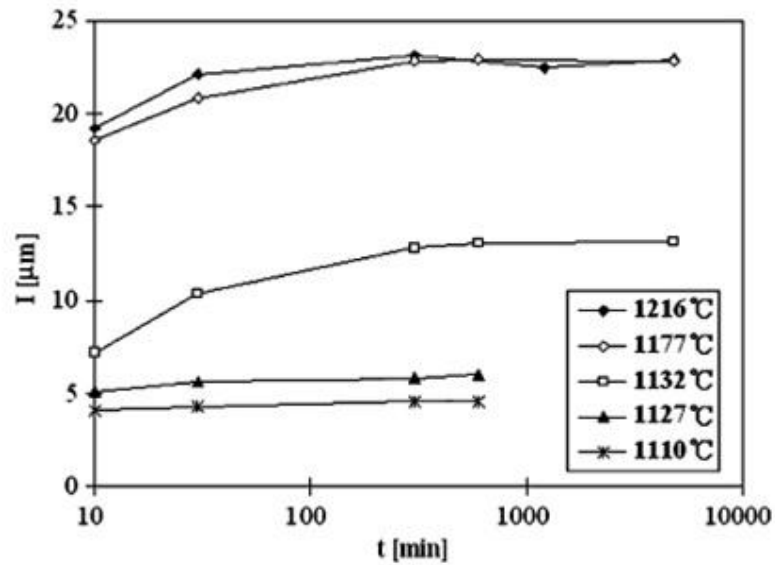


Figure 2-23. Variation of the mean γ grain size, I , with heat treatment time, t , for samples heat treated at five different temperatures [132].

2.2.6.2 The effect of heat treatment on phase composition

As already mentioned, the main aim of a solution heat treatment applied to Ni-based superalloys is the dissolution of coarse γ' formed during solidification, reduction of chemical segregations as well as dissolution of γ/γ' eutectic [7,103,122].

The microstructural evolution of Mar-M247 Ni-based superalloy after solution heat treatment at 1260 °C for 8 h is presented in Fig. 2-24. It is observed the presence of cubic γ' precipitates with approximately 0.5 μm in the dendritic region of the as-cast material (Fig. 2-24 (a)) and with 0.1 μm after solution heat treatment (Fig. 2-24 (b)). Performing the solution heat treatment, the primary γ' phase begins to break down and dissolve gradually into a smaller piece of secondary γ' up to the complete dissolution of the γ' phase, obtaining a homogeneous γ matrix [39]. The decomposition of primary γ' occurs from the surface toward the core. Solutioning at a higher temperature or for a longer time causes the decomposition of the primary γ' into secondary γ' more thoroughly, and hence reduces the size of the primary γ' . The secondary γ' phase is relatively stable at high temperature, and disperses uniformly in the matrix [42].

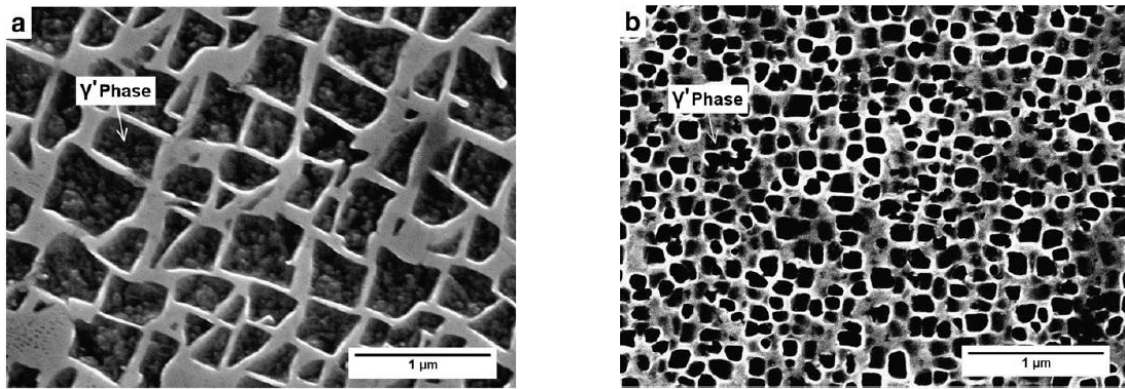


Figure 2-24. Micrographs of Nb-modified Mar-M247 Ni-based superalloy showing the γ' phase precipitated in γ matrix: (a) dendritic region of as-cast material; and (b) after solution heat treatment at 1260 °C for 8 h [39].

The TEM micrographs of γ' precipitates in Fig. 2-25 depict the changes in the microstructure that take place during ageing at 704 and 725 °C for 1000 and 4000 h. According to the Fig. 2-25, with increasing aging temperature and time, the γ' precipitates have an obvious growth, particularly with temperature increment. In all specimens, the morphology of γ' precipitates

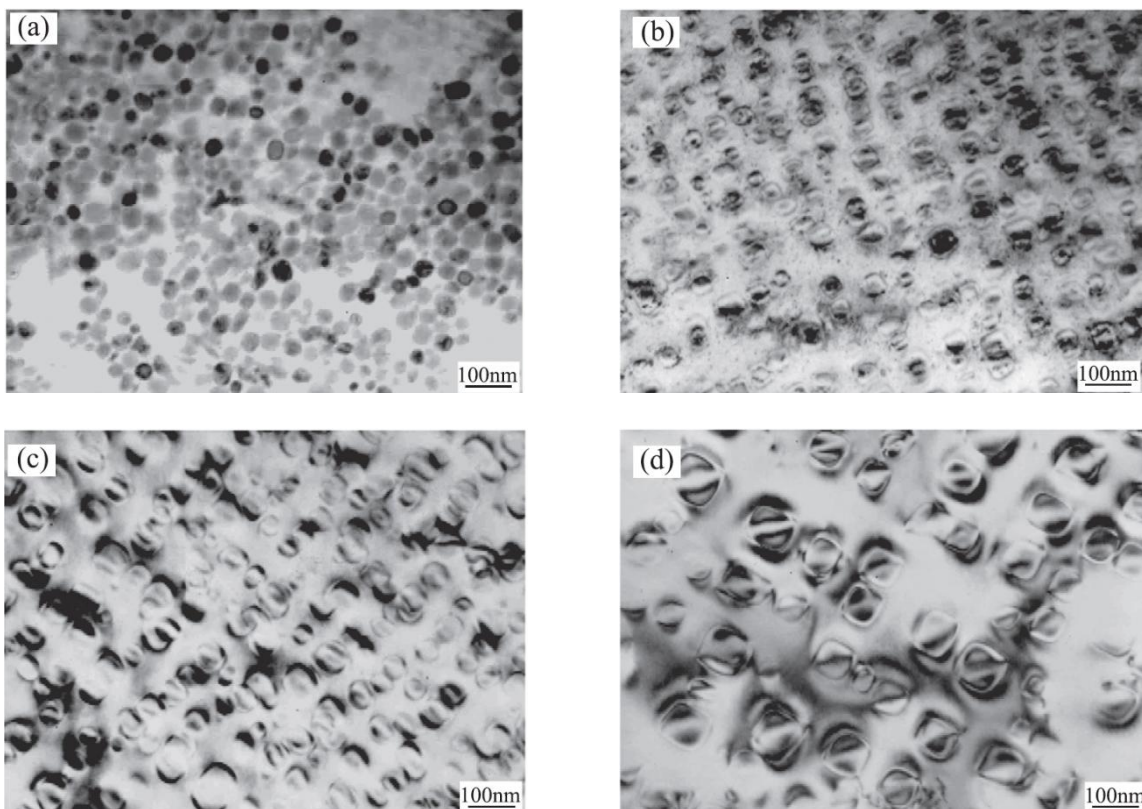


Figure 2-25. TEM micrographs of γ' precipitates in the Ni-based superalloy aged at (a,b) 704 and (c,d) 725 °C for 1000 and 4000 h [133].

indicates no remarkable change in shape during heat treatment but takes a cubic form although the small γ' particle exhibits a rounded cubic shape. In addition, no coalescing behavior is evident after prolonged ageing [133,134].

The influence of solution heat treatment temperature and time on the eutectic microconstituent and microsegregation of Mar-M247 Ni-based superalloy is shown in Fig. 2-26. With respect to the micrograph of the alloy heat treated at 1210 °C for 1230 min in Fig. 2-26 (a), it is observed that at 1210 °C even after long time heat treatment, the eutectic microstructure remains in the interdendritic region. Whereas heating at 1250 °C for just 77 min (Fig. 2-26 (b)) leads to almost complete dissolution of the eutectic constituent, which implies the strong effect of temperature and diffusion on solution heat treatment [40,122,130]. Increasing the duration of heat treatment from 77 to 310 min at 1250 °C has the excessive effect on reduction of segregation in interdendritic are, as it shown in Fig. 2-26 (c). The time required for total elimination of interdendritic segregation would be quite long, as the segregation consists of heavy elements diffusing slowly [40].

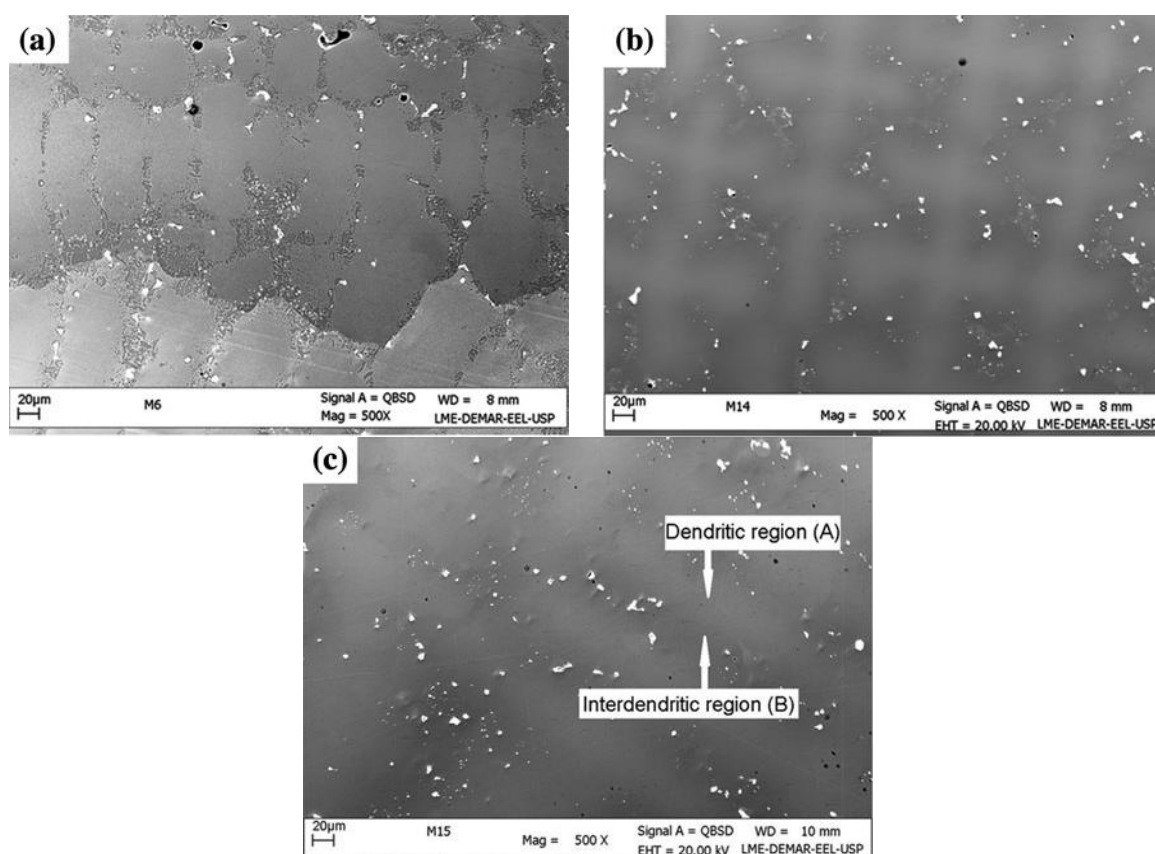


Figure 2-26. Micrographs of solution heat treatments at: (a) 1210 °C for 1230 min; (b) 1250 °C for 77 min; (c) 1250 °C for 310 min [40].

2.2.6.3 The effect of heat treatment on carbide characteristic

As it is known, elevated temperature activates the diffusion mechanism and materials reaction, so it is expected that carbide particles are dissolved and transformed during heat treatment. Changes in the size, morphology, and composition of carbides during solutioning have been observed, as the carbides became smaller in size and more rounded in morphology compared with the carbides in the initial as-cast microstructure [40]. However, Bor et al. demonstrated that there is no significant change in size and distribution of carbides after heat treatment of Mar-M247 Ni-based superalloy [7].

The typical process of primary MC carbide degradation in Ni-based superalloys is illustrated in Fig. 2-27. With increasing the exposure temperature and time during long term thermal exposure, the primary MC carbide severely deteriorates and various decomposition products are sequentially present on the periphery of the original MC core. A thin γ' layer with small and discrete Cr-rich $M_{23}C_6$ particles are formed on the MC/ γ interface at the initiation of thermal exposure (Fig. 2-27 (a)). These $M_{23}C_6$ particles grow larger and larger and tend to link each other to form a γ' - $M_{23}C_6$ dual microstructure (DM) (Fig. 2-27 (b)) or a γ' - $M_{23}C_6$ - γ' sandwich microstructure (SM) with prolonged exposure time (Fig. 2-27 (c)). As the primary MC carbide decomposes, it acts as a source of C and Ti while the γ matrix is the source of Ni, Al and Cr. Since C diffuses a lot faster than any other elements, it combines with Cr to form $M_{23}C_6$ on the MC/ γ interface; and then, the local enrichment of γ' forming elements (Ni, Al and Ti), which is caused by the precipitation of the $M_{23}C_6$ carbide, leads to the formation and growth of γ' precipitate around the $M_{23}C_6$ carbide [103,105].

The reduction of carbide volume fraction with increasing the temperature and time of solution heat treatment is reported by Tang et al. Considering the Fig. 2-28, the reduction of carbide volume fraction is seen from 1230 to 1270 °C, while there is no noticeable change of carbide volume fraction from 1270 to 1300 °C. At 1300 °C for 120 min, the volume fraction of carbides is reduced to 1.62 % [135].

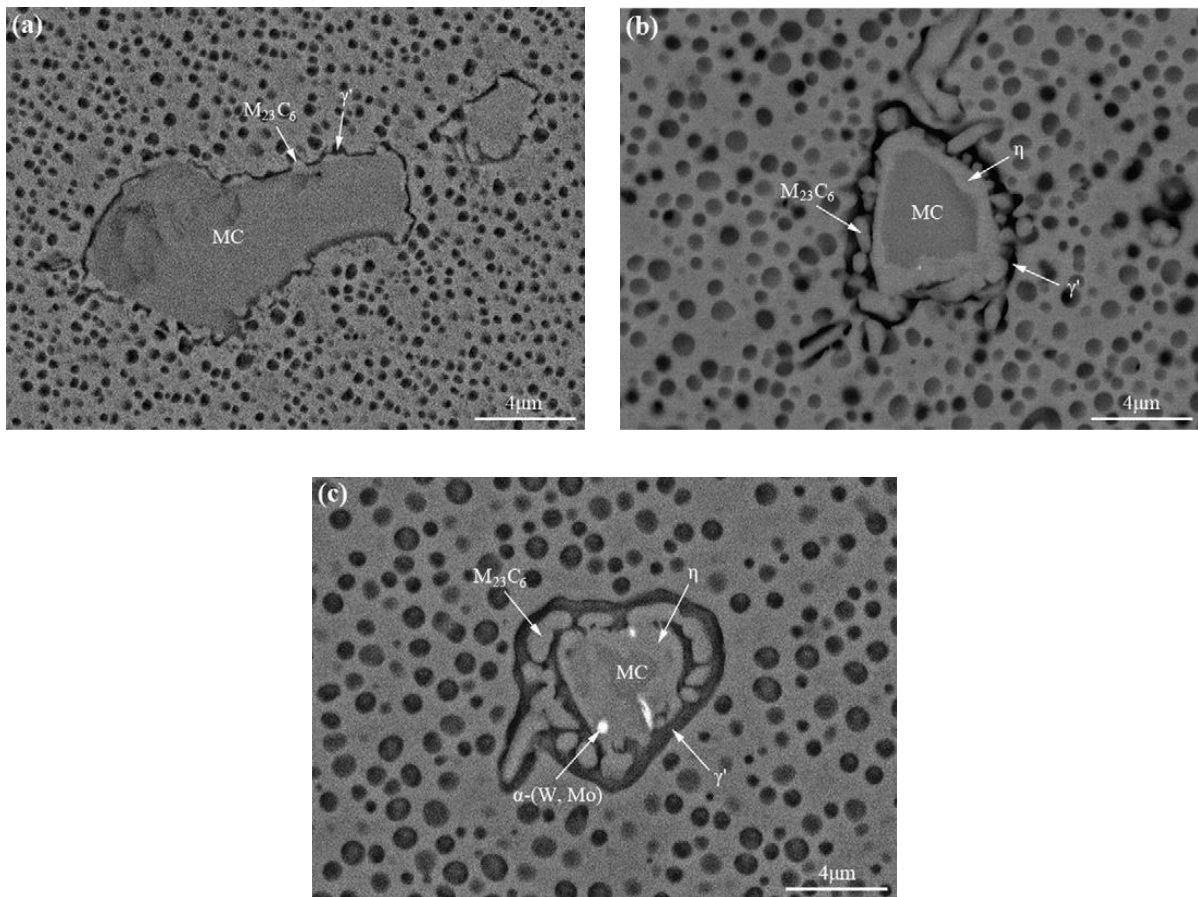


Figure 2-27. Back scattered electron (BSE) micrographs of primary MC degradation under different thermal exposure conditions in the K452 Ni-based superalloy: (a) 800 °C for 1000 h; (b) 850 °C for 5000 h; (c) 900 °C for 10,000 h [105].

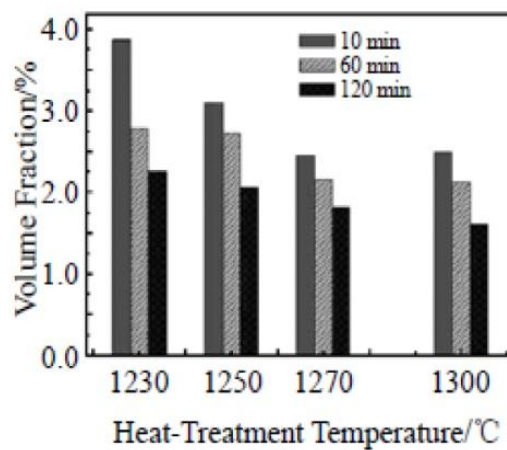


Figure 2-28. Relationship between volume fraction of carbides and heat treatment conditions [135].

3 Material and experimental techniques

3.1 Material

The material used in this study was a Mar-M247 Ni-based superalloy supplied by Precicast Bilbao (Bilbao, Spain). Chemical composition of the material is presented in Table 3-1.

Table 3-1. Chemical composition of the Mar-M247 Ni-based superalloy.

elements	C	Cr	Mo	Ti	Co	W	Ta	Al	Hf	B	Zr	Ni
content (wt%)	0.15	8	0.6	1	10	10	3	5.5	1.5	0.02	0.03	bal.

Mar-M247 Ni-based superalloy contains the variety of elements each of which plays a specific role to establish the characteristics of this alloy. For instance, Al and Ti together with Ni are major elements for the formation of γ' precipitation in Ni-based superalloys controlling effectively mechanical properties. Moreover, volume fraction and the size of carbides increase obviously with the increasing of carbon content, but the carbon addition does not impose an obvious change in the carbide morphology [136]. As mentioned, the addition of carbon, in amount from 0.05 to 0.2 %, and carbide forming elements, such as Cr, W, Mo, Nb, Ta, Ti, and Hf, enables the precipitation of mainly $M_{23}C_6$, MC and M_6C types carbides in Ni-based superalloys [22,95]. In addition to the carbide formation role of the Cr

and W, the γ' precipitation shape is also governed by the concentration of these elements in Ni-based superalloys [6]. Also refractory elements, such as Nb and Ta, accompanied by Cr are known to affect corrosion resistance and alloy stability [137]. The results show that Co influences the solubility of elements in the γ matrix which results in the increment of the γ' volume fraction and the stabilization of MC-type carbides [138].

This chapter describes in detail experimental techniques some of which constitute the physical simulation tool considered later in chapter 5.

3.2 Prediction of local cooling rates during investment casting of NGVs from Mar-M247 Ni-based superalloy using thermal model

Physical simulation of investment casting begins with calculation of local cooling rates during solidification of complex shape part using thermal model. The obtained data serve as input parameters, cooling rates, for physical simulation of melting/solidification experiments in the Gleeble 3800 thermo-mechanical simulator that allows reproducing various local thermal profiles seen by the material during solidification. Thus, obtained specimens, named Gleeble specimens, can be further used for microstructural and/or mechanical characterization which can be compared with the characteristics of NGVs specimens to validate the physical simulation tool. So, the databank on effect of cooling rate on the microstructure and mechanical properties is generated to predict the local microstructure and local mechanical properties at each point of casting. Melting and solidification experiment is described in details below in section 3.3. It should be noted that the thermal model and NGVs casting trial were carried out by Precicast Bilbao.

3.2.1 Development of the thermal model

The basis for reliable simulation of investment casting is a very accurate prediction of the thermal history at each point of the casting. Development of the thermal model requires the optimal selection of the thermo-physical parameters along with the proper establishment of boundary conditions as noted in the ASM Handbook [139]. It should also be noted that each manufacturing process has unique boundary conditions that have to be identified, understood and characterized for the specific application being simulated. The boundary conditions can also be equipment specific, meaning that a furnace may not have the same boundary conditions as another furnace under the same nominal processing conditions.

During investment casting, heat flows by conduction through the metal, ceramic mould and insulation wrap and is removed from the surface by natural convection and radiation. The heat flow is transient, i.e. the temperatures in the casting, mould, and insulation wrap change with time. In this work, the thermal history was modeled using the three-dimensional finite element solver ProCAST (a trademark of ESI group) which is described in the ProCAST manual guide [140]. The governing partial differential equation of heat flow by conduction is expressed as,

$$\rho \frac{\delta H}{\delta T} \frac{\delta T}{\delta t} - \nabla[K\nabla T] - S(r) = 0 \quad (3-1)$$

where $\nabla = \frac{\partial}{\partial x} + \frac{\partial}{\partial y} + \frac{\partial}{\partial z}$, ρ stands for the density, T temperature, t time, K thermal conductivity, $S(r)$ is a spatially varying heat source, and H is the enthalpy of solidification, which encompasses both the specific heat term (c_p) and the evolution of latent heat (L) during solidification according to,

$$H(T) = \int_0^T c_p dr + L(1 - f_s(T)) \quad (3-2)$$

where f_s is the fraction of solid. Conservation of mass is enforced through the continuity equation

$$\frac{\delta \rho}{\delta t} + \frac{\delta(\rho u_i)}{\delta x_i} = 0 \quad (3-3)$$

where u_i is the corresponding component of superficial velocity. And the momentum equation is given as

$$\rho \frac{\delta u_i}{\delta t} + \rho u_j \frac{\delta u_i}{\delta x_j} + \frac{\delta}{\delta x_j} \left(p \zeta_{ij} (\mu + \mu_T) \frac{\delta u_i}{\delta u_j} \right) = \rho g_i - \frac{\mu}{K} u_i \quad (3-4)$$

where ζ_{ij} is the Kronecker delta, p the pressure, g_i the gravitational acceleration, and K the permeability. These equations are solved under assumption that the spatial derivatives of viscosity are small and the fluid is nearly incompressible. To simulate the effect of flow in mushy regions and to drive the velocities to zero when the material is fully solid, a source

term is added to the standard momentum equation. Initial and boundary conditions for the resolution of previous equations are applied on:

- Temperature,
- Velocity,
- Pressure,
- Fixed turbulent kinetic energy,
- Fixed turbulent dissipation rate,
- Specific heat flux,
- Convective heat flux,
- Radiation heat flux.

For the more complex view factor radiation capability, ProCAST, uses a net flux model. Rather than tracking the reflected radiant energy from surface to surface, an overall energy balance for each participating surface is considered. It allows the net radiant flux to appear as a boundary condition for the heat conduction analysis in ProCAST. More detailed explanations about the resolution of previous equations can be found in [141].

Several software packages were used to generate the thermal model. The NGV design was created with Solid Works software (powered by Dassault Systems SolidWorks Corporation), while the feeding system was created with Unigraphics software (powered by Unigraphics Solutions Incorporation). Both packages are linked to the casting simulation software ProCAST. Surface and volume meshes were generated by Visual-Mesh (ProCAST Software Package), considering a maximum distance between nodes of 2 mm inside the NGV, and 6 mm for the gating system and pouring cup. The investment casting ceramic mould was composed of layers which were created by ProCAST 3D-Mesh. The ceramic mould has an average thickness of 13 mm. The thickness of the insulation wrap was also 13 mm and was created and meshed following the same procedure. Only one half of the mould was considered due to symmetry (Fig. 3-1) in order to speed up the simulations.

Data from different sources were carefully analysed to assign the thermo-physical properties to all the components of the casting system. Those sources include the ProCAST database which was described in detail by Pequet et al. [142], experimental data from industrial companies (Precicast Bilbao and Precicast Novazzano), as well as technical references from previous similar exercises. The thermo-physical properties of the Mar-M247 Ni-based superalloy were extracted from the ProCAST Database (Table 3-2). Figure 3-2 illustrates dependence of these properties on temperature. The values of the liquidus and solidus temperatures (1366 and 1266

°C, respectively) were also taken from this source. It should be noted that a comparison with the Lever Rule Model and Scheil Model (both described in the ASM Handbook [143]) was made to confirm these data. Regarding the ceramic mould and wrap insulation, the density and specific heat as a function of temperature were taken from the ProCAST database (Table 3-2).

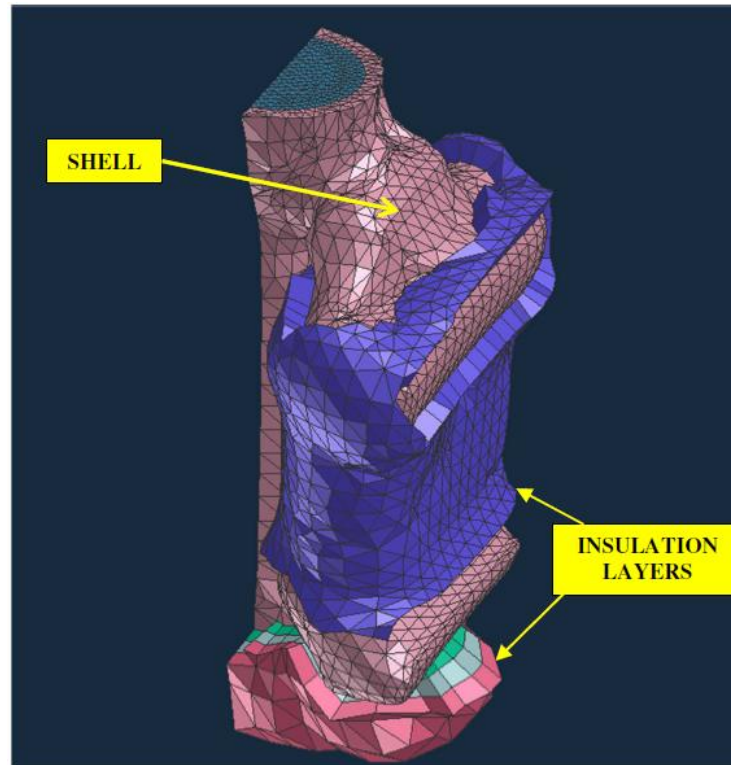
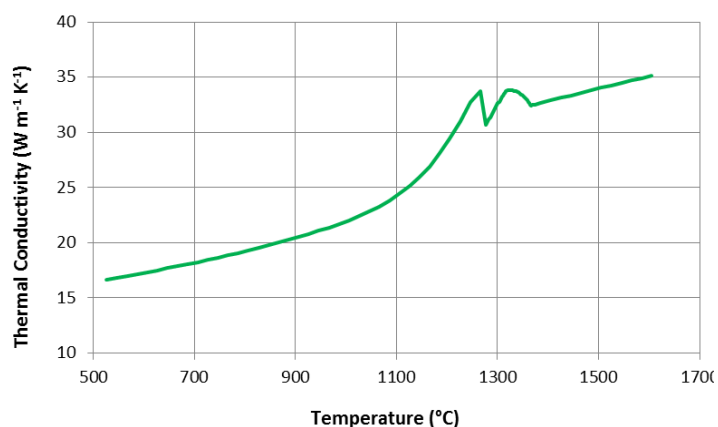


Figure 3-1. Model of half shell with insulation wrapping, showing geometry and layer distribution of the insulation.

Values for the thermal conductivity as a function of temperature (Fig. 3-3 (a)) were obtained by an inverse simulation procedure by comparing the simulation results for simple casting geometries with experimental data generated earlier by Precicast Bilbao. The description of the inverse simulation procedure can be found in O'Mahoney and Browne [144]. Figures 3-3 and 3-4 illustrate dependence of properties on temperature for ceramic mould and wrap, respectively.

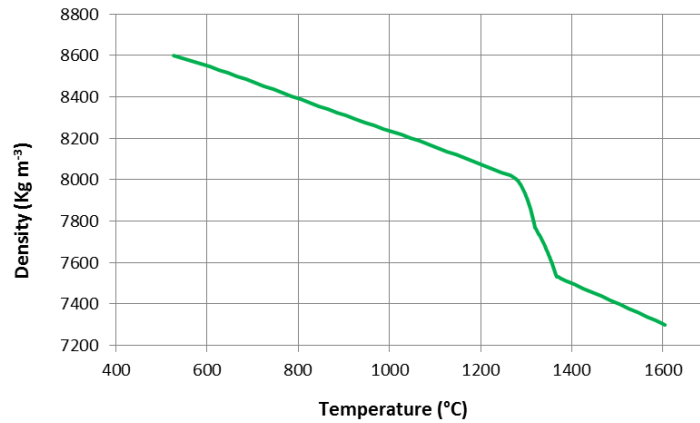
Table 3-2. Thermo-physical properties and boundary conditions used in the thermal model.

Material	Property (units)	Value
Mar-M247 Ni-based superalloy	Thermal conductivity ($\text{W}\cdot\text{m}^{-1}\cdot\text{K}^{-1}$)	15-35 *
	Density ($\text{kg}\cdot\text{m}^{-3}$)	7300-8600 *
	Enthalpy (kJ/kg)	100-800 *
	Viscosity ($\text{kg}\cdot\text{m}^{-1}\cdot\text{s}^{-1}$)	$2-3.25\cdot 10^{-3}$ *
	Liquidus temperature ($^{\circ}\text{C}$)	1366
	Solidus temperature ($^{\circ}\text{C}$)	1266
Mould	Thermal conductivity ($\text{W}\cdot\text{m}^{-1}\cdot\text{K}^{-1}$)	0.4-1.7 *
	Density ($\text{kg}\cdot\text{m}^{-3}$)	1860-1915 *
	Specific heat ($\text{kJ}\cdot\text{kg}^{-1}\cdot\text{K}^{-1}$)	0.7-1.3 *
	Emissivity	0.7
Insulation wrap	Thermal conductivity ($\text{W}\cdot\text{m}^{-1}\cdot\text{K}^{-1}$)	0.1-0.5*
	Specific heat ($\text{kJ}\cdot\text{kg}^{-1}\cdot\text{K}^{-1}$)	0.9-1.3 *
	Emissivity	0.7
Metal-mould	HTC ($\text{W}\cdot\text{m}^{-2}\cdot\text{K}^{-1}$)	200-2500 *
Mould-wrap	HTC ($\text{W}\cdot\text{m}^{-2}\cdot\text{K}^{-1}$)	100
Mould-enclosure	HTC ($\text{W}\cdot\text{m}^{-2}\cdot\text{K}^{-1}$)	3
Wrap-enclosure	HTC ($\text{W}\cdot\text{m}^{-2}\cdot\text{K}^{-1}$)	10.6
Enclosure	Emissivity	0.9
Melt pouring velocity	(mm/s)	1700
Melt temperature	($^{\circ}\text{C}$)	1549
Pre-heating temperature	($^{\circ}\text{C}$)	1200

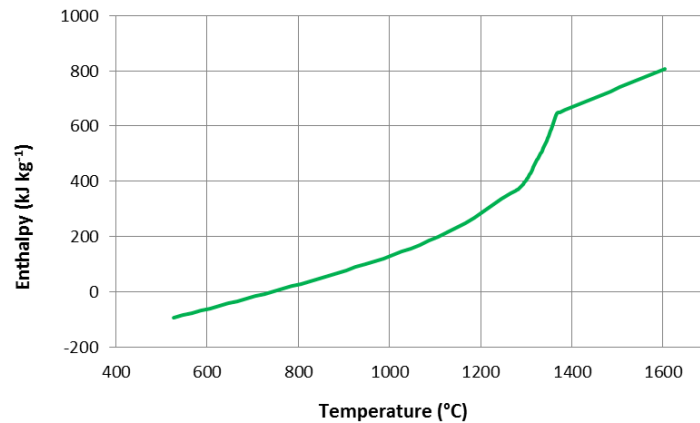


(a)

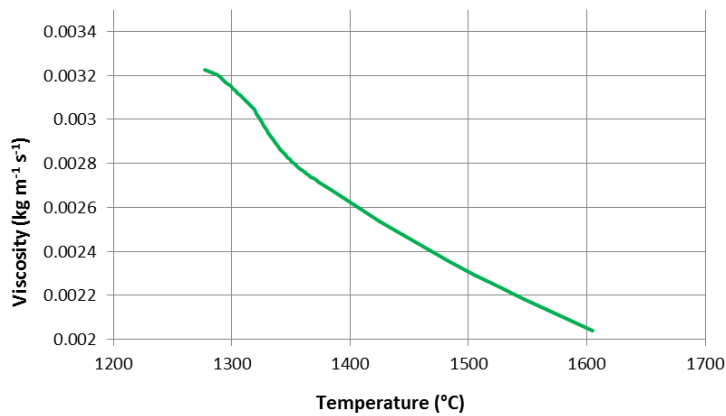
* The value depends on the temperature



(b)



(c)



d)

Figure 3-2. Properties of the Mar-M247 Ni-based superalloy vs. temperature: a) thermal conductivity, b) density, c) enthalpy, d) viscosity.

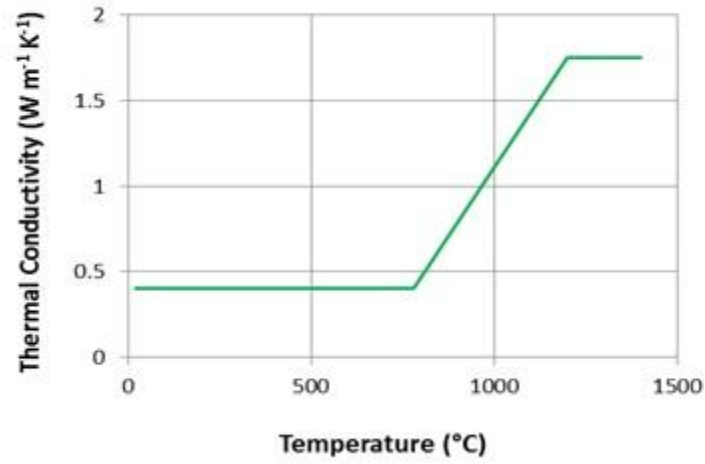
It is known that pouring of the melt at high temperature leads to radiation heat loss, as this heat loss is not always correctly taken into account during the modelling process; the value of mould conductivity at high temperatures should be increased to account for this phenomenon. Experimental studies on this topic were earlier carried out by Precicast Bilbao and the

experimental data from earlier measurements using the laser flash method (according to the ASTM E1461-07 standard) were considered. Analysis of all available data led to a final interval of mould conductivity in the range from 0.4 to 1.75 $\text{W}\cdot\text{m}^{-1}\cdot\text{K}^{-1}$ (Table 3-2), which is in a very good accordance with the data provided by Konrad et al. [145] for low temperatures, and coincide with the experimental data measured by the laser flash method at high temperature (Fig. 3-3 (a)). The ProCAST database, data from the manufacturer of the Kaolin wool and Precicast Bilbao were considered to define the thermal conductivity of the insulation wrap. The final values of the thermal conductivity in the insulation wrap were in the range of 0.1 to 0.5 $\text{W}\cdot\text{m}^{-1}\cdot\text{K}^{-1}$ (Fig. 3-4 (a), Table 3-2).

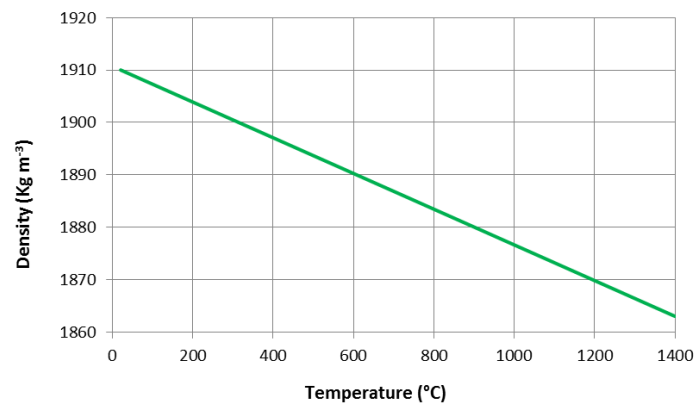
A suitable temperature dependent functional form (shown in Fig. 3-3 (d)) was used to determine the values of heat transfer coefficient (HTC) at the metal-mould interface. It is known that the HTC at the metal-mould interface is influenced by many factors such as casting geometry, pouring and pre-heating temperature, mould thickness, etc. Inverse and direct simulations were carried to obtain the final form of this function, which is plotted in Fig. 3-3 (d) as a function of temperature. This function is slightly different from the one proposed by the ProCAST database as was demonstrated by Santos et al. [146] and Dong et al. [147]. Nevertheless, the final HTC at the metal-mould interface was in a very good agreement with the data reported in the literature for molten Ni-based superalloys in contact with ceramic moulds. For example, Sahai and Overfelt [148] reported a HTC in the range 50-5000 $\text{W m}^{-2} \text{K}^{-1}$ for IN718 Ni-based superalloy. The HTC at the mould-wrap, mould-enclosure and wrap-enclosure interfaces have less influence on the final result of the thermal model as shown by Yang et al. [149]. Thus, it was assumed that they were constant with temperature and time, and the data from the ProCAST database were used (Table 3-2). Values of emissivity for mould, wrap and enclosure were also taken from the ProCAST database, and the environmental conditions were fitted to those registered during experimental casting trials (Table 3-2). Finally, the pouring velocity (calculated from the filling time of the mould and applied on a specified surface of the top surface of the pouring cap), the preheating temperature of the mould and temperature of melt poured into mould were also specified (Table 3-2).

The same filling steps performed during the experimental procedure are simulated by the software, using 2 seconds of filling to introduce the entire liquid alloy into the mould. Thus, the full solidification process is completed after 830 seconds of computation after the pouring. All experimental data were taken into account during the simulations to synchronize the experimental data with the simulation results. The simulation process was operated by the

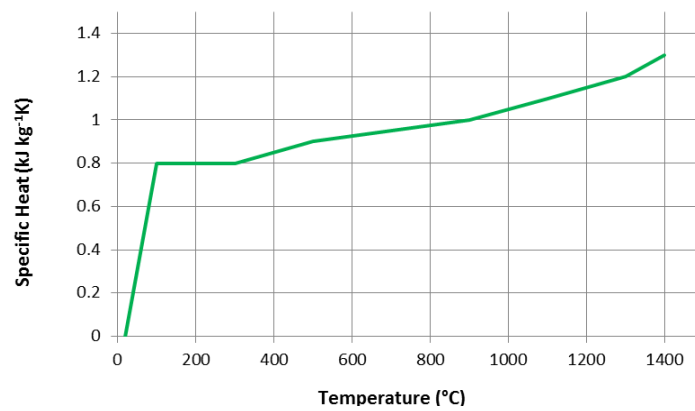
ProCAST Parallel Solver with 4 processors (2.40 GHz), and took nearly 11 hours to simulate the whole thermal history of the NGV investment casting process.



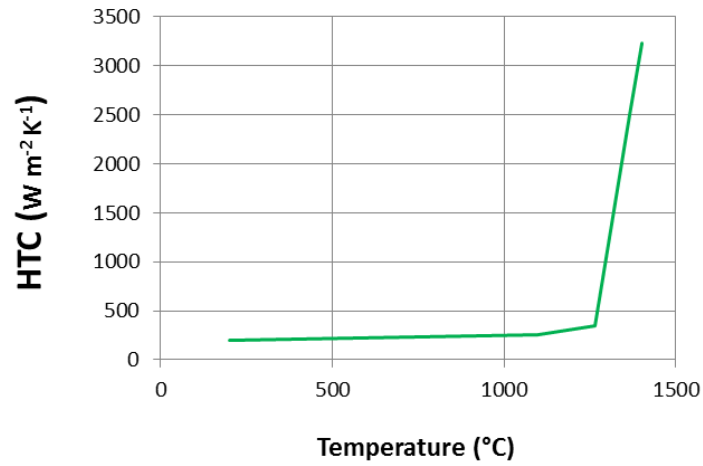
(a)



(b)

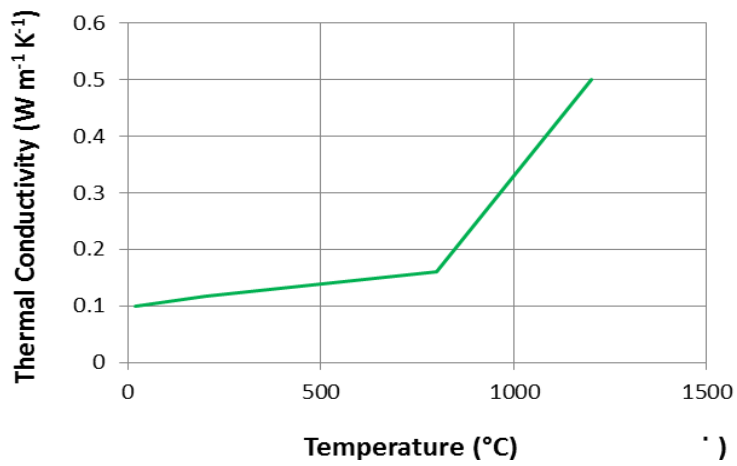


(c)

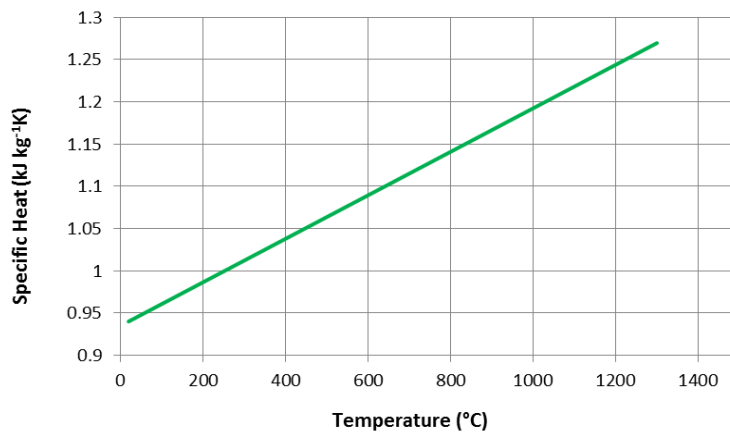


(d)

Figure 3-3. Properties of ceramic mould vs. temperature: a) thermal conductivity, b) density, c) specific heat, d) heat transfer coefficient (HTC) at the metal-mould interface.



(a)



(b)

Figure 3-4. Properties of wrap vs. temperature: a) thermal conductivity, b) specific heat.

3.2.2 Experimental validation of the thermal model

Experimental casting trials were carried out for validation of the thermal model as described below (see Section 3.6). Figure 3-5 illustrates the experimental temperature-time plots for metal, ceramic mould and insulation wrap during investment casting. Temperature recording was started once the thermocouples were located in the defined spots. The thermocouple placed in the metal is close to reach the pre-heating temperature 1200 °C, while the thermocouple placed in the mould records a temperature slightly over 1100 °C. In the readings from the thermocouple fixed to the insulation wrap, temperature rises up to 900 °C. Significant difference of temperatures between metal and wrap was registered at the beginning since it took time to place correctly each thermocouple into the tubes. This loss of time leads to partial cooling of the mould that, in turn, increases the temperature gradient between metal and mould.

After the mould entered the vacuum casting furnace, vacuum was pumped and melt was poured into the ceramic mould. The thermocouples placed in the metal and wrap clearly registered this event by showing a rapid temperature rise, whereas the thermocouple located in the ceramic mould showed a temperature decrease (Fig. 3-5). The liquidus-solidus transition in the metal can be easily identified in the experimental temperature-time as change in the reduced slope. The cooling rate increases once the melt is solidified.

The temperature-time plots generated by the thermal model are compared with the experimental results in Fig. 3-5. A very good agreement is observed for the thermal history in the metal and in the wrap, where the simulation results match very well the experimental results during first 6000 s of the solidification/cooling process. However, a difference of nearly 100 °C is found between the predicted temperature and the experimental data in the ceramic mould. Despite the close location of the thermocouple to the inner surface of the ceramic mould, the temperature registered by this thermocouple hardly achieves 1100 °C, though the melt was poured into the ceramic mould at 1459 °C. The reasons for such discrepancy will be discussed in Section 3.2.3.

A proper prediction of the liquidus-solidus transition has to be achieved in a reliable thermal model. A deeper analysis of the liquidus-solidus transition is found in Fig. 3-6, which shows a perfect match between simulation and experimental results. The most significant deviation between numerical predictions and experimental results occurs at 300 seconds after pouring, and the difference is just 4 °C.

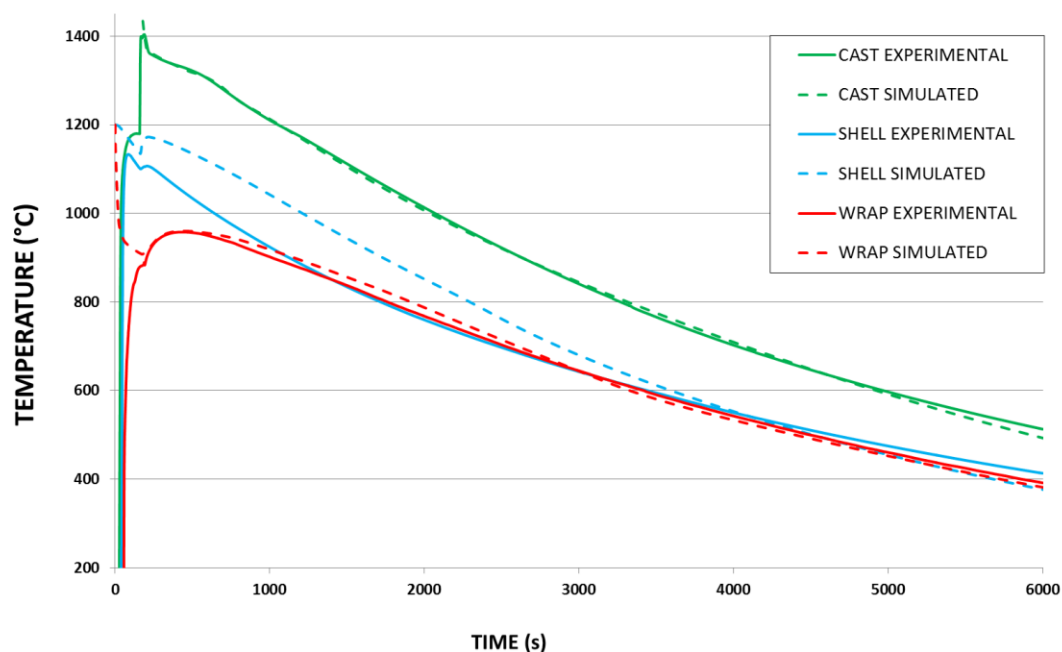


Figure 3-5. Temperature-time plots for metal, mould (shell) and insulation wrap: comparison of the thermal model prediction with the experimental results.

Since the solidification process of the metal and its thermal history is correctly described, the thermal model can be further utilized for physical simulation of investment casting process. The next Section of this thesis focuses on the physical simulation of investment casting using Gleeble 3800 thermo-mechanical simulator for the reproduction of investment casting process.

3.2.3 Explanation of discrepancy

The analysis of the simulation results and their comparison with the experimental data clearly show that the thermal history of the metal and wrap is very well described by the thermal model during the solidification and cooling processes (Fig. 3-5). The differences between predictions and experimental measurements in the mould do not seem to be due to the model.

The thermal plot measured from the ceramic mould seems to underestimate its real thermal history since they record slightly higher temperatures for the insulation wrap compared to the ceramic mould in the time range of 1300-3000 s (Fig. 3-5) that cannot be true. This discrepancy can be rationalized on the basis of the shortcomings of the experimental procedure utilized to measure the temperature in the ceramic mould. In particular,

- 1) There can be 'air gap' between the thermocouple and the tube when the latter is placed into the tube;

- 2) The cement was used to fix the ceramic tube to the ceramic mould;
- 3) There could also be some deviations from the correct positioning of the thermocouple in the ceramic mould during its fixing to the ceramic mould, since this operation has to be performed manually at extreme conditions in limited time.

The air gap and cement can significantly reduce the heat transfer from the mould to the thermocouple since they have lower thermal conductivity compared to the ceramic mould. Therefore, the experimental measurements on ceramic mould can yield lower temperatures than the real ones, as seen from (Fig. 3-5). These shortcomings could also lead to the drop of temperature readings from the thermocouple placed in the ceramic mould at the moment of melt pouring which could result in thermocouple shifting due to thermal expansion of ceramic mould (Fig. 3-5).

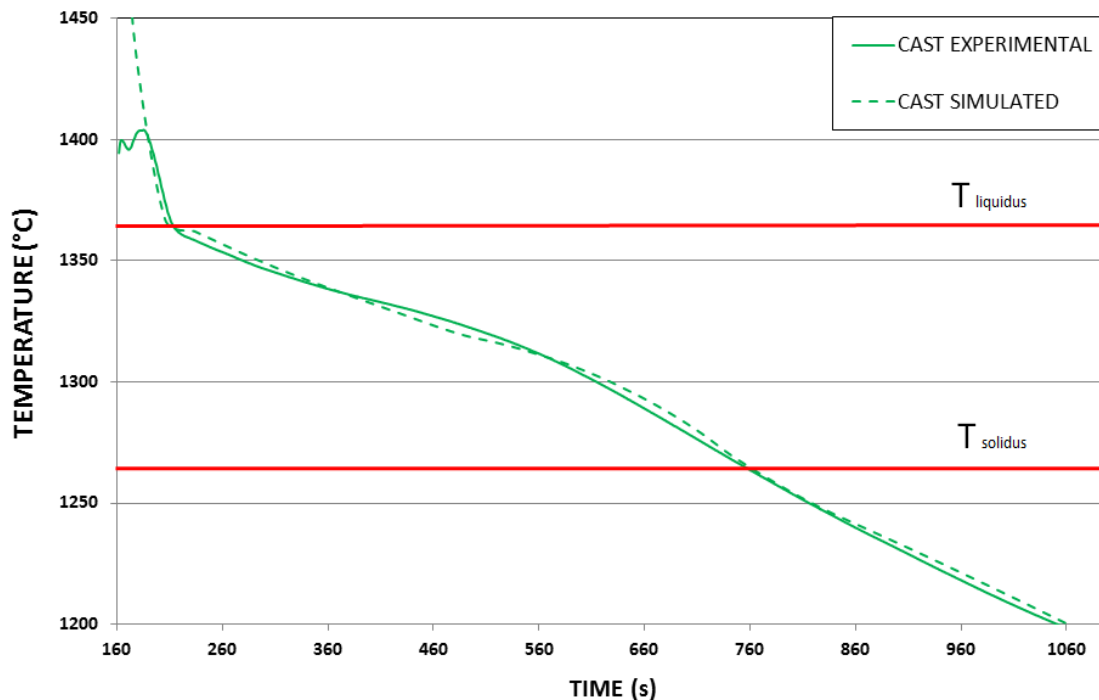


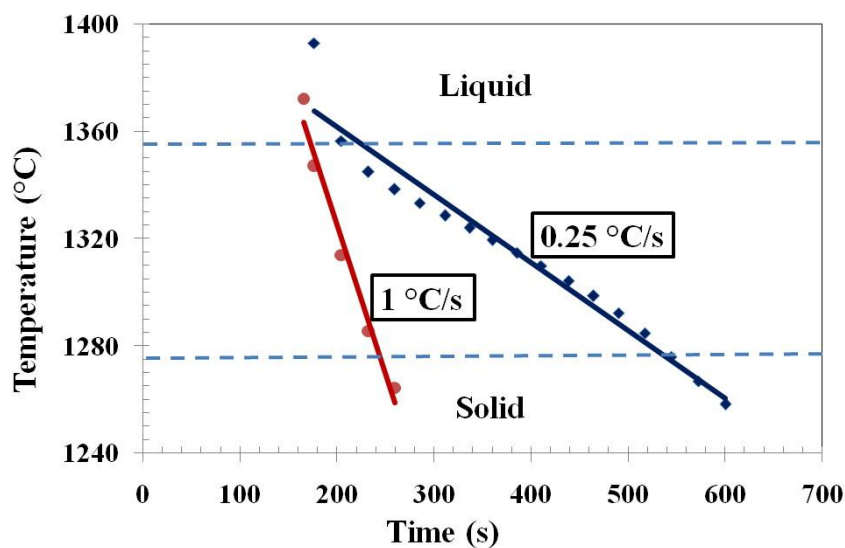
Figure 3-6. Comparison of experimental measurements from metal with the thermal model prediction in the temperature range between liquidus (1366 °C) and solidus (1266 °C).

It should be noted that the tube, the 'air gap' in its interior, and the cement were not considered in the thermal model, since it would increase enormously the time required for calculations. Another experimental procedure should be developed for more accurate recording of thermal history in the ceramic mould. Nevertheless, the thermal histories of

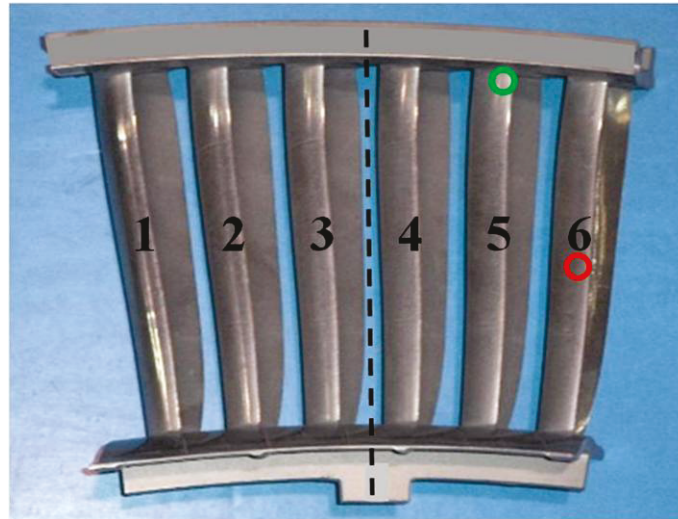
metal and wrap were accurately predicted as a result of the right selection of thermo-physical parameters of the ceramic mould in the thermal model.

3.3 Melting/solidification experiments in Gleeble 3800 thermo-mechanical simulator

As it mentioned above, in order to carry out the physical simulation of investment casting, the obtained data of thermal model (Fig. 3-7), serve as input parameters for melting/solidification experiments in the Gleeble 3800 thermo-mechanical simulator that allows to reproduce various local thermal profiles seen by the material during solidification. The thermal calculations were carried out, and the thermal profiles during solidification and cooling were determined for different areas of the casting. In Fig. 3-7 (a), typical temperature - time plots predicted by the thermal model for one area with a low cooling rate and for another area with higher cooling rate are presented. Locations of these areas are marked on the as-cast NGV (Fig. 3-7 (b)). It is clearly seen that evolution of temperature in the solidification temperature range shows a linear character with time, and the cooling rate can be easily determined for both cases: ~ 0.25 and 1 °C/s (Fig. 3-7).



(a)



(b)

Figure 3-7. (a) Theoretical temperature-time plots predicted by thermal model for (b) areas marked by green (cooling rate of 0.25 °C/s) and red (cooling rate of 1 °C/s) circles on the as-cast NGV.

3.3.1 Preparation of samples for melting/solidification experiments

Samples with a length of 121.5 mm and a diameter of 10 mm threaded at both ends have been used for melting/solidification experiments. A specimen drawing is presented in Fig. 3-8.

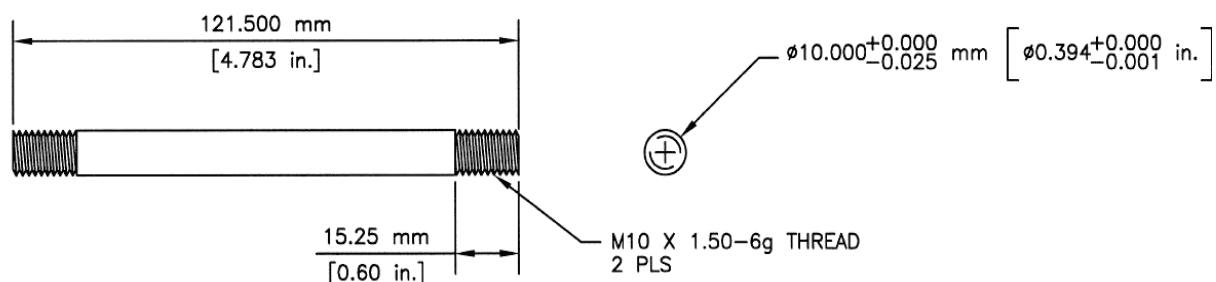


Figure 3-8. Drawing of a specimen for melting/solidification experiments.

Thin wire thermocouple (R-type) is welded to the midsection of a specimen to control the temperature during melting/solidification experiment (Fig. 3-9). To cover the liquid metal zone, a quartz tube with length of 30 mm and a slot of 3.4 mm is put onto the specimen with the control thermocouple in the slot (Fig. 3-10). The inner diameter of the quartz tube is 10.2 mm, the outer diameter of the quartz tube is 12.45 mm (Fig. 3-10). Thermocouple wires are fixed to the surface of the quartz tube by cement (Fig. 3-9). Nuts made from high strength

steel are put on both threaded ends of the specimen (Fig. 3-11). The specimen is placed between copper grips (Fig. 3-11) so that these copper grips cover both ends of the specimen and are in perfect touch with the specimen surface in the contact area (Fig. 3-12).

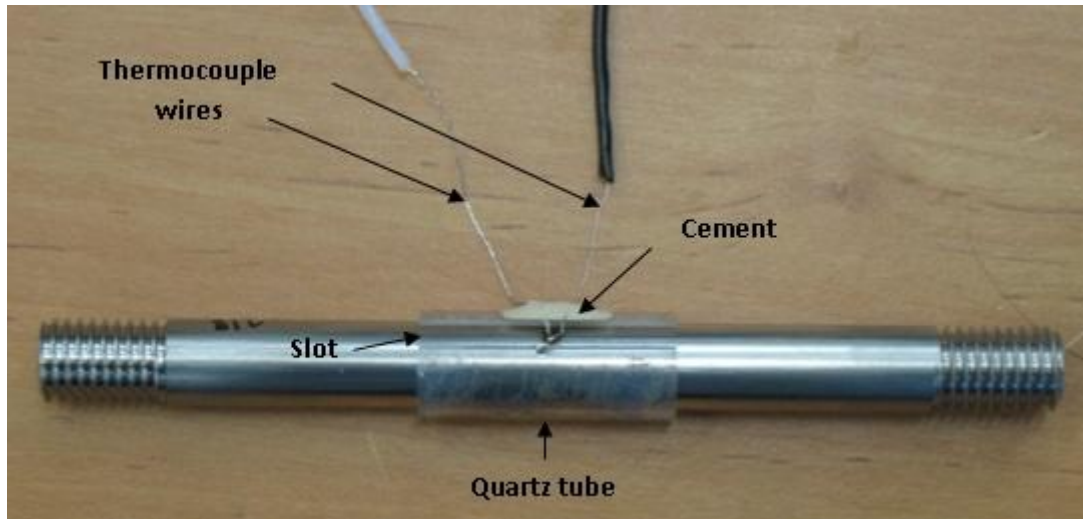


Figure 3-9. Specimen for melting/solidification experiments.

Two different geometries of copper grips are used in the experimental work. For high cooling rates, 5 and 10 °C/s, full contact copper grips having a length of the contact area with the specimen of 30.5 mm are used (Fig. 3-13). The full contact grips are also shown on Fig. 3-12. For low cooling rates, 0.25 and 1 °C/s, partial contact copper grips having a length of the contact area with the specimen of 12 mm are used (see Fig. 3-14). Figure 3-15 illustrates contact between grips and specimen for both types of grips.

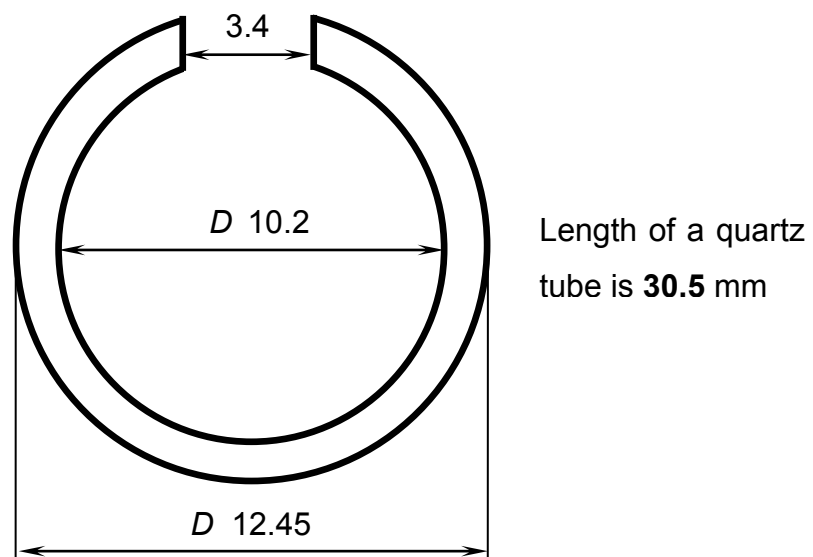


Figure 3-10. Drawing of a quartz tube.

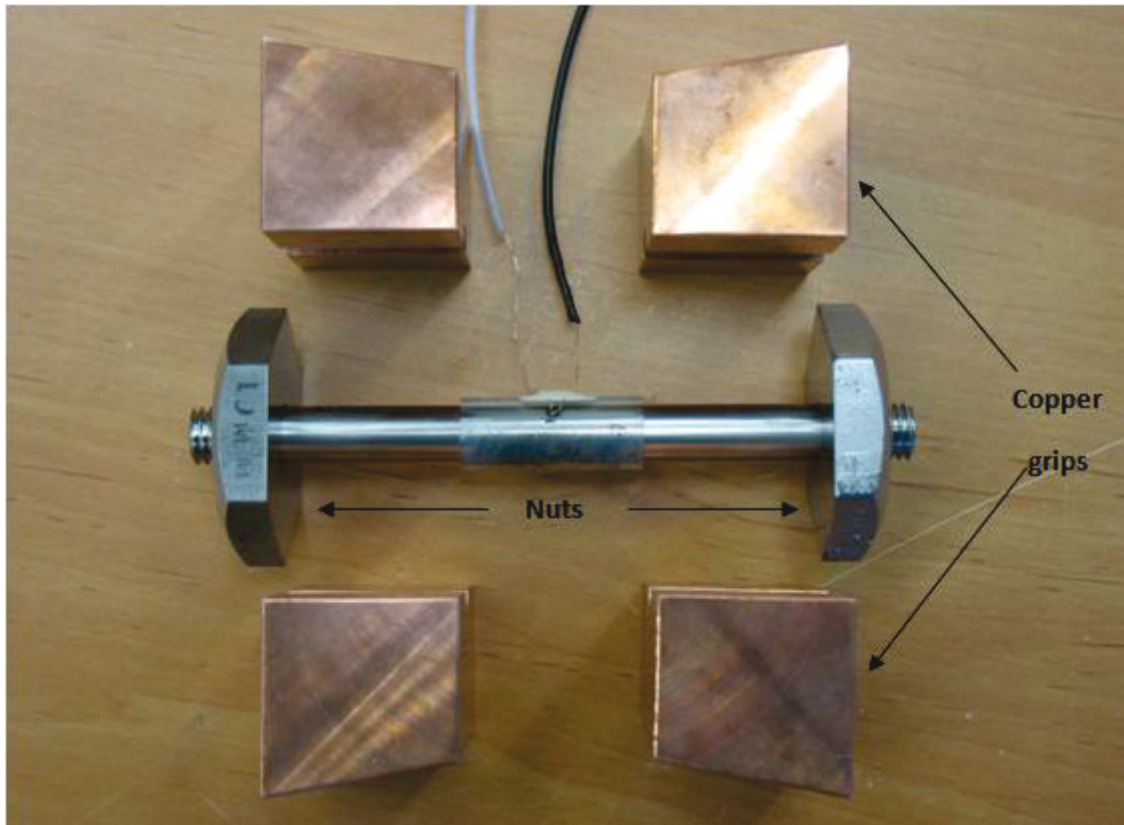


Figure 3-11. Preparation of specimen for melting/solidification experiments.

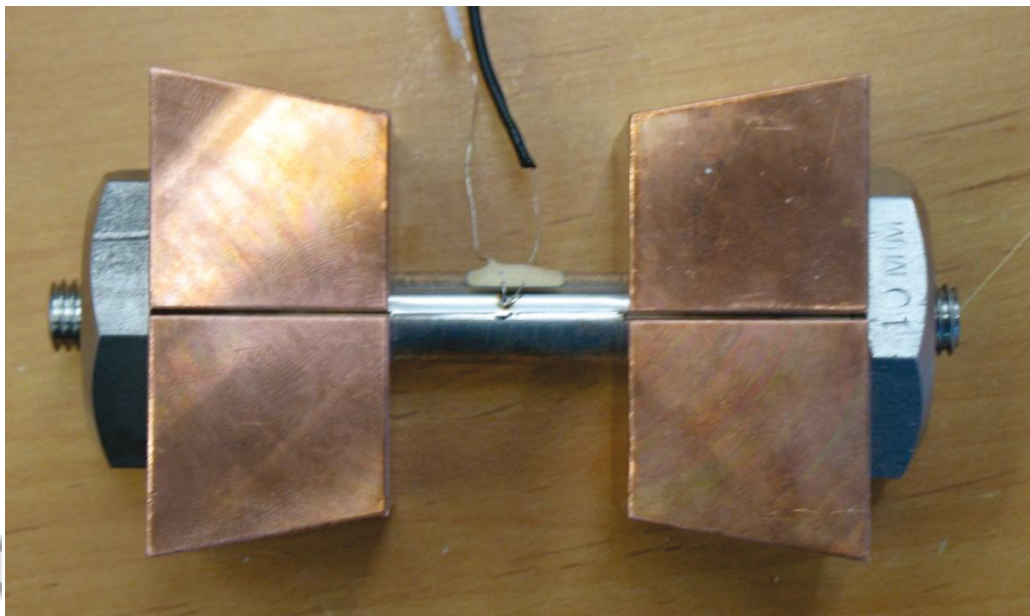


Figure 3-12. Experimental setup ready for melting/solidification experiments.

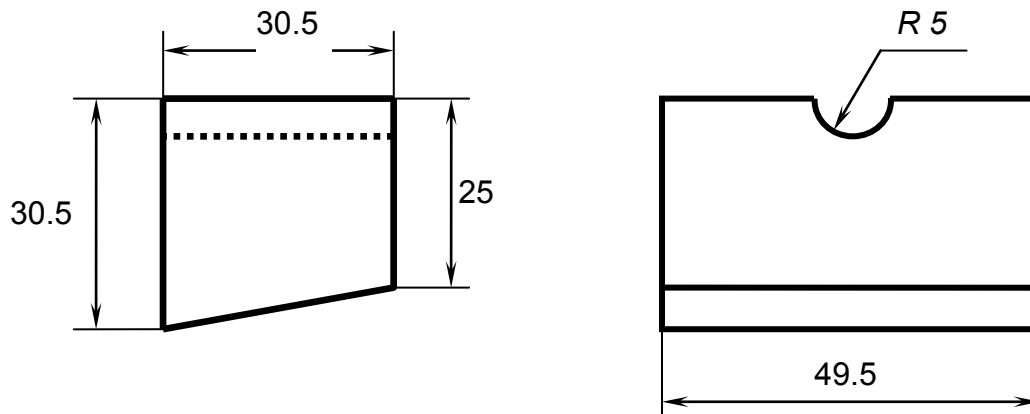


Figure 3-13. Drawing of a full contact copper grip used in the melting/solidification experiments with high cooling rates.

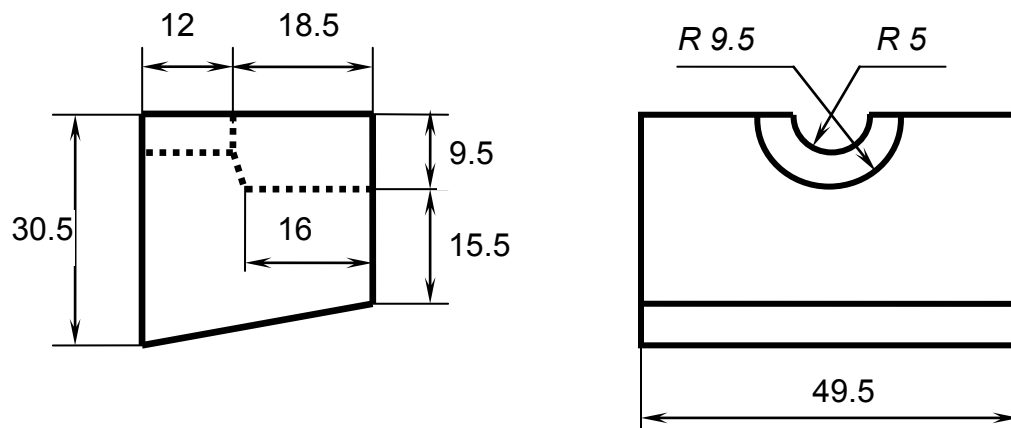
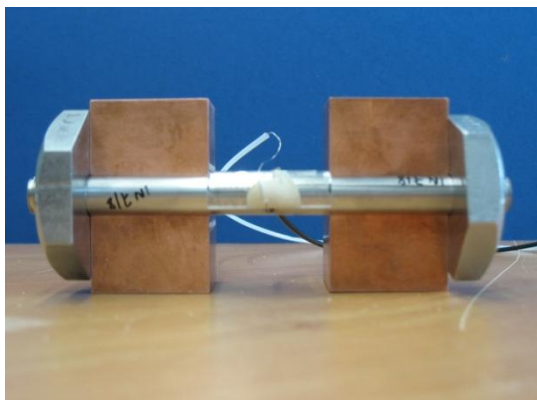
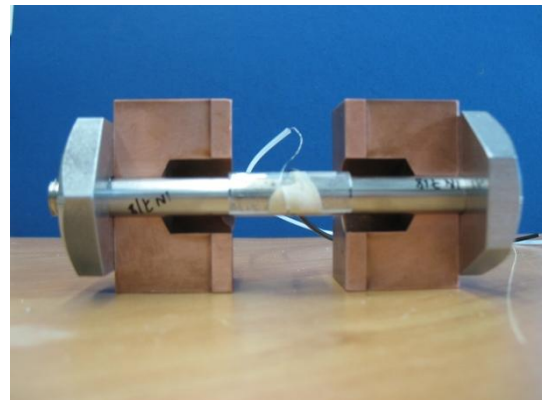


Figure 3-14. Drawing of a partial contact copper grip used in the melting/solidification experiments with low cooling rates.



a)



b)

Figure 3-15. Contact between full contact grip (a) and partial contact grip (b).

3.3.2 Melting/solidification experiments in a Gleeble 3800 system

Specimen ready for the melting/solidification experiments (Fig. 3-16) is maintained in the jaws in the Gleeble chamber so the copper grips are in perfect touch with the jaws (see Fig. 3-16). The vacuum is applied for testing chamber and then the testing chamber is filled by argon gas. The specimens are heated via resistance heating (Fig. 3-17).

The Mar-M247 Ni-based superalloy sample is heated with a heating rate of 40 °C/s to a temperature of 1240 °C. In the temperature range of 1240-1320 °C, the heating rate is reduced to 2 °C/s. After the temperature reached 1320 °C, the temperature is increased in a very slow manually controlled manner up to ~1360 °C until the evidence(s) of melting is observed. Then, the specimen is hold at this temperature for 10 s. Thereafter, the specimen is cooled down for 100 °C at a given solidification rate. The cooling rates of 0.25 and 1 °C/s, obtained by thermal model, were used for solidification of Gleeble specimens. Experimental cooling rate is estimated as a slope of the experimental Temperature–Time curve corresponding to the solidification stage. During solidification and further cooling, the sample is compressed in a stroke controlled manner to suppress formation of shrinkage porosity and to compensate the thermal contraction.

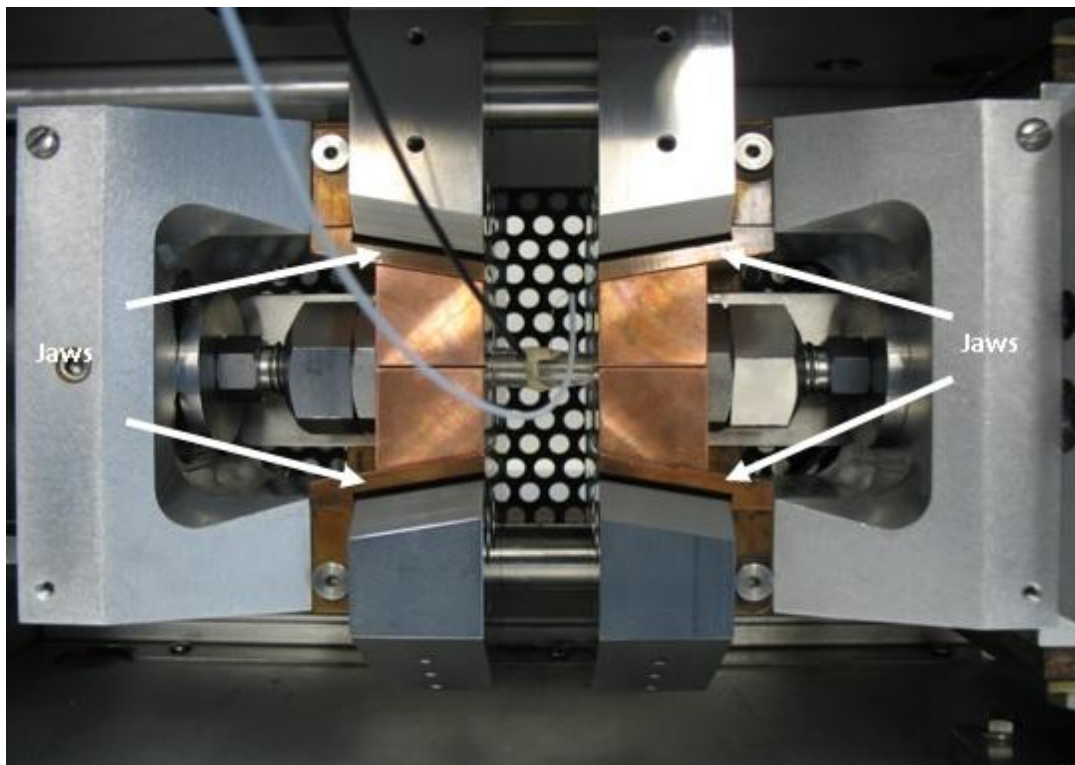


Figure 3-16. Specimen maintained in the jaw system in the testing chamber.

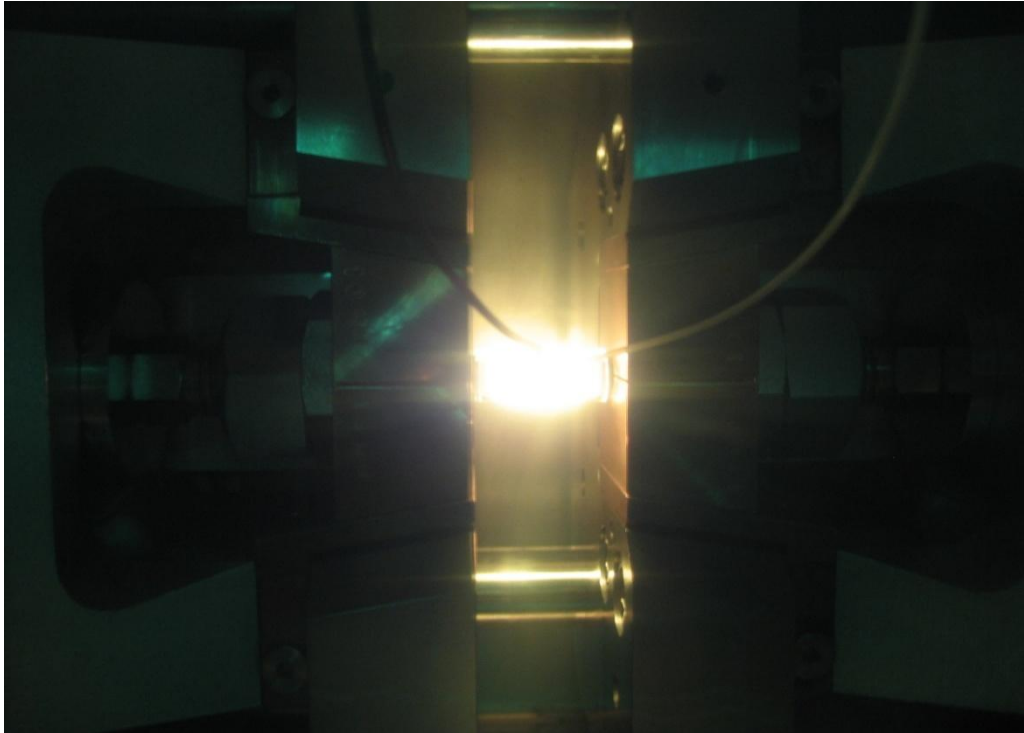


Figure 3-17. A specimen with a melted zone in the testing chamber.

The rate that the heat is transferred to the grips and then to the jaws during solidification/cooling depends on the specimen diameter, contact length between grips and specimen, and the materials of grips and jaws. The cooling system maintained inside of the jaws keeps their temperature constant during experiment (the temperature of the running cooling solution is 19 °C). Very high thermal conductivity of copper used for grips and jaws and perfect touch between the cooled surface of jaws and grips provide an effective heat removal from the sample during solidification and/or cooling of specimens resulting in smooth temperature–time profile. It should be noted that the partial contact grips with a contact length of 12 mm (Figs. 3-14 and 3-15 (b)) provided very smooth temperature – time profile at low cooling rates, 0.25 and 1 °C/s.

3.4 Microstructural characterization

In this thesis, in order to investigate the microstructural and hardness characteristics of the as-cast and physical simulation samples, the variety of tools were utilized which will be explained below. It should be noted that different methods of sample preparation were applied for each experiment. More than 20 different kinds of etchant solutions were tried to

reveal good quality image of microstructure. The microstructural study was performed by means of Optical Microscope (OM), Secondary electron microscope (SEM) as well as Electron Backscatter Diffraction (EBSD). The specimens' composition was recognized by Energy-dispersive X-ray spectroscopy (EDX). Also, for hardness measurement of various microstructures, micro and nanoindentation were used.

3.4.1 Optical Microscopy (OM)

The necessity of obtaining high quality picture is the application of appropriate and precise sample preparation method. Samples for microstructural characterization were prepared using standard metallographic techniques. At the first step of sample preparation, samples were cut and mounted in a proper size. Thereafter, abrasive grinding papers of Al-SiC, with different degrees, containing 400-1200 degrees, were used to remove rough scratches from the sample surface. It should be noted that, before starting a new step, sample cleaning was done by the vibration of immersed samples in the ethanol. After that, the polishing machine, adjusted for 20-25 N force, was used to eliminate remaining scratches utilizing various diamond polishing paste of 9, 6, 3, and 1 μm . Having the mirror-like surface, colloidal silica was employed in the final polish.

After sample preparation, three different etching solutions were used to reveal all the microstructural features. The specimens were etched with Glyceregia (15 ml HCl, 10 ml glycerol, and 5 ml HNO_3) to reveal microstructure. The etching solution consisting of 50 ml HCl, 3.5 ml H_2SO_4 , and 15 g Cu_2SO_4 was used to depict dendrite structure. Grain boundaries were revealed using etchant having a composition of 25g FeCl_3 , 60 ml HCl, and 25 ml H_2O .

Microstructure formed in the temperature-controlled area of the tested samples (the area under the weld point of thermocouple) was studied in the as-solidified and the heat treated specimens. The optical microscope Olympus BX51 was employed to study grain structure and dendritic structure. Quantitative analysis of the microstructure was performed using Analysis software.

3.4.2 Scanning Electron Microscopy (SEM)

The development of SEM in the early 1950s caused the establishment of new area of study in different fields of science like medicine and physics. The SEM (Fig. 3-18) is a microscope

using focused beam of high energy electrons instead of light to create an image. With interaction of electrons with atoms in the sample, different signals can be released. These signals contain information about the sample's surface topography and composition. With scanning of sample in raster pattern by electron beam and then combining the beam's position with detected signal the image is produced.

SEM has many advantages over optical microscopes. The magnification and resolution of SEM is much higher than optical microscope. As this microscope uses electromagnets rather than lenses, the user has much more control in degree of magnification. These advantages and the actual significantly clear images, make the SEM one of the most useful instrument in research world today [150,151].

The sample preparation method in SEM investigation was similar to that applied in OM. The utilized SEM in this study was EVO[®] MA15 manufactured by Carl Zeiss Company and FIB-FEGSEM dual-beam microscope (Helios NanoLab 600i, FEI). The SEM parameters were tuned, as in this case voltage and working distance were chosen 18 KV and between 8-10 mm, respectively.

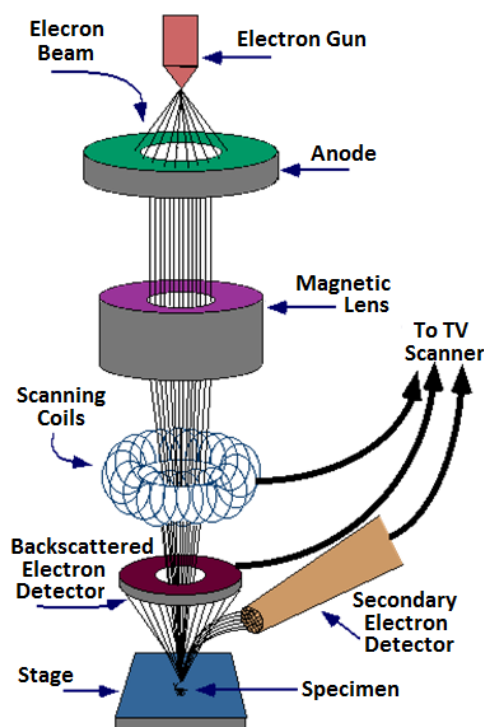


Figure 3-18. Schematic drawing showing the components of the SEM column.

3.4.3 Electron Backscatter Diffraction (EBSD)

EBSD is used to perform quantitative microstructure analysis on a millimeter to a nanometer scale. EBSD, also known as backscatter Kikuchi diffraction (BKD), allows crystallographic information to be obtained from small volumes of material in a SEM which provides versatility in mapping orientation and crystal type. EBSD can be used to index and identify the seven crystal systems, and it is able to determine crystal orientation, misorientation, grain size, texture, recrystallised/deformed fractions, substructure and strain analysis, grain boundary characterization, etc.

In EBSD a stationary electron beam strikes a tilted crystalline sample and the diffracted electrons form a pattern on a fluorescent screen. A beam of electrons is directed at a point of interest on a tilted crystalline sample, turning approximately 70° relative to normal incidence of the electron beam in the SEM, to increase the quality of the pattern obtained (Fig. 3-19). The diffraction pattern, consisting of a set of Kikuchi bands, is the characteristic of the crystal structure and orientation of the sample region, with sub-micron resolution, from which it was generated [152,153].

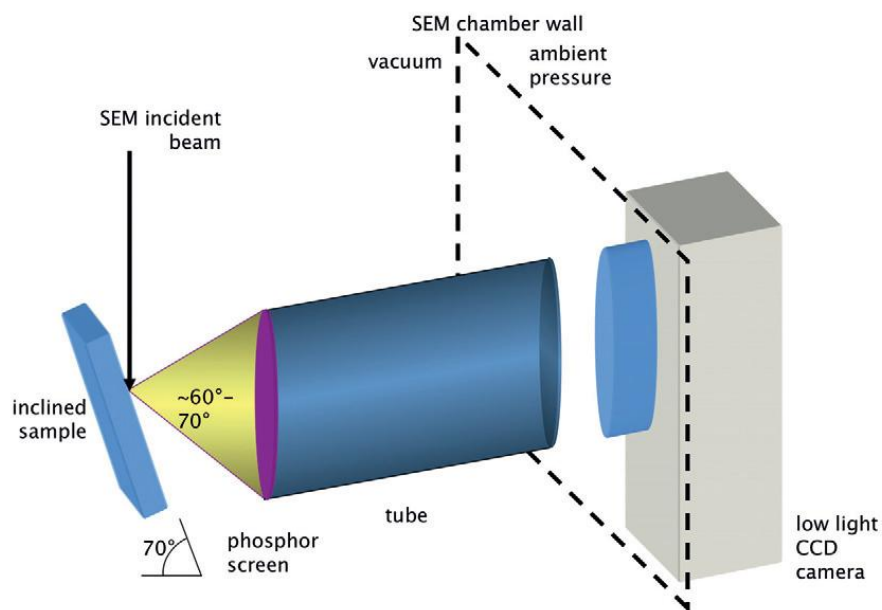


Figure 3-19. Schematic diagram showing the experimental set-up for EBSD observations [152].

The mechanism by which the diffraction patterns are formed is complex, but following model describes the principal features. The atoms in the material elastically scatter a fraction of the electrons with a small loss of energy to form a divergent source of electrons close to the surface of the sample. Some of these electrons hit on atomic planes at angles which satisfy the Bragg equation:

$$n\lambda=2d\sin\theta \quad (3-5)$$

where n is an integer, λ the wavelength of the electrons, d the spacing of the diffracting plane, and θ the angle of incidence of the electrons on the diffracting plane. Considering the Fig. 3-20, these electrons are diffracted to form a set of paired large angle cones corresponding to each diffracting plane. When used to form an image on the fluorescent screen the regions of enhanced electron intensity between the cones produce the characteristic Kikuchi bands of the electron backscatter diffraction pattern (Fig. 3-20). The centre lines of the Kikuchi bands correspond to the projection of the diffracting planes on the phosphor screen. Kikuchi bands appear at first glance to have parallel straight edges but in fact the edges are slightly curved and are the hyperbola formed by the intersection of cones with the plane of the detector (Fig. 3-19).

Since each Kikuchi band can be indexed by the Miller indices of the diffracting crystal plane which formed it, so each point on the phosphor screen corresponds to the intersection of a crystal direction with the screen. Because the diffraction pattern is bound to the crystal structure of the sample, as the crystal orientation changes the resultant diffraction pattern also changes. The positions of the Kikuchi bands can therefore be used to calculate the orientation of the diffracting crystal [152,153].

To prepare the sample for EBSD, the standard metallographic processes of sectioning, grinding and polishing are the starting point but additional care must be taken to ensure that the final polishing steps leave the sample surface free of any sectioning damage, as the EBSD pattern is generated from a very thin surface layer (~40 nm) of material. If material near the surface is deformed, contaminated, or oxidized, then EBSD pattern formation may be suppressed.

For many materials, standard preparation methods may be employed successfully with care. As a general rule standard preparation methods can be progressed to the final polishing stage without any deviation from the normal route employed. Thereafter, an additional steps like polishing with colloidal silica, chemical etching, electro-polishing, ion milling, and plasma

etching are all methods that have been shown to work in various material systems. In practice, there is no one way of correctly setting up an EBSD scan as the parameters used depend on many competing factors including the nature of the sample and the information that is required. Therefore the material under investigation should be considered on an individual basis and prepared appropriately [152,153].

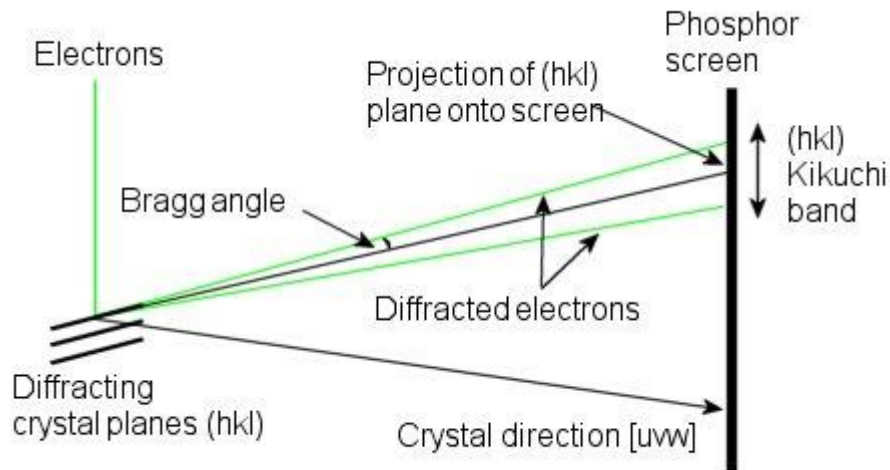


Figure 3-20. Formation of diffraction pattern of a crystal structure in EBSD [153].

The initial grinding stage selected should minimize aggression, and cause less damage than the sectioning. For this reason, surfaces such as grinding stones and other aggressive grinding surfaces are not normally recommended.

Plane grinding can be achieved in a variety of ways, using a variety of abrasives. Fixed abrasive surfaces are available using diamond, Al_2O_3 or cubic boron nitride (BN). The method used to bind the abrasives to the wheel largely defines the grinding characteristics - the harder or more rigid the bonding medium, the more aggressive the grinding action of the surface. The type of grinding surface used to make the specimen plane will depend on the material being prepared.

For softer materials coarse grit of grinding paper with SiC or Al_2O_3 abrasives may be used, but the durability or characteristics of such materials may be inappropriate for certain materials. Generally, in order to maintain sharp abrasive particles, grinding papers need frequent changing. For harder and mixed materials, diamond grinding discs are often the best choice.

To remove deformations and scratches from Fine Grinding and obtain a surface that is highly reflective, samples must be polished before they can be examined under the microscope. To

achieve efficient material removal and to cut consistently through all materials and phases, the hardest known abrasive is used - diamond. Diamond polishing can be carried out on many different preparation surfaces/polishing cloths and with different diamond grain sizes [153].

To polish samples in this study, the diamond paste of size 9, 6, 3, and 1 μm were used for removing residual scratches and deformations, and finally high quality surface can be achieved by polishing with 0.3 μm deagglomerated alpha alumina. It is observed that, using the colloidal silica in the last step of preparation, an appropriate diffraction patterns were not collected. It is probably, utilizing the colloidal silica at the last stage led to etching the surface affecting the emission of diffraction pattern from the surface of the sample. It should be noted that the sample cleaning was performed via vibration of immersed samples in the methanol. For EBSD investigation of the study the Oxford EBSD model NordlyNano was employed [153]. The voltage, current and working distance were tuned 18 KV, 5.5 nA and 8-10 mm, respectively.

3.4.4 Energy Dispersive X-ray (EDX) Spectroscopy

Energy-dispersive X-ray spectroscopy (EDS that also refer to EDX or EDXS) is an analytical technique used for the elemental analysis or chemical characterization. The base of this technique relies on the analyzing of X-rays released because of exciting of atoms by electron beam. The fundamental principle used as characterization capabilities is that each element with a specific atomic structure allowing emission of unique set of peaks on its X-ray spectrum.

The way for the emission of characteristic X-rays from a specimen is the charge of particles with a high energy beam such as electron or proton. During SEM operation, once the beam hits the sample, electrons or and X-rays are released from the sample (Fig. 3-21). The number and energy of the X-rays emitted from a specimen can be measured by an energy-dispersive spectrometer [150,151].

The sample preparation applied for EDX is similar to that explained for SEM (section 3.4.2.), but samples should not be etched for EDX experiment. Chemical analysis during the present investigation performed by EDX using an Oxford INCA 330 microanalysis system attached to the SEM.

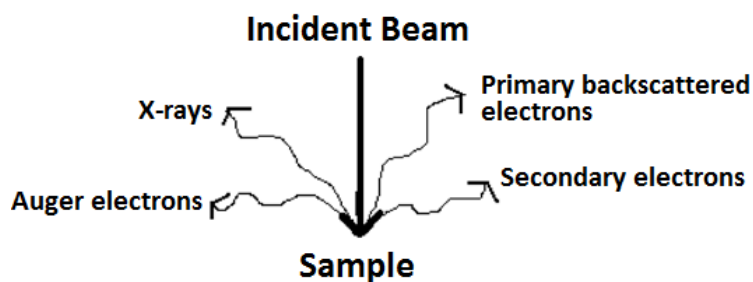


Figure 3-21. Schematic drawing of an electron beam incident on a solid sample, showing some of the signals generated that can be used to help characterize the microstructure.

3.5 Microhardness and Nanohardness testing

The aim of this thesis was to study the hardness of microstructure formed at various solidification conditions and/or heat treatment. The microhardness test is done to achieve the hardness of microstructure cooled at different temperature. Moreover, the variation of hardness after applying heat treatment is measured by microhardness. The nanoindentation test was utilized to measure the hardness and elastic modulus of skin formed at various solidification condition, since the skin thickness is not enough big to be measured by microhardness tester.

3.5.1 Microindentation tests

The microhardness, or microindentation, test is referred to the hardness testing of materials where low load is applied. In microhardness test, a diamond pyramid indenter with specific geometry (Fig. 3-22) is impressed into the surface of the test specimen using a known applied force chosen with respect to the material. The hardness number, having the unit in kgf/mm^2 , is calculated measuring the surface area made by indenter divided by the applied force. Two methods of Vickers as well as Knoop can be applied for microindentation hardness testing. In this study, the Vickers hardness test (HV) is employed in which both the diagonals are measured and the average value is used to calculate the hardness. It should be noted that microhardness values can be affected by load and work-hardening effects of materials.

The sample preparation for microhardness measurement coincides with the EDX experiment (section 3.4.4). Microhardness of the material was measured using SHIMADZU HMV-2

microhardness tester equipped with Vickers diamond indenter. The load of 300 g was applied for 15 s. Ten measurements were carried out in each sample.

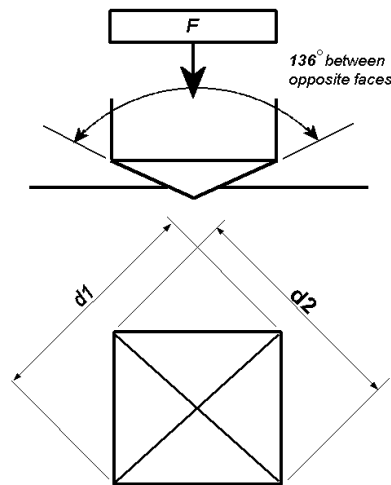


Figure 3-22. The indenter of Vickers hardness test.

3.5.2 Nanomechanical testing: Basic principles of instrumented nanoindentation

In instrumented nanoindentation, force and depth are measured continuously during loading and unloading while a hard tip with a well defined geometry is pressed into the sample surface. Instrumented nanoindentation relies on the precise knowledge of the real shape of the indenter to estimate the contact area between the indenter and the flat surface from the loading-unloading sequence, allowing the hardness and elastic modulus to be derived. An important component of the indentation system is the probe tip. The indenter tip is generally made of single crystal diamond but other kinds of hard materials such as sapphire, quartz, tungsten carbide (WC), and cubic BN can be used. Different shapes of tips are available depending on the type of experiment to carry out. The most common tip in nanoscale testing for probing hardness and elastic modulus is the Berkovich tip.

Hardness and elastic modulus determination

The most commonly used method to analyze nanoindentation data for pyramidal indenters was developed by Oliver and Pharr in 1992 [154]. This method is based on analytical solutions for the elastic contact problem between an indenter and a flat surface. As the direct measurement of the contact area is not always accurate and convenient, they proposed a

procedure to determine the contact area based on the depth of indentation and the indenter shape function. The contact between an indenter and a flat surface can be modeled by the sequence of events illustrated in Fig. 3-23. At peak load, P_{max} , the material conforms to the shape of the indenter. The total displacement h_{max} is the sum of the contact depth h_c (the vertical distance along which contact is made) and the displacement of the surface at the perimeter of contact h_s , due to elastic deformation of the flat surface:

$$h_c = h_{max} - h_s \quad (3-6)$$

During unloading, the elastic displacements are recovered, and the final depth of the residual impression is h_f when the indenter is fully withdrawn. To determine the contact depth h_c from the experimental data, the displacement of the surface at the contact perimeter h_s , must be obtained. This displacement h_s depends on the geometry of the indenter.

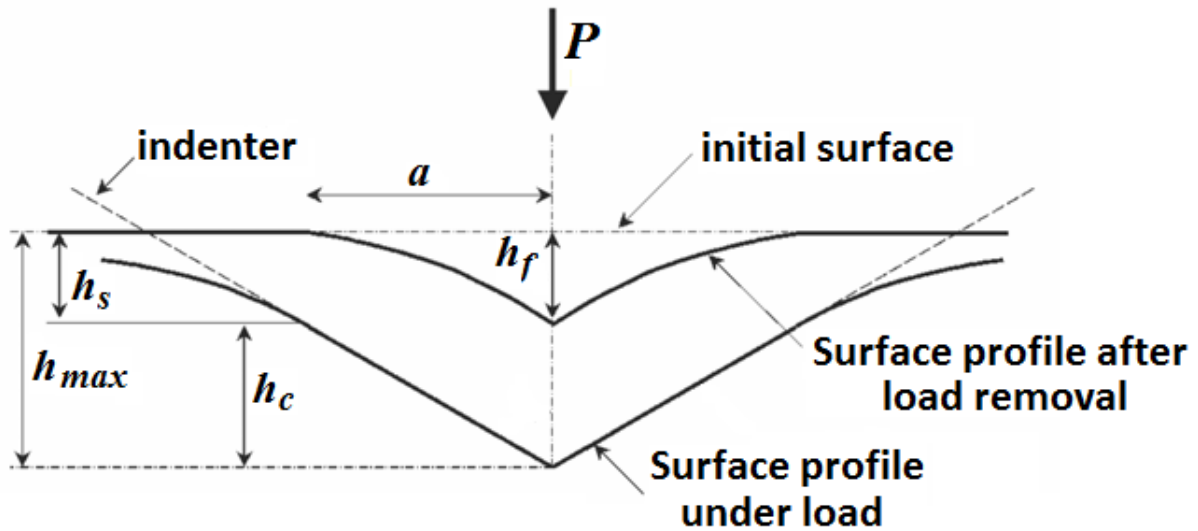


Figure 3-23. Cross-section of nanoindentation profile at peak load and at full unloading for an elasto-plastic material.

Oliver and Pharr assumed that the equations describing the elastic unloading of a flat, semi-infinite half space are the same as those for an indented surface. That is, Sneddon's solutions [155] can be applied to a flat surface or to a surface with a hardness impression. Sneddon derived general relationships among the load, elastic displacement and contact area for any indenter that can be described as a solid of revolution of a smooth function. Sneddon's expressions for the shape of the surface outside the area of contact can be used to obtain h_s :

$$h_s = \varepsilon \frac{P}{S} \quad (3-7)$$

where P is the indentation load, S the stiffness of the contact, $S = dP/dh$, and ϵ a indenter geometrical constant that has a value of 1 for a flat punch, 0.75 for a paraboloidal indenter and 0.72 for a conical indenter. Oliver and Pharr obtained that the value of ϵ , that best described the unloading behavior of a Berkovich indenter, was 0.75.

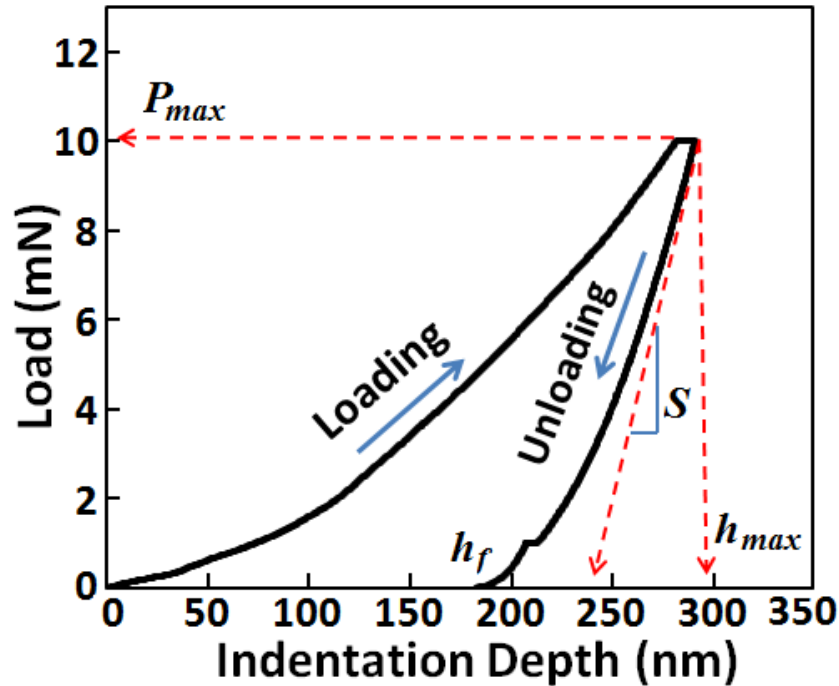


Figure 3-24. A loading-unloading sequence for an indentation in an Al/SiC nanolaminate, indicating the parameters used to estimate the contact depth h_c .

The maximum depth, h_{max} , and the maximum stiffness of the unloading curve, S , can be obtained from the loading and unloading sequence of an indentation, as shown in Fig. 3-24. They can be used to estimate the contact depth h_c according to Eq. 3-7. The contact area A_c at peak load is determined from the geometry of the indenter and the contact depth h_c . The indenter geometry is described by an area function $F(h)$ which relates the cross-sectional area of the indenter to the distance from its tip h . The projected contact area A_c is then determined using the relation:

$$A_c = F(h_c) \quad (3-8)$$

Whereas the functional form of F must be estimated experimentally prior to the analysis using a standard calibration material (fused quartz) with a well-known elastic modulus. Alternatively, the shape function can be determined directly by careful measurement of the

dimensions of the tip using a traceably calibrated, precision metrology device such as an Atomic Force Microscope (AFM).

Both the hardness and the elastic modulus can be determined as follows:

3.5.2.1 Hardness determination

The hardness can be determined as:

$$H = \frac{P}{A(h_c)} \quad (3-9)$$

where P is the load and $A(h_c)$ the cross-sectional area of the indenter at a distance h_c from its tip. According to this definition, the measured hardness may be different from the one obtained from the more conventional definition in which the contact area is determined by direct measurement of the size of the residual impression.

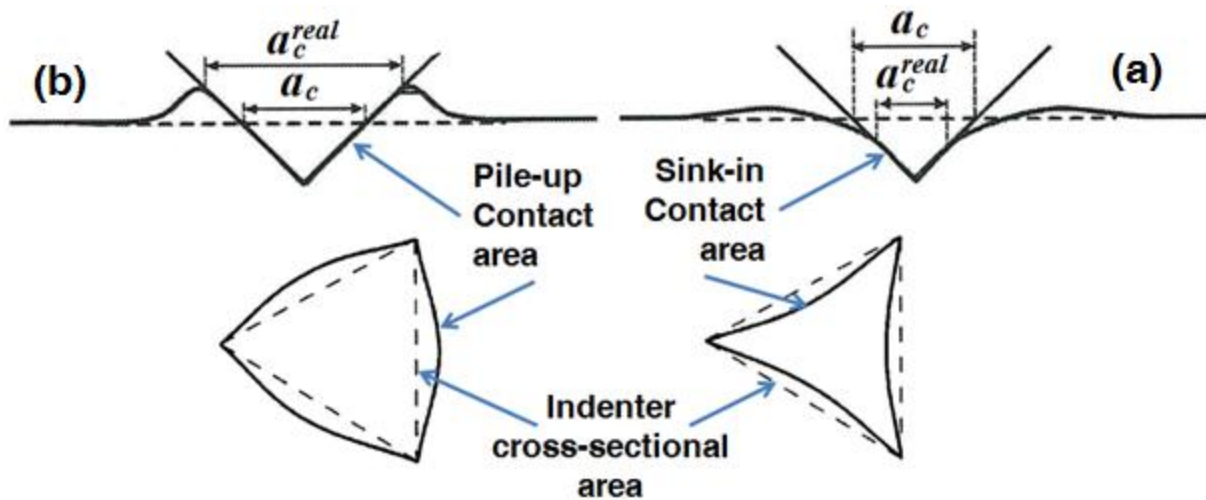


Figure 3-25. Effect of (a) pile-up and (b) sink-in on the real contact area a_c^{real} compared to the contact area a_c derived from instrumented nanoindentation. The dashed line indicates the height of the original surface.

There are two reasons for this difference. Firstly, the material around the indentation may pile-up (or sink-in), as shown in Fig. 3-25, and the real contact area will be larger (or smaller) than the one derived from Eq. 3-9. As a result the hardness will be overestimated (underestimated). Secondly, elastic recovery at the sides of the indentation mark may happen, and therefore the residual size of the indentation will be smaller than that in Eq. 3-9.

However, the size of the residual hardness imprint coincides with the size of contact area a at peak load for metals, whose deformation is mainly controlled by plastic deformation. Elastic recovery during unloading in this case usually affects the depth of the residual indentation mark, which decreases from h_{max} to h_f , while the size of contact area a remains constant during unloading. However, this may not be true when elastic recovery is important, as in the case of materials with a very high E/σ_y ratio (> 20) [156]. To avoid uncertainties, the real contact area for most nanolaminates tested in this work was actually measured by direct observation of the residual imprints by either SEM or atomic force microscopy (AFM).

3.5.2.2 Elastic modulus determination

The elastic modulus E can be calculated from:

$$S = \frac{2}{\sqrt{\pi}} E_r \sqrt{A(h_c)} \quad (3-10)$$

where S is the initial slope of the unloading curve, as shown in Fig. 3-24, and E_r the reduced modulus that accounts for the elastic deformation of both the specimen and the indenter and is given by:

$$\frac{1}{E_r} = \frac{1 - \nu^2}{E} + \frac{1 - \nu_i^2}{E_i} \quad (3-11)$$

where E_i and E are the elastic modulus and ν_i and ν are the Poisson's ratio of the indenter and the specimen, respectively.

In this study nanoindentation testing was performed using a TI 950 Triboindenter™, manufactured by Hysitron, to determine the hardness and elastic modulus of the skin microstructure. There is no difference of sample preparation method between micro and nanoindentation, since the samples should have mirror like surface in both cases. The Berkovich type indentation tip (Fig. 3-26) was assembled on the load transducer to utilize for nanoindentation test, with an axial-loading system, at room temperature. Two types of indentation tests were carried out at room temperature: Conventional loading-unloading up to a maximum penetration depth of 200 nm and multiple loading-unloading cycles to extract

hardness and modulus as a function of indentation depth. The indentations were carried out at a rate of 20 nm s^{-1} with a hold period of 2 seconds at maximum depth.



$$a = 65.27^\circ$$

$$\text{Area} = 24.5 d^2$$

Figure 3-26. The Berkovich indenter used in this study [157].

3.6 Experimental validation of developed physical simulation tools

Investment casting of the NGVs was carried out using the Mar-M247 Ni-based superalloy. The chemical composition of the material is presented in Table 3-1. The Mar-M247 Ni-based superalloy is characterized by high temperature strength and excellent corrosion and oxidation resistance at elevated temperatures [74].

Figure 3-27 (a) depicts the complete set used for the validation of thermal model and physical simulation of investment casting. The ceramic moulds for the experimental casting trials were prepared using the standard manufacturing route. The wax pattern of NGV was prepared via injection molding and then assembled with a wax feeding system. The obtained wax cluster was immersed into ceramic slurry and allowed to dry, and this step was repeated until the desired thickness of ceramic mould was reached. The obtained assembly was dewaxed in autoclave for 15 minutes at elevated temperature and high pressure. To burn the wax remains, the ceramic cluster was fired at $900 \text{ }^\circ\text{C}$ for 1 hour. Finally, the interior of ceramic cluster was thoroughly rinsed.

The ceramic cluster was wrapped by an insulation layer (made from Kaolin wool) having a thickness of 13 mm and pre-heated to $1200 \text{ }^\circ\text{C}$. The geometry and mesh for the model, including sectional view, are presented in Fig. 3-27 (b). Before entering the casting furnace, the thermocouples for recording the thermal history during investment casting were quickly set on the assembly. The equipment for in-situ temperature measurements consisted of K- and S-type thermocouples and a standalone data logger able to withstand high vacuum (10^{-3}

mbar), magnetic fields (coming from the induction furnace) and thermal radiation due to the high temperature of the melt. Thermocouples were placed at defined points in the insulation wrap, ceramic mould, and metal. Temperature in wrap was measured by a thermocouple



Figure 3-27. a) Recording temperature history during cooling of the assembly after investment casting; b) model and mesh of the model for half shell with insulation wrapping, showing geometry and layer distribution of the insulation; c) location of thermocouples (in

yellow color) to measure temperature on the alloy (left in gray color), shell (mid in green color) and insulation (right in violet color).

placed in the centre of the wrap layer (marked by blue spot). Shell temperature was measured by a thermocouple placed on the leading edge of one external airfoil. Three thermocouples were used to measure the temperature in the alloy. The thermal plot for only of them result is shown, since other thermocouples failed during investment casting. The location of each thermocouple is illustrated in Fig. 3-27 (c), in which each thermocouple was surrounded by a ceramic tube for mechanical protection. The location of each thermocouple was identified by nodes in the thermal model (see Section 3.2.1).

The pre-heated assembly was placed in the vacuum casting furnace where the ceramic mould was filled by the molten metal poured at 1549 °C with a melt pouring velocity of 1700 mm/s. The assembly was then removed from the furnace and allowed to cool. The thermal history at defined location of the metal, the ceramic mould and the wrap was recorded. The schematic picture of whole process is observed in Fig. 3-28.

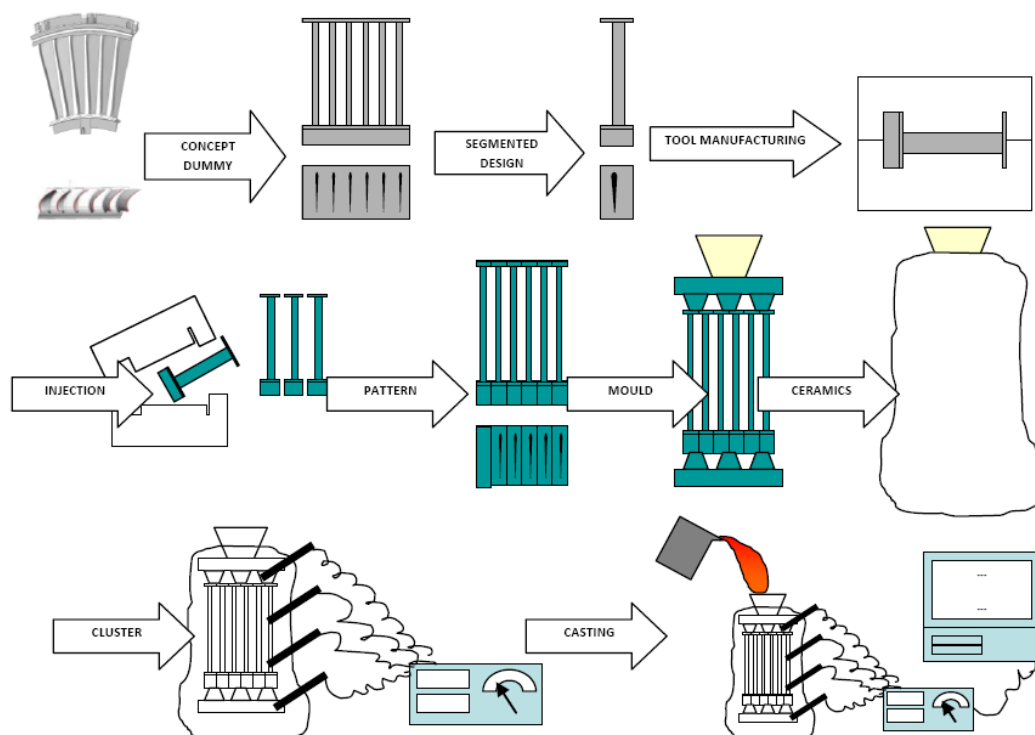


Figure 3-28. The manufacturing route for investment casting utilized in the VANCAST project.

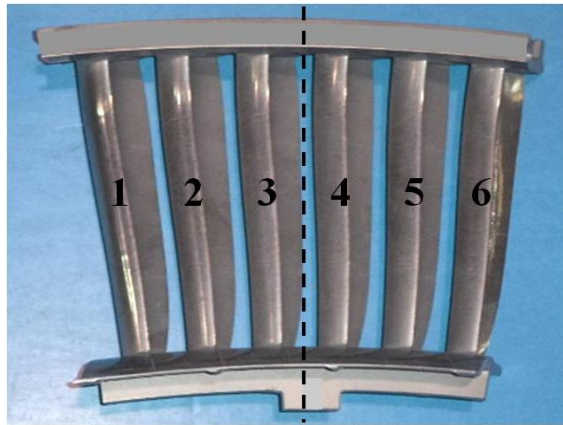
The as-cast NGV (Fig. 3-29 (a)) was cut into smaller specimens for further investigation. The vanes 2 and 5 are solid and other vanes are hollow. Since the as-cast NGV has a symmetrical geometry and the gating system was located in its midsection (Fig. 3-29 (a)), it can be assumed that microstructure and properties of the left half of NGV (vanes 1, 2, 3 and corresponding part of platform) is similar to that of the right half of NGV (vanes 6, 5, 4 and corresponding part of platform). Therefore, microstructural characterization of some defined areas (Fig. 3-29 (b)) in right part of NGV was performed. The selected areas in vanes 4, 5 and 6, based on the cooling rate, are listed in the Table 3-3. According to the thermal model, these areas have a cooling rate during solidification of ~ 0.25 or ~ 1 °C/s.

Microstructure of as-cast NGV and samples after physical simulation experiments were characterized and compared to validate the physical simulation of investment casting. The standard metallographic techniques were used for preparation of specimens with mirror-like surface. The surface was etched using chemical solution containing 25g FeCl₃, 60 ml HCl, and 25 ml H₂O to reveal grain boundaries and dendritic microstructure. It should be noted that it is hard to reveal the grain boundaries in a Mar-M247 Ni-based superalloy, as it explained by Szczotok et al. [158]. The optical microscope Olympus BX51 was employed to study grain and dendritic structure. The Analysis software was used for quantitative analysis of microstructure. The calculation of SDAS was done by counting the number of secondary arms over a measured length on at least five well defined trunks. To estimate the grain size on each selected area, at least 13 grains were measured. Phases and carbide investigation were done using SEM EVO MA 15 operating at 18 kV. Equivalent circle diameter (ECD) of grains and carbide particles was considered due to their complex shape.

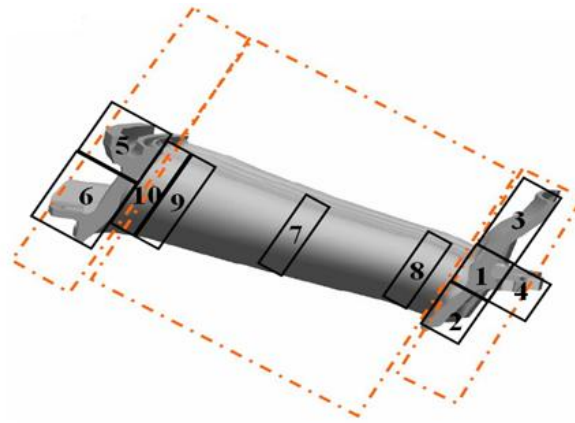
Microhardness of the samples was measured using Shimadzu HMV-2 microhardness tester with Vickers diamond indenter. In this test, the 300 g load was applied for 15 s. At least ten measurements were done on each selected area. The average microhardness values and their standard deviation were calculated.

Table 3-3. Investigated parts and areas of the as-cast investment casting NGVs.

As-cast NGV										
Vane	4		5			6				
Area	7	5	7	8	9	2	3	4	5	7



(a)



(b)

Figure 3-29. a) View of the as-cast NGV; b) schematic view of the NGV with marked areas for microstructural studies.

4 Effect of thermal variables and post-cast heat treatment on microstructure and hardness of Mar-M247 Ni-based superalloy

4.1. Effect of cooling rate and post-cast heat treatment on microstructure and hardness

As mentioned in Section 3.3.1, the prevailing cooling rates during solidification of NGVs were in the range of 0.25-1 °C/s according to the outcomes of thermal model. Nevertheless, cooling rates up to 5 and 10 °C/s were observed rarely at some thinner areas. Therefore, the melting/solidification experiments, evaluating the effect of thermal variation on microstructure and hardness of Mar-M247 Ni-based superalloy, were performed at four different cooling rates including 0.25, 1, 5 and 10 °C/s. Temperature-time plots for different cooling rates are presented in Fig. 4-1. They show that the cooling rate was very well controlled at lower cooling rates of 0.25, 1, and 5 °C/s. Some instabilities appeared at the highest cooling rate of 10 °C/s, but did not affect the average cooling rate. Therefore, the experimental average cooling rates matched the set ones. This indicates that the casting

process with precisely controlled cooling rates can be successfully reproduced in the Gleeble thermo-mechanical simulator.

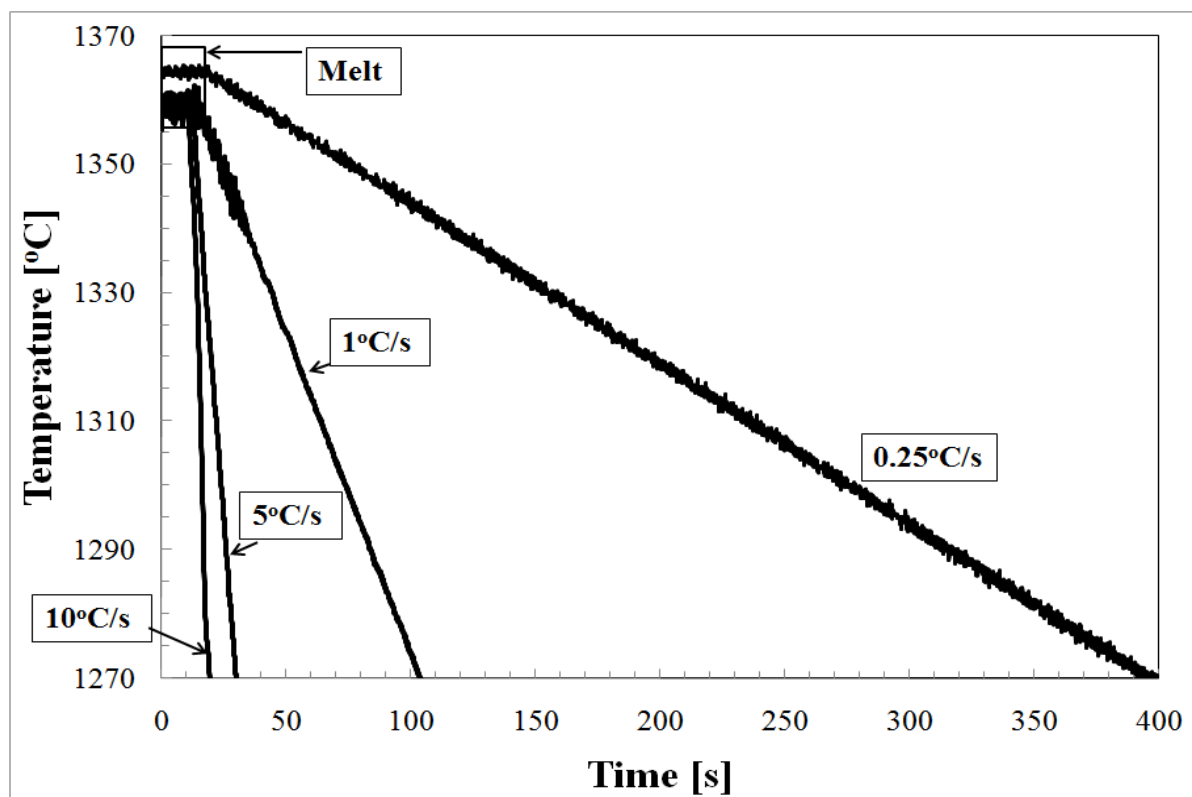
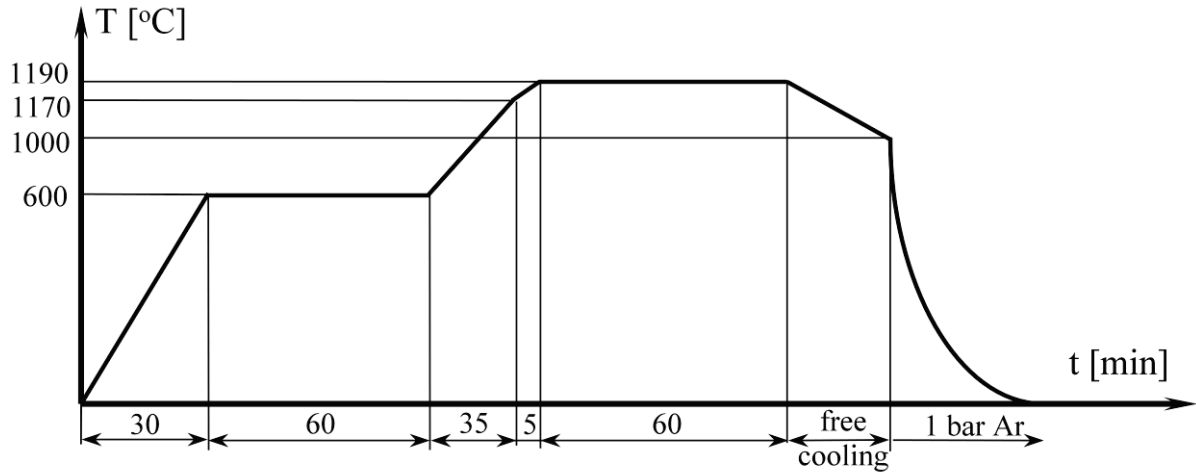
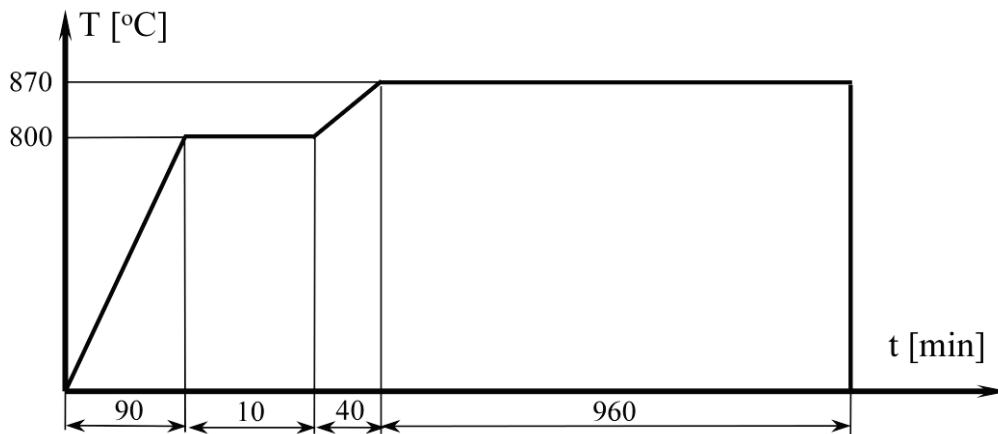


Figure 4-1. Temperature versus time curves recorded during melting/solidification experiments.

The melted and solidified part of the Gleeble samples was cut out for further investigations after solidification process. Thereafter, the Gleeble specimens were subjected to standard double heat treatment consisting of solution treatment followed by precipitation ageing in the Nabertherm RHTH 120-600/16 furnace with controlled atmosphere (Fig. 4-2). The solution treatment (Fig. 4-2 (a)) was carried out in vacuum. The as-solidified specimens were treated at 600 °C for 60 min and then at 1190 °C for 60 min. The Gleeble specimens were furnace cooled under argon atmosphere. Precipitation ageing was performed in argon atmosphere (Fig. 4-2 (b)). The specimens were treated at 800 °C for 10 min and 870 °C for 16 h. The specimens were taken out of the furnace and cooled down to room temperature in air. The as-solidified specimens subjected to double heat treatment will be referred to as heat treated specimens.



(a)



(b)

Figure 4-2. Solution and precipitation heat treatment used in this study.

Below the effect of thermal variables on microstructural features and the hardness of materials is considered in details.

4.1.1 Grain structure

Figs 4-3 and 4-4 (a, b) illustrates the influence of cooling rate on the grain size in the Gleeble specimens. It is seen that the average grain size increases moderately with decreasing cooling rate which is in agreement with the results reported in [51]. Also, it is well known that the grain size is related to heterogeneous nucleation and the undercooling of the melt [48,159]. During an initial stage of solidification, the process is essentially controlled by nucleation. After some time, the number of grains remains constant and solidification proceeds via the

dendrite lengthening and dendrite arm thickening. Hence, the second stage is governed by the growth. Therefore, it can be deduced that nucleation is dominant process at the beginning of solidification and leads very rapidly to the establishment of the final grain population, with each nucleus forming one grain. According to the general theory of nucleation, critical radius (r^*) of a crystal which can be in equilibrium with the melt decreases with increase in the undercooling [48]:

$$r^* \propto \frac{1}{\Delta T} \quad (4-1)$$

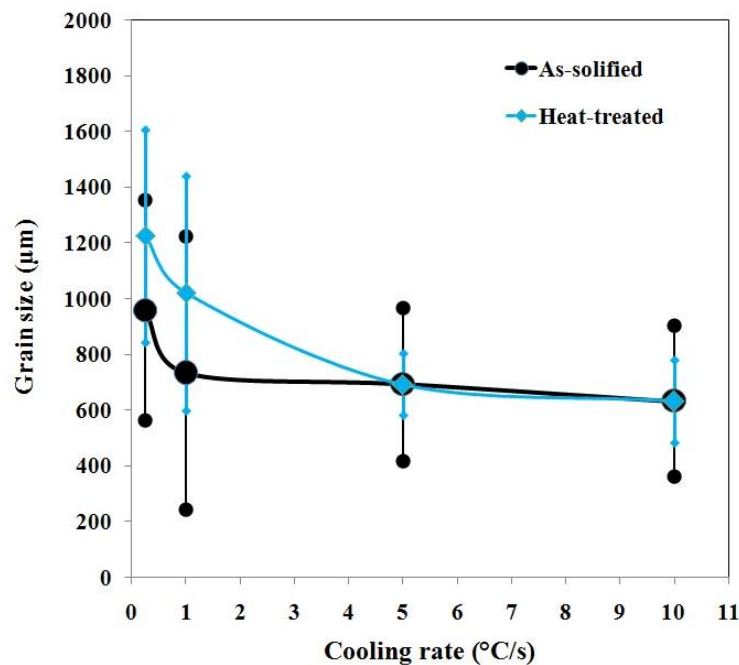


Figure 4-3. Effect of cooling rate on the grain size.

Also, critical free energy of nucleation (ΔG^*), regarded as an activation energy which has to be overcome in order to form a nucleus that will continue to grow is reversely proportional to the undercooling:

$$\Delta G^* \propto \frac{1}{\Delta T^2} \quad (4-2)$$

In addition, the nucleation rate (I) is reversely proportional to the critical free energy of nucleation ΔG^* as well [48,160].

$$I \propto \frac{1}{e^{\Delta G^*}} \quad (4-3)$$

All above mentioned indicate that the grain size decreases with increasing cooling rate as the number of particles which act as a nucleation site increases due to lower critical radius, which in turn, results in higher nucleation rate.

The influence of double heat treatment on average grain size is illustrated in Figs 4-3 and 4-4 (c, d). It can be observed that the double heat treatment essentially did not affect the grain size, indicating that no significant grain growth took place. It should be noted that the discrepancy in size and large standard deviation at lower cooling rates are caused by the limited number of analyzed grains (< 10), as a result of small samples with large grain size.

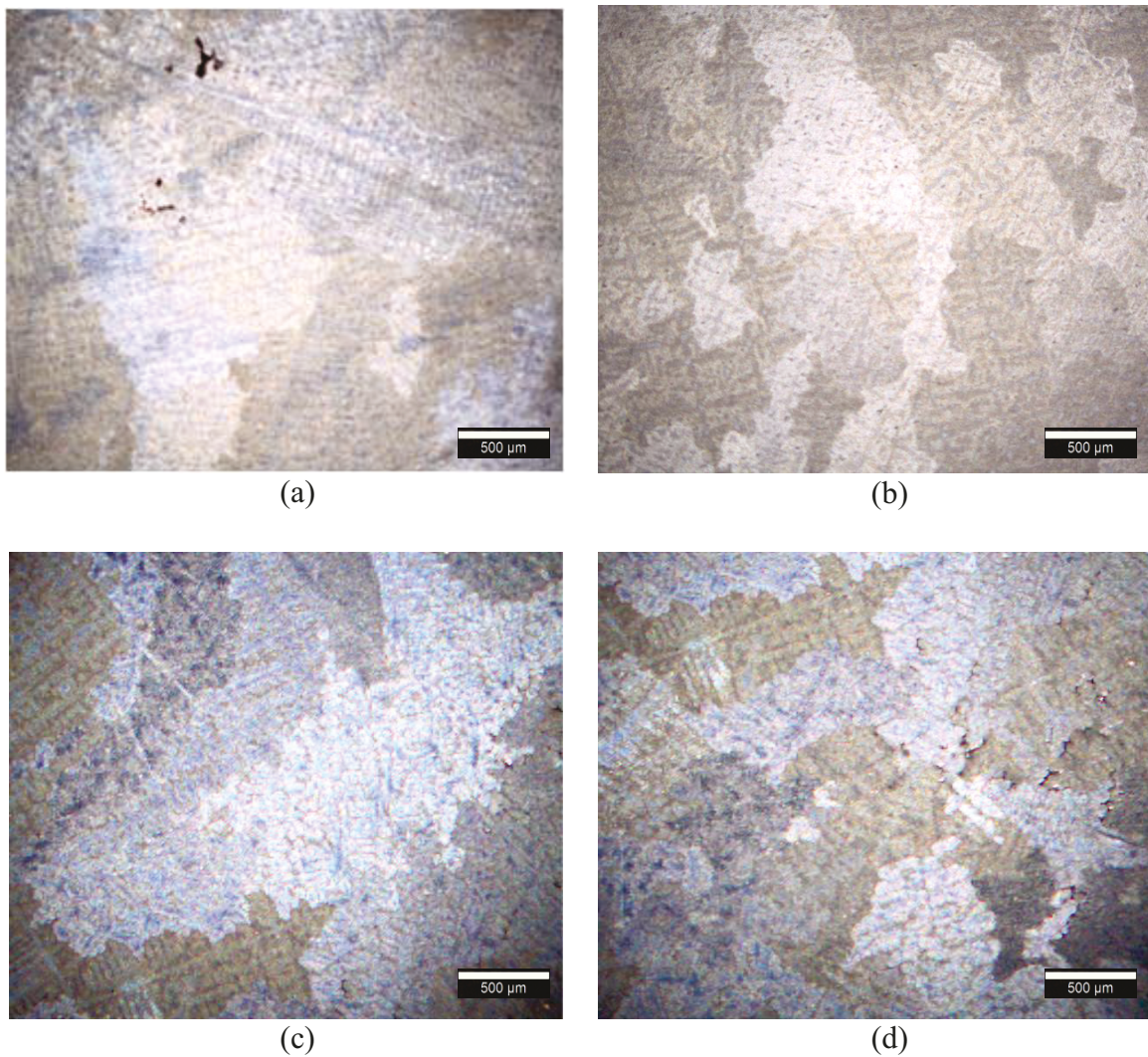


Figure 4-4. Grain structure of as-solidified (a, b) and post-casting heat treated (c, d) cooled at 0.25 (a, c) and 10 °C/s (b, d).

4.1.2 Dendritic structure

Secondary dendrites result from capillarity instabilities at the dendrite tip. These perturbations are small at first and then grow at the expense of the smaller arms in a process similar to Ostwald ripening. The driving force for this coarsening is the increase in interfacial energy at the tips of the smaller arms due to the higher curvature there [161].

SDAS was measured by counting the number of secondary arms over a measured length on a minimum of five well aligned dendrite trunks. The results are shown in Figs 4-5 and 4-6. It can be seen that the SDAS decreased as the cooling rate increased according to the following relation:

$$\lambda_2 = KR^n \quad (4-4)$$

where, λ_2 is the secondary arm spacing, K and n material constants, and R the cooling rate. $K = 1.54$ and $n \approx 0.3$ were obtained by the least square fitting of the experimental data and they were in good agreement with the theory [162].

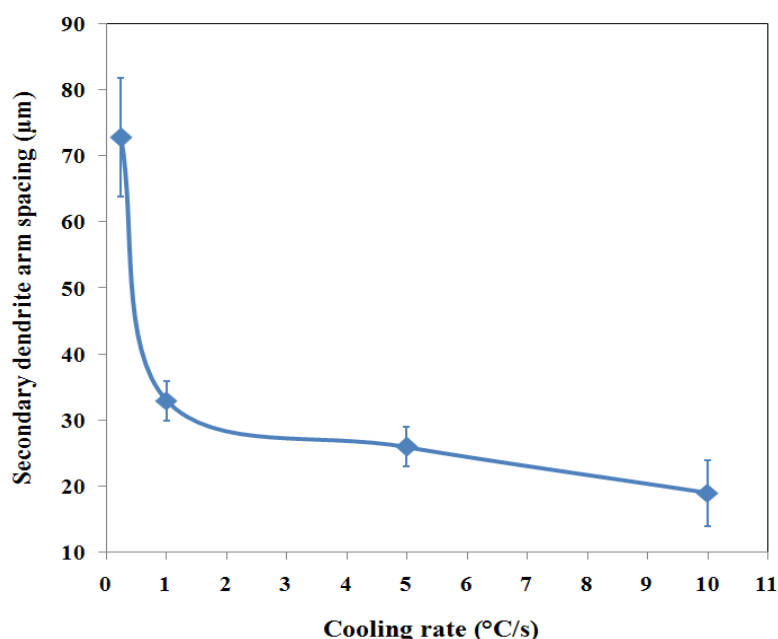


Figure 4-5. Variation of SDAS with cooling rate in Mar-M247 Ni-based superalloy.

Heat treatment process could not affect the SDAS, as dendrite microstructure is formed and grew in the melt during the solidification process. Therefore, the solidification process should

be well controlled with respect to dendritic microstructure formed during solidification, since dendritic structure cannot be modified by heat treatments after solidification.

4.1.3 Phase composition

The initial microstructure of the Mar-M247 Ni-based superalloy consisted of γ Ni-rich solid solution containing a dispersion of γ' precipitates, discrete metal carbide particles, and γ/γ' eutectic pools as depicted in Fig. 4-7. After solidification, the microstructure varied with the cooling rate. Common observation was the absence of pores, except from central shrinkage, whose size decreased with the solidification rate.

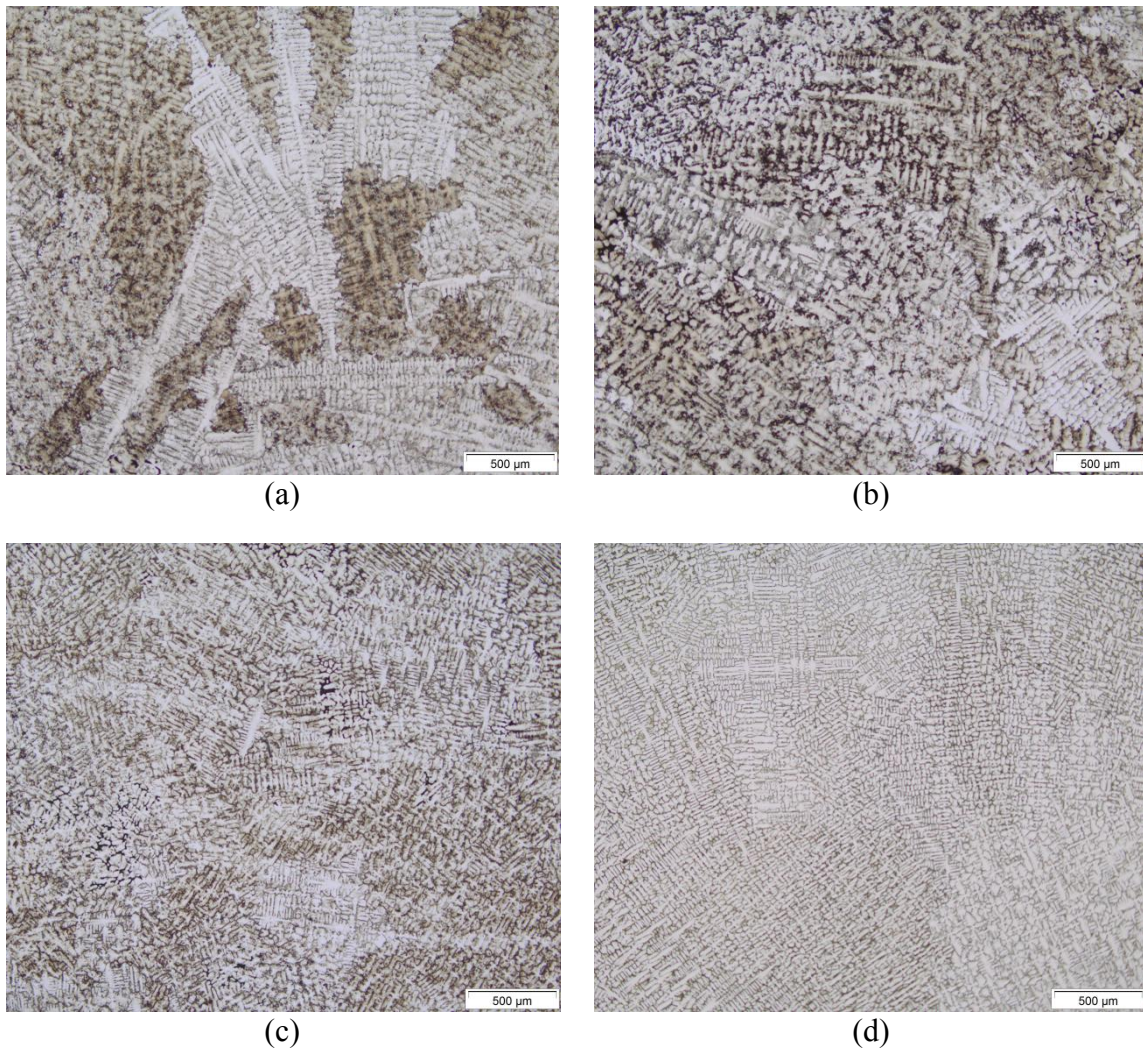


Figure 4-6. Dendritic structure of Mar-M247 Ni-based superalloy cooled at (a) 0.25, (b) 1 (c) 5 and (d) 10 °C/s.

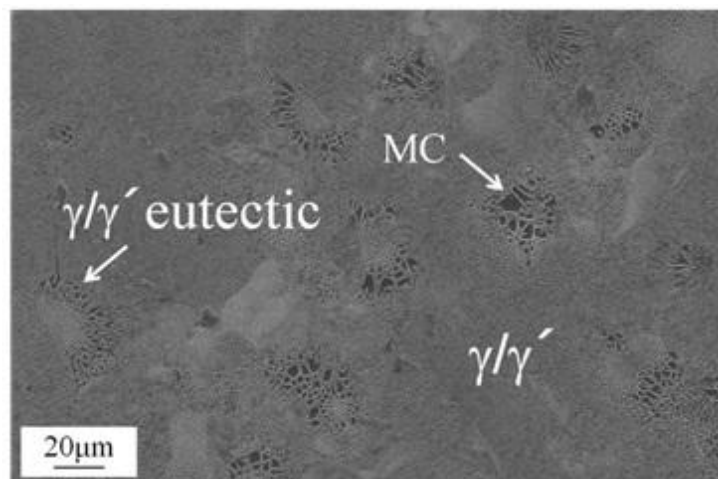


Figure 4-7. Typical as-cast microstructure of Mar-M247 Ni-based superalloy.

The microstructure of the Gleeble specimen solidified at a cooling rate of 0.25 °C/s had a dendritic structure consisting of γ/γ' matrix, metal carbides, and some amount of γ/γ' eutectic (volume fraction of 10.4 %) formed in the inter-dendritic areas during the last stage of solidification (Fig. 4-8 (a)). The specimen cooled at 1 °C/s demonstrated dendritic structure with well defined primary and secondary dendrites and only γ/γ' matrix and carbides were present in this specimen (Fig. 4-8 (b)).

Microstructure of the samples solidified at 5 and 10 °C/s was similar and contained carbides and γ/MC eutectic pools resulting from the reaction $L \rightarrow \gamma + \text{MC}$ in which liquid transforms into two solid phases, γ and MC (Figs. 4-8 (c, d)).

The presence of the eutectic microstructure indicates that the undercooling of the last to solidify liquid and its composition fulfilled the conditions for eutectic solidification inside the coupled-growth zone (CGZ). CGZ is defined as a range of alloy composition and interface temperature (or velocity) where eutectic growth prevails upon solidification [162–165]. The observed microconstituents are summarized in Table 4-1 as a function of the cooling rate.

The main aim of a solution heat treatment applied to Ni-based superalloys is the dissolution of coarse γ' formed during solidification. Moreover, it reduces chemical segregations of some elements accumulated in the dendrite cores and interdendritic regions [7,103,166] as well as leads to dissolution of γ/γ' eutectic (if it is present) [122]. The microstructures of the heat-treated specimens are depicted in Fig. 4-9 and information on microstructural constituents is given in Table 4-1. It is seen that the double heat treatment did not affect the constituent phases of specimens cooled at 0.25 °C/s and 1 °C/s. The only effect was the reduction of the amount of γ/γ' eutectic in the specimen cooled at 0.25 °C/s from 10 % to 7 %. On the other

hand, the heat treatment of the specimens solidified at cooling rates of 5 and 10 °C/s resulted in the dissolution of γ /MC eutectic. This shows that the γ /MC eutectic was metastable constituent formed during high cooling rates.

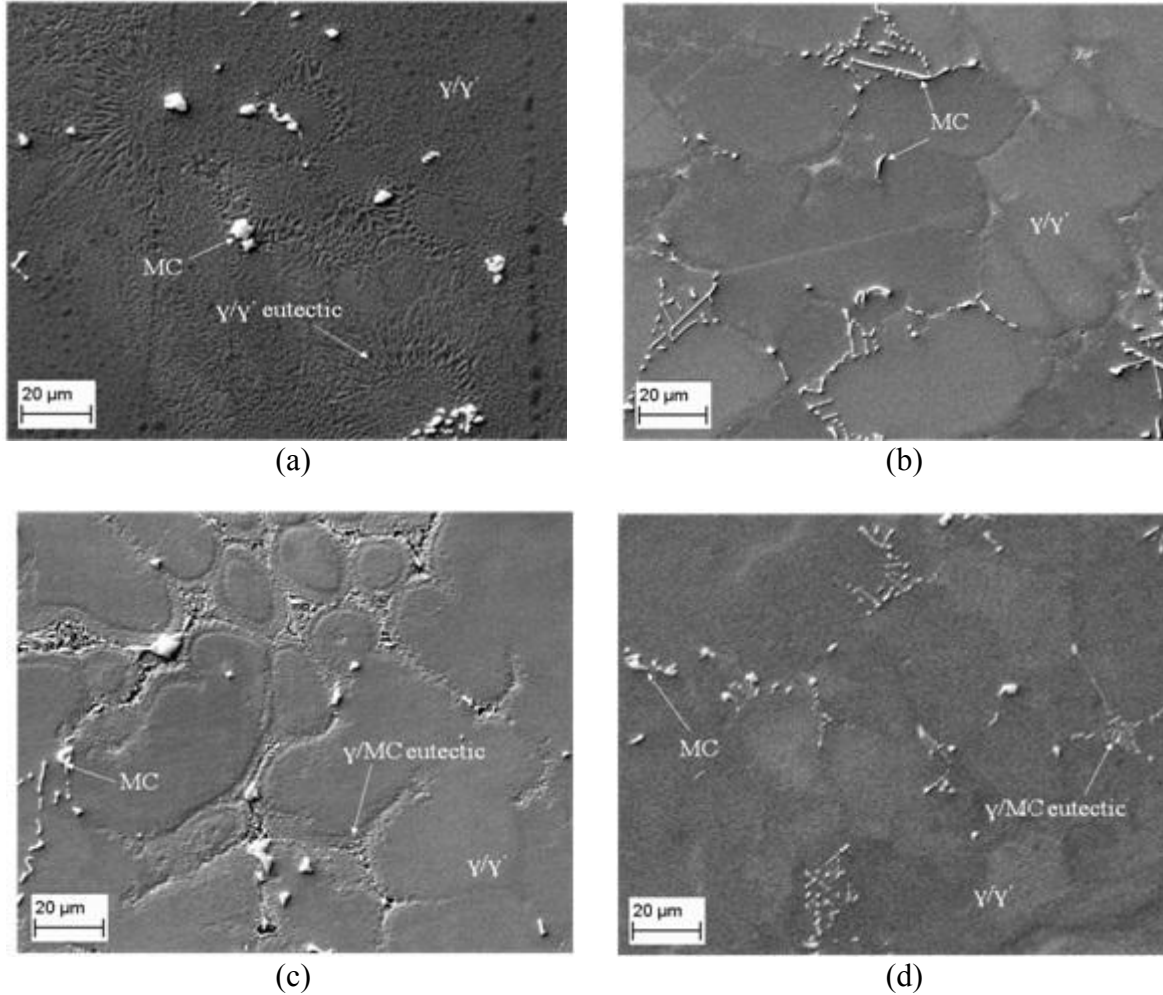


Figure 4-8. Microstructures of Gleeble specimens made of Mar-M247 cooled at: a) 0.25 °C/s, b) 1 °C/s, c) 5 °C/s and d) 10 °C/s.

Table 4-1. Constituent phases after controlled cooling and double heat treatment.

Cooling rate (°C/s)	Constituent phases in the as-solidified specimens	Constituent phases in the heat-treated specimens
0.25	$\gamma/\gamma' + MC + \gamma/\gamma'$ eutectic	$\gamma/\gamma' + MC + \gamma/\gamma'$ eutectic
1	$\gamma/\gamma' + MC$	$\gamma/\gamma' + MC$
5	$\gamma/\gamma' + MC + \gamma/MC$ eutectic	$\gamma/\gamma' + MC$
10	$\gamma/\gamma' + MC + \gamma/MC$ eutectic	$\gamma/\gamma' + MC$

Other important microstructural constituents in Ni-based superalloys are carbides. Carbide particles were observed in the microstructure of all as-solidified Gleeble specimens (Fig. 4-8). They were located mainly in the interdendritic areas. Figure 4-10 shows the effect of cooling rate on their average size and volume fraction. The average carbide size monotonously decreases with increasing cooling rate from 6.45 μm at cooling rate of 0.25 $^{\circ}\text{C/s}$ to 4.33 μm at cooling rate of 10 $^{\circ}\text{C/s}$, whereas the volume fraction of carbides shows an opposite trend. Similar behavior was observed in [14].

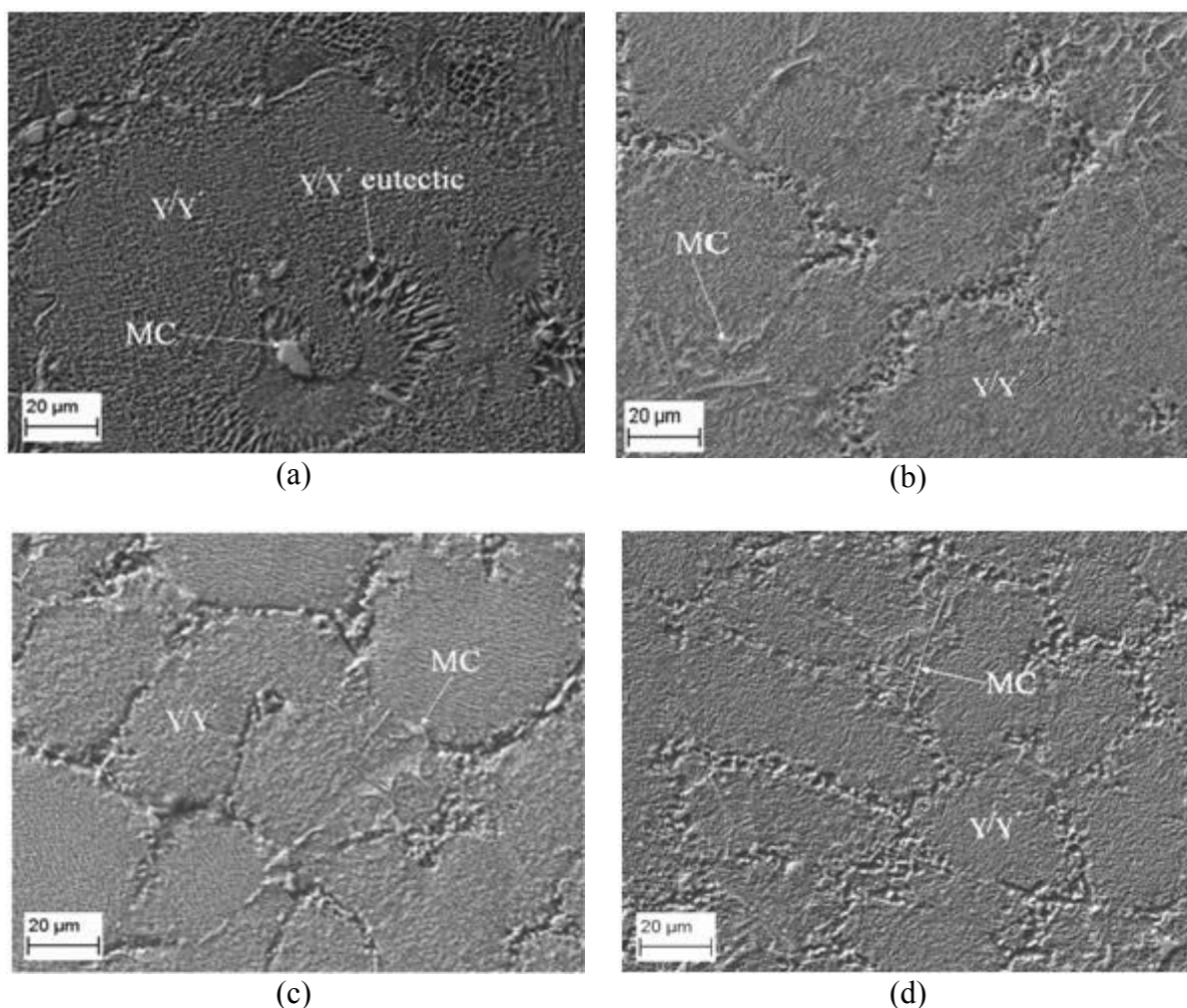


Figure 4-9. Microstructure of the heat treated samples cooled at a) 0.25 $^{\circ}\text{C/s}$, b) 1 $^{\circ}\text{C/s}$, c) 5 $^{\circ}\text{C/s}$ and d) 10 $^{\circ}\text{C/s}$.

This behavior can be explained from the view point of carbide nucleation. The critical nucleation radius of carbides which is stable within liquid can be calculated with following equation:

$$r_0 = \frac{(2\sigma T_m)}{(\Delta T_r \Delta h_m)} \quad (4-5)$$

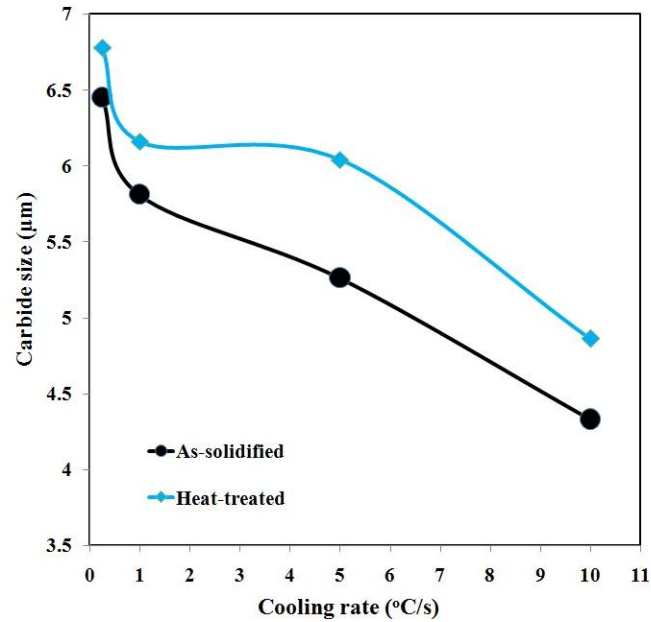
where r_0 is critical radius for growing carbide, σ the carbide-liquid interface energy, T_m and ΔT_r are carbide melting temperature and undercooling, respectively, and Δh_m the latent heat of carbide fusion per unit volume [14]. It is evident from the Eq. (4-5) that the undercooling has the strong effect on the critical nucleation radius. According to the microstructural evaluation, the prevailing carbides were TiC and HfC with melting temperatures of 3065 and 3930 °C respectively. Therefore, at melting temperature of Mar-M247 Ni-based superalloy, which in this research has been obtained around 1360 °C, the amount of undercooling (ΔT_r) for TiC and HfC can be 1432 and 2297 °C, respectively. If in Eq. (4-5) for this alloy other parameters are defined as follow: $\sigma = 2 \text{ J m}^{-2}$, T_m (TiC) = 3065 °C, T_m (HfC) = 3930 °C, ΔT_r (TiC) = 1432 °C, ΔT_r (HfC) = 2297 °C and $\Delta h_m = 1 \times 10^9 \text{ J m}^{-3}$, the critical nucleation radius are r_0 (TiC) = 7.8 nm and r_0 (HfC) = 6.5 nm [14]. These sizes of nuclei are very small for carbide nucleation and under these condition carbide nuclei are formed and grow easily. Also with increasing cooling rate, diffusion drops and the result is a finer carbide size.

Basically, having required carbide forming elements, inter-secondary dendrite arm spacing is an appropriate region for the growing of carbide nuclei [34,165]. Therefore, with refinement of SDAS at higher cooling rate, carbide size also becomes smaller. Higher cooling rate causes higher nucleation rate which leads to the increasing volume fraction and decreasing carbide size. No noticeable effect of the heat treatment on the size and volume fraction of carbide particles was observed. However, the volume fraction of carbide particles in the heat treated specimens is somewhat lower compared to that in the as-solidified ones. This can be related to dissolution of primary carbides in the Ni matrix and formation of new carbides during solution treatment [23,110,135].

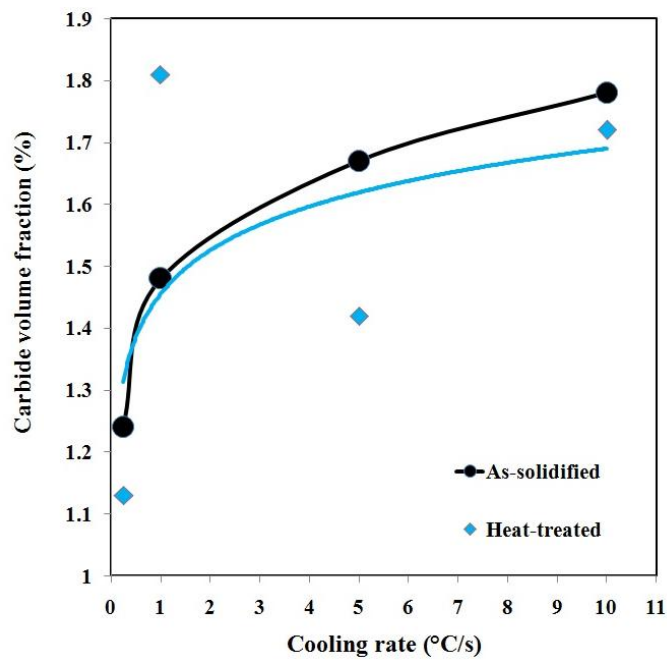
4.1.4 Hardness

The variation of hardness in the Gleeble specimens solidified at different cooling rates is shown in Fig. 4-11. It is seen that hardness increased with increasing cooling rate. This is quite expected, since the different cooling rates yielded very different microstructures, as explained in the previous section. The lowest hardness was observed at the cooling rate at

0.25 °C/s, and may be explained by the low volume fraction and blocky morphology of carbides as well as by the presence of 10 % γ/γ' eutectic.



(a)



(b)

Figure 4-10. Effect of cooling rate on a) carbide size and b) carbide volume fraction.

At low growth rates, the carbon and carbide forming elements accumulate at the bottom of the mushy zone, which solidifies very slowly, so the carbides formed are large and have equilibrium faceted morphology. On the other hand, the presence of the γ - γ' eutectic further decreased the hardness, as the eutectic possesses lower strength and greater ductility than the dendrite cores. It has been shown that the room temperature yield strength decreases and the elongation-to-failure increases with the volume fraction of γ - γ' eutectic [122].

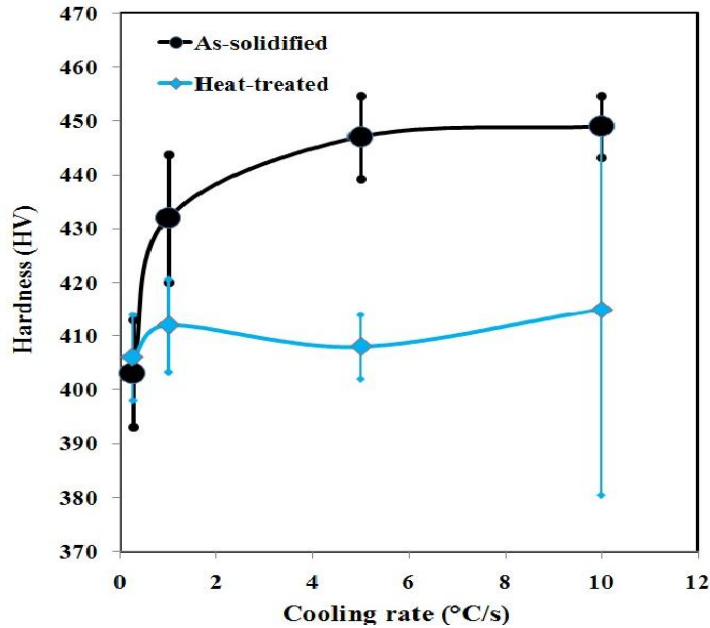


Figure 4-11. Effect of cooling rate on the hardness of the as-solidified and heat-treated specimens.

Carbide's volume fraction and size can influence the hardness of Ni-based superalloys. In fact, carbides act as reinforcement in Ni-based superalloys, so increasing the volume fraction of the carbides, which are the hardest phase in Ni-based superalloys, leads to the increase in hardness. In addition, the size and volume fraction of carbides are correlated to their distance (inter particle spacing) [167]:

$$\lambda = d_r \left[\left(\frac{\pi}{6V_f} \right)^{\frac{1}{3}} - 1 \right] \quad (4-6)$$

where λ is the distance between carbides, V_f is the volume fraction, and d_r is the carbide diameter, assuming them as spherical. It can be seen that carbide spacing is proportional to the carbide size and inversely proportional to the volume fraction.

Indeed, carbide spacing, inter particle spacing, (λ) decreased with increasing cooling rate as a result of both lower carbide size and larger volume fraction as depicted in Fig. 4-12.

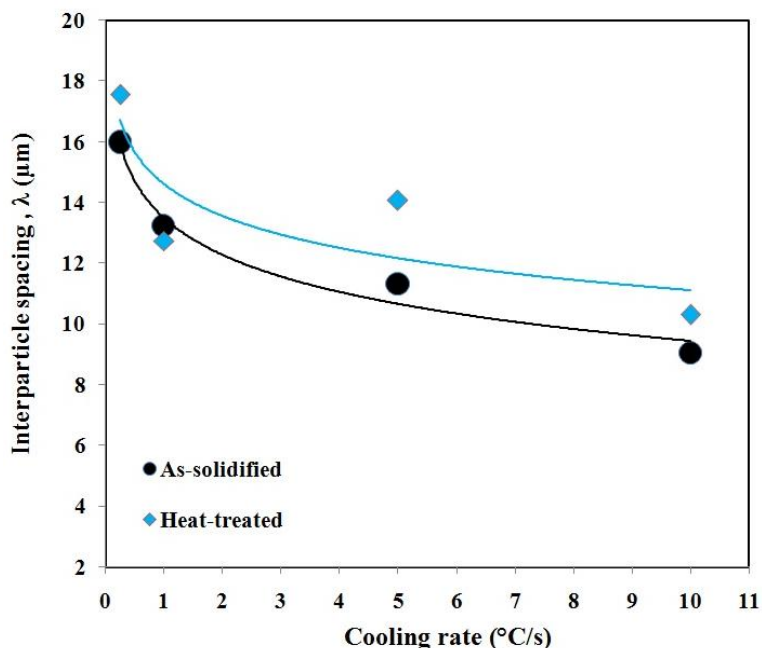


Figure 4-12. The effect of cooling rate on the carbide spacing, λ .

Since carbides act as obstacles to dislocation movement at the time of deformation by indenter in hardness test, decreasing the distance between particles increases the number of obstacles against dislocation glide [168]. Furthermore, decreasing the distance between the carbide particles according to Eq. (4-7) will increase the required tension for dislocations movement between the carbide particles leading to an increase in the material strength [168].

$$\tau_0 = \frac{Gb}{\lambda} \quad (4-7)$$

In Eq. (4-7), τ_0 is the required stress for forcing dislocations to move among reinforcement particles, G the shear modulus and b the Burger's vector [38]. Therefore, increasing hardness at higher cooling rates was on account of higher volume fraction and finer carbides as well as the absence of γ/γ' eutectic.

The effect of heat treatment on the hardness of specimens is shown in the Fig. 4-11. As can be observed the hardness is nearly constant in all samples. As a result of carrying out the

same heat treatment for all samples, it is expected the constant hardness for all specimens. On the other hand, when compared with the as-solidified Gleeble samples, the hardness in the heat treated samples is to some extent lower. The reduction of residual stresses after heat treatment can be a factor for decreasing of hardness. Also, after heat treatment the carbide size was somewhat bigger which was accompanied by reduction of carbide volume fraction. This could play some role for decreasing hardness, as well [168].

4.1.5 Conclusions

The microstructure and hardness evolution have been investigated in the Mar-M247 Ni-based superalloy processed by controlled cooling in the Gleeble thermo-mechanical simulator and double heat treatment. The following conclusions may be drawn:

- 1- Melting/solidification experiments under controlled cooling with cooling rates in the range 0.25–10 °C/s can be successfully performed.
- 2- Temperature profiles were smooth and minor instabilities were only present at the highest cooling rate of 10 °C/s but they did not affect the overall cooling rate;
- 3- The grain size decreased with increasing cooling rate and remained essentially unaffected by the heat treatment;
- 4- SDAS decreased as the cooling rate increased.
- 5- An increase in the cooling rate led to change in microconstituents from γ/γ' matrix with carbides and eutectic at 0.25 °C/s over γ/γ' matrix with carbides at 1 °C/s to γ/γ' matrix with carbides and γ/MC eutectic at 5 and 10 °C/s. The heat treatment led to partial dissolution of γ/γ' eutectic at 1 °C/s and dissolution of metastable γ/MC eutectic observed in samples solidified at 5 and 10 °C/s.
- 6- The increase in cooling rate was accompanied by the increase in carbides volume fraction and the decrease in carbide size and their interparticle spacing. With raising cooling rates from 0.25 to 10 °C/s, volume fraction increased by 44 %, while carbide size and spacing decreased by 33 % and 43 %, respectively. The heat treatment led to lower carbides volume fraction and spacing, as well as to larger carbide size.
- 7- The hardness of the as-solidified samples was affected by carbide size, volume fraction and interparticle spacing. Hardness rose with increasing carbide volume fraction and decreasing carbide size. As a result of identical heat treatment the hardness was constant in heat-treated samples.

4.2 Effect of temperature gradient on secondary dendrite arm spacing of Mar-M247 Ni-based superalloy

To study the influence of temperature gradient on dendritic structure of Mar-M247 Ni-based superalloy, the same sample preparation (see section 3.3.1) and melting/solidification experiments (see section 3.3.2) were carried out. However, in order to find the temperature gradient along the rod, instead of utilizing one thermocouple recording temperature in the midsection of sample (see section 3.3.1), four thermocouples were employed along the sample. A thermocouple (R-type) was welded to the midsection of each sample (marked as TC4 on Fig. 4-13 (a)) to control the temperature during melting/solidification experiments. Three other R-type thermocouples were also welded at 4, 8, and 12 mm distance from the midsection of the sample to record the temperature distribution along the sample axis during the experiment. In Fig. 4-13 (a), these thermocouples are marked as TC3, TC2, and TC1, respectively. The selected cooling rates, 0.25 and 10 °C/s, were chosen from the relevant range of the cooling rates during investment casting of nozzle guide vanes from Mar-M247 Ni-based superalloy, considering this issue to maximize generated temperature gradient for better observation of its effect on microstructure [7]. It should be noted that, despite some temperature gradient along the radius of the sample (~ 30 °C/mm), the cooling rate of the surface and the center is the same. At least two samples were tested for each condition and the results were found to be reproducible.

The melted/solidified sections of the tested samples were cut out. From these sections, specimens for microstructural characterization were prepared using standard metallographic techniques. To reveal the dendritic microstructure, the specimens were etched using a chemical solution consisting of 25g FeCl₃, 60 ml HCl, and 25 ml H₂O. The temperature-controlled areas of these specimens (areas under the welded thermocouples) were studied using an optical microscope Olympus BX51. The qualitative analysis of dendritic microstructure was performed using Analysis software. The measurement of SDAS was achieved by counting the number of secondary arms over a length on at least five well-defined trunks.

The temperature-time plots recorded during solidification at nominal cooling rates of 0.25 and 10 °C/s are shown in Figs. 4-13 (b,c), respectively. It should be noted that the data from the thermocouple TC2 for the sample cooled at 10 °C/s are not presented since this sample did not melt at a distance of 8 mm from the midsection of the sample. The linear character of

the plots shows that the cooling rate was very well controlled. Thus, from these plots, the true cooling rate during solidification $R=dT/dt$ can be easily estimated for each area with the spot-welded thermocouple. It has been reported that solidification of the melt occurs in the temperature range of 1280-1350 °C [166]. Data on the true cooling rate at different thermocouple locations for samples solidified at both set cooling rates are listed in Table 4-2. It can be seen that the true cooling rate tends to increase slightly with distance from the midsection.

The same data were used to plot the temperature variation along the axis of the sample, as shown in Fig. 4-14. It is assumed that the distribution of temperature along the specimen axis is symmetrical with respect to the midsection [122]. It is seen that the temperature decreases with increasing distance from the midsection. Also, the temperature profile at the set cooling rate of 10 °C/s (Fig. 4-14 (b)) is much steeper compared to that at the set cooling rate of 0.25 °C/s (Fig. 4-14 (a)) on account of the different geometries of the copper grips providing different thermal diffusivity during heating/cooling [122]. The obtained T - x plots can be described by a polynomial function

$$T=ax^2+bx+c \quad (4-8)$$

as shown in Figs. 4-14 (a,b) and the constants a , b and c easily determined. These data are listed in Table 4-3. The derivative of this quadratic function describes the thermal gradient G along the sample axis

$$G=dT/dx=2ax+b \quad (4-9)$$

Thus, the temperature gradient can be easily estimated from these T - x plots for any point along the sample axis using data from Table 4-3. Figures 4-14 (c, d) illustrate the distribution of the thermal gradient along the axis in both samples. It should be noted that the G -values in the midsection ($x=0$) due to melt convection were taken to be 1 °C/mm despite the fact that Eq. (4-9) yields $G=0$ °C/mm.

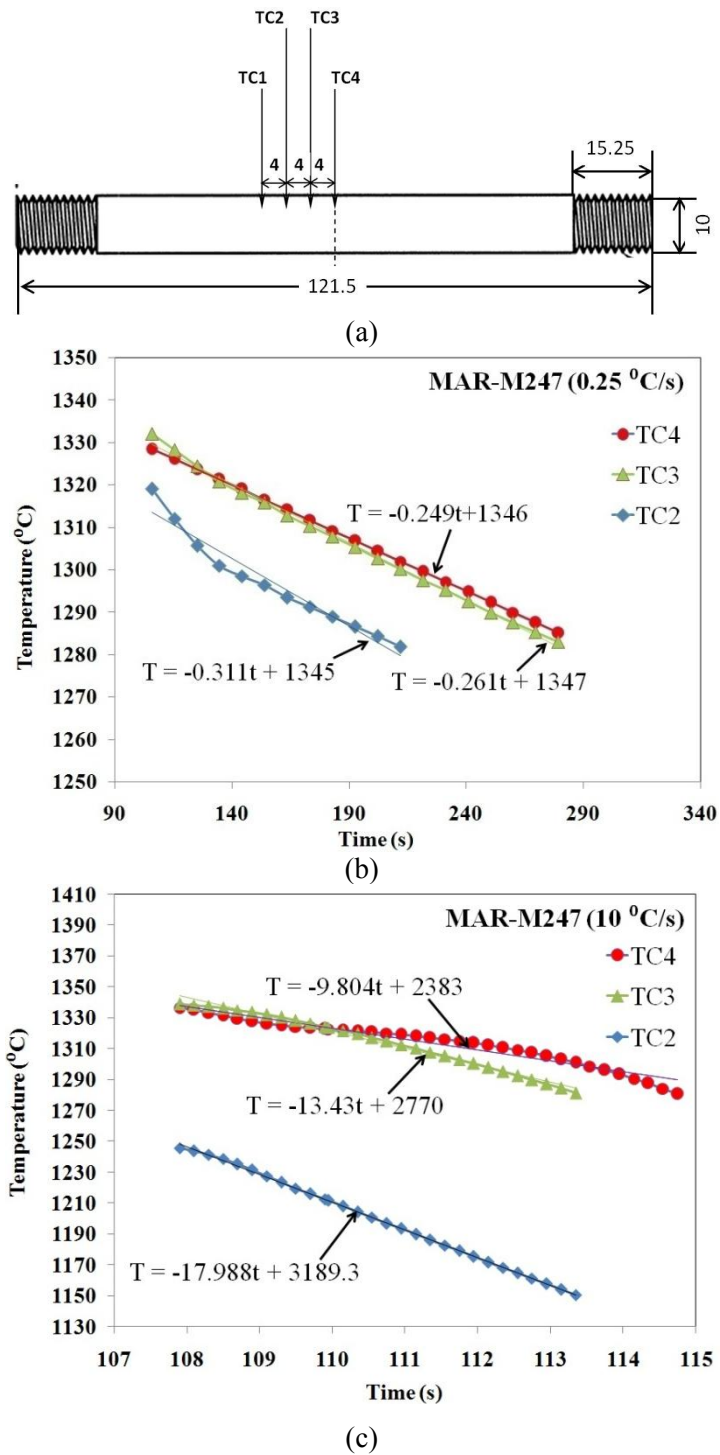


Figure 4-13. a) Schematic presentation of the sample with four welded thermocouples. All dimensions are in mm. Temperature-time plots recorded by different thermocouples during solidification at cooling rates of: b) 0.25 °C/s, c) 10 °C/s.

Table 4-2. Data on thermal gradient, true cooling rate and solidification rate in the studied areas of the melted/solidified samples.

Set cooling rate		0.25 °C/s			10 °C/s		
Materials	Distance [mm]	R [°C/s]	G [°C/mm]	V [µm/s]	R [°C/s]	G [°C/mm]	V [µm/s]
MAR-M247	0	0.25	1	250	9.8	1	9800
	4	0.27	3.128	83	13.43	16.83	790
	8	0.31	4.272	73	-	-	-

Considering Figs. 4-14 (c, d), the variation of thermal gradient with distance shows a linear relationship, in which the thermal gradient increases with distance from the midsection. Also in the case of the higher cooling rate (10 °C/s), the thermal gradient increased much more rapidly than in the case of the lower cooling rate (0.25 °C/s).

The *G*-values for the points located at distances of 4 and 8 mm from the midsection are listed in Table 4-2. The results depicted in Fig. 4-14 clearly show two things. First, the temperature gradient increases linearly from the midsection of the sample toward the cooling extremities and second, the gradient is much steeper in the case of the higher cooling rate. It may be observed that the central part of the sample solidified at very low temperature gradients <1 °C/mm, whereas the parts at the end of the melting zone, at a distance of 8 mm from the midsection, were subjected to a temperature gradient as high as 40 °C/mm.

It is well known that the solidification rate *V* is determined by temperature gradient *G* and cooling rate *R*. It can be calculated as [14]

$$V = R/G \tag{4-10}$$

The *V*-values were estimated for each studied area along the specimen axis. The data are provided in Table 4-2. Although the cooling rate and thermal gradient increase with distance from the midsection, the solidification rate follows the opposite trend, as the difference of solidification rates between midsection and 4 mm from the midsection were 9010 µm/s and 167 µm/s for samples cooled at 10 °C/s and 0.25 °C/s, respectively.

The variation of microstructure with distance from the midsection is depicted in Fig. 4-15. It is found that the SDAS increases with distance from the midsection. For example, the SDAS

increases from 19.4 mm (Fig. 4-15 (a)) in the midsection of the sample cooled at 10 °C/s to 60.9 mm at the distance of 4 mm from the midsection (Figs. 4-15 (b) and 4-16).

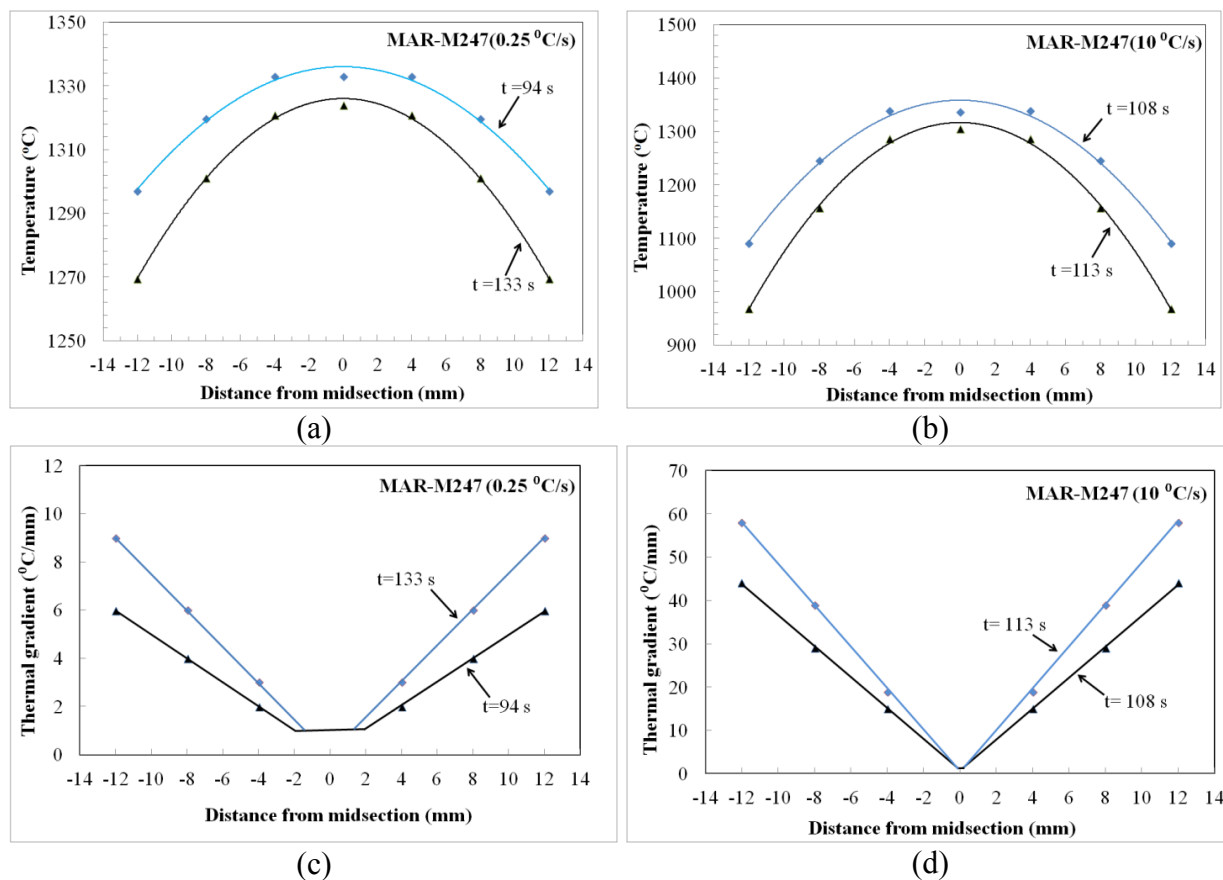
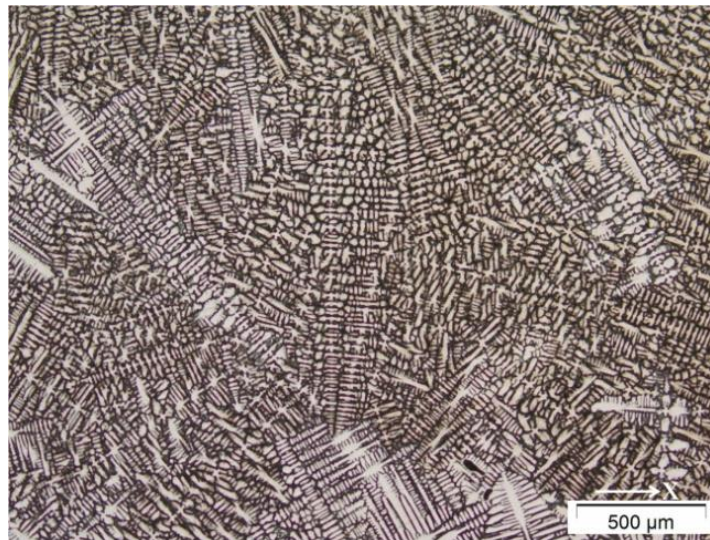


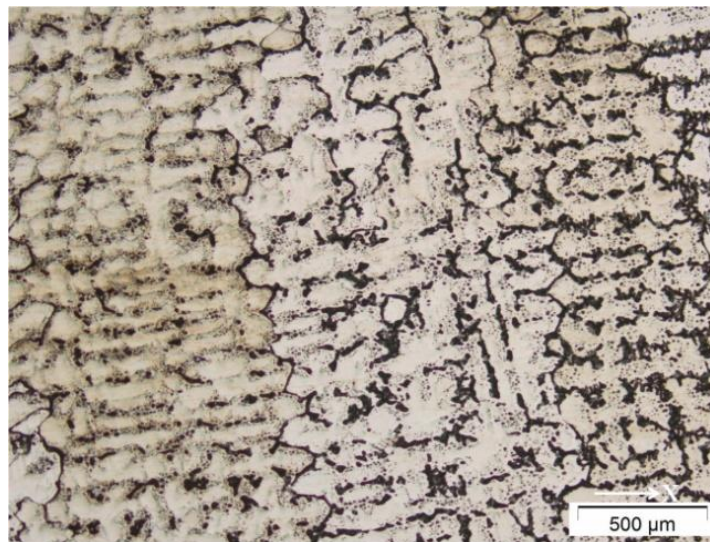
Figure 4-14. Temperature distribution in the samples cooled at: a) 0.25 °C/s, b) 10 °C/s and thermal gradient along the axis of the samples cooled at: c) 0.25 °C/s, d) 10 °C/s.

Table 4-3. Constants of the $T-x$ equations under various conditions.

Cooling rate [°C/s]	Time [s]	Constants		
		a	b	c
0.25	94	-0.2671	0	1336
	133	-0.3917	0	1326
10	108	-1.836	0	1358
	113	-2.422	0	1316



(a)



(b)

Figure 4-15. The dendritic microstructure of Mar-M247 Ni-based superalloy at the cooling rate of 10 °C/s in (a) midsection and (b) at 4 mm distance from the midsection.

A significant body of research has focused on the relationship between solidification parameters and dendritic structure in Ni-based superalloys and suggests that the SDAS decreases with increasing cooling rate according to the Kurz-Fisher model,

$$\lambda_2 = AR^{-1/3} \quad (4-11)$$

where λ_2 is the SDAS, R the cooling rate and A a constant [14]. The reduction of SDAS can be explained by two effects: first, increasing the cooling rate causes a reduction in the

diffusion time which affects the solute distribution [34]. Second, a higher temperature gradient and cooling rate shortens the length of the solid-liquid phase zone, so that the solidification time decreases and consequently the solidification rate increases [23,34]. Moreover, the coarsening time of the SDAS is shortened at the higher cooling rate, so a finer SDAS is obtained [110].

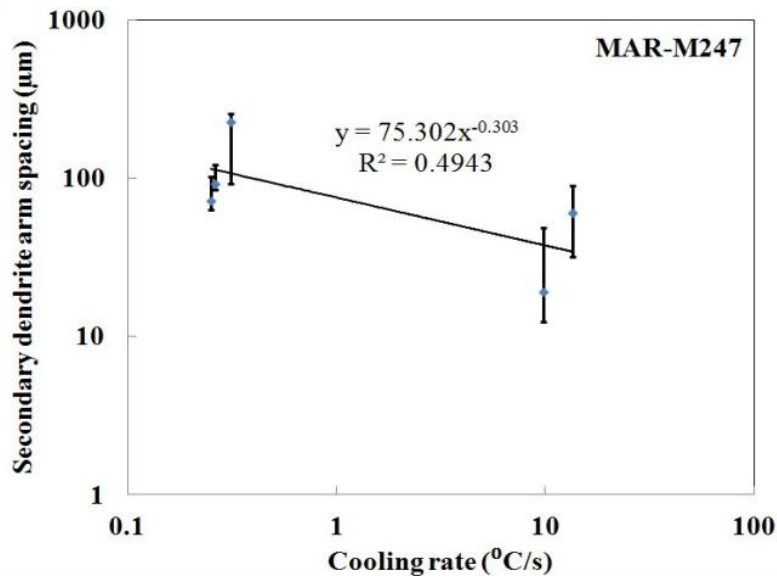
In Fig. 4-16 (a), the measured SDAS values are plotted vs. the true cooling rate (Table 4-2). The regression analysis of these data leads to the trendline equation

$$\lambda_2 = 75.30R^{0.303} \quad (4-12)$$

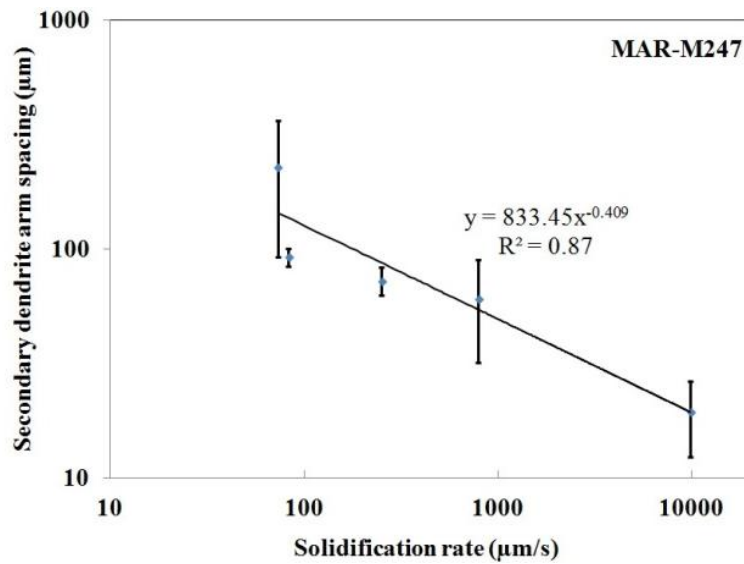
which is in accordance with the relationship reported earlier (Eq. (4-11)) [14]. However, a significant deviation of the experimental points from the trendline is clearly seen (Fig. 4-16 (a)), resulting in a low value of correlation coefficient ($R^2=0.49$). This deviation can be rationalized based on the significant variation of the thermal gradient along the axis of samples solidified at both cooling rates (Table 4-2) in contrast with earlier investigations [51,162–164] which were carried out at a constant thermal gradient. Therefore, the effect of thermal gradient on the SDAS should not be ignored in our analysis. Figure 4-16 (b) illustrates the SDAS values plotted vs. solidification rate which takes into account both cooling rate and thermal gradient (see Eq. (4-10)). It is seen that the SDAS values decrease with increasing solidification rate. Similar results were also reported in earlier works [23,51,110,135,161–164,167,168]. The trendline equation

$$\lambda_2 = 833.5V^{0.41} \quad (4-13)$$

is derived from the regression analysis of these data (Fig. 4-16 (b)). It should be noted that the deviation of the experimental results from the trendline is much lower ($R^2=0.87$) compared to that observed in Fig. 4-16 (a). Equation 4-13 is relevant in some extent to the models developed to relate PDAS and solidification parameters, where PDAS is presented as a function of both solidification rate and temperature gradient [161]. It should be also noted that the SDAS was found to be proportional to $V^{-1/3}$ in the directionally solidified DD3 Ni-based superalloy [159].



(a)



(b)

Figure 4-16. The variation of secondary dendrite arm spacing with: a) cooling rate, b) solidification rate.

Conclusions

The effect of thermal variations on the secondary dendrite arm spacing in the Mar-M247 Ni-based superalloy has been studied by a novel method, based on physical simulation of melting/solidification experiment with a constant cooling rate and variable temperature gradient. The following conclusions may be drawn:

1- It proved to be effective as a range of solidification rates were obtained in a single sample subjected to a constant cooling rate, but varying temperature gradient. This in turn enabled a

spread of microstructures corresponding to a range of well-controlled solidification rates to be obtained, which were produced in a single melting/solidification experiment.

2- The presented method has many advantageous features, as it may be applied to virtually all metallic materials and it is also not time consuming. In addition, it can be used for microstructure screening and optimizing relevant solidification processes, from directional solidification, to investment casting to rapid solidification.

3- The obtained results indicate that the SDAS does not obey a simple relationship taking into account only the cooling rate if there are significant variations of other thermal parameters (local thermal gradient and, therefore, local solidification rate) during the solidification process.

4- The thermal gradient can be a very important factor affecting SDAS in the investment casting process. Therefore, the local solidification rate can act as a better parameter to relate SDAS and solidification parameters in this case. This finding can be very important for investment casting where dramatic variations of the thermal parameters during solidification can occur, owing to the complex shape of the cast products.

5 Physical simulation of investment casting of NGVs from Mar-M247

Investment casting in vacuum, also often referred to as lost-wax process, is the only commercially used manufacturing route of these parts, that have very complex shapes [13]. As it was mentioned above, due to excellent surface finish and dimensional accuracy, this process is especially useful for casting of complex shape containing thin sections [13]. NGVs are important structural parts of gas turbines [169] which are typically made from Ni-based superalloys because they have to withstand very high temperatures and aggressive environments [11]. The search for reduced weight and increased efficiency of aero-engines and gas turbines is driving changes in design of parts to more complex shapes and thinner geometries. However, these innovations are hindered by the complexity of the manufacturing process, which makes it difficult to control defects and microstructural aspects playing an important role on creep resistance of NGVs serving at elevated temperatures. Development of investment casting routes for the new generation of NGVs is carried out via a trial and error approach or, in other words, via experimental casting trials. The casting parameters are varied until good quality castings are produced. However, this strategy is very expensive and time consuming and thus dramatically limits the rate of innovation [17].

Presently, a paradigm shift is underway in which the experimental casting trials are partially replaced by the numerical simulation of the investment casting process to overcome the

limitations of standard trial and error approach [13,18]. Reconfiguration of the mould, which was made on the foundry floor, can now be made on a computer and simulated. In addition, the thermal history of a casting can be examined by means of simulations, and the effect of the casting parameters on the microstructure and quality of the as-cast parts can be evaluated. Simulation of casting is reliable when the accurate data of materials are known at processing conditions, and boundary conditions are defined precisely. Casting simulation was applied by Gonzales et al. [170] to visualize mould filling and heat transfer during casting and solidification in order to predict microstructure and location of internal defects. The existing casting simulation tools are able to predict the local thermal profile, local grain structure and defects (gas porosity, shrinkage pores, etc.) in the as-solidified complex shape parts [171]. However, the microstructural prediction by modelling tool, depending strongly on reliable input data, is limited to the recognition of some microstructural features.

Physical simulation of metallurgical processes is often employed for development of novel manufacturing routes. Physical simulation involves the exact reproduction of the thermal and mechanical processes in the laboratory, as the material has to undergo in the full scale fabrication process. There is a body of research where physical simulation of continuous casting was successfully performed. In continuous casting, the liquid metal is poured into a crystallizer chamber in which its outer shell has to solidify to the extent securing the liquid core inside. When a vertically cast slab or billet has to be bent into horizontal position, the ductility of outer shell must allow this. Gaining physical data for such operation includes melting/solidification experiments on numerous samples followed by hot tensile testing them at various temperatures after solidification, to create hot ductility maps, as was done for steel by Suzuki and Yamaguchi [19]. Michalik and Kolmasiak performed physical simulation of continuous casting of St2S steel in order to predict internal stresses and their relaxation during metallurgical process [20]. Ferguson et al. described another technique which was developed specifically to simulate continuous casting followed by semi-solid or direct *in situ* hot rolling [21]. This metallurgical process is characterized by complex three-dimensional heat flow which is determined by the melt temperature, the temperature of the walls of the caster, the geometry and thickness of the slab, and the velocity of the slab. The modes and directions of solidification directly affect the dendritic and grain structure and impurity segregations in the as-solidified slab. The HDSV40 CC-DR simulator can control multiple dimensions of heat flow while performing semi-solid deformation for a physical simulation that closely simulates the real process. Various multi-state forming and multi-stage cooling combinations can be carried out in this way. Temperature, strain, strain rate, force, and

cooling rates can all be controlled and measured precisely to yield a quantitatively understood experiment. The investment casting process is also characterized by complex three-dimensional heat flow determined by numerous casting parameters including melt temperature, temperature of ceramic mould, casting shape, thermo-physical properties of ceramic mould and metal, etc. Thus, significant variations of local cooling rate during solidification of complex shape part can be expected in its different sections. As it is well known, the thermal profile during solidification and cooling process can significantly affect the local dendritic structure, grain structure, phase composition, thus, resulting in varying local properties over as-solidified parts.

Mar-M247 Ni-based superalloy was chosen as a material for this investigation (see Table 3-1). The tool for physical simulation of investment casting consists of thermal model (see Section 3-2), melting/solidification experiments in a thermo-mechanical simulator (see Section 3-3), and microstructural and mechanical characterization of the melted/solidified specimens (see Sections 3-4 and 3-5) as demonstrated schematically in Fig. 5-1. In the present work, Physical simulation of investment casting began with calculation of the local cooling rates during solidification of NGVs using the ProCAST based thermal model (Fig. 5-1) (see Section 3-2). The outcomes from modeling, namely cooling rates, were served as input parameters for the melting/solidification experiments in the thermo-mechanical simulator Gleeble 3800. Detailed microstructural and mechanical characterization of the melted/solidified specimens provided a databank on the microstructure and hardness of the material depending on the cooling rate. Finally, NGVs casting trials were successfully carried out for validation of the tool (Fig. 5-1) (see Section 3-6). The validation of physical simulation of investment casting occurred with the microstructural and microhardness comparison of NGVs casting trails with Gleeble specimens.

This chapter describes the microstructure of the Gleeble samples compared with the microstructure of the NGV samples. SDAS, grain structure, phase composition and morphology of carbides were analyzed, since these are the main microstructural features determining properties of Ni-based superalloys.

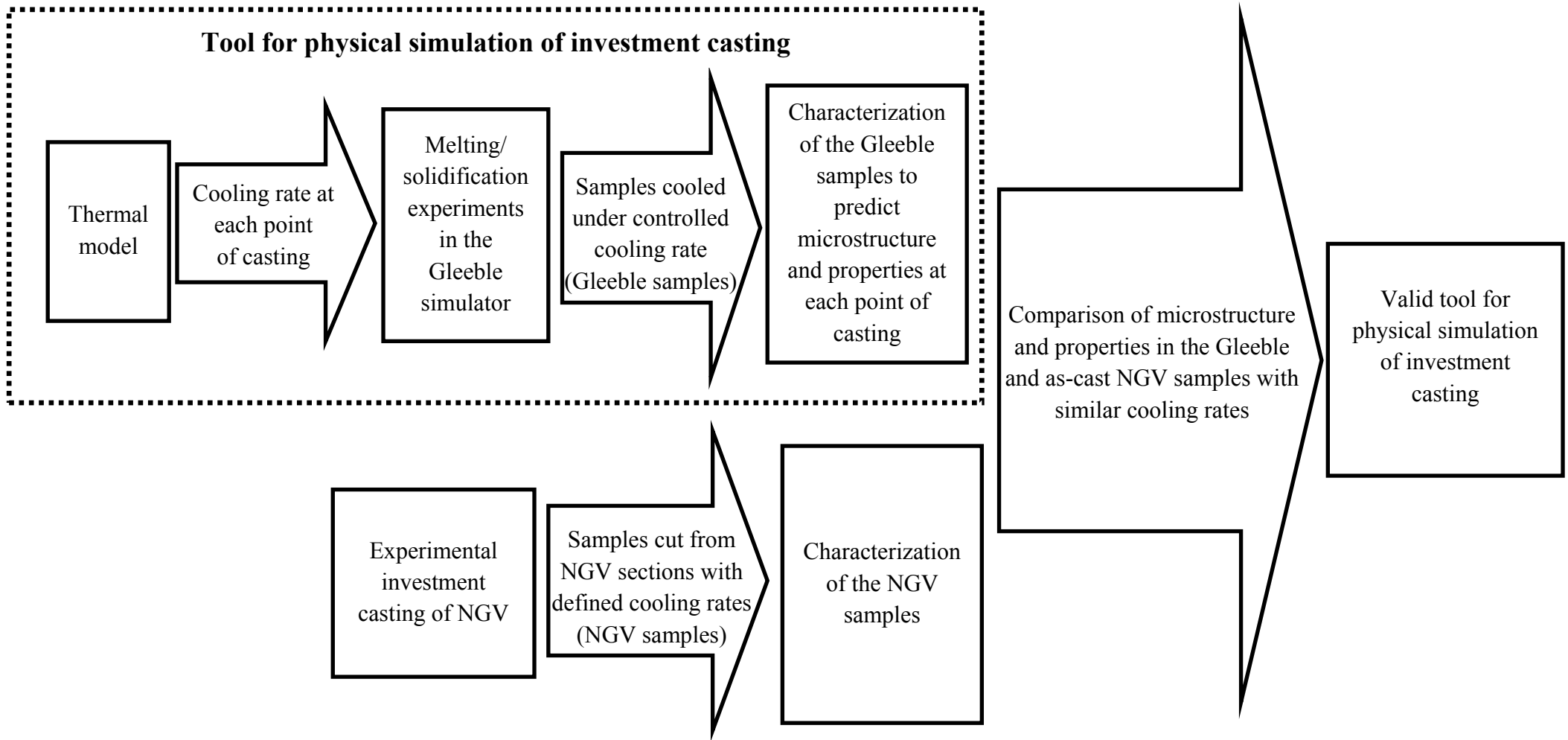


Figure 5-1. Schematic presentation of the tool for physical simulation of investment casting and its validation performed in the present work.

5.1 Secondary dendrite arm spacing

As it is was already described above, SDAS has a strong effect on mechanical strength of the Ni-based superalloys [172]. Figure 5-2 shows dendritic microstructure of the Mar-M247 Ni-based superalloy in the Gleeble samples (left images) and in the NGV samples (right images). It is seen that morphology of dendritic structure in the Gleeble samples (Figs. 5-2 (a,c)) is very similar to that of the NGV samples (Figs. 5-2 (b,d)) at both cooling rates. The results of SDAS measurements are listed in Table 5-1. The SDAS in the Gleeble samples at cooling rate of ~ 0.25 °C/s (70 ± 12 μm) nearly coincides with SDAS in the NGV samples (66 ± 13 μm). A very good accordance of SDAS in the Gleeble samples and in the as-cast NGV samples is also observed for cooling rate of 1 °C/s, 35 ± 8 μm and 39 ± 9 μm , respectively (Table 5-1).

The SDAS-values decrease with increasing cooling rate (Table 5-1) that is in a good agreement with the results reported earlier by Zhang et al. [70] and many other research groups. According to Kurz and Fisher [64], the SDAS is determined by the total time that a given secondary branch spends in contact with the liquid during solidification process (in other words, by local solidification time) because the diffusion coefficient of the solute is significantly larger in the liquid than in the solid. The local solidification time decreases with increasing cooling rate resulting in finer SDAS.



a) Gleeble sample, 0.25 °C/s.



b) NGV sample (transversal section of the solid vane 5 marked by green circle on Fig. 3-7b), 0.25 °C/s.



c) Gleeble sample, 1 °C/s.



d) NGV sample (transversal section of the hollow vane marked by red circle on Fig. 3-7b), 1 °C/s.

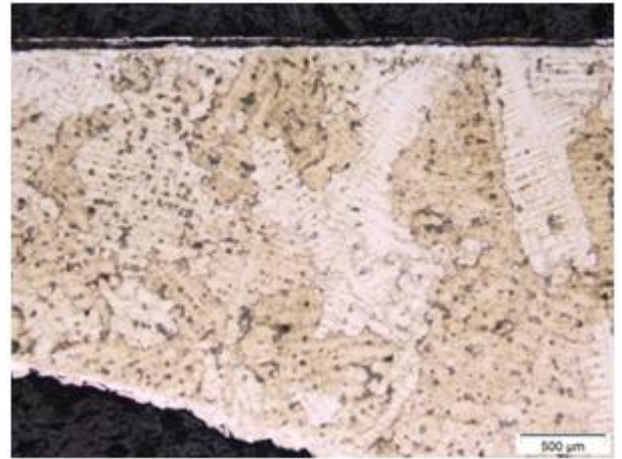
Figure 5-2. Dendritic microstructure of (a, c) the Gleeble samples and (b, d) as-cast NGV samples cooled at (a, b) 0.25 °C/s and (c, d) 1 °C/s.

5.2 Grain structure

Figure 5-3 demonstrates grain structure of the Gleeble samples (Figs. 5-3 (a,c)) and NGV samples (Figs. 5-3 (c,d)) at cooling rates of 0.25 °C/s (Figs. 5-3 (a,b)) and 1 °C/s (Figs. 5-3 (c,d)). It is seen that physical simulation can reproduce well the grain structure of the as-cast NGV at both cooling rates. The average grain sizes in the specimens after physical simulation and in the NGV are in a good accordance. The average grain size tends to decrease with increasing cooling rate, though the values of standard deviation are high, due to large grain size and small number of grains available for quantitative analysis. Comparing the microstructures, it can be also observed that the morphology of the grains is identical too. This observation is confirmed by comparing the average aspect ratios of the grains (Table 5-1). The values of average aspect ratio of 2.10 and 2.36 obtained in the Gleeble samples for the cooling rates of 0.25 and 1 °C/s match perfectly with the values of 2.19 and 2.44 in the as-cast NGV samples. However, the average aspect ratio demonstrates the opposite tendency of the grain size, i.e. it slightly increased with the cooling rate.



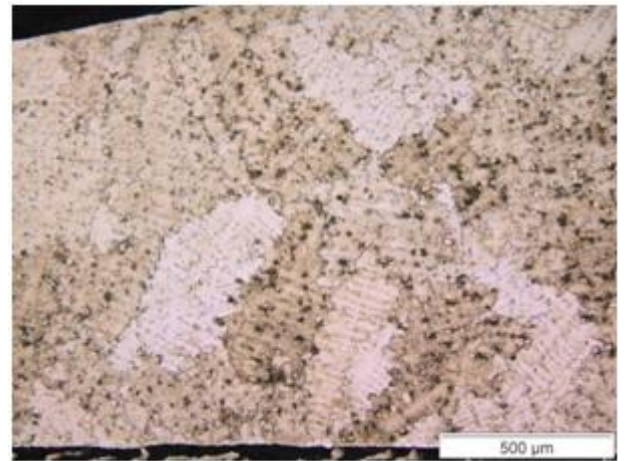
a) Gleeble sample, 0.25 °C/s.



b) NGV sample (transversal section of the solid vane 5 marked by green circle on Fig. 3-7 (b)), 0.25 °C/s.



c) Gleeble sample, 1 °C/s.



d) NGV sample (transversal section of the hollow vane 6 marked by red circle on Fig. 3-7 (b)), 1 °C/s.

Figure 5-3. Grain structure of (a, c) the Gleeble samples and (b, d) as-cast NGV samples cooled at (a, b) 0.25 °C/s and (c, d) 1 °C/s.

5.3 Phase composition

5.3.1 Carbide particles

As it is well known, the morphology, size and volume fraction of carbide particles can strongly affect mechanical strength and creep resistance of Ni-based superalloys [95]. Figure 5-4 depicts the morphology of carbides in the Gleeble samples (Figs. 5-4 (a,c))

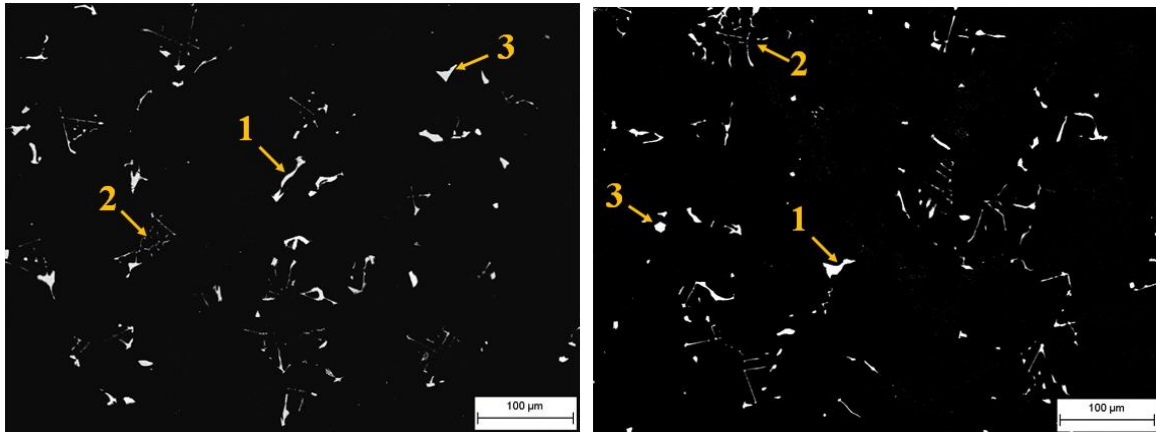
and in the as-cast NGV samples (Figs. 5-4 (b, d)) cooled at 0.25 °C/s (Figs. 5-4 (a,b)) and 1 °C/s (Figs. 5-4 (c,d)).

It is clearly seen that physical simulation reproduces well morphology of carbide particles at both cooling rates. Various types of carbides (script-like, blocky, and carbides of irregular shape) are observed in the microstructure of all studied specimens. Carbides of irregular shape prevail in the specimens cooled at 0.25 °C/s, while script-like carbides dominate in the microstructure of specimens cooled with 1 °C/s. At higher cooling rates carbides tend to transform into strips, since it is the fastest way to access large amounts of carbide-forming elements.

Table 5-1. Results of microstructural characterization and microhardness measurements of the Gleeble and NGV samples.

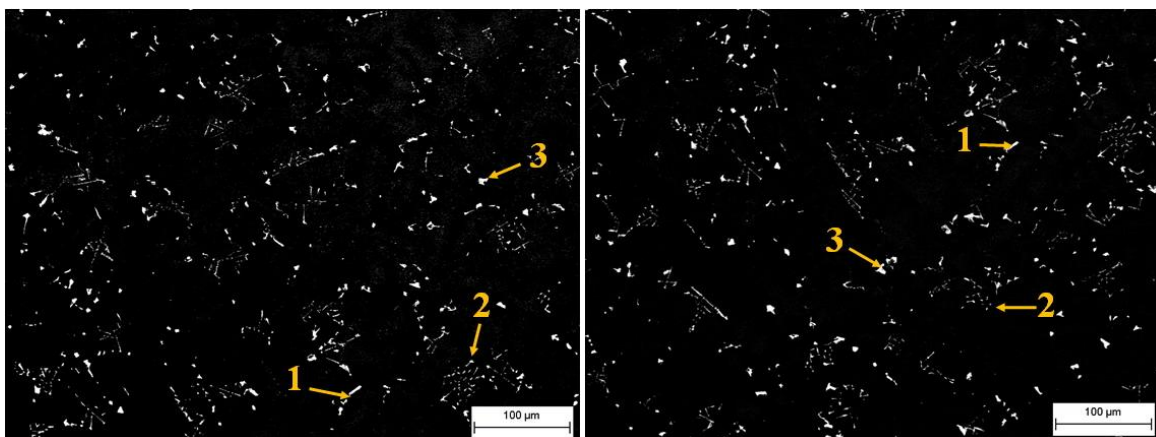
Processing		<i>Gleeble samples</i>		<i>NGV samples</i>		
Cooling rate (°C/s)		0.25	1	0.25	1	
SDAS	(μm)	70 \pm 12	35 \pm 8	66 \pm 13	39 \pm 9	
Grain structure	grain size (μm)	1279 \pm 347	1050 \pm 284	1264 \pm 693	1018 \pm 437	
	aspect ratio	2.1	2.36	2.19	2.44	
Phase composition	Carbide	size (μm)	8 \pm 2	4 \pm 2	7 \pm 3	4 \pm 2
		volume fraction (%)	1.1	1.8	1.2	1.7
		inter-particle spacing λ (μm)	23 \pm 4	9 \pm 1	18 \pm 2	9 \pm 1
	γ/γ' eutectic	volume fraction (%)	10.4	3.4	10.2	3.2
		size (μm)	44 \pm 9	24 \pm 5	41 \pm 8	23 \pm 6
Microhardness	(HV)	382 \pm 20	408 \pm 15	381 \pm 16	415 \pm 7	

Further growth and coalescence of these fine strips leads to formation of script-like carbides as observed in the Gleeble and NGV samples cooled at 1 °C/s (Figs. 5-4 (c,d)). At low cooling rates, the carbides tend to have equilibrium morphology (in shape of octahedron) in order to minimize carbide-liquid interface energy [114]. The cooling rate of 0.25 °C/s is still too high for formation of carbides with equilibrium morphology, so carbides of irregular shapes are mainly formed at this cooling rate.



a) Gleeble sample, 0.25 °C/s.

b) NGV sample (transversal section of solid vane marked by green circle on Fig. 3-7 (b)), 0.25 °C/s.



c) Gleeble sample, 1 °C/s.

d) NGV sample (transversal section of hollow vane marked by red arrow on Fig. 3-7 (b)), 1 °C/s.

Figure 5-4. The carbide characteristics of (a, c) the Gleeble samples and (b, d) as-cast NGV samples cooled at (a, b) 0.25 °C/s and (c, d) 1 °C/s. 1 - carbides of irregular shape, 2 - script-like carbides, 3 - blocky carbides.

Chapter 5

The reduction of cooling rate results in reduction of average carbide size and inter-particle spacing in the as-cast NGV, and this is also well captured in physical simulation (Table 5-1). Volume fraction of carbide particles in the as-cast NGV samples tends to increase from 1.2 % to 1.70 % with increasing cooling rate, which is also reproduced by physical simulation, where it increases from 1.1 % to 1.8 % (Table 5-1). It can be rationalized based on reduction of time for diffusion of alloying elements (in other words, carbide growth time) with increasing cooling rate. Smaller SDAS at higher cooling rates results in reduction of carbide inter-particle spacing, since according to He et al. [99], interdendritic areas are preferred location for segregation of carbide forming elements and carbide formation in Ni-based superalloys (Fig. 5-5). Formation of larger number of carbide nuclei together with the smaller interdendritic area could be the reason for increasing carbide volume fraction with increasing cooling rate.

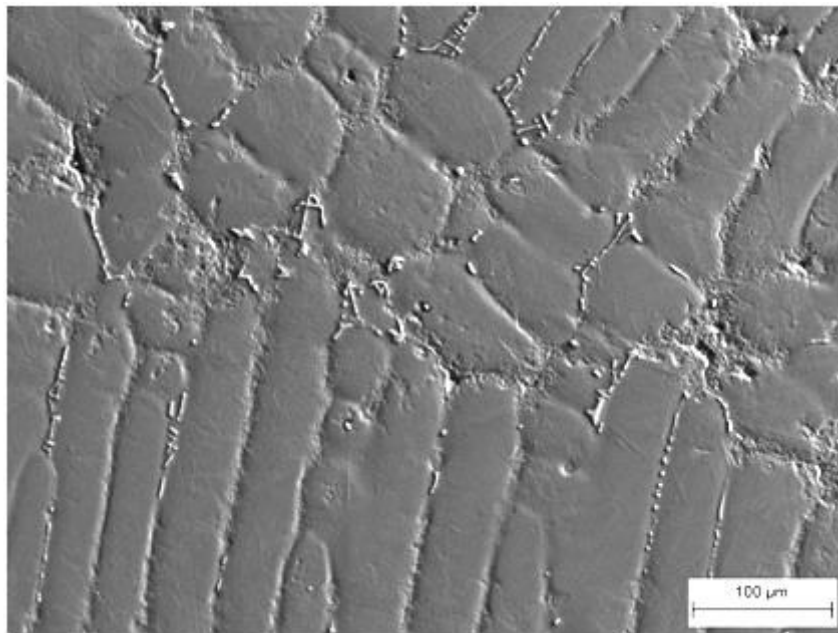
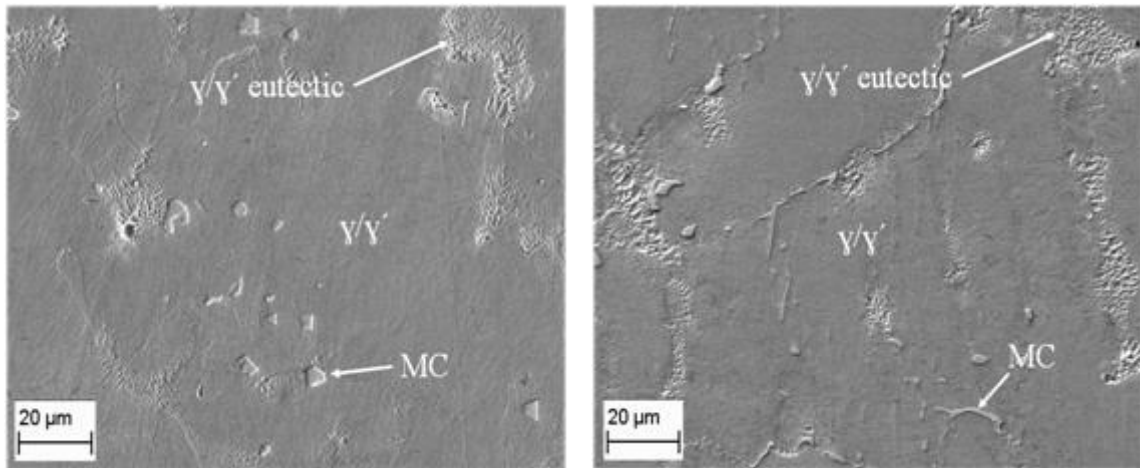


Figure 5-5. Carbides in inter-dendritic area of the specimen after physical simulation with cooling rate of 1 °C/s (some carbides are marked by white arrows).

5.3.2 The γ/γ' eutectic

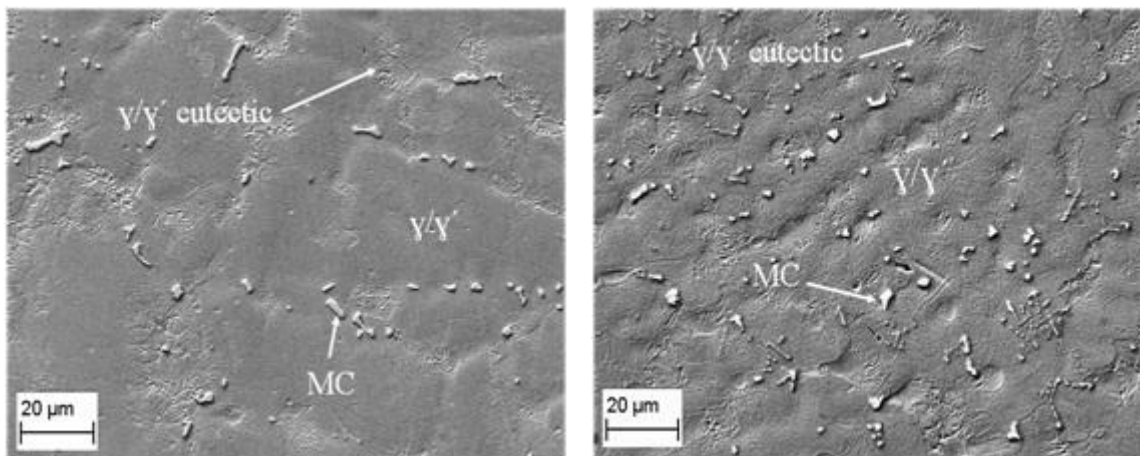
In Ni-based superalloys, γ/γ' eutectic is a non-equilibrium solidification micro constituent caused by segregation of eutectic forming elements such as Ti and Al in interdendritic areas during solidification process [120]. Formation of γ/γ' eutectic pools

is controlled by chemical composition of the alloy and cooling rate during alloy solidification. Figure 5-6 illustrates their morphology observed in the Gleeble specimens (Figs. 5-6 (a,c)) and in the as-cast NGV samples (Figs. 5-6 (b,d)) cooled at 0.25 °C/s (Figs. 5-6 (a,b)) and 1 °C/s (Figs. 5-6 (c,d)).



a) Gleeble sample, 0.25 °C/s.

b) NGV sample (transversal section of solid vane marked by green circle on Fig. 3-7b), 0.25 °C/s.



c) Gleeble sample, 1 °C/s.

d) NGV sample (transversal section of hollow vane marked by red arrow on Fig. 3-7b), 1 °C/s.

Figure 5-6. Microstructure of the (a, c) the Gleeble samples and (b, d) as-cast NGV samples cooled at (a, b) 0.25 °C/s and (c, d) 1 °C/s.

The results of their quantitative analysis are listed in Table 5-1. It is seen that physical simulation (Gleeble samples) can very well predict morphology, size and volume

fraction of γ/γ' eutectic pools in the as-cast NGV at both cooling rates. Their average size decreases from $41\pm 8\ \mu\text{m}$ to $23\pm 6\ \mu\text{m}$ with increasing cooling rate in the as-cast NGV, that matches well with the outcomes of physical simulation (Gleeble samples), where it drops from $44\pm 9\ \mu\text{m}$ to $24\pm 5\ \mu\text{m}$ (Table 5-1). Similar trend is shown by volume fraction of γ/γ' eutectic phase. Gleeble samples predict its reduction from 10.4 % to 3.4 % with increasing cooling rate, which is in a very good accordance with the results for the as-cast NGV, 10.2 % and 3.2 %, respectively (Table 5-1). As demonstrated by Liu et al. [61], higher cooling rates result in dendrite refinement leading to lower amount of segregations and smaller eutectic pools. It should be noted that no γ/γ' eutectic was observed in the Mar-M247 Ni-based superalloy after physical simulation with cooling rate of 1 °C/s in our previous work [165]. This discrepancy in results can be related to possible variations in chemical composition (especially in content of the eutectic forming elements) of the studied material.

5.4 Microhardness

The results of microhardness measurements on all studied specimens are listed in Table 5-1. A very good agreement between microhardness data measured on the as-cast NGV and on specimens after physical simulation can be noted. It is seen that the average microhardness values increase with increasing cooling rate from 381 HV to 415 HV and from 382 HV to 408 HV in the as-cast NGV and Gleeble samples, respectively. This result can be expected; since microhardness is governed by microstructural features which were very well reproduced in physical simulation (see Sections 5.1-5.3). Reduction of SDAS with increasing cooling rate (see Section 5.1) improves strength, as was shown by Milenkovic et al. [173]. Finer carbides, higher carbide volume fraction and lower inter-particle spacing in the specimens cooled at higher cooling rate also result in contribution to higher particle strengthening. It should be noted that grain size effect on strength of the material cannot be analyzed in this case, since grains (having size $> 1\ \text{mm}$, Table 5-1) are much larger than the diameter of plastic zone in microhardness testing ($\sim 100\ \mu\text{m}$).

5.5 Advantages of application of physical simulation in development of new investment casting process

The present work clearly demonstrates that physical simulation of investment casting can precisely predict the local microstructure and properties in the complex shape parts produced via investment casting. Therefore, physical simulation can be of great help in development of new investment casting process (investment casting process using new material or investment casting process of new complex shape parts). Following advantages of application of physical simulation can be noted:

1) Reduction of material amount required for development of new investment casting process. Significant amount of material typically goes in waste in numerous experimental casting trials required for development of new manufacturing process. The related costs can be very high if expensive materials, as Ni-based superalloys, are used in the investment casting process. Very small specimens used in physical simulation greatly reduce the amount of material required for development of the casting process, thus, reducing its cost.

2) Higher efficiency of experimental work in development of new investment casting process. In the 'trial-and-error' approach, as-cast complex shape parts are typically sectioned into small specimens, and careful microstructural analysis is performed in all sections in order to analyze the local microstructure. Such microstructural analysis is especially important in the case of multiphase materials, where significant variations of local solidification conditions can result in significant variations of local phase composition and, thus, local properties of the complex shape part. Application of physical simulation can significantly increase the efficiency of experimental work: The range of local solidification conditions (i.e. cooling rates) in casting process can be determined by thermal model and further reproduced in the thermo-mechanical simulator. Detailed microstructural analysis of the specimens after physical simulation yields a databank of microstructures present in the as-cast complex shape part. This databank can also be extended to include information on mechanical and/or functional properties of these microstructures, which can be studied using specimens after physical simulation.

3) Direct impact on quality of final product. The as-cast complex shape parts are often subjected to additional homogenization thermal treatments. The obtained data-bank can

be utilized for choosing the optimum parameters of thermal treatments which can improve the quality of final product. For example, the γ/γ' eutectic (which is often formed in Ni-based superalloys solidified at low cooling rates) reduces strength of the material, as it was already discussed in Section 4.1.4 above [122], and homogenization heat treatment is applied for dissolution of this microconstituent. The areas containing such phases can be missed in microstructural analysis of the sectioned complex shape part, whereas it will be definitely revealed in microstructural analysis of the specimens after physical simulation. The correct choice of thermal treatment parameters for complete dissolution of non-desirable microstructural elements will allow tailoring local microstructures and properties in the as-cast complex shape parts in order to avoid any 'weakest link' in the structure.

5.6 Conclusions

- 1) Combination of thermal modeling with melting/solidification under controlled cooling rate in thermo-mechanical simulator yields physical simulation of investment casting of complex shape parts. In physical simulation, the local cooling rate during solidification at each point of cast is predicted via thermal modeling. Melting/solidification experiments are carried out under controlled cooling rates determined by the model. Further microstructural and mechanical characterization of the specimens after melting/solidification experiments provides the information on the local microstructure and mechanical properties at each point of the as-cast complex shape part.
- 2) Physical simulation of investment casting of NGV from MAR-M247 Ni-based superalloy was performed for selected areas of NGV. It is demonstrated that physical simulation predicts well the local SDAS, grain structure, phase composition, morphology of carbide particles and microhardness.
- 3) Physical simulation of investment casting has numerous advantages over standard trial-and-error approach for development of new investment casting process. It leads to higher efficiency of experimental work and to reduction of material's amount required for development of the new investment casting process, as well as it improves quality of the final product.

6 Physical simulation of skin formation during investment casting of NGVs from Mar-M247

Solidification of the Nickel-based superalloys in investment casting usually begins with the skin formation due to freezing of the melt got in contact with the ceramic shell having a temperature well below solidification range. Skin, first studied by Suzuki et al. [174], plays a critical role for manufacturing high-quality casting products, since the formation of thick skin results in misrun in complex and thin investment casting parts. There is a body of research concerning the formation mechanism and characteristics of skin formed in Al and Mg alloys [174–178]. It is reported that skin exhibits higher hardness due to the prevalence of small grains along with saturation of alloying elements as well as existence of intermetallics [175–180]. Although, Barresi et al. mentioned the continuous structure for skin [181], Chen showed that it is dynamic and depends on casting conditions (mould temperature, mould geometry, melt temperature, cooling conditions, etc.) in high pressure die casting of the Al alloy [174]. Chen demonstrated that skin is not continuous in a casting, as skin cannot be found at the area where the temperature of mould is close to melting point, in other words, the skin formation is attributed to the temperature in the mould-melt interface at which skin

formed [174]. In addition, Tsumagari et al. [178] found out that both thermal and flow conditions in the vicinity of die surfaces can affect the skin, but they could not identify the skin formation mechanism. Later, Chen [174] made an effort to understand the forming mechanism of the skin, referred as the surface layer, in the high pressure die casting of Al alloy. In order to understand the effect of thermal variables on the skin formation, casting experiments were established with two dies, differing in thickness and shape, which resulted in different thermal and flow conditions. However, the die surface temperature and melting temperature after contact with the mould could not be determined. On the other hand, the skin thicknesses were compared for estimated time of 0.15 s, solidification time under pressure intensification in high pressure die casting, seemed not to be the accurate time of skin formation. Moreover, the skin thickness was calculated by the equation in which temperature variable were specified based on estimation which had not been validated.

Yang et al. observed that skin in Mg-La alloy is much more uniform and continuous than in the Mg-Al alloys. Moreover, the thickness and hardness of skin of Mg alloys are governed by chemical composition, as adding 3.4 mass% of La to Mg alloy both mentioned characters will be promoted [175].

The skin formation in the continuously cast rods of a GMR 235 Ni-based superalloy was investigated by Zupanic et al. [182]. Two kinds of skin, including dynamic and static skin, were recognized from which dynamic skin grows during rod movement in the opposite direction of drawing stroke, whereas static skin, growing in the casting direction, will not move upon drawing stroke [182].

However, there is no study related to the skin formation in investment casting of Ni-based superalloys. Considering the importance of controlling skin thickness and microstructure especially in the thin and complex parts such as NGVs, this section aims to have the deeper insight on the skin microstructure and variation of that in different thermal condition. Achieving this purpose the effect of mould temperature and melting cooling rate on skin microstructure and hardness were assessed. Therefore, microstructural characterization was performed by OM, SEM, EDX and EBSD. Also the nanoindentation technique was employed to measure hardness of skin at various thermal conditions.

6.1 Development of the tool for physical simulation of skin formation

Mar-M247 Ni-based superalloy was chosen as the material for this investigation (see Table 3-1). The tool for physical simulation of skin formation consists of thermal model (see Section 3-2), melting/solidification experiments in Gleeble 3800 thermo-mechanical simulator (see Section 3-3), and microstructural and mechanical characterization of the melted/solidified specimens. The outcomes from thermal model, namely cooling rates, served as input parameters for the melting/solidification experiments in the thermo-mechanical simulator Gleeble 3800.

In physical simulation of casting process using a GLEEBLE system, the liquid melt zone is usually contained in a tube made from quartz, as was described in previous chapters, or metallic materials such as copper, carried out by Schendera et al. (2003) [183]. To study the effect of casting conditions on the skin formation, a ceramic tube should be made from the same material used for fabrication of ceramic moulds in industrial casting processes. In this part of thesis, a special technique was developed for fabrication of ceramic tubes for melting/solidification experiments using the GLEEBLE systems by project partners from Precicast Bilbao.

Fifteen wax patterns in form of tubes having a diameter of 10 mm and a height of 300 mm were prepared and assembled on a H-shaped runner as shown on Fig. 6-1. The wax patterns were manually dipped into ceramic slurry, which is used for fabrication of ceramic moulds for industrial investment casting, and then dried for 4 h. This operation was repeated, so two primary coats were formed with the total thickness of ~2 mm. Five reinforcement coats were added by automatic dipping of the assembly and drying for 5 h between coats. Thus obtained ceramic clusters were placed into an autoclave at specified pressure in the temperature range of 150-200 °C for dewaxing. To burn the wax remains, the hollow ceramic tubes were heat treated at 900 °C for 1 h. Finally, these ceramic tubes were cut into shorter ones having a length of 30 mm. The final internal diameter of the ceramic tubes was 10.2 mm and the outer diameter was ~36 mm Fig. 6-2. A slot of 3 mm was cut in each ceramic tube for the thermocouple controlling specimen temperature. A 'hole' was drilled in the midsection of each ceramic tube for a thermocouple measure the temperature of the ceramic tube at the outer surface of the primary coat as sketched in.



Figure 6-1. The wax tubes utilized for ceramic tube production.



Figure 6-2. Ceramic tubes used in physical simulation of skin formation.

The rod shape sample (Fig. 3-8), made of the Mar-M247 Ni-based superalloy, was used in this study. Two various kinds of thermocouples, R and K type thermocouples, were employed for temperature measurements during melting/solidification experiments by Gleeble. According to the Fig. 6-3 (a), R-type thermocouple was welded at the midsection of sample to control the specimen temperature during experiment. A slot of 2 mm was cut in each ceramic tube for this R-type thermocouple (Fig. 2b). A 2 mm 'hole' was drilled in the midsection of each ceramic tube for passing K-type thermocouple measuring the temperature of the ceramic tube at the outer surface of the primary coat, at the 0.9 mm distance from mould-sample interface, as sketched in Fig. 2b. According to the Fig. 2c, both R and K-type thermocouple wires were fixed by cement to the surface of the ceramic tube.

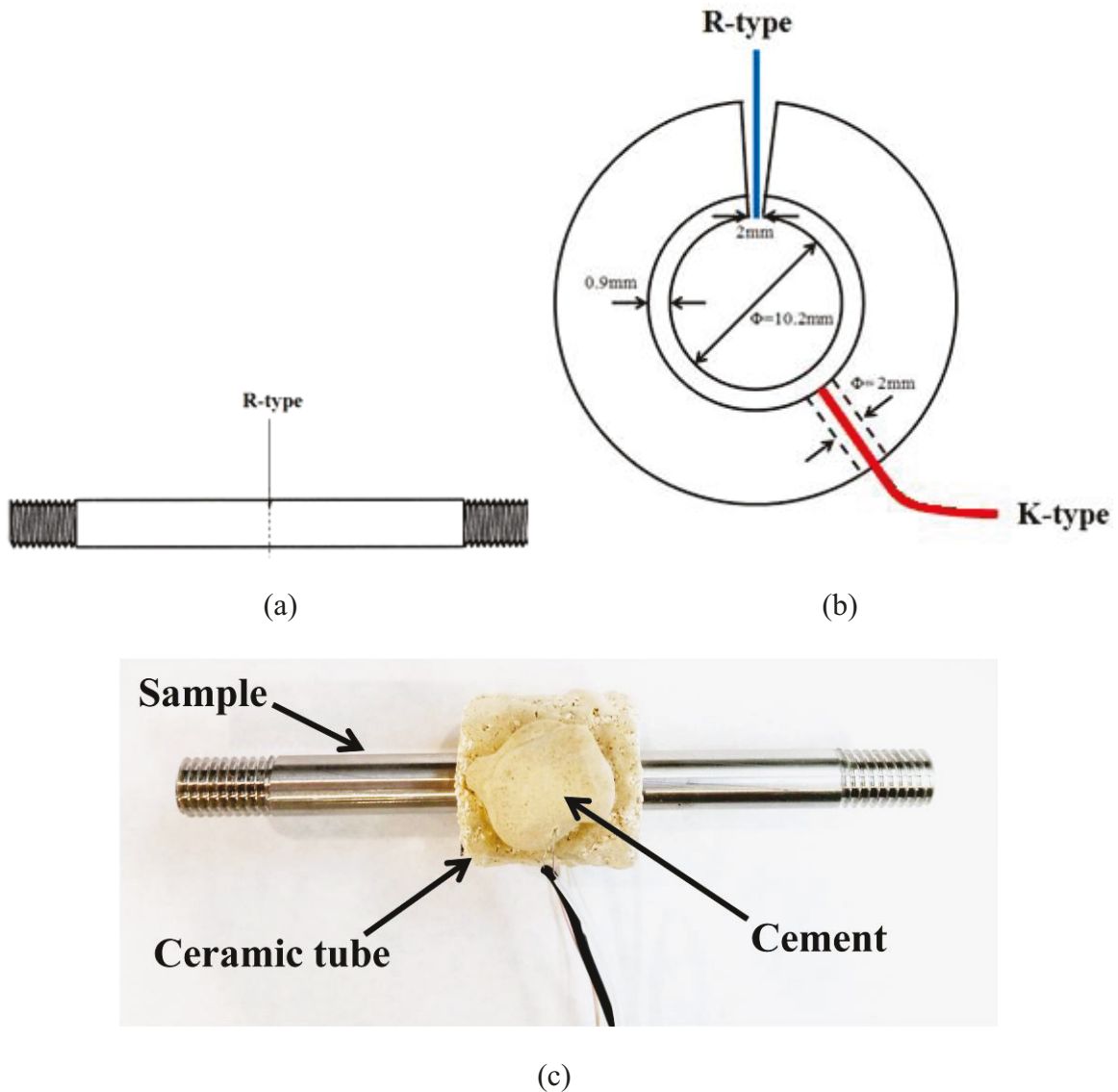


Figure 6-3. a) Schematic presentation of a R-type thermocouple joined to the midsection of rod, b) Schematic presentation of transversal section of rod, ceramic tube, with slot and hole and location of thermocouples at the midsection of experimental set, c) Appearance of the sample with ceramic tube and fixed thermocouples.

The experimental setup, being ready for physical simulation of skin formation by Gleeble 3800 system in argon atmosphere, is depicted in Fig. 6-4.

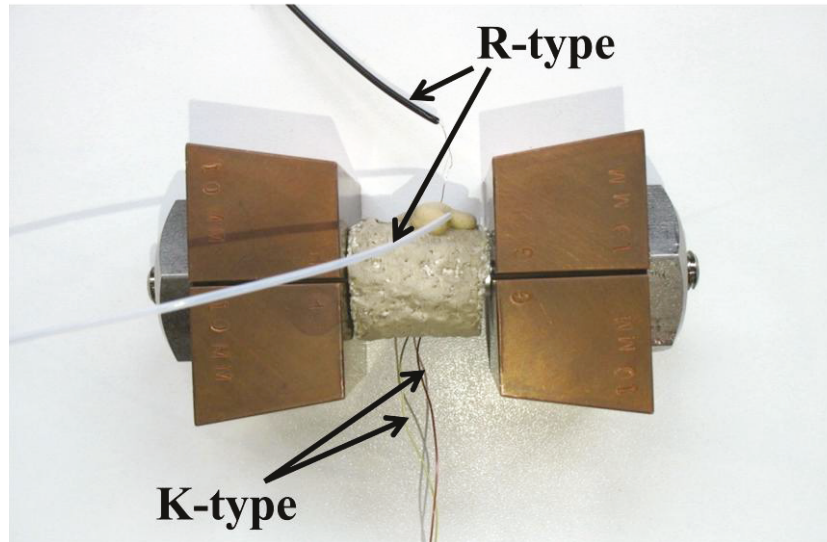


Figure 6-4. The experimental setup used for the physical simulation of skin formation.

Three different cooling rates and ceramic tube temperatures were examined (Table 6.1). For the confirmation of reliability of the results, three samples were tested for each condition and it was found that the results are reproducible. The microstructural investigation was done applying OM, SEM, EDX and EBSD (see chapter 3). Since the thickness of skins is in the range of 30-90 microns, nanoindentation technique was utilized for hardness measurement (see section 3.5.2). For each obtained sample, three various areas were defined and the reported results are the average of 30 nanoindentation tests for each area. Detailed microstructural and mechanical characterization of the melted/solidified specimens provided a databank on the microstructure and hardness of the material depending on the cooling rate. Finally, skin microstructure and hardness of experimental casting trials, produced according the detailed explanation of Section 3-6, were compared with Gleeble specimens to validate the physical simulation of skin formation tool.

6.1.1 Effect of thermal variable on skin formation

6.1.1.1 Effect of contact time (ceramic tube temperature) on the skin formation

To evaluate the effect of ceramic tube temperature on the thickness of skin formed in investment casting process, three various heating regimes were used (Fig. 6-5). The idea

is that varying the contact time of hot sample and ceramic tube, various temperatures can be reached in ceramic tube, as longer contact time of hot sample and ceramic tube resulted in higher temperature of ceramic tube and vice versa. Figure 6-5 shows three different heating regimes, the main differences of which are the variation of contact time between hot sample and ceramic tube resulting in different temperatures of the latter.

The short contact time heating regime was designed for lowest ceramic tube temperature where the sample was heated with the rate of 40 °C/s from ambient temperature to 1355-1360 °C and was held at this temperature for 10 s (Fig. 6-5 (a)). The second heating regime named medium contact time (Fig. 6-5 (b)) at which the heating rate in the temperature range of 1240-1360 °C, was dropped to 2 °C/s and then sample was kept for 10 s at 1360 °C. The long contact time heating regime, considered for highest ceramic tube temperature, was carried out by heating specimen with the rate of 0.5 °C/s from 1280 to 1355-1360 °C/s along with keeping sample in contact with ceramic tube at 1355-1360 °C/s for 320 s (Fig. 6-5 (c)).

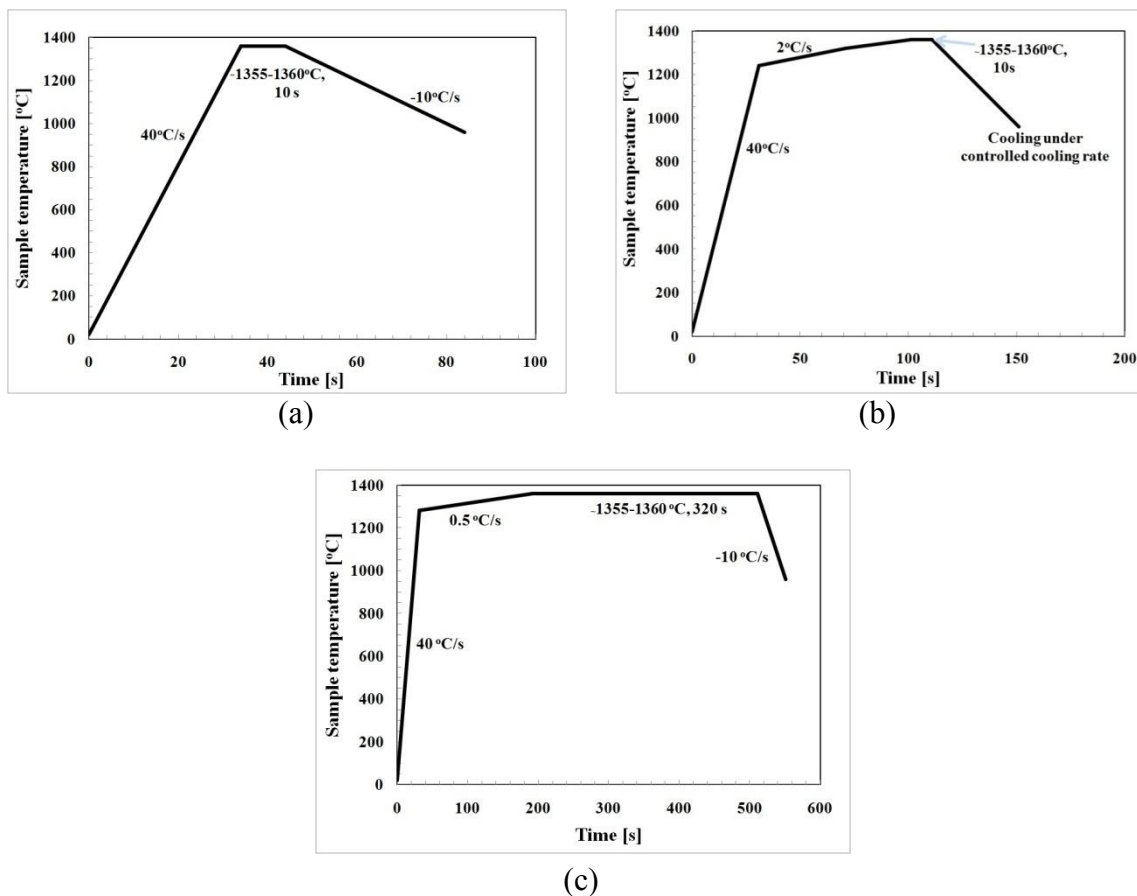


Figure 6-5. Heating regimes used to control ceramic tube temperature.

Chapter 6

Considering the Fig. 6-6 (a), short contact time led to generation of temperature well below of 1000 °C in the 0.9 mm distance from the sample-ceramic tube interface. While, at medium contact time regime the ceramic tube was heated up to ~1030 °C at the same point of ceramic tube (Fig. 6-6 (b)). Unfortunately, the long contact time experiment was not successful, as the thermocouple was detached due to high temperature exposure of welded joint for the long time. Nevertheless, with the extrapolation of existing data, it could be assumed that the ceramic tube was heated up to the solidification temperature range of superalloy at the mentioned point of ceramic tube before beginning the solidification process (Fig 6-6 (c)).

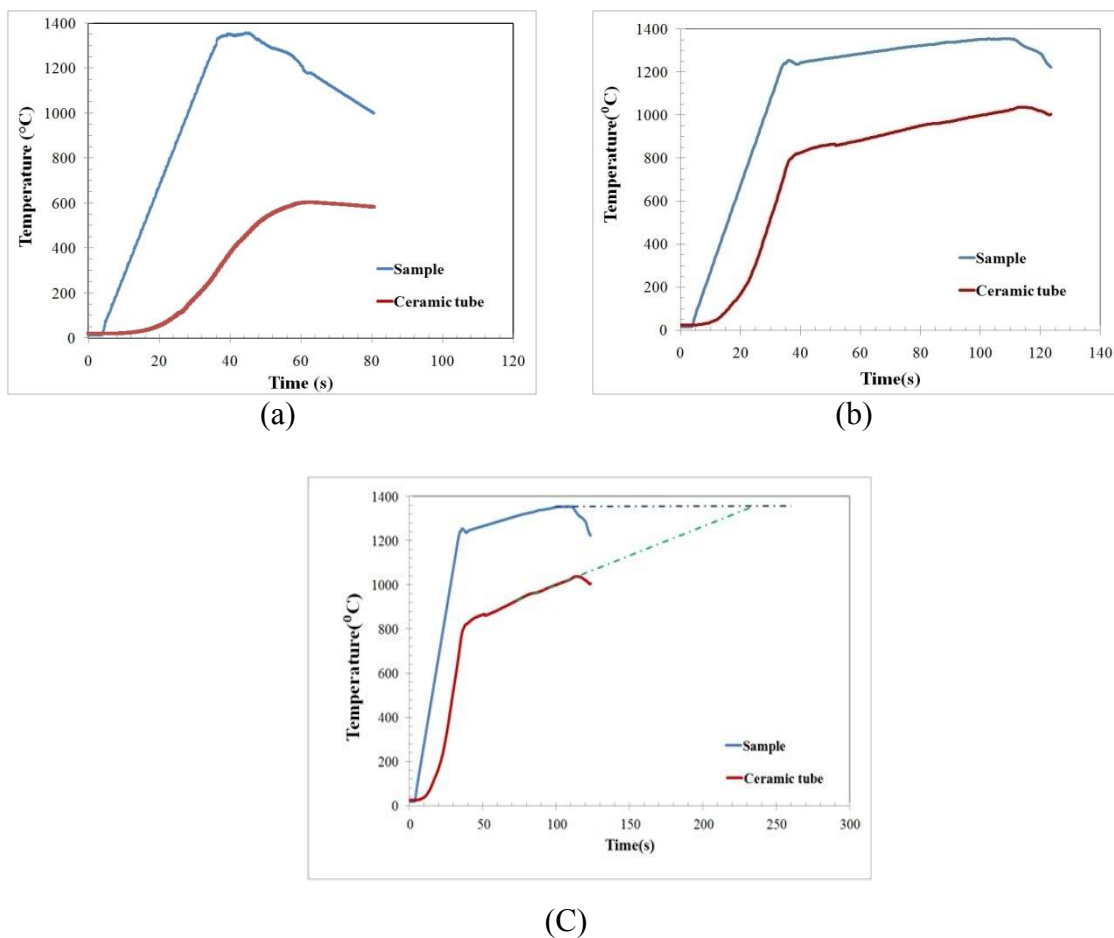


Figure 6-6. Temperature-time plots of samples and ceramic tubes for a) short contact time, b) medium contact time and c) long contact time regimes.

In order to reveal the effect of ceramic tube temperature on the skin microstructure of the alloy, similar solidification conditions were applied for all heating regimes, and all samples were cooled down to room temperature with the constant cooling rate of 10

°C/s (Fig. 6-5). The effect of ceramic tube temperature on skin formation is depicted in Fig. 6-7. It is clearly observed that in the case if temperature of ceramic tube does not exceed 1030 °C (short and medium contact time), solidification of melt begins with formation of skin followed by growth of dendrites from skin (Fig. 6-5 (a, b)). It should be noted that skin thickness decreases from 104 μm to 32 μm with increasing mold temperature due to lower undercooling (Fig. 6-7). However, if the temperature of ceramic tube reaches the solidification temperature range (long contact time), no skin is formed and dendrites are formed and grow directly from contact area with ceramic tube, since undercooling is not sufficient for freezing of melt (Fig. 6-7 (c)). These observations are in a good agreement with the study of Chen, who demonstrated that the thickness of skin, formed at mould/specimen interface, depends on the temperature of mould [174].

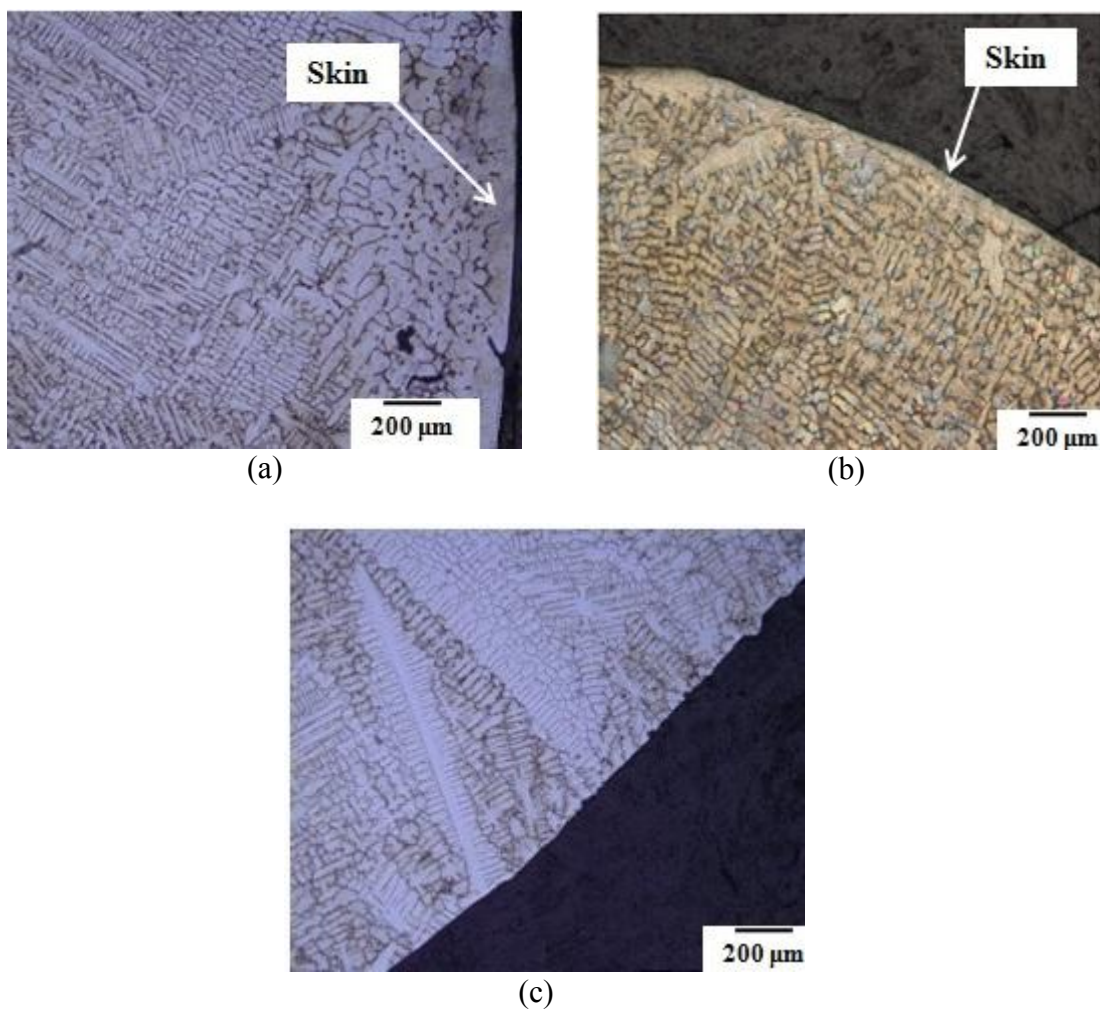


Figure 6-7. The skin formation at various ceramic tube temperatures, a) $T_{tube} \ll 1000$ °C, b) $T_{tube} \sim 1030$ °C and c) $T_{tube} \sim T_{solidification\ range}$.

It should be noted that the temperature of ceramic tube at medium contact time, being ~1030 °C, is in the good accordance with the temperature of the ceramic mould in investment casting of Ni-based superalloys reported between 1000 and 1150 °C. Consequently, the medium contact time heating regime was chosen as an appropriate heating regime for the further investigations of the effect of cooling rate on the skin characteristics.

6.1.1.2 Effect of cooling rate on the skin formation

The effects of cooling rates on the skin microstructure were assessed at 0.25, 1 and 10 °C/s cooling rates (Table 6-1). The skin thickness varies at different cooling rates and it reduces from 92 to 30 µm with increasing cooling rates from 0.25 to 10 °C/s as illustrated in Fig. 6-8 and Table 6-1.

Table 6-1. Thermal variables applied in physical simulation of skin formation.

Temperature of ceramic tube (°C)	<<1000 °C	1030 °C			Near melt <i>T</i>
Cooling rate (°C/s)	10	0.25	1	10	10
Thickness (µm)	104	92	82	30	0

Although, formation of skin strongly depends on the adequate undercooling resulting in freezing phenomenon, the skin growth is a diffusion controlled process [184]. Therefore, observed differences in skin thickness can be interpreted based on changing diffusion with cooling rate. Since increasing cooling rate decreases the diffusion time of elements, the growth rate of skin reduced with the increment of cooling rate.

Since the prevailing cooling rates during solidification of NGVs are in the range of 0.25-1 °C/s, physical simulation of investment casting of skin formation will be focused on these cooling rates as we have more possibility for the experimental validation of physical simulation tool.

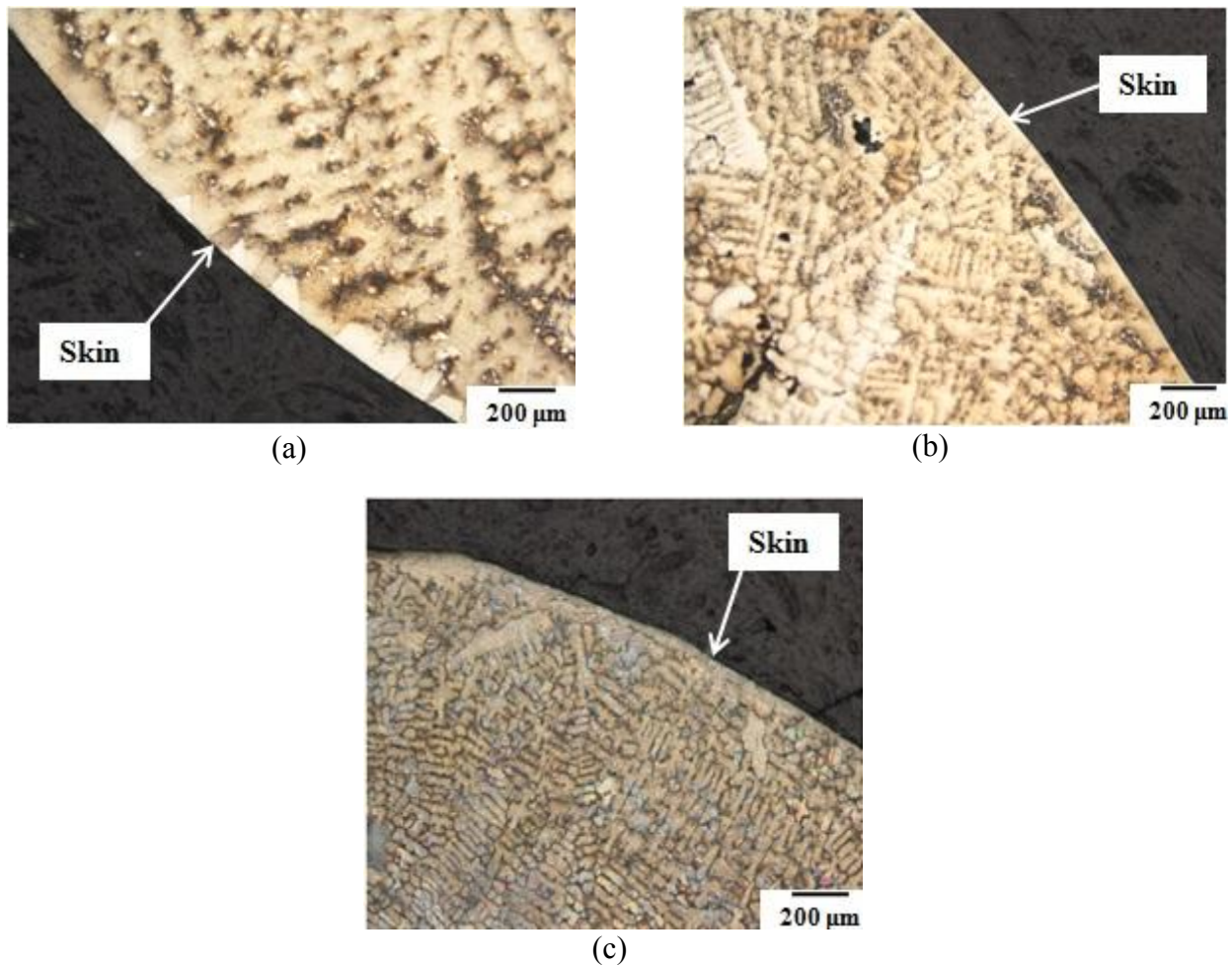


Figure 6-8. Morphology of skin in Mar-M247 alloy at a) 0.25, b) 1 and c) 10 °C/s cooling rates.

6.1.2 Validation of physical simulation of skin formation (microstructural and nanohardness study)

6.1.2.1 OM and SEM investigation of skin

As it was mentioned above, the skin microstructure might have a significant influence on the quality of as-cast thin complex shape parts. To demonstrate the reliability of physical simulation as a comprehensive tool for the prediction of skin characteristics in complex shape parts produced by investment casting process, the validation of Gleeble parts via comparing with the NGVs casting trails is considered. The validation process consists of the gathering of skin characteristics of Gleeble and NGV specimens, produced at various thermal conditions, and the comparison of their properties to determine the degree of discrepancy.

Chapter 6

The optical microscopy evaluation is the first stage for the validation of physical simulation of skin formation. The skin can be easily recognized at Fig. 6-9, as it surrounds the surface of specimens and has a microstructure different from the interior one (Fig. 6-9). According to the Table 6-2, the skin thickness decreases from 92 to 82 μm in the Gleeble specimens with increasing cooling rate from 0.25 to 1 $^{\circ}\text{C}/\text{s}$ (Figs. 6-9 (a, b)). As noticed above, although skin formation strongly depends on the undercooling, skin growth is governed by the diffusion. Therefore, skin growth is shortened with rising cooling rate resulting in decreasing diffusion time. The same trend is observed for NGV parts cooled at this condition, as the thickness of skin decreases from 95 to 83 μm because of rising cooling rate from 0.25 to 1 $^{\circ}\text{C}/\text{s}$ (Figs. 6-9 (c, d)). On the other hand, it is indicated by Fig. (6-9) that the skin thickness in the Gleeble samples is in a very good agreement with that in the NGVs specimens at both cooling rates (Table 6-2). Therefore, it can be concluded that physical simulation method could precisely imitate the skin thickness of Mar-M247 Ni-based superalloy at both cooling rates.

Phase composition of skin was studied in SEM. Fig. 6-10 (a, b) illustrates skin microstructure. No eutectic phase is present in skin. This observation can be explained by the freezing of melt with very high solidification rate as a skin formation mechanism. It is known that the volume fraction and the size of γ/γ' eutectic pools decreases with increasing cooling rate [31,61,120], and rapid solidification can fully suppress formation of eutectic phase. Similar microstructure is formed in the NGVs specimens, where eutectic phase is not observed in skin (Fig. 6-10 (c, d)). No carbides are seen in the skin of Gleeble samples, that can be also explained by high cooling rate suppressing carbide precipitation (Figs. 6-10 (a, b)). It should be noted that a few carbides, observed in skin of the as-cast NGVs (Figs. 6-10 (c, d)), might be coming from the primary ingot used for melting. Regardless of partial dissolution of carbides during melting, complete solution of them cannot take place because the melting temperature of carbides is much higher than the melting point of superalloys.

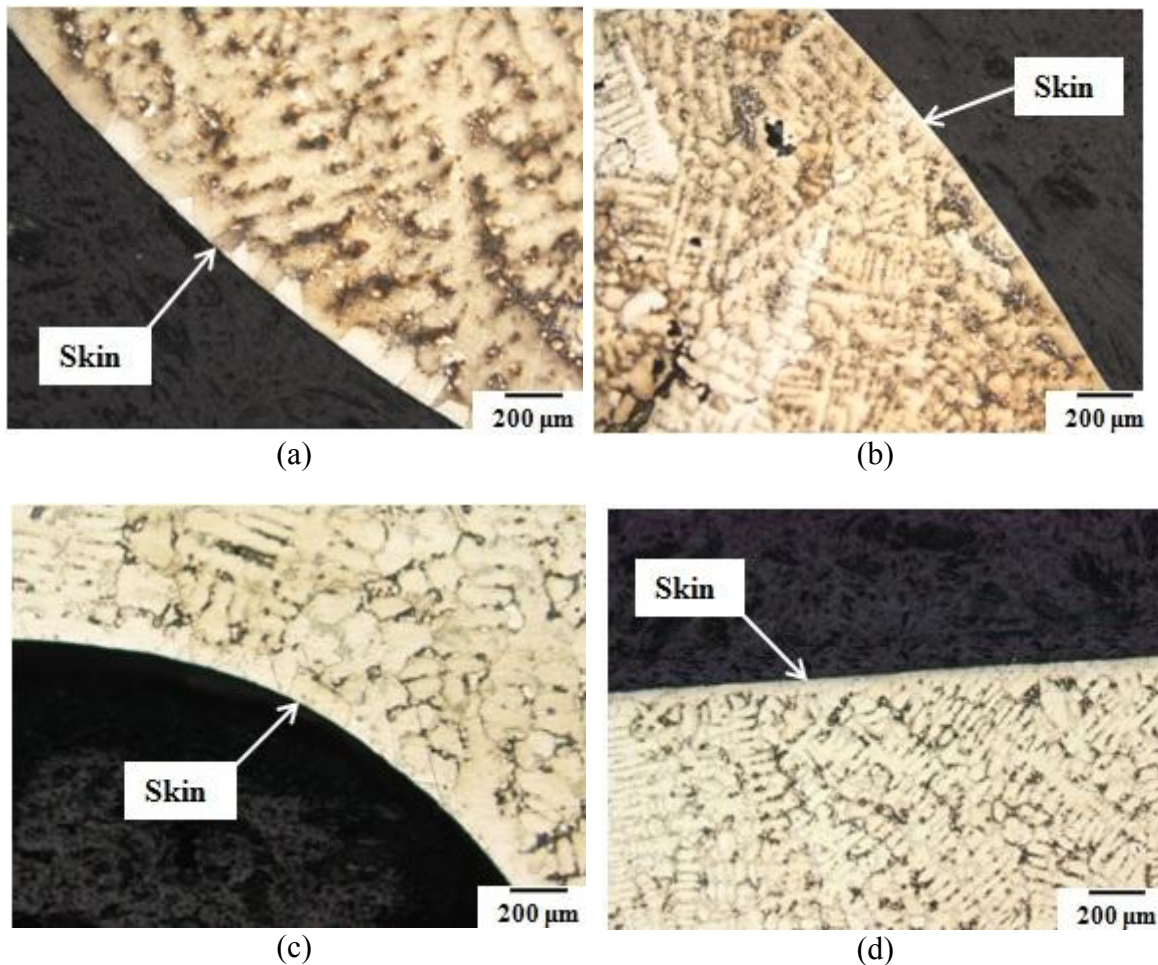


Figure 6-9. Optical microstructures of formed skin using Gleeble (a,b) and in NGV part (c,d) cooled at: (a,c) 0.25 °C/s, (b,d) 1 °C/s.

As shown in Table 6-2, different aspects of the γ' precipitation at skin and interior area is evaluated at various cooling rates in both Gleeble and NGVs specimens. Figures 6-11 (a, c) represent the variation of γ' with cooling rate, as with increasing cooling rate from 0.25 to 1 °C/s, γ' size decreases from 0.5 to 0.4 μm at skin of Gleeble sample. While, the γ' volume fraction follows opposite trend, since γ' volume fraction increases by 6 % at the skin of sample cooled at 1 °C/s compared with that of cooled at 0.25 °C/s. As known, higher cooling rate leads to increasing undercooling encouraging the nucleation of γ' . Higher number of γ' nucleus along with the reduction of growing time of γ' , because of shortening of diffusion time at higher cooling rates, cause the refining of γ' precipitation and increasing its volume fraction [73,83–85]. However, the precipitation shape was not transformed in skin with changing cooling rate and the prevailing γ' shapes were cuboidal shape together with a few number of semi-spherical shape (Figs. 6-11 (a, c)).

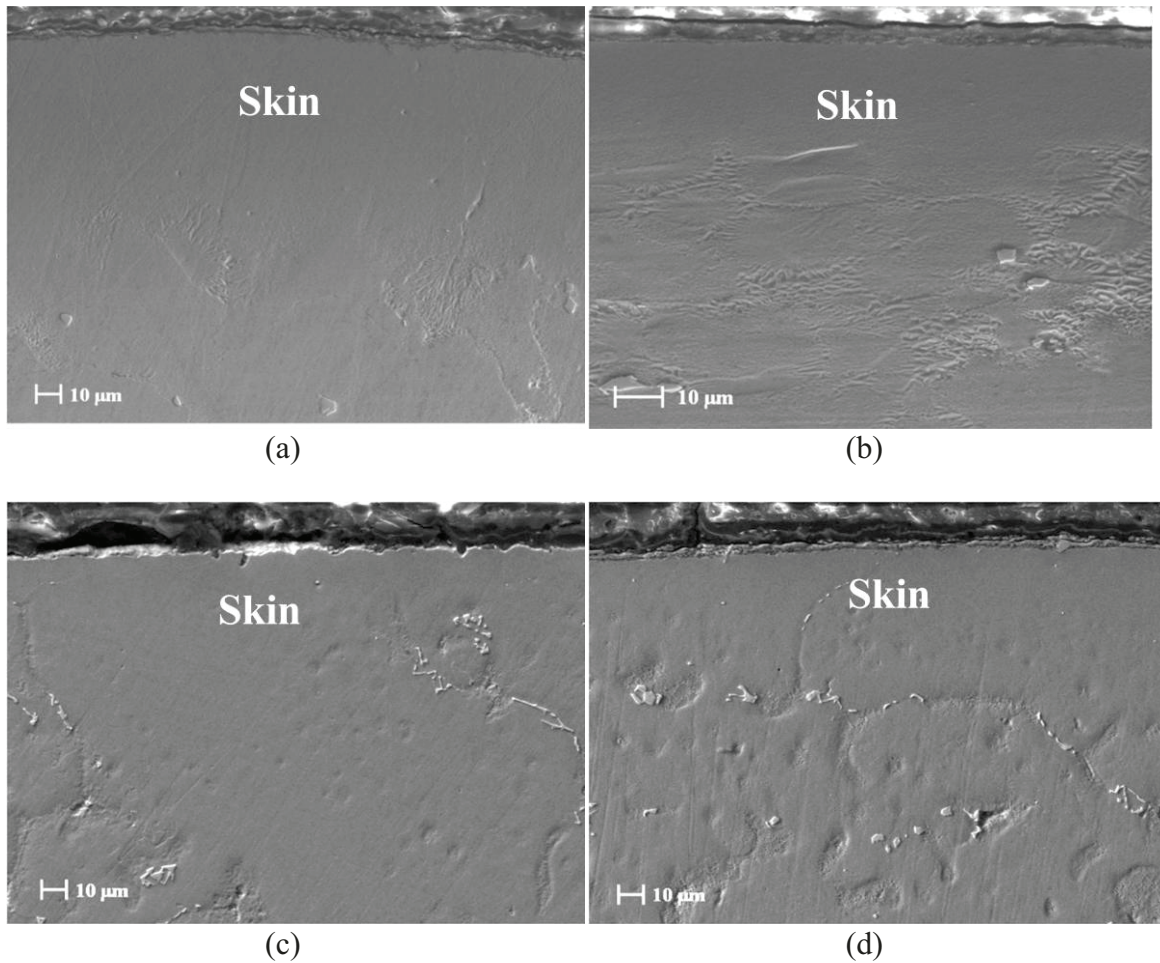


Figure 6-10. SEM microstructures of formed skin in the Gleeble samples (a, b) and in NGV part (c, d) cooled at 0.25 °C/s (a, c), 1 °C/s (b, d).

The same trend is observed for the center area of Gleeble samples (Table 6-2) which means that in addition to the reduction of precipitation size with rising cooling rate from 0.25 to 1 °C/s, volume fraction of γ' at 1 °C/s is higher than 0.25 °C/s cooling rate at center (Figs. 6-11 (b, d)). It should be noted that similar γ' shape, consisting of irregular shape along with few cuboidal precipitation, was formed at the center of Gleeble specimen at both cooling rates (Figs. 6-11 (b, d)).

Apart from a variation of skin and center microstructure with changing cooling rate, there is a significant difference between the microstructure of skin and center. On the one hand, γ' precipitation at skin differs from the interior section in Gleeble samples meaning that the size, volume fraction and shape of γ' vary in center compared with skin at both cooling rates (Fig. 6-11). At 0.25 °C/s cooling rate (Figs. 6-11 (a, b)), while γ' size in the center is 28 % bigger than that of skin area, γ' volume fraction reduces by 29 % at the center in comparison with the skin area of Gleeble specimens (Table 6-2).

Similar trend is reported for the sample exposed the cooling rate of 1 °C/s during solidification (Figs. 6-11 (c, d)). In other words, with moving from the center toward the skin in the Gleeble specimen, the γ' size declines from 0.5 to 0.4 μm , whereas volume fraction of γ' precipitates increases by 38 % (Table 6-2).

Since the skin is formed due to freezing effect, it can be assumed that the solidification rate of skin microstructure is much higher than center resulting in the change of microstructure at skin and center.

Although the γ' shape at skin at both cooling rates is almost the same, there is a transition of γ' shape from skin toward the center. The cuboidal γ' shape prevailing in skin, was transformed to the irregular shape γ' dominating in the center (Table 2 and Fig. 6-11).

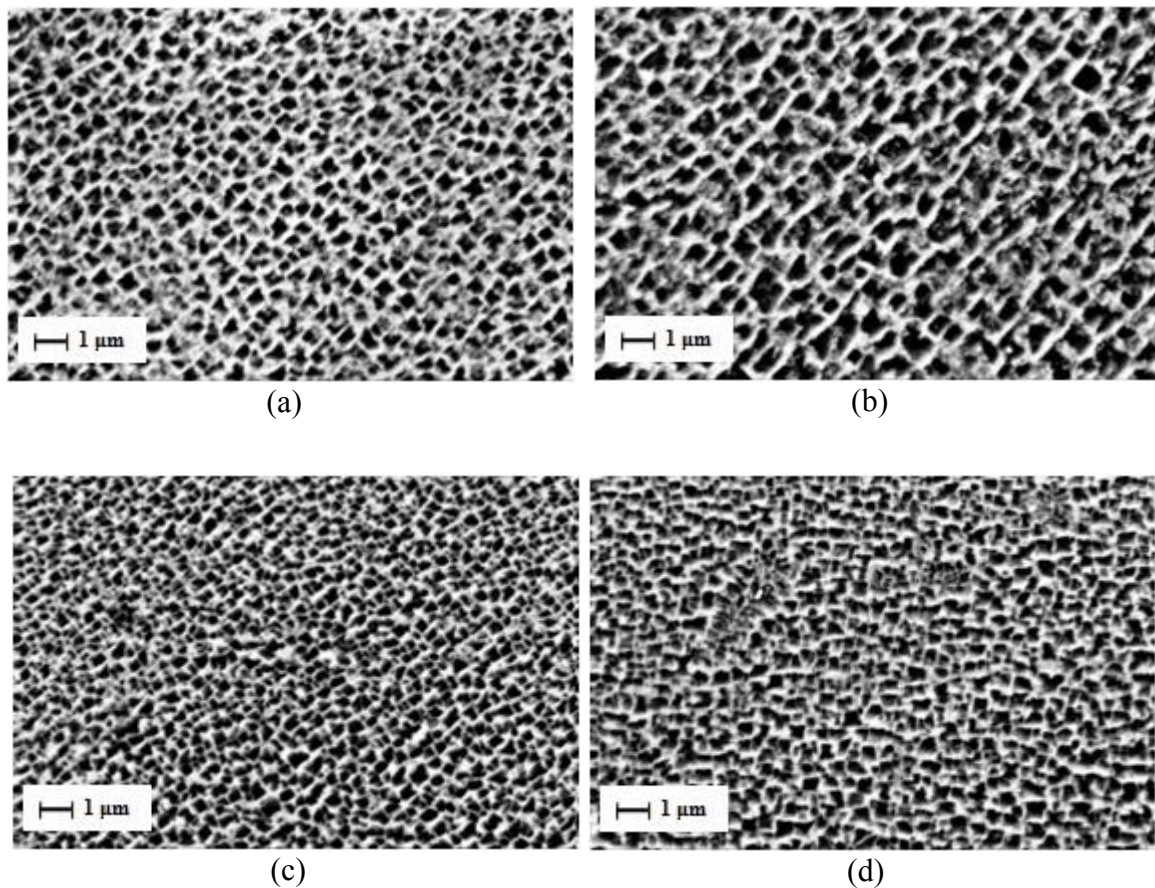


Figure 6-11. SEM microstructures of γ' in the skin of Gleeble samples (a, c) and centre (b, d) cooled at 0.25 °C/s (a, b) and 1 °C/s (c, d).

The influence of cooling rate on the center and skin microstructure of NGV samples is similar to that of Gleeble specimens. As a brief interpretation, rising cooling rate at both

skin and center of NGV leads to increasing of the γ' volume fraction and decreasing of the γ' size (Table 6-2 and Fig. 6-12). Despite the Gleeble specimens at which cuboidal shape γ' prevails in the skin, the irregular shape γ' is the predominant shape at both skin and center of NGV samples. Furthermore, while the center of NGV shows the finer γ' precipitates compared with skin at both cooling rates, the higher volume fraction of γ' precipitates is measured at skin area of NGV.

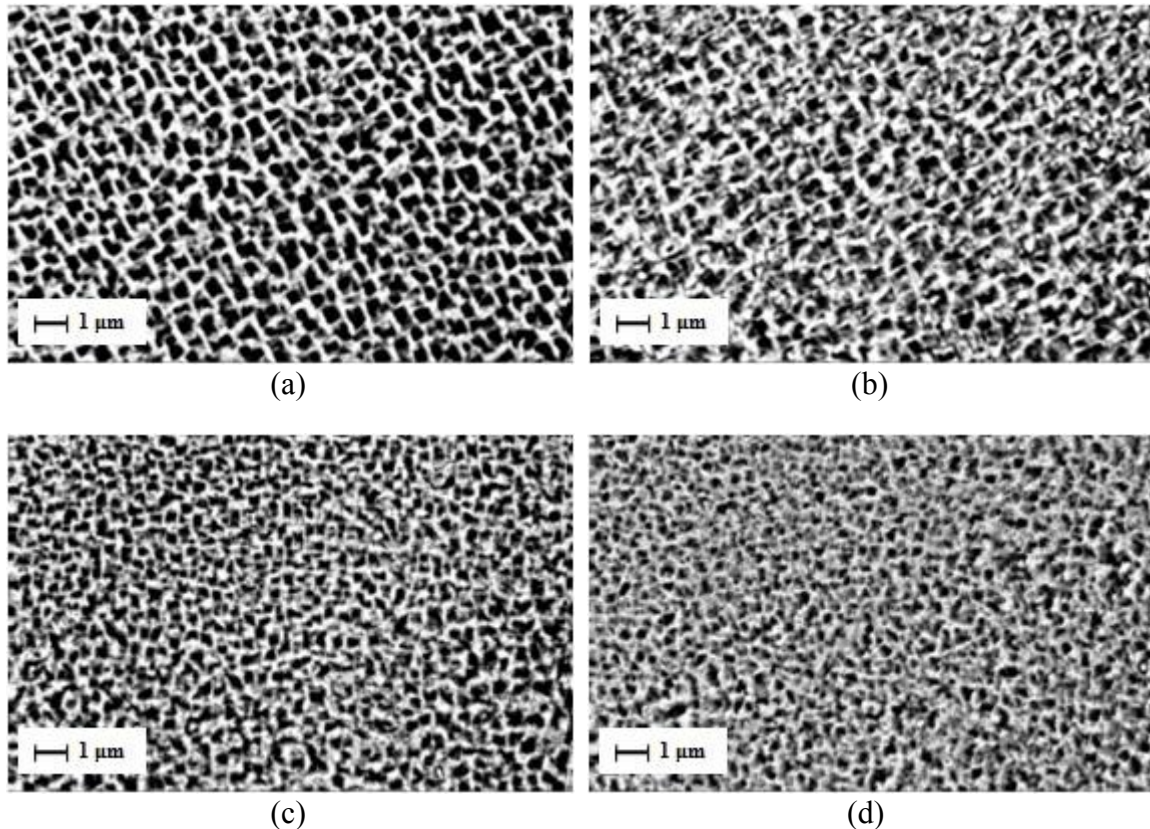


Figure 6-12. SEM microstructures of γ' in the NGV part at skin (a, c) and centre (b, d) cooled at 0.25 °C/s (a, b) and 1 °C/s (c, d).

The prediction and control of the thickness of skin, formed at the first contact of melt with cold mould, is considered as a challenge in casting technology. On the one hand, in some alloys and casting methods skin represents lower mechanical properties resulting in need for final treatment to eliminate the skin. On the other hand, skin formation at thin and complex shape parts can cause the misrun making it impossible to produce the sound casting parts. The thick solid skin acts as an obstacle for reaching the melt to the rest area of the casting part. Under this condition, the skin thickness should be controlled. The evaluation of skin thickness at Gleeble and NGV parts, shown at the

Fig. (6-9) and Table 6-2, demonstrates that the main objective of this study was fulfilled meaning that the physical simulation technique employed in this study could reproduce the skin thickness with acceptable precision at both cooling rates. However, further study was carried out to compare γ' precipitation characteristics in the Gleeble and NGV specimens.

In spite of lower size of γ' precipitates at skin of Gleeble specimens compared with the center, the γ' size at NGV parts shows opposite trend (Figs. 6-11 and 6-12). In other words, the γ' size in the NGV specimens decrease from 0.7 ± 0.3 to 0.5 ± 0.2 and 0.6 ± 0.2 to 0.4 ± 0.2 μm at skin toward center at cooling rates of 0.25 and 1 $^{\circ}\text{C/s}$, respectively (Table 6-2).

However, regardless of few amount of observed discrepancy, the variation of volume fraction of γ' at skin and center of NGV specimens is almost similar to that of Gleeble samples at both cooling rates (Table 6-2).

Cuboidal shape γ' is the prevailing γ' morphology in the skin of the Gleeble specimens at both cooling rates, the γ' shape is transformed to the irregular shape in the NGV specimens. Furthermore, there is no presence of cuboidal shape γ' in the center of NGV specimens, but few of them exist at the center of the Gleeble specimens (Table 6-2). This can be interpreted by (1) the difference of heat transfer and (2) size of ceramic mould in physical simulation and real investment casting. First, the direction of heat transfer in the GLEEBLE specimens is mostly through the rod toward the copper grips meaning that the large amount of heat is absorbed by Gleeble machine, but in investment casting of NGV the heat is absorbed by mould and heat passes through the mould. Secondly, the volume proportion of melt to ceramic mould at investment casting process, for production of NGV parts, is much higher than the same proportion in physical simulation process. As a result, ceramic mould at investment casting keeps a lot of heat resulting in longer exposure time of NGV's skin at higher temperature. Therefore, the larger γ' size of skin at NGV can be explained by the longer diffusion time of alloying elements at skin due to longer contact time of skin with high temperature ceramic mould.

Table 6-2. The microstructural and nanohardness characteristics of skin formed in the Gleeble specimens and as-cast NGV.

Sample	Gleeble				NGV			
	0.25		1		0.25		1	
	Skin	Centre	Skin	Centre	Skin	Centre	Skin	Centre
Skin thickness (μm)	92 \pm 14	–	82 \pm 12	–	95 \pm 13	–	83 \pm 12	–
γ' size (μm)	0.5 \pm 0.1	0.7 \pm 0.3	0.4 \pm 0.1	0.5 \pm 0.2	0.70 \pm 0.3	0.5 \pm 0.2	0.6 \pm 0.2	0.4 \pm 0.2
γ' volume fraction (%)	31 \pm 1	24 \pm 2	33 \pm 1	24 \pm 1	32 \pm 2	29 \pm 2	30 \pm 2	29 \pm 1
γ' Shape	Cuboidal with few semi-spherical	Irregular with few cuboidal	Cuboidal with few semi-spherical	Irregular with few cuboidal	Irregular with few cuboidal	Irregular	Irregular with few cuboidal	Irregular
Grain size (μm)	97 \pm 46	1297 \pm 347	–	1050 \pm 284	300 \pm 30	1264 \pm 693	–	1018 \pm 43 7
Nanohardness (GPa)	7.3 \pm 0.4	6.7 \pm 0.6	7.6 \pm 0.3	7 \pm 0.4	6.9 \pm 0.3	8.1 \pm 0.2	7.4 \pm 0.4	8.5 \pm 0.2

6.1.2.2 EBSD investigation of skin

EBSD was employed to achieve a deeper insight into the nature of skin and its microstructural characteristics. In order to understand the skin nature some questions should be responded. For instance, a skin is a single layer or it is polycrystalline, what are the grain boundaries in the skin? Also the preferred direction of grain growth in the skin, if exists, and its correlation with interior grain structure should be clarified.

Figure 6-13, represents the skin microstructure in the NGV and Gleeble samples at 0.25 °C/s cooling rate. Also, Figs. 6-14 and 6-15 (a, b) show the transversal and longitudinal view of skin structure in Gleeble specimens cooled at 0.25 and 10 °C/s, respectively. The figures indicate that the skin consists of several grains meaning that it has polycrystalline structure. Also it is found that the physical simulation of skin formation well reproduces the skin thickness at the same cooling condition, so the main aim of physical simulation is achieved (Figs. 6-13 and Table 6-2).

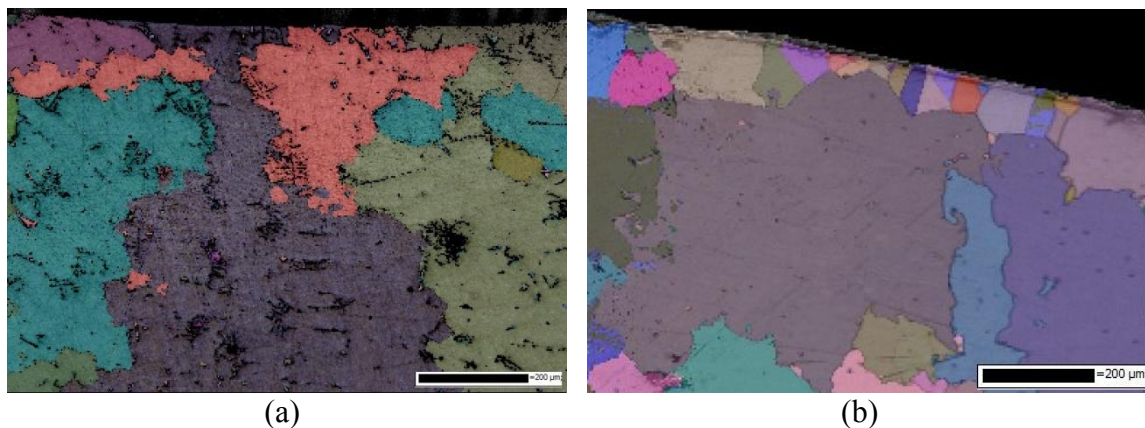


Figure 6-13. The skin microstructure of (a) NGV and (b) transversal section of the Gleeble specimens cooled at 0.25 °C/s.

Whereas the skin thickness is the same in both Gleeble and NGV specimens, skin's grains in the NGV specimen are considerably bigger than that of Gleeble specimen solidified at the same cooling rate. This is related to the difference in the heat transfer mechanism in the GLEEBLE and NGV specimens. While in investment casting of NGV the largest proportion of heat is released through the ceramic mould, in physical simulation method, Gleeble machine controls the cooling rate by which the heat transfer direction is aligned to the sample axis toward the copper grips. Therefore, in the investment casting of NGV, the large ceramic mould receives almost all heat of melt

Chapter 6

making it capable to keep higher amount of heat as compared to ceramic tube. As a result, skin microstructure in NGV is exposed at high temperature for a longer time resulting in larger grains.

Figures 6-14 and 6-15 (a, b) show the grain structure in the transversal and longitudinal sections of the Gleeble sample cooled at cooling rates of 0.25 and 10 °C/s, respectively. According to the figures, the grain size in transversal section of skin is larger than that in longitudinal section (Table 6-3). The average grain size of transversal section is 36 µm bigger than that of longitudinal section at cooling rate of 0.25 °C/s, since skin microstructure, having less than 100 µm thickness, can be affected seriously by the heat of ceramic mould. Considering the heating mechanism of Gleeble machine, the highest temperature is concentrated in the midsection of sample in which the ceramic mould reaches the highest temperature dropping gradually with increasing distance from midsection. Hence, the skin grains at midsection, exposed at higher temperature, grow more and represent larger size compared with the skin grains at longitudinal section aligned with the direction of heat flow.

In addition to the grain size, the grain aspect ratio at transversal section differs from that of at longitudinal section. As the grain aspect ratio increase from 1.8 to 2 at transversal and longitudinal section, respectively. As mentioned above, in physical simulation the ceramic mould releases a few proportion of heat, but the large proportion of heat is controlled by the Gleeble machine using the copper grips. Therefore, it can be concluded that the grains are elongated in the direction of heat flow.

The analysis of the data in Table 6-3 demonstrates that the same trend of skin's grains and aspect ratio at 0.25 °C/s cooling rate takes place for the Gleeble sample cooled at cooling rate of 10 °C/s, which is also shown by Figs 6-14 and 6-15 (a, b). The above explanation, commented for 0.25 °C/s cooling rate, also well describes the variation of grains for cooling of 10 °C/s. However, grain refining is observed at the higher cooling rate, since the grain size decreases from 97 to 42 µm on the transversal section of samples cooled at 0.25 and 10 °C/s cooling rates, respectively. Moreover, increasing cooling rate intensifies the difference of the aspect ratio of skin grains between transversal and longitudinal section, which leads to the increasing of grain aspect ratio from 2 to 2.7 at transversal and longitudinal section, respectively.

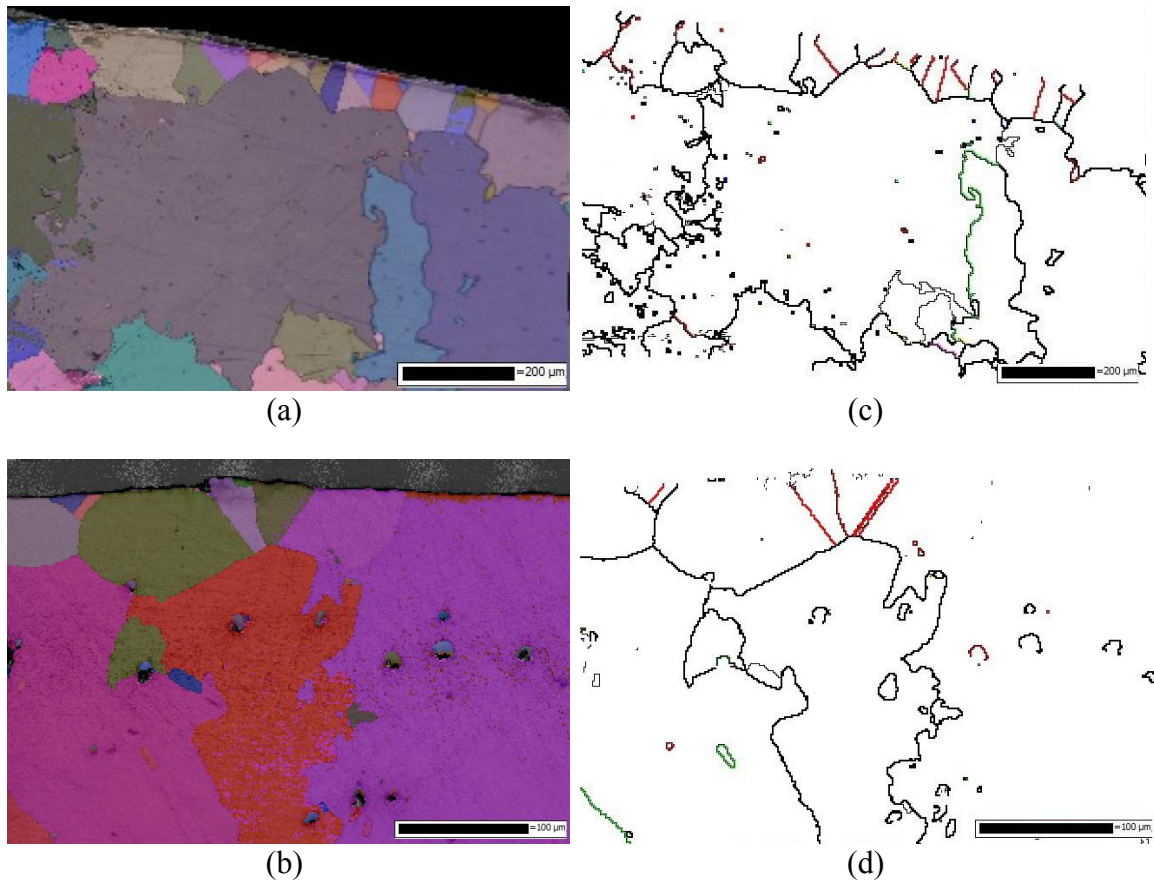


Figure 6-14. EBSD grain (a, b) and grain boundary (c, d) maps taken from the transversal (a, c) and longitudinal (b, d) sections of Gleeble sample cooled at 0.25 °C/s cooling rate. The red and black colors are representative of twin and high angle grain boundaries, respectively.

The various types of skins' grain boundaries are depicted in the Figs. 6-14 and 6-15 (c, d) for the transversal and longitudinal section of samples cooled at 0.25 and 10 °C/s cooling rates, respectively. The red and black colors are representative of twin and high angle grain boundaries, respectively.

Considering the Table 6-3, twin boundaries constitute a large fraction of grain boundaries at skin microstructure at both cooling rates. In the transversal section of Gleeble specimens, while twin boundaries represent 47 % of skin's grain boundaries at 0.25 °C/s cooling rate, they are prevailing grain boundaries, with 55 % of fraction, at 10 °C/s cooling rate. Longitudinal sections of skin at both cooling rates also show that nearly half of the fraction of grain boundaries belongs to the twin boundaries (Table 6-3).

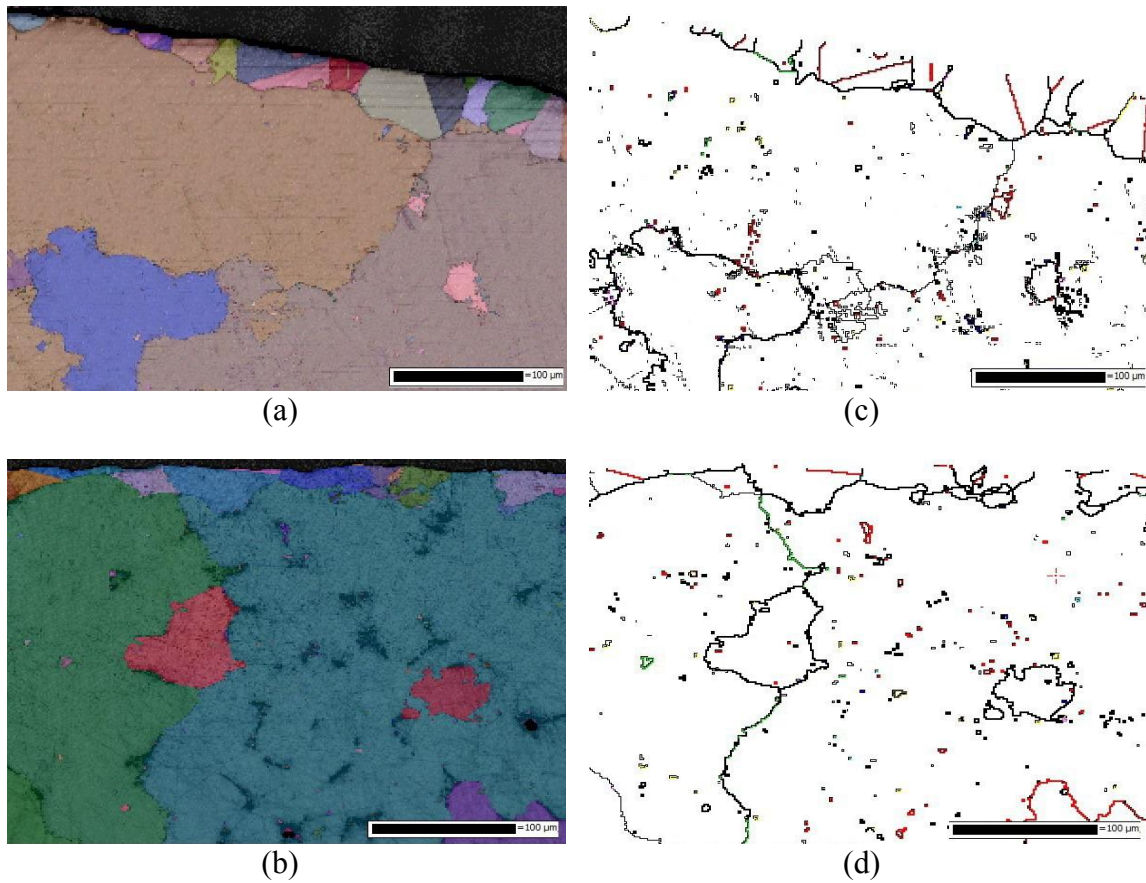


Figure 6-15. EBSD grain (a, b) and grain boundary (c, d) maps taken from the transversal (a, c) and Longitudinal (b, d) sections of Gleeble sample cooled at 10 °C/s cooling rate. The red and black colors are representative of twin and high angle grain boundaries, respectively.

Table 6-3. Grain and grain boundary characteristics of skin in the Gleeble specimens and as-cast NGV.

Sample	Gleeble				NGV
	0.25		10		0.25
Skin section	Transversal	longitudinal	Transversal	Longitudinal	Transversal
Grain size (µm)	97±46	61±26	42±20	32±15	300±30
Aspect ratio	1.8±0.4	2±0.5	2±0.8	2.7±0.5	2.5
Fraction of twin grain boundary (%)	47	50	55	52	-

As known, the rapid solidification in crystalline materials is accompanied by the saturation of solute alloying elements, grain refinement, reduction of segregation as well as considerable formation of defects in crystalline structure resulting in increasing stress concentration in the specimen [185]. Therefore, residual stresses and strains are induced into the crystalline lattice due to skin formation. Under this condition, two explanations can be proposed for the formation of large number of twin boundaries in skin microstructure. First, in the Ni-based superalloys the lowest energy configuration was observed for the twin grain, coherent Σ_3 , boundaries explaining its abundance in the measured EBSD analysis, as shown by Sangid et al. [54]. In fact, forming twin grain boundaries, skin microstructure makes an effort to reduce lattice energy which increases because of residual stress generated by freezing of melt.

Second, inducing a few strains to the microstructure along with the exposing of microstructure at intermediate temperature regime are taken into account as the main reasons for formation of the considerable fraction of twin boundaries in skin microstructure as it is demonstrated by Kovarik et al. [186]. Kovarik et al. studied the microtwinning at intermediate temperatures in Ni-based superalloys. The study indicates that the twins are commonly observed in the deformed microstructure at creep temperature, 650-750 °C in Ni-based superalloys, considered as the intermediate temperatures. This condition nearly coincides with the same condition that the skin is experienced at melting/solidification experiment by Gleeble, as the temperature of skin area is estimated to be in the mentioned range. They argue that the twinning contributes significantly to the total creep strain at smaller strain levels which is at 1 and 2% strain in Ni-based superalloys. The formation of twinning grain boundaries is attributed to the thermally activated nature mechanism in the Ni-based superalloys which is linked to the diffusion-mediated reordering of the ordered structure. An important conclusion from the present knowledge of the mechanisms depending on reordering is that they may initiate at temperatures that are lower than those required for general climb of dislocations. Reordering is a conservative process involving diffusion distances of atomic dimensions, while climb by-pass requires long-range diffusion over distances comparable to the precipitate size [186].

The crystallographic orientation of grain is investigated by the IPF maps of grains in longitudinal section of both cooling rates (Figs. 6-16 (a, b)). Considering the Fig. 6-17, it is seen that some grains of skin tend to overgrow adjacent grains and form giant grains. The pink and blue grains at 0.25 and 10 °C/s cooling rates, respectively, are the

representatives of the giant grains formed at skin and continue to grow toward center (Figs. 6-17 (a, b)). The evaluation of IPF maps at both cooling rates depicts that the giant grains are localized at one area in IPF maps meaning that their growth directions are aligned at one direction, in other words, they show a preferred growth direction (Figs. 6-16 (a, b)). Despite the giant grains, the grains of skin are dispersed occasionally at IPF maps showing that the grains of skin do not follow the preferred growth direction. The generally accepted model indicates that the grain, whose fast growing crystallographic direction is the most closely aligned to the temperature gradient, can overgrow all less favourably oriented grains [52]. It is assumed that the same 'scenario' takes place in the Gleeble samples, but it is very difficult to define the exact heat flow direction in physical simulation, so we cannot definitely say that the giant grain growth direction coincides with the heat flow direction in our study. Nevertheless, the IPF images reveal that the growth directions of all giant grains are aligned to one specific direction which can be the heat flow direction (Figs. 6-16 (a, b)).

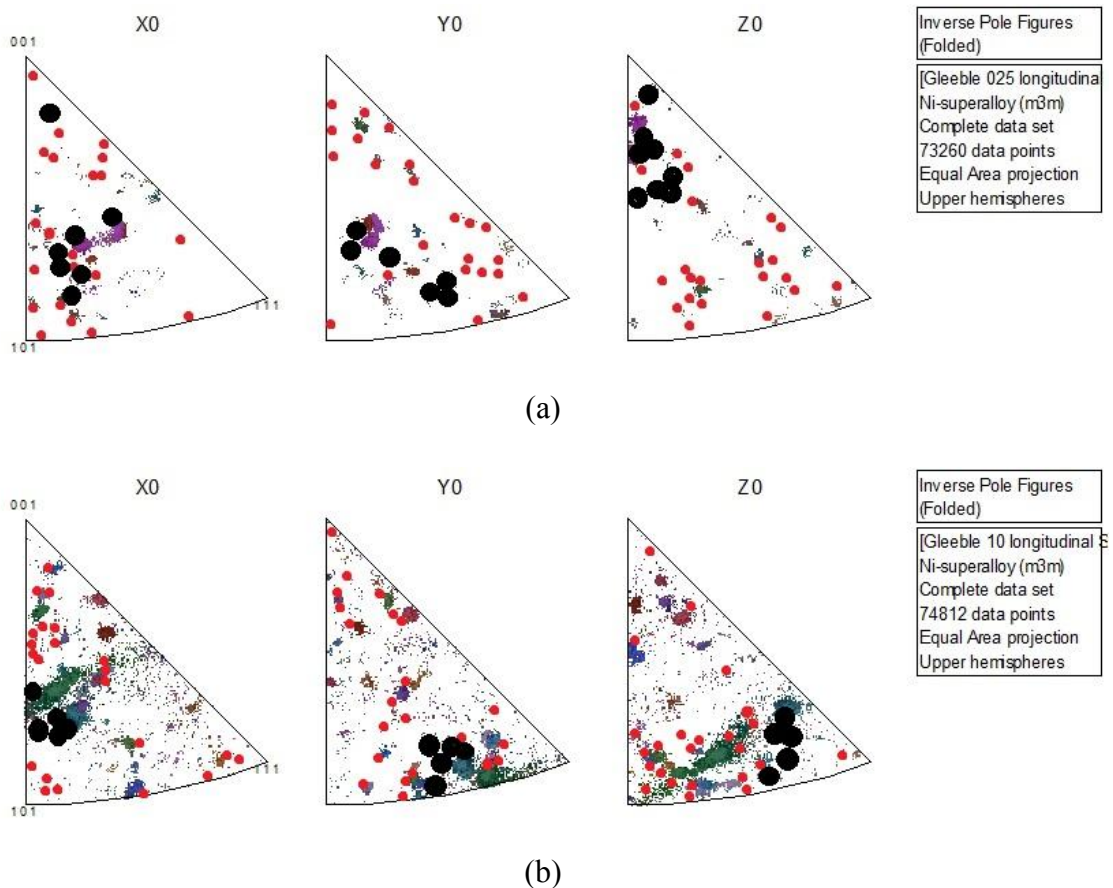


Figure 6-16. Inverse pole figures of longitudinal section of the Gleeble specimens cooled at (a) 0.25 and (b) 10 °C/s cooling rates, respectively. Small red and big black circles are the representatives of grains 'skin and giant grains, respectively.

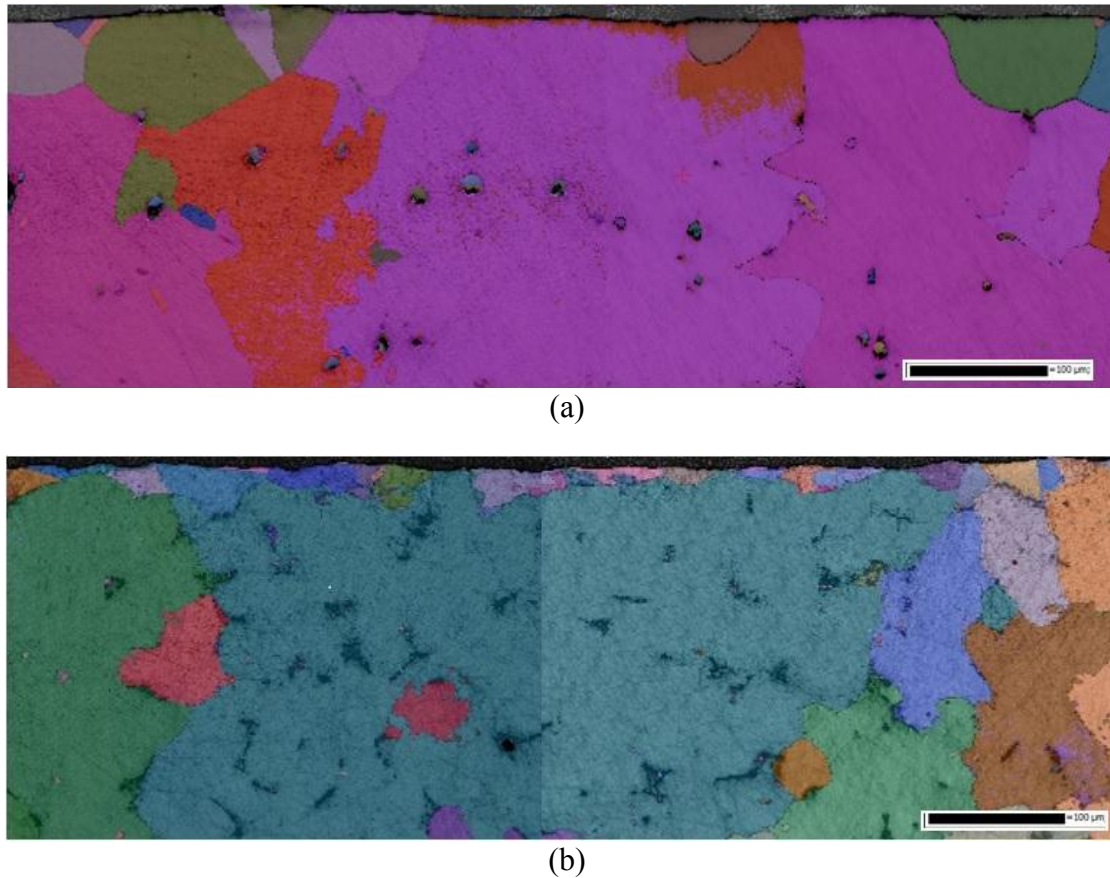


Figure 6-17. EBSD grain maps of longitudinal section of the Gleeble specimens cooled at (a) 0.25 and 10 °C/s cooling rates.

The three dimensional pictures of the sample cooled at 0.25 and 10 °C/s are shown in Figs. 6-18 (a) and 6-18 (b), respectively. The skin microstructure and the difference of skin and interior microstructure are easily distinguished.

6.1.2.3 Nanohardness study of skin

With respect to the thickness of skin, which is less than 100 µm, the nanoindentation technique (see section 3.5.2) was employed for hardness assessment of skin in the Gleeble specimens and NGV parts. Representative load-indentation depth curves of skin and center of the Gleeble specimens at room temperature for three cooling rates of 0.25, 1 and 10 °C/s are plotted in Fig. 6-19.

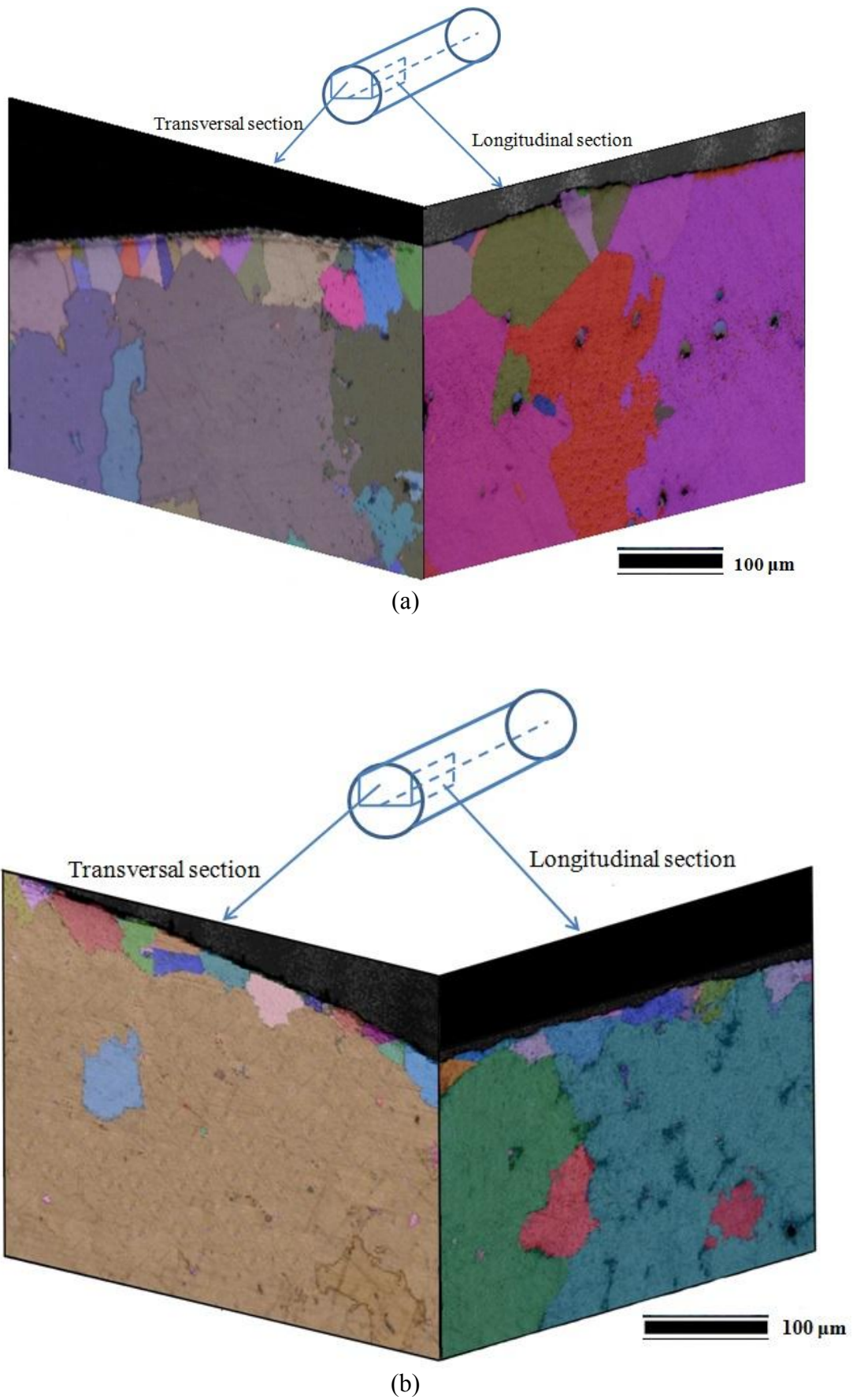


Figure 6-18. The 3D EBSD image of Gleebles samples cooled at (a) 0.25 and (b) 10 °C/s cooling rates.

As can be seen the indentation depth was adjusted to be constant at 200 nm and the applied load varies. The results depict that the higher load is needed, for the constant indentation depth, at all cooling rates on skin compared with the center, since skin has higher mechanical properties than center in all Gleeble specimens. The increment of load for constant indentation displacement at skin corresponds to the variation of microstructure of skin and center.

As mentioned above, the γ' size at skin is finer than in the center and also volume fraction of γ' precipitates at skin is higher than in the center. Since γ' precipitates, act as obstacles for dislocation glide, the reduction of inter-particle spacing due to finer γ' and its higher volume fraction of (Eq. 4-6) results in elevating of applied load (Eq. 4-7) for dislocation glide associated with deformation (Fig. 6-19). This finding is in a good accordance with the study carried out for the high-pressure die-cast of Mg alloys [176]. It is demonstrated that the microhardness of skin is higher than center because of finer microstructure of skin as compared to the center [176,178]. The similar study on the ordinary casting of compacted graphite (CG) iron was performed by Boonmee and Stefanescu indicating that lower hardness of interior part corresponds to the coarser microstructure of interior area [187].

Other fact which should be considered is the dependency of indentation load at both skin and center to cooling rate. As shown in Fig. 6-20, the applied load increased moderately with increasing cooling rates at both skin and center of specimens. Whereas, rising cooling rate increases the precipitation volume fraction, it causes the reduction of γ' size [73,83–85] both of which encourage the promotion of hardness. It is observed that the difference of indentation load with cooling rate is significantly intensified at skin more than interior area which can be attributed to deeper effect of cooling rate on skin microstructure.

The nanohardness, calculated from the load-indentation depth graphs (see section 3.5.2), are plotted versus cooling rate in Fig. 6-21. The increment of nanohardness with cooling rate can be interpreted based on the transition of γ' precipitation microstructure due to changing cooling rate. Increasing cooling rate leads to the higher volume fraction and finer size of γ' precipitation resulting in the growth of nanohardness. A role of mixture in multi component materials can be employed to support this claim, as the total hardness in a multi component material is measured by

$$H_t = H_\gamma V_\gamma + H_{\gamma'} V_{\gamma'} + \dots \quad (6-1)$$

Where the H_t , H_γ and $H_{\gamma'}$ are elastic modulus of a bulk material, γ and γ' , respectively. V_γ and $V_{\gamma'}$ are representative of the volume fraction of γ and γ' phases, respectively [38].

As know the nanohardness of γ' precipitation in a CMSX-6 Ni-based superalloy, which is almost 8.5 GPa, is higher than the nanohardness of its matrix reported almost 6 GPa [188,189]. It is expected that the same behavior is seen in other Ni-based superalloys. Hence, precipitation of higher volume fraction of γ' results in the increasing nanohardness value. It can be predictable that the γ' intermetallic phase with an ordered crystalline lattice has higher hardness than γ alloy matrix with in-ordered crystalline lattice.

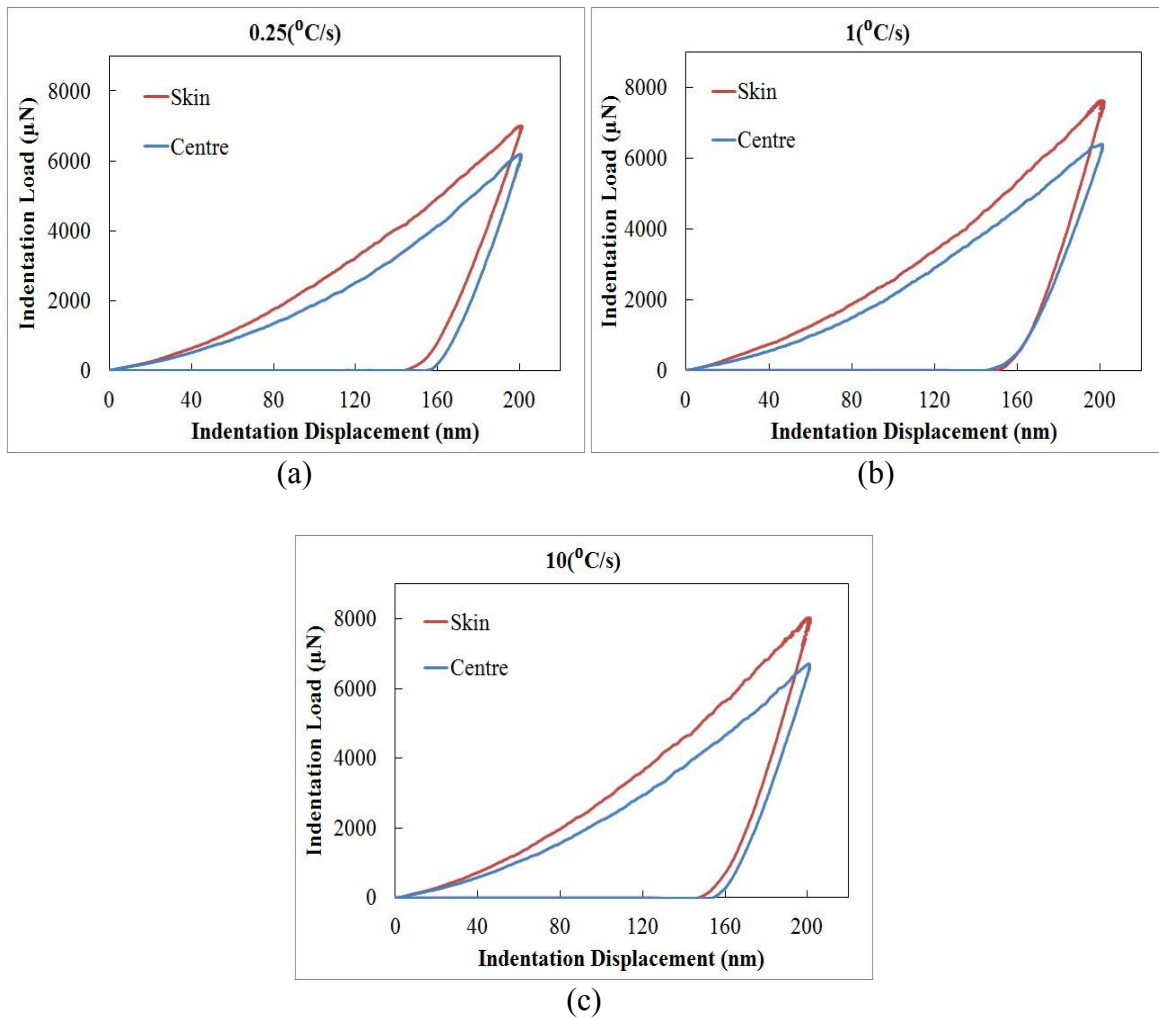
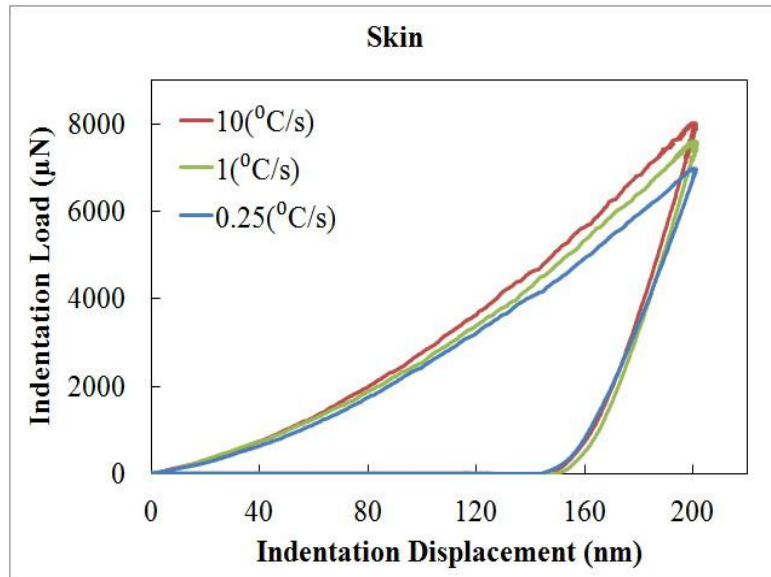
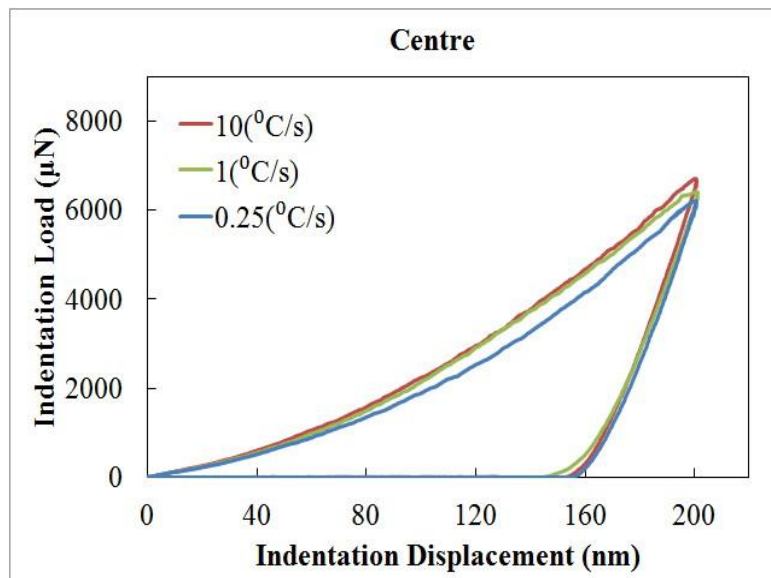


Figure 6-19. Load-displacement graphs of nanoindentation test at skin and center of the Gleeble specimens at a) 0.25 b) 1 and c) 10 °C/s.



(a)



(b)

Figure 6-20. Variation of load-displacement graph with cooling rates at skin and center of the Gleeble specimens.

On the other hand, the presence of cuboidal shape of γ' precipitation in the skin of Gleeble specimens, compared with the irregular shape γ' precipitation at center of samples, intensifies induced plastic constraint and associated pressures resulting in higher mechanical properties and hardness of alloy [6,190].

However, the center of NGV seems to be harder than the skin, as the nanohardness increases from 6.9 ± 0.3 to 8.1 ± 0.2 at 0.25°C/s cooling rate and from 7.4 ± 0.4 to 8.5 ± 0.2 at 1°C/s cooling rate (Table 6-2). This behavior can arise from the precipitation of finer

γ' at center compared with skin of NGV, while the volume fraction of γ' remained nearly constant at both center and skin.

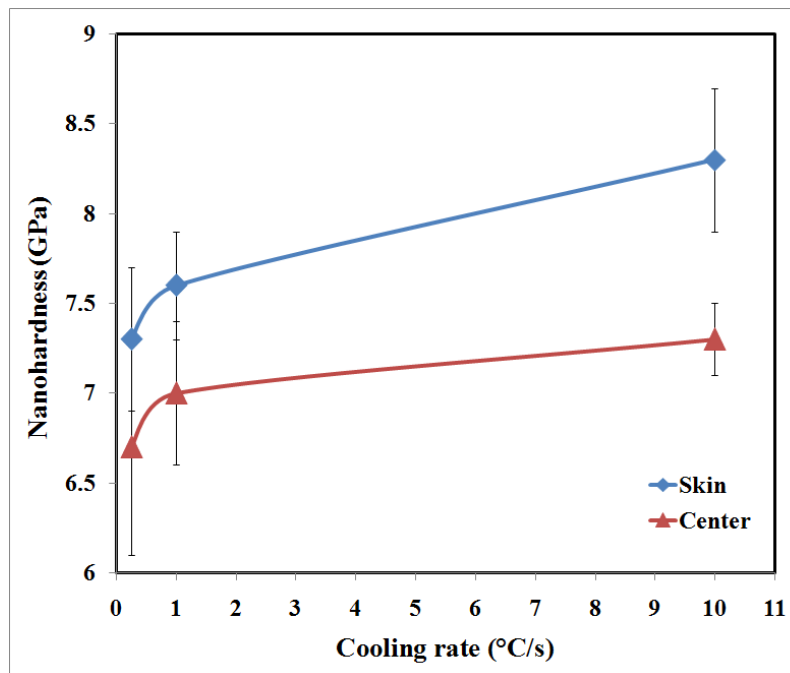


Figure 6-21. Variation of nanoindentation hardness with cooling rate at skin and center of Gleeble specimens.

6.1.3 Conclusions:

The physical simulation tool was applied for the reproduction of skin microstructure, formed at interface of mould and melt in investment casting, by Gleeble 3800 thermo-mechanical simulator. The physical simulation tool consisted of thermal model, melting/solidification experiments by Gleeble 3800 and the validation of physical simulation tool performed via comparison of characteristics of Gleeble specimens and as-cast NGV. Following findings are obtained from this study:

- 1- The skin is formed due to freezing of melt got in contact with colder ceramic. No skin is formed if the ceramic temperature is high and enters the solidification temperature range.
- 2- The skin thicknesses predicted by physical simulation are in a very good accordance with the skin thickness in the as-cast NGV at 0.25 and 1 °C/s cooling rates, provided

that temperature of ceramic tube is relevant to that of ceramic mould during investment casting (1030 °C).

3- Cooling rate affects skin thickness. The skin thickness decreased from 92 to 30 μm with increasing cooling rate from 0.25 to 10 °C/s.

4- Finer γ' precipitates are observed in skin of the Gleeble samples at both cooling rates, whereas coarser γ' were formed in skin of the as-cast NGV. However, γ' volume fraction decreased from skin to center in both Gleeble and NGV samples at 0.25 and 1 °C/s cooling rates.

5- Skin consists of grains having very small size compared to that of the grains in the center.

6- The transversal and longitudinal assessment of Gleeble samples depicted that approximately 50 % of skin's grain boundaries, in samples cooled at 0.25 and 10 °C/s, are twin boundaries categorized as a lowest energy grain boundaries.

7- While nanohardness of skin is higher than center in Gleeble specimens at all cooling rates, it follows opposite trend in NGV specimens.

8- Reduction of cooling rate resulted in decreasing skin nanohardness.

7 References

- [1] Whitesell HS, Overfelt R. Influence of solidification variables on the microstructure, macrosegregation, and porosity of directionally solidified Mar-M247. *Mater Sci Eng A* 2001;318:264–76.
- [2] Amouyal Y, Seidman DN. The role of hafnium in the formation of misoriented defects in Ni-based superalloys: An atom-probe tomographic study. *Acta Mater* 2011;59:3321–33.
- [3] El-Bagoury N, Nofal A. Microstructure of an experimental Ni base superalloy under various casting conditions. *Mater Sci Eng A* 2010;527:7793–800.
- [4] Roskosz S, Adamiec J. Methodology of quantitative evaluation of porosity, dendrite arm spacing and grain size in directionally solidified blades made of CMSX-6 nickel alloy. *Mater Charact* 2009;60:1120–6.
- [5] Al-Jarba K, Fuchs G. Effect of carbon additions on the as-cast microstructure and defect formation of a single crystal Ni-based superalloy. *Mater Sci Eng A* 2004;373:255–67.
- [6] Van Sluytman JS, Pollock TM. Optimal precipitate shapes in nickel-base γ/γ' alloys. *Acta Mater* 2012;60:1771–83.
- [7] Bor HY, Wei CN, Jeng RR, Ko PY. Elucidating the effects of solution and double ageing treatment on the mechanical properties and toughness of Mar-M247 superalloy at high temperature. *Mater Chem Phys* 2008;109:334–41.
- [8] Bor HY, Hsu C, Wei CN. Influence of hot isostatic pressing on the fracture transitions in the fine grain Mar-M247 superalloys. *Mater Chem Phys* 2004;84:284–90.
- [9] Karaköse E, Keskin M. Microstructure evolution and mechanical properties of intermetallic Ni-xSi (x=5, 10, 15, 20) alloys. *J Alloys Compd* 2012;528:63–9.
- [10] Royer A, Bastie P, Veron M. In situ determination of γ' phase volume fraction and of relations between lattice parameters and precipitate morphology in Ni-based single crystal superalloy. *Acta Mater* 1998;46:5357–68.
- [11] Reed RC. *The superalloys fundamentals and applications*. Cambridge University Press; 2006.

References

- [12] Liao JH, Bor HY, Wei CN, Chao CG, Liu TF. Influence of microstructure and its evolution on the mechanical behavior of modified Mar-M247 fine-grain superalloys at 871°C. *Mater Sci Eng A* 2012;539:93–100.
- [13] Pattnaik S, Karunakar DB, Jha PK. Developments in investment casting process—A review. *J Mater Process Technol* 2012;212:2332–48.
- [14] Chen J, Lee JH, Jo CY, Choe SJ, Lee YT. MC carbide formation in directionally solidified Mar-M247 LC superalloy. *Mater Sci Eng A* 1998;247:113–25.
- [15] Wilson BC, Cutler ER, Fuchs GE. Effect of solidification parameters on the microstructures and properties of CMSX-10. *Mater Sci Eng A* 2008;479:356–64.
- [16] Okada M, Tsutsumi M, Kitamura T, Ohtani R. Initiation and growth of small crack in directionally solidified Mar-M247 under creep-fatigue. part I: effect of microstructure. *Fatigue Fract Eng Mater Struct* 1998;21:741–50.
- [17] Mandziej ST. Physical simulation of metallurgical processes. *Mater Tehnol* n.d.;44:105–19.
- [18] Hamilton RW, See D, Butler S, Lee PD. Multiscale modeling for the prediction of casting defects in investment cast aluminum alloys. *Mater Sci Eng A* 2003;343:290–300.
- [19] Suzuki HG, Nishimura S, Yamaguchi S. Physical simulation of the continuous casting of steels. *proc Phys. Simul. Welding, Hot Form. Contin. Cast., Canmet, Canada: 1988, p. vol MTL 92–43(TR).*
- [20] Michalik J, Kolmasiak C. Physical modeling of stresses during continuous casting of ST3S steel. *Metalurgija* n.d.;48:71–4.
- [21] Ferguson D, Chen W, Bonesteel T, Vosburgh J. A look at physical simulation of metallurgical processes, past, present and future. *Mater Sci Eng A* 2009;499:329–32.
- [22] Sims CT, Stoloff NS, Hagel WC. *Superalloys II*. John Wiley & Sons; 1987.
- [23] Donachie MJ, Donachie SJ. *Superalloys: A technical guide*. Second Edi. USA: ASM International; 2002.
- [24] Pollock TM, Rene N. Nickel-Based Superalloys for Advanced Turbine Engines : Chemistry , Microstructure , and Properties. *J Propuls Power* 2006;22:361–74.
- [25] Gizan X, Liu E, Zheng Z, Yu Y, Tong J, Zhai Y. Solidification behavior and segregation of Re-containing cast Ni-base superalloy with different Cr content. *J Mater Sci Technol* 2011;27:113–7.

References

- [26] Sifeng G, Lin L, Yiku X, Chubin Y, Jun Z, Hengzhi F. Influences of processing parameters on microstructure during investment casting of nickel-base single crystal. *China Foundry* 2012;159–64.
- [27] Image of the trent 800 courtesy. Rolls-Royce. <http://www.thomas-sourmail.net/coatings/turbine.html>.
- [28] Cervenka M. The different materials used in a Rolls-Royce jet engine. Rolls-Royce. <http://thomas-sourmail.net/coatings/materials.html>.
- [29] Nathal M V, Maier RD, Ebert LJ. The influence of cobalt on the tensile and stress-rupture properties of the nickel-base superalloy Mar-M247. *Metall Trans A* 1982;13:1767–74.
- [30] Nathal M V, Maier RD, Ebert LJ. The influence of cobalt on the microstructure of the nickel-Base Superalloy Mar-M247. *Metall Trans A* 1982;13:1775–83.
- [31] Seo SM, Kim IS, Lee JH, Jo CY, Miyahara H, Ogi K. Eta phase and boride formation in directionally solidified Ni-base superalloy IN792 + Hf. *Metall Mater Trans A* 2007;38:883–93.
- [32] Szczotok A. Quantitative evaluation of carbides in nickel-base superalloy Mar-M247. *IOP Conf Ser Mater Sci Eng* 2011;22:012007.
- [33] Szczotok A, Szala J, Cwajna J, Hetmańczyk M. Selection of etching methods of primary carbides in Mar-M247 nickel–base superalloy for computer-aided quantitative metallography. *Mater Charact* 2006;56:348–54.
- [34] AIH Committee. *ASM Specialty Handbook: nickel, cobalt, and their alloys*. USA: ASM International; 2001.
- [35] Harris K, Erickson GL, Schwer RE. Proceedings of the Superalloys. In: Gell M, Kortovich CS, Bricknell RH, Kent WB RJ, editor. *Proc. Superalloys, TMS-AIME*; 1984, p. 443–54.
- [36] Kaufman M. Proceedings of the Superalloys. In: Gell M, Kortovich CS, Bricknell RH, Kent WB RJ, editor. *Proc. Superalloys, TMS-AIME*; 1984, p. 43–52.
- [37] Trent xwb engine. Rolls-Royce.<http://airinsight.com/wpcontent/uploads/2011/11/trent-1.jpg>.
- [38] Dieter GE. *Mechanical metallurgy*. Third ed. USA: McGraw-Hill; 1976.
- [39] Soares Azevedo e Silva PR, Baldan R, Nunes CA, Coelho GC, Da Silva Costa AM. Solution heat-treatment of Nb-modified Mar-M247 superalloy. *Mater Charact* 2013;75:214–9.

References

- [40] Baldan R, Pereira da Rocha RL, Tomasiello RB, Nunes CA, Da Silva Costa AM, Ribeiro Barboza MJ, et al. Solutioning and aging of Mar-M247 nickel-based superalloy. *J Mater Eng Perform* 2013;22:2574–9.
- [41] Kattus JR. *Aerospace Structural Metals Handbook*. West Lafayette: Purdue Research Foundation; 1999.
- [42] Lee HT, Lee SW. The morphology and formation of gamma prime in nickel-base superalloy. *J Mater Sci Lett* 1990;9:516–7.
- [43] Ohta Y, Yoshizawa H, Nakagawa YG. Microstructural changes in a Ni-base superalloy during service. *Scr Metall* 1989;23:1609–14.
- [44] Hall EO. The deformation and ageing of mild steel: III discussion of results. *Proc Phys Soc Sect B* 1951;64:747–53.
- [45] Petch NJ. The cleavage strength of polycrystals. *I Iron Steel Inst* 1953:25–8.
- [46] Ashby MF. The deformation of plastically non-homogeneous materials. *Philos Mag* 1970;21:399–424.
- [47] Li JCM, Chou YT. The role of dislocations in the flow stress grain size relationships. *Metall Mater Trans* 1970;1:1145–59. doi:10.1007/BF02900225.
- [48] Porter DA, Easterling KE. *Phase transformations in metals and alloys*. McGraw-Hill; 1981.
- [49] Klein L, von Bartenwerffer B, Killian MS, Schmuki P, Virtanen S. The effect of grain boundaries on high temperature oxidation of new γ' -strengthened Co–Al–W–B superalloys. *Corros Sci* 2014;79:29–33.
- [50] Bozzolo N, Agnoli A, Souai N, Bernacki M, Loge RE. Strain induced abnormal grain growth in nickel base superalloys. In: Barnett M, editor. *5th Int. Conf. Recryst. grain growth*, Sydney: 2013, p. 1–4.
- [51] Jingchen Z, Ping Y. The effect of cooling rate of solidification on microstructure and alloy element segregation of AS cast alloy 718. *Superalloys 718, 625, 706 Var. Deriv.*, TMS; 2001, p. 133–40.
- [52] Wagner A, Shollock BA, McLean M. Grain structure development in directional solidification of nickel-base superalloys. *Mater Sci Eng A* 2004;374:270–9.
- [53] Souza ND, Ardakani MG, Wagner A, Shollock BA, Lean MMC. Morphological aspects of competitive grain growth during directional solidification of a nickel-base superalloy, CMSX4. *J Mater Sci* 2002;7:481–7.
- [54] Sangid MD, Sehitoglu H, Maier HJ, Niendorf T. Grain boundary characterization and energetics of superalloys. *Mater Sci Eng A* 2010;527:7115–25.

References

- [55] Olmsted DL, Foiles SM, Holm EA. Survey of computed grain boundary properties in face-centered cubic metals: I. Grain boundary energy. *Acta Mater* 2009;57:3694–703.
- [56] Olmsted DL, Holm EA, Foiles SM. Survey of computed grain boundary properties in face-centered cubic metals—II: Grain boundary mobility. *Acta Mater* 2009;57:3704–13.
- [57] Whitesell HS, Li L, Overfelt RA. Influence of solidification variables on the dendrite arm spacings of Ni-based superalloys. *Metall Mater Trans B* 2000;31:546–51.
- [58] Xue X, Xu L. Numerical simulation and prediction of solidification structure and mechanical property of a superalloy turbine blade. *Mater Sci Eng A* 2009;499:69–73.
- [59] Kostic S, Golubovic A, Valcic A. Primary and secondary dendrite spacing of Ni-based superalloy single crystals. *J Serbian Chem Soc* 2009;74:61–9.
- [60] Zhang J, Li J, Jin T, Sun X, Hu Z. Effect of solidification parameters on the microstructure and creep property of a single crystal Ni-base superalloy. *J Mater Sci Technol* 2010;26:889–94.
- [61] Liu C, Shen J, Zhang J, Lou L. Effect of withdrawal rates on microstructure and creep strength of a single crystal superalloy processed by LMC. *J Mater Sci Technol* 2010;26:306–10.
- [62] Franke MM, Hilbinger RM, Konrad CH, Glatzel U, Singer RF. Numerical determination of secondary dendrite arm spacing for IN738LC investment castings. *Metall Mater Trans A* 2010;42:1847–53.
- [63] Hunt JD. *Solidification and casting of metals*. London: The Metals Society; 1979.
- [64] Kurz W, Fisher DJ. *Fundamentals of solidification*. Fourth rev. Aedermannsdorf, Switzerland: Trans Tech Publications; 1998.
- [65] Bouse GK, Mihalisin JR. *Superalloys, supercomposites and superceramics*. London: Academic Press Inc.; 1989.
- [66] Quested PN, McLean M. Solidification morphologies in directionally solidified superalloys. *Mater Sci Eng* 1984;65:171–80.
- [67] Vijayakumar M, Tewari SN, Lee JE, Curreri PA. Dendrite spacings in directionally solidified superalloy PWA-1480. *Mater Sci Eng A* 1991;132:195–201.

References

- [68] Kim H., Earthman J., Lavernia E. Directional solidification of Ni₃Al. *Acta Metall Mater* 1992;40:637–47.
- [69] Lapin J, Klimová A, Velíšek R, Kursa M. Directional solidification of NiAlCrFe alloy. *Scr Mater* 1997;37:85–91.
- [70] Zhang Y, Huang B, Li J. Microstructural evolution with a wide range of solidification cooling rates in a Ni-based superalloy. *Metall Mater Trans A* 2013;44:1641–4.
- [71] Zhang W, Liu L, Zhao X, Huang T, Yu Z, Qu M, et al. Effect of cooling rates on dendrite spacings of directionally solidified DZ125 alloy under high thermal gradient. *Rare Met* 2009;28:633–8.
- [72] Sun F, Mao S, Zhang J. Identification of the partitioning characteristics of refractory elements in σ and γ phases of Ni-based single crystal superalloys based on first principles. *Mater Chem Phys* 2014;147:483–7.
- [73] Liu G, Liu L, Ai C, Ge B, Zhang J, Fu H. Influence of withdrawal rate on the microstructure of Ni-base single-crystal superalloys containing Re and Ru. *J Alloys Compd* 2011;509:5866–72.
- [74] Harris K EG, Schwer RE. Mar-M247 derivations - CM247 LC DS alloy, CMSX single crystal alloys, properties and performance. In: Gell M, Kortovich CS, Bricknell RH KW, Radvich JF, editors. *Proc. 5th Int. Symp. Superalloys, USA: TMS; 1984, p. 221–30.*
- [75] Caron P, Khan T. Improvement of creep strength in a nickel-base single-crystal superalloy by heat treatment. *Mater Sci Eng* 1983;61:173–84.
- [76] Nathal M V. Effect of initial gamma prime size on the elevated temperature creep properties of single crystal nickel base superalloys. *Metall Trans A* 1987;18:1961–70.
- [77] Booth-Morrison C, Noebe RD, Seidman DN. Effects of a tantalum addition on the morphological and compositional evolution of a model Ni-Al-Cr superalloy. In: Reed R, Green K, Caron P, editors. *Superalloys 2008, Minerals, Metals & Materials Society, 184 Thorn Hill RD USA; p. 73–9.*
- [78] Giamei AF, Anton DL. Rhenium additions to a Ni-base superalloy: Effects on microstructure. *Metall Trans A* 1985;16:1997–2005.
- [79] Ricks RA, Porter AJ, Ecob RC. The growth of γ' precipitates in nickel-base superalloys. *Acta Metall* 1983;31:43–53.

References

- [80] Ardell A. The effect of volume fraction on particle coarsening: theoretical considerations. *Acta Metall* 1972;20:61–71.
- [81] Thornton K. Large-scale simulations of Ostwald ripening in elastically stressed solids: I. Development of microstructure. *Acta Mater* 2004;52:1353–64.
- [82] Fährmann M, Fratzl P, Paris O, Fährmann E, Johnson WC. Influence of coherency stress on microstructural evolution in model Ni-Al-Mo alloys. *Acta Metall Mater* 1995;43:1007–22.
- [83] Klepser CA. Effect of continuous cooling rate on the precipitation of gamma prime in nickel-based superalloys. *Scr Metall Mater* 1995;33:589–96.
- [84] Wang F, Ma D, Zhang J, Liu L, Bogner S, Bührig-Polaczek A. Effect of local cooling rates on the microstructures of single crystal CMSX-6 superalloy: A comparative assessment of the Bridgman and the downward directional solidification processes. *J Alloys Compd* 2014;616:102–9.
- [85] Wang F, Ma D, Zhang J, Liu L, Hong J, Bogner S, et al. Effect of solidification parameters on the microstructures of superalloy CMSX-6 formed during the downward directional solidification process. *J Cryst Growth* 2014;389:47–54.
- [86] Yang A, Xiong Y, Liu L. Effect of cooling rate on the morphology of γ' precipitates in a nickel-base superalloy under directional solidification. *Sci Technol Adv Mater* 2001;2:105–7.
- [87] MacSleyne J, Uchic MD, Simmons JP, De Graef M. Three-dimensional analysis of secondary γ' precipitates in René-88 DT and UMF-20 superalloys. *Acta Mater* 2009;57:6251–67.
- [88] Paulonis D, Oblak J, Duvall D. Precipitation in nickel-base alloy 718. *ASM Trans Q* 1969;62:611 – &.
- [89] Cozar R, Pineau A. Morphology of gamma-prime and gamma-double prime precipitates and thermal stability of inconel 718 type alloys. *Metall Trans* 1973;4:47–59.
- [90] Tan XP, Mangelinck D, Perrin-Pellegrino C, Rougier L, Gandin C-A, Jacot A, et al. Atom probe tomography of secondary γ' precipitation in a single crystal Ni-based superalloy after isothermal aging at 1100°C. *J Alloys Compd* 2014;611:389–94.
- [91] Wilson BC, Fuchs GE. The effect of secondary gamma-prime on the primary creep behavior of single-crystal nickel-base superalloys. *Metall Mater Trans A* 2009;41:1235–45.

References

- [92] Tsai Y-L, Wang S-F, Bor H-Y, Hsu Y-F. Effects of alloy elements on microstructure and creep properties of fine-grained nickel-based superalloys at moderate temperatures. *Mater Sci Eng A* 2013;571:155–60.
- [93] Mitchell A, Cockcroft S, Schvezov C, Schmalz A, Loquet J, Fernihough J. Primary carbide and nitride precipitation in superalloys containing niobium. *High Temp Mater Process* 1996;15:27–40.
- [94] Liu LR, Jin T, Zhao NR, Sun XF, Guan HR, Hu ZQ. Formation of carbides and their effects on stress rupture of a Ni-base single crystal superalloy. *Mater Sci Eng A* 2003;361:191–7.
- [95] Szczotok A, Rodak K. Microstructural studies of carbides in Mar-M247 nickel-based superalloy. *IOP Conf Ser Mater Sci Eng* 2012;35:012006.
- [96] Yang J, Zheng Q, Sun X, Guan H, Hu Z. Relative stability of carbides and their effects on the properties of K465 superalloy. *Mater Sci Eng A* 2006;429:341–7.
- [97] Chen QZ, Jones CN, Knowles DM. Effect of alloying chemistry on MC carbide morphology in modified RR2072 and RR2086 SX superalloys. *Scr Mater* 2002;47:669–75.
- [98] Bor HY, Chao CG, Ma CY. The influence of magnesium on carbide characteristics and creep behavior of the Mar-M247 superalloy. *Scr Mater* 1997;38:329–35.
- [99] He LZ, Zheng Q, Sun XF, Hou GC, Guan HR, Hu ZQ. M23C6 precipitation behavior in a Ni-base superalloy M963. *J Mater Sci* 2005;40:2959–64.
- [100] Zhang W, Liu L, Fu H. Effect of cooling rate on MC carbide in directionally solidified nickel-based superalloy under high thermal gradient. *China Foundry* 2012;9:11–4.
- [101] Auburtin P, Cockcroft SL MA. Liquid density inversions during the solidification of superalloys and their relationship freckle formation in casting. In: Kissinger RD, Deye DJ AD et al., editor. *Superalloys*, Warrendale: TMS; 1996, p. 443.
- [102] Jinxia Y, Qi Z, Xiaofeng S, Hengrong G, Zhuangqi H. Morphological evolution of MC carbide in K465 superalloy. *J Mater Sci* 2006;41:6476–8.
- [103] Safari J, Nategh S. On the heat treatment of Rene-80 nickel-base superalloy. *J Mater Process Technol* 2006;176:240–50.

References

- [104] Yang JX, Zheng Q, Sun XF, Guan HR, Hu ZQ. Topologically close-packed phase precipitation in a nickel-base superalloy during thermal exposure. *Mater Sci Eng A* 2007;465:100–8.
- [105] Qin XZ, Guo JT, Yuan C, Chen CL, Hou JS, Ye HQ. Decomposition of primary MC carbide and its effects on the fracture behaviors of a cast Ni-base superalloy. *Mater Sci Eng A* 2008;485:74–9.
- [106] Lvov G, Levit VI, Kaufman MJ. Mechanism of primary MC carbide decomposition in Ni-base superalloys. *Metall Mater Trans A* 2004;35:1669–79.
- [107] Zhao K, Ma YH, Lou LH. Improvement of creep rupture strength of a liquid metal cooling directionally solidified nickel-base superalloy by carbides. *J Alloys Compd* 2009;475:648–51.
- [108] Stevens RA, Flewitt PEJ. The effects of γ' precipitate coarsening during isothermal aging and creep of the nickel-base superalloy IN-738. *Mater Sci Eng* 1979;37:237–47. doi:10.1016/0025-5416(79)90157-5.
- [109] Koul AK, Castillo R. Assessment of service induced microstructural damage and its rejuvenation in turbine blades. *Metall Trans A* 1988;19:2049–66.
- [110] He LZ, Zheng Q, Sun XF, Guan HR, Hu ZQ, Tieu a. K, et al. Effect of heat treatment on microstructures and tensile properties of Ni-base superalloy M963. *Mater Sci Eng A* 2005;398:128–36.
- [111] Kotval PS, Venables JD, Calder RW. The role of hafnium in modifying the microstructure of cast nickel-base superalloys. *Metall Trans* 1972;3:457–62.
- [112] Panwisawas C, Mathur H, Gebelin J-C, Putman D, Rae CMF, Reed RC. Prediction of recrystallization in investment cast single-crystal superalloys. *Acta Mater* 2013;61:51–66.
- [113] Bor HY, Chao CG, Ma CY. The effects of Mg microaddition on the mechanical behavior and fracture mechanism of Mar-M247 superalloy at elevated temperatures. *Metall Mater Trans A* 1999;30:551–61.
- [114] Liu L, Sommer F, Fu HZ. Effect of solidification conditions on MC carbides in a nickel-base superalloy IN 738 LC. *Scr Metall Mater* 1994;30:587–91.
- [115] Li XW, Wang L, Dong JS, Lou LH. Effect of solidification condition and carbon content on the morphology of MC carbide in directionally solidified nickel-base superalloys. *J Mater Sci Technol* 2014:1–5.

References

- [116] Fernandez R, LeComte JC, Kattamis TZ. Effect of solidification parameters on the growth geometry of MC carbide in IN- 100 dendritic monocrystals. *Metall Trans A* 1978;9:1381–6.
- [117] Wang HM, Zhang JH, Tang YJ, Hu ZQ, Yukawa N, Morinaga M, et al. Rapidly solidified MC carbide morphologies of a laser-glazed single-crystal nickel-base superalloy. *Mater Sci Eng A* 1992;156:109–16.
- [118] Yu Z, Liu L, Zhao X, Zhang W, Zhang J, Fu H. Effect of solidification rate on MC-type carbide morphology in single crystal Ni-base superalloy AM3. *Trans Nonferrous Met Soc China* 2010;20:1835–40.
- [119] Zickler GA, Radis R, Schnitzer R, Kozeschnik E, Stockinger M, Leitner H. The precipitation behavior of superalloy ATI Allvac 718Plus. *Adv Eng Mater* 2010;12:176–83.
- [120] Seo SM, Lee JH, Yoo YS, Jo CY, Miyahara H, Ogi K. A comparative study of the γ/γ' eutectic evolution during the solidification of Ni-base superalloys. *Metall Mater Trans A* 2011;42:3150–9.
- [121] Karunaratne MSA, Rae CMF, Reed RC. On the microstructural instability of an experimental nickel-based single-crystal superalloy. *Metall Mater Trans A* 2001;32:2409–21.
- [122] Gasko KL, Janowski GM, Pletka BJ. The influence of γ/γ' eutectic on the mechanical properties of conventionally cast Mar-M247. *Mater Sci Eng A* 1988;104:1–8.
- [123] Groh J. Effect of cooling rate from solution heat treatment on waspaloy microstructure and properties. In: Kissinger R D , Deye D J, Anton D L, Cetel A D, Nathal M V, Pollock T M WDA, editor. *Superalloys 1996*, Minerals, Metals & Materials SOC, 184 Thorn hill RD, Warrendale, USA; 1996, p. 621–6.
- [124] Gabb TP, Gayda J, Telesman J, Garg A, Glenn N, Rd B. The effects of heat treatment and microstructure variations on disk 2008:121–30.
- [125] Kramb RC, Antony MM, Semiatin SL. Homogenization of a nickel-base superalloy ingot material. *Scr Mater* 2006;54:1645–9.
- [126] Hegde SR, Kearsey RM, Beddoes JC. Designing homogenization–solution heat treatments for single crystal superalloys. *Mater Sci Eng A* 2010;527:5528–38.
- [127] Semiatin SL, Kramb RC, Turner RE, Zhang F, Antony MM. Analysis of the homogenization of a nickel-base superalloy. *Scr Mater* 2004;51:491–5.

References

- [128] Fuchs GE. Solution heat treatment response of a third generation single crystal Ni-base superalloy. *Mater Sci Eng A* 2001;300:52–60.
- [129] Wolff IM. Precipitation accompanying overheating in nickel-base superalloy. *Mater Charact* 1992;29:55–61.
- [130] Huang HE, Koo CH. Effect of solution-treatment on microstructure and mechanical properties of cast fine-grain CM 247 LC superalloy. *Mater Trans* 2004;45:1360–6.
- [131] Soucail M, Messina R, Cosnuau a, Kubin L. Monte Carlo simulation of Zener pinning in two dimensions. *Mater Sci Eng A* 1999;271:1–7.
- [132] Song K, Aindow M. Grain boundary curvature in a model Ni-based superalloy. *Metall Mater Trans A* 2007;38:1–6.
- [133] Zhao S, Xie X, Smith GD, Patel SJ. Gamma prime coarsening and age-hardening behaviors in a new nickel base superalloy. *Mater Lett* 2004;58:1784–7.
- [134] Kim H, Chun S, Yao X, Fang Y, Choi J. Gamma prime (γ') precipitating and ageing behaviours in two newly developed nickel-base superalloys. *J Mater Sci* 1997;32:4917–23.
- [135] Zengwu T, Jinshan L, Rui H, Yi L, Guanghai B. Effects of solution heat treatment on carbide of Ni-Cr-W superalloy. *Rare Met Mater Eng* 2010;39:1157–61.
- [136] Hu Q, Liu L, Zhao X, Gao S, Zhang J, Fu H. Effect of carbon and boron additions on segregation behavior of directionally solidified nickel-base superalloys with rhenium. *Trans Nonferrous Met Soc China* 2013;23:3257–64.
- [137] Tien JK, Collier JP, Vignoul G. The role of niobium and other refractory elements in superalloys. In: Loria EA, editor. *Superalloy, USA*: TMS; 1989, p. 553–66.
- [138] Tien JK, Jarrett RN. Effects of cobalt in nickel-base superalloys. In: Brunetaud R, Coutouradis D, Gibbons TB, Lindblom Y, Meadowcroft DB SR, editor. *High Temp. Alloy. Gas Turbines 1982*, Springer Netherlands; 1982, p. 423–46.
- [139] Furrer D, Semiatin SL, editors. *ASM handbook:metals process simulation*. Ohio: ASM International; 2010.
- [140] ProCast user Manual & Technical Reference. Version 6. France: ESI software.
- [141] Rappaz M, Bellet M, Deville M O. *Numerical modeling in materials science and engineering*. Verlag. Berlin, Germany: Springer; 2002.

References

- [142] Pequet C, Gremaud M, Rappaz M. Modeling of microporosity, macroporosity, and pipe-shrinkage formation during the solidification of alloys using a mushy-zone refinement method: Applications to aluminum alloys. *Metall Mater Trans A* 2002;33:2095–106.
- [143] ASM International Handbook Committee. *ASM handbook:casting*. Ohio: ASM International; 2008.
- [144] O’Mahoney D, Browne DJ. Use of experiment and an inverse method to study interface heat transfer during solidification in the investment casting process. *Exp Therm Fluid Sci* 2000;22:111–22.
- [145] Konrad CH, Brunner M, Kyrgyzbaev K, Völkl R, Glatzel U. Determination of heat transfer coefficient and ceramic mold material parameters for alloy IN738LC investment castings. *J Mater Process Technol* 2011;211:181–6.
- [146] Santos C, Quaresma J, Garcia A. Determination of transient interfacial heat transfer coefficients in chill mold castings. *J Alloys Compd* 2001;319:174–86.
- [147] Dong Y, Bu K, Dou Y, Zhang D. Determination of interfacial heat-transfer coefficient during investment-casting process of single-crystal blades. *J Mater Process Technol* 2011;211:2123–31..
- [148] Sahai V, Overfelt RA. Contact conductance simulation for alloy 718 investment casting of various geometries. *Tran Amer F* 1995;103:627–32.
- [149] Yang X, Lee P, Brooks R. The sensitivity of investment casting simulations to the accuracy of thermophysical property values. In: KA Green, Pollock TM, Harada H, editors. *10th Int. Symp. Superalloys*, Champion: TMS; 2004, p. 951–8.
- [150] Brandon DG, Kaplan WD. *Microstructural characterization of materials*. John Wiley & Sons; 2008.
- [151] Goldstein J, Newbury DE, Joy DC, Lyman CE, Echlin P, Lifshin E SL, Michael JR. *Scanning electron microscopy and X-ray microanalysis*. Third ed. 2003.
- [152] Wilkinson AJ, Britton TB. Strains, planes, and EBSD in materials science. *Mater Today* 2012;15:366–76.
- [153] Oxford Instruments PLc. *EBSD Electron Backscatter Diffraction - Educational Website* 2013.
- [154] Oliver W, Pharr G. An improved technique for determining hardness and elastic-modulus using load and displacement sensing indentation experiments. *J Mater Res* 1992;7:1564–83.

References

- [155] Sneddon IN. The relation between load and penetration in the axisymmetric boussinesq problem for a punch of arbitrary profile. *Int J Eng Sci* 1965;3:47–57.
- [156] Cheng YT, Cheng CM. Scaling, dimensional analysis, and indentation measurements. *Mater Sci Eng R Reports* 2004;44:91–149.
- [157] Micro Star Tech. Nano indenters from Micro Star Technologies 2014. <http://www.microstartech.com/>.
- [158] Szczotok A, Sozanska M. A comparison of grain quantitative evaluation performed with standard method of imaging with light microscopy and EBSD analysis. *Pract Metallogr* 2009;46:454–68.
- [159] Dobrzański LA, Maniara R, Sokołowski J, Kasprzak W. Effect of cooling rate on the solidification behavior of AC AlSi7Cu2 alloy. *J Mater Process Technol* 2007;191:317–20.
- [160] Ashby MF, Jones DRH. *Engineering Materials 2*. First edit. UK: 1986.
- [161] Flemings MC. Solidification processing. *Metall Trans* 1974;5:2121–34.
- [162] Kurz W, Fisher DJ. Dendrite growth in eutectic alloys: the coupled zone. *Int Met Rev* 1979;24:177–204.
- [163] Hellawell A. The growth and structure of eutectics with silicon and germanium. *Prog Mater Sci* 1970;15:3–78.
- [164] LLorca J, Orera V. Directionally solidified eutectic ceramic oxides. *Prog Mater Sci* 2006;51:711–809.
- [165] Milenkovic S, Sabirov I, LLorca J. Effect of the cooling rate on microstructure and hardness of Mar-M247 Ni-based superalloy. *Mater Lett* 2012;73:216–9.
- [166] Furrer DU, Shankar R, White C. Optimizing the heat treatment of Ni-based superalloy turbine discs. *JOM* 2003;55:32–4.
- [167] Tan M., Zhang X. Powder metal matrix composites: selection and processing. *Mater Sci Eng A* 1998;244:80–5.
- [168] Rahimian M, Parvin N, Ehsani N. Investigation of particle size and amount of alumina on microstructure and mechanical properties of Al matrix composite made by powder metallurgy. *Mater Sci Eng A* 2010;527:1031–8.
- [169] Razak AMY. *Industrial gas turbines: Performance and operability*. Cambridge, UK: Woodhead; 2007.
- [170] Gonzalez M, Goldschmit MB, Assanelli AP, Dvorkin EN, Berdaguer EF. Modeling of the solidification process in a continuous casting installation for steel slabs. *Metall Mater Trans B* 2003;34:455–73.

References

- [171] Guo J, Samonds M. Modeling of casting and solidification processes. In: Furrer D, Semiatin SL, editors. ASM handbookmetals Process Simul. Vol. 22B, ASM International; 2010.
- [172] Rahimian M, Milenkovic S, Sabirov I. A physical simulation study of the effect of thermal variations on the secondary dendrite arm spacing in a Ni-based superalloy. *Philos Mag Lett* 2014;94:86–94.
- [173] Milenkovic S, Rahimian M, Sabirov I. A novel high-throughput technique for establishing the solidification-microstructure relationships. *Metall Mater Trans B* 2013;45:482–8.
- [174] Chen ZW. Skin solidification during high pressure die casting of Al-11Si-2Cu-1Fe alloy. *Mater Sci Eng A* 2003;348:145–53.
- [175] Yang KV, Easton M a., Cáceres CH. The effect of solidification dynamics on the formation of the skin in die cast Mg-Al and Mg-RE alloys. *Adv Eng Mater* 2013;15:302–7.
- [176] Shan Z, Gokhale AM. Utility of micro-indentation technique for characterization of the constitutive behavior of skin and interior microstructures of die-cast magnesium alloys. *Mater Sci Eng A* 2003;361:267–74.
- [177] Zhang J, Zhang M, Meng J, Wu R, Tang D. Microstructures and mechanical properties of heat-resistant high-pressure die-cast Mg-4Al-xLa-0.3Mn (x=1, 2, 4, 6) alloys. *Mater Sci Eng A* 2010;527:2527–37.
- [178] Peng Q, Wang L, Wu Y, Wang L. Structure stability and strengthening mechanism of die-cast Mg-Gd-Dy based alloy. *J Alloys Compd* 2009;469:587–92.
- [179] Weiler JP, Wood JT, Klassen RJ, Berkmortel R, Wang G. Variability of skin thickness in an AM60B magnesium alloy die-casting. *Mater Sci Eng A* 2006;419:297–305.
- [180] Song J, Xiong S-M, Li M, Allison J. In situ observation of tensile deformation of high-pressure die-cast specimens of AM50 alloy. *Mater Sci Eng A* 2009;520:197–201.
- [181] Barresi J, Chen Z, Davidson C, Murray M, Nguyen T, Stjohn D, et al. Casting of aluminium alloy components. *Mater Forum* 1996;20.
- [182] Zupanič F, Bončina T, Lojen G, Markoli B, Spaić S. Structure of the continuously cast Ni-based superalloy GMR 235. *J Mater Process Technol* 2007;186:200–6.

References

- [183] Schendera C, Schwarz S, Möser M, Müller T. Advanced Die Casting Simulation for a Systematical Development of Magnesium Structural Components. In: Kainer KU, editor. *Magnes. Proc. 6th Int. Conf. Magnes. Alloy. Their Appl.*, Weinheim, FRG: Wiley-VCH Verlag GmbH & Co. KGaA; 2003, p. 811–6.
- [184] Boonmee S, Stefanescu D. On the mechanism of casting skin formation in compacted graphite cast iron. *Int J Met* 2009;19–24.
- [185] Watanabe T, Fujii H, Oikawa H, Arai K. Grain boundaries in rapidly solidified and annealed Fe-6.5 mass% Si polycrystalline ribbons with high ductility. *Acta Metall* 1989;37:941–52.
- [186] Kovarik L, Unocic RR, Li J, Sarosi P, Shen C, Wang Y, et al. Microtwinning and other shearing mechanisms at intermediate temperatures in Ni-based superalloys. *Prog Mater Sci* 2009;54:839–73.
- [187] Boonmee S, Stefanescu D. Effect of casting skin on fatigue properties of CG iron. *Int J Met* 2013:15–26.
- [188] Durst K, Göken M. Micromechanical characterisation of the influence of rhenium on the mechanical properties in nickel-base superalloys. *Mater Sci Eng A* 2004;387-389:312–6.
- [189] Hysitron Inc. Strength engineering in a Nickel-base superalloy. Hysitron Inc 2014.
- [190] Pollock TM, Argon AS. Creep resistance of CMSX-3 nickel base superalloy single crystals. *Acta Metall Mater* 1992;40:1–30.

8 Publications

Peer-reviewed journals:

- ❖ M. Rahimian, S. Milenkovic, L. Maestro, A. Eguidazu Ruiz De Azua, I. Sabirov “Physical simulation of investment casting of complex shape parts” **Metallurgical and Materials Transactions A**, 46A (2015) 2015-2227.
DOI: 10.1007/s11661-015-2815-6
- ❖ A.J. Torroba, O. Koeser, L. Calba, L. Maestro, E. Carreno-Morelli, M. Rahimian, S. Milenkovic, I. Sabirov, J. LLorca “Investment casting of nozzle guide vanes from Ni-based superalloys: Part I - Thermal calibration and porosity prediction” **Integrating Materials and Manufacturing Innovation**, (2014) 3:25.
DOI: 10.1186/s40192-014-0025-5
- ❖ A.J. Torroba, O. Koeser, L. Calba, L. Maestro, E. Carreno-Morelli, M. Rahimian, S. Milenkovic, I. Sabirov, J. LLorca “Investment casting of nozzle guide vanes from Ni-based superalloys: Part II - Grain structure prediction” **Integrating Materials and Manufacturing Innovation**, (2014) 3:26.
DOI: 10.1186/s40192-014-0026-4
- ❖ M. Rahimian, S. Milenkovic, I. Sabirov “A physical simulation study of the effect of thermal variations on the secondary dendrite arm spacing in a Ni-based superalloy” **Philosophical Magazine Letters**, 94(2) (2014) 86-94.
DOI: 10.1080/09500839.2013.870670
- ❖ S. Milenkovic, M. Rahimian, I. Sabirov “A Novel High-throughput Technique for Establishing the Solidification-Microstructure Relationships” **Metallurgical and Materials Transactions B**, 45B (2014) 482-488.
DOI: 10.1007/s11663-013-9846-4
- ❖ M. Rahimian, S. Milenkovic, I. Sabirov “Microstructure and hardness evolution in MAR-M247 Ni-based superalloy processed by controlled cooling and double heat treatment” **Journal of Alloys and Compounds**, 550 (2013) 339–344.
DOI: <http://dx.doi.org/10.1016/j.jallcom.2012.10.129>
- ❖ S. Milenkovic, M. Rahimian, I. Sabirov, L. Maestro “Effect of solidification parameters on the secondary dendrite arm spacing in MAR M-247 superalloy determined by a novel approach **MATEC Web of Conferences 14**, 13004 (2014).
- ❖ M. Rahimian, S. Milenkovic, L. Maestro, A. Eguidazu Ruiz De Azua, I. Sabirov “Physical simulation of skin formation in investment casting” **Journal of Materials Processing Technology**, Submitted.